Dissertation
submitted to the
Combined Faculties for the Natural Sciences and for Mathematics
of the Ruperto-Carola University of Heidelberg, Germany
for the degree of
Doctor of Natural Science

Put forward by
Dipl.-Phys. Dominikus Heinzeller
born in Weilheim i. OB (Germany)
Oral examination: July 16th 2008

Black hole accretion disks

Sources of viscosity and signatures of super-Eddington accretion

Referees: Prof. Dr. Wolfgang J. Duschl
Prof. Dr. Shin Mineshige

Zusammenfassung

Akkretionsscheiben um Schwarze Löcher
Quellen der Viskosität und Spuren von über-Eddington Akkretion

Wir untersuchen die Rolle der Konvektion in Akkretionsscheiben um Schwarze Löcher, insbesondere den Einfluss auf den Energietransport und die Auswirkung konvektiver Turbulenz auf die Viskosität in der Scheibe. Wir zeigen, dass Konvektion den Energietransport durch Strahlung im Falle einer masselosen Scheibe effizient unterstützt, während es im umgekehrten Fall einer selbstgravitierenden Scheibe zu negativen Rückkopplungseffekten kommt. Obwohl konvektive Turbulenz einen signifikanten Beitrag zur gesamten Viskosität leistet, kann sie nicht alleine als Erklärung dafür dienen.

Im zweiten Teil untersuchen wir die spektrale Energieverteilung von über-Eddington akkretierenden Schwarzen Löchern, basierend auf 2D strahlungs-hydrodynamischen Simulationsdaten. Wir berechnen die Kontinuumemission und die Emission und Absorption der Eisen-K-Linien mittels einer Ray-tracing Methode. Wir zeigen, dass relativistische Beaming-Effekte für frontal betrachtete Scheiben zu über-Eddington Leuchtkräften führen. Die Eisen-Linien erweisen sich als guter Indikator für den Akkretionsprozess in den inneren Scheibenregionen: Es zeigt sich eine enge Korrelation zwischen dem Verhältnis der K_β-Linien zu den K_α Linen und der Zentralmasse, sowie zwischen der Linienbreite und dem Beobachtungswinkel.

Abstract

Black hole accretion disks
Sources of viscosity and signatures of super-Eddington accretion

We study the role of convection in black hole accretion flows. We investigate the influence of convection on the energy transport as well as the effect of convective turbulence on the disk's viscosity. The results reveal that convection supports the radiative energy transport efficiently in massless disks, while it can turn into a negative feedback if self-gravity becomes important. Convective turbulence adds significantly to the total viscosity, but cannot account for it on its own.

In the second part, we study the spectral energy distribution of super-Eddington accretion flows onto a black hole, based on 2D RHD simulation data. We model the continuum emission as well as the iron K line emission and absorption features with a ray-tracing radiative transfer code. We find that mild relativistic beaming effects become important, leading to super-Eddington luminosities for face-on seen disks. We confirm the diagnostic power of the iron K lines on the accretion process in the inner disk region, finding a strong correlation between the central black hole mass and the ratio of the K_α to the K_β lines. We also detect a trend of line broadening for edge-on seen disks.

Contents

1 A small bubble in the Universe

> *When I began my physical studies [in Munich in 1874] and sought advice from my venerable teacher Philipp von Jolly … he portrayed to me physics as a highly developed, almost fully matured science … Possibly in one or another nook there would perhaps be a dust particle or a small bubble to be examined and classified, but the system as a whole stood there fairly secured, and theoretical physics approached visibly that degree of perfection which, for example, geometry has had already for centuries.*
>
> – from a 1924 lecture by Max Planck (Sci. Am, Feb 1996)

On the very day when this introduction was written (April 23, 2008), we were celebrating the 150^{th} birthday of Max Planck. Fortunately, Planck decided to study physics despite the bleak future for research that was presented to him. In 1901, he published an article with the title “On the Law of Distribution of Energy in the Normal Spectrum”, describing the spectral radiance of electromagnetic radiation at all wavelengths of a blackbody at a given temperature. This was not only the cornerstone in his career, it also paved the way for modern physics and astronomy. Only through Planck’s law, astronomers were able to model the emitted spectrum of a star, a blackbody radiator in zeroth order, without running into the ultraviolett catastrophe. Quantum mechanics and atomic physics would not exist without this fundamental discovery.

Nowadays, more than 100 years later, we know that von Jolly could not have been further off the mark. Although our understanding of the Universe broadened to an extent almost beyond belief, it seems that with the answer of one question, at least ten others are rising. And so it happens that this thesis deals with two out of many open questions in one of von Jolly’s small bubbles. And even there, we again encounter Planck’s blackbody radiation law and its offsprings in atomic physics.

In this dissertation, we study the properties of accretion disks around black holes. Having called them one of von Jolly’s small bubbles, it needs to be put into the right context. Yes, it is certainly only one corner of physics where questions remain to be answered. At the same time, accretion disks are ubiquitous! They can be found almost everywhere in the Universe, from today back in time until the Cosmos was less than one million years old, from sizes of about one solar radius (10^{11}cm) in low mass X-ray binary systems up to one parsec (10^{18}cm) in active galactic nuclei, and around a wealth of objects like protostars, white dwarfs, neutron stars or black holes. Despite this huge variety, the driving physical principle, the accretion of matter onto a central object through a disk-like structure, remains the same. Understanding the key process of accretion is therefore one of the big challenges, but also one of the big chances of astronomy in the 21^{st} century. Here, we investigate two pixels of the overall picture.

The source of viscosity in astrophysical disks Theoretical modeling of accretion disks dates back to the year 1948, when Weizsäcker published his article about the rotation of cosmic gas (Weizsäcker, 1948). A key ingredient to describe the accretion process is the origin of the viscosity, which causes friction in the disk and an inward motion of the material. In those early years, it was generally believed that molecular viscosity is responsable for this effect. However, the first observations of accretion disks in cataclysmic variables, which allowed to deduce the typical timescales of the accretion process, threw over the theoretical expectations (see, e. g., Prendergast & Burbidge (1968); Pringle & Rees (1972)). They revealed, that the numbers measured in the lab and those needed to account for the observations differed by about ten orders of magnitude. The following decades saw a plethora of attempts to resolve this puzzling situation, but none of them succeeded. Only Shakura & Sunyaev (1973) proposed a parameterization, the α-viscosity, by which all of a sudden most observations could be fitted adequately. Despite this success, the Shakura-Sunyaev viscosity remains a purely empirical description and no physical explanation, and it is limited to thin disks with negligible disk masses.

Among the physical theories, the most promising ones are:

- **Differential rotation.** Accretion disks are mostly showing a nearly Keplerian rotation profile. An obvious candidate for the turbulence in such a disk is therefore differential rotation. From early laboratory experiments on rotating Couette-Taylor flows (Wendt, 1933; Taylor, 1936), this possibility was first ruled out. However, in recent re-investigations, Richard & Zahn (1999) and Richard (2001) concluded that differential rotation can give rise to turbulence, despite published arguments. At the same time, Duschl et al. (2000) formulated the β-viscosity description. Although being a parameterization like its ancestor, it can actually be related to the process of differential rotation. Contrary to the α-prescription, the β-viscosity accounts properly for the selfgravity of the disk. At the same time, it includes the α-viscosity in the case of a shock dissipation limited, non-selfgravitating disk.

- **Convection.** The process of accretion is the most efficient way of producing energy, outclassing nuclear fission by a factor of at least 100. In order to account for the transport of these huge amounts of energy, convection is considered to support or even dominate in some cases over radiation. It is therefore natural to regard the turbulence caused by convective motion as a possible candidate for viscosity. Again, first (semi-)analytical investigations gave discouraging results, since they led to hugely massive disks which could not be explained, given the α-viscosity description (Vila, 1981; Duschl, 1989). Ruden et al. (1988); Ryu & Goodman (1992) studied convective instabilities in thin gaseous disks and confirmed that angular momentum transport can be supported by convective turbulence. Goldman & Wandel (1995) investigated accretion disks where viscosity is given by convection solely and where the energy transport is maintained by radiation and convection. They found the resulting viscosity being too low by a factor of 10 to 100, but could not draw a final conclusion, since their disk model was oversimplified.[1]

- **Magneto-rotational instability.** The magneto-rotational instability (MRI) was first noticed in a non-astrophysical context by Velikhov (1959); Chandrasekhar (1960) when considering the stability of a Taylor-Couette flow of an ideal hydromagnetic fluid. More than

---

[1] The authors applied a one-zone approximation (c. f., Sect.2.1) in their models and estimated the contribution of convection to the energy transport in an overly simple way.

> 30 years later, these early results were brought back to life when Balbus & Hawley (1991) established, that weak magnetic fields can substantially alter the stability character of accretion disks, giving rise to a generic and efficient angular momentum transport. Today, the MRI is considered as the primary candidate for solving the long lasting riddle of viscosity in disk accretion flows. Yet again, we find ourselves in one of von Jolly's nooks, since the MRI basically requires two essential conditions to hold. Firstly, the angular velocity has to decrease with the distance from the central object. Secondly, a (weak) poloidal magnetic field must be present. While the former criterium is usually met in accretion disks, the latter one can pose a severe problem. A further weak point are magneto-rotationally stable *dead zones* in disks (see Sect. 3.7 for a further discussion). More fundamental, King et al. (2007) pointed out a discrepancy of at least one order of magnitude between the viscosities generated by the MRI and those inferred from observations.

Thus, the question if one of these candidates, a combination of them, or even some other process is responsible for generating viscosity in astrophysical disks, is very much open. In their conclusions, Goldman & Wandel (1995) stressed the need for a convective disk model where the vertical structure is calculated self-consistently. We follow their suggestion in Chapt. 3 and construct a disk model where we calculate the effect of convection in a self-consistent way by means of the mixing-length theory. Hereby, the total viscosity is given by convection and a supporting β-viscosity, accounting for turbulence due to differential rotation and allowing or potential self-gravitating effects. Beforehand, in Chapt. 2, we discuss the limitations of the β-viscosity as a description of subsonic turbulence, i. e., the constraints of the shock dissipation limit on these disks. There, we also investigate a possible feedback of convection on the upward energy transport, i. e., a downward motion of heat-carrying elements, in preparation for Chapt. 3.

Spectral energy distribution of super-Eddington flows In the second part of this thesis, we investigate the long standing problem of the limit on the accretion rate onto a black hole. This topic became a matter of debate already in the 1970's (Begelman, 1978; Burger & Katz, 1980) and the final word is not yet spoken. In earlier work, we showed that the classical Eddington limit cannot be applied in a straightforward way to the accretion disk case (Heinzeller & Duschl, 2007). The major difference to the stellar case is the different geometry, which leads to an anisotropic limit. Along with that, the accretion rate may exceed the value derived from the classical limit significantly. This is mainly due to the fact that apart from radiation, energy can be transported efficiently by other processes such as advection in the disk. This has not been taken into account in the classical calculations. However, numerous investigations have been carried out in order to circumvent the limitations imposed by the Eddington limit (see Sect. 4.1 for a further discussion).

The final answer to this question will have a considerable impact on our understanding of accretion physics: over the whole range of central black hole masses, from stellar mass black holes with a few solar masses up to supermassive black holes (SMBH) with up to one billion solar masses, key questions about their formation and evolution remain to be answered. Here, we focus on one important aspect.

Ultraluminous X-ray sources: Do they contain intermediate mass black holes or not? Recent observations of ultraluminous X-ray sources (ULX, see e. g. Makishima et al. (2000); Kubota et al. (2006)) reveal a puzzling situation for black hole accretion theories. With a bolometric luminosity exceeding $10^{39}\,\mathrm{erg\,s^{-1}}$ (derived from X-ray observations), at least some of

Figure 1.1. The Seyfert 2 galaxies M51 (left) and M102 (right). Although the central engine in both galaxies works in a similar way, their appearance on the sky is completely different. While the dense disk blocks the emitted radiation from the core of the edge-on oriented M102, the face-on view on M51 allows a close look at the central region. Credits: Hubble Heritage Team.

them show relatively low radiation temperatures (~ 0.1 keV). These systems have been suggested to be intermediate mass black hole, sub-Eddington accretion disk systems (Miller et al., 2003; Cropper et al., 2004). Controversially, from time-variability observations, it seems to be likely that these objects are instead low-mass X-ray binary systems (Liu et al., 2002). Radio observations show that the distribution of ULXs can as well be fitted by stellar mass black holes with mildly relativistic jets (Körding et al., 2004).

The substantial amount of observational data from X-ray satellites such as *Chandra*, *XMM-Newton* or *Suzaku*, also reveals that a distinct class of ULX sources exists, showing higher temperatures – sometimes exceeding 1 keV – than can be explained by IMBHs. Contrary, stellar mass black holes accreting above their Eddington limit can account for these sources (Watarai et al., 2001; Ebisawa et al., 2003; Vierdayanti et al., 2006). Alternatively, mild beaming effects could be important (King et al., 2001). A controversial debate about the origin of ULXs is still ongoing (see, for example, Roberts (2007) for a review).

A key point for a proper understanding and interpretation is the comparison with theory. Considerable efforts have been made in the last decades to model black hole accretion disks in detail, which are partially summarized in Sect. 4.1. Among them, Ohsuga et al. (2005); Ohsuga (2007) performed two-dimensional radiation-hydrodynamic simulations (2D RHD) of super-Eddington accretion flows onto a central black hole. We investigate the spectral energy distribution of their results by focussing on the continuum emission features in Chapt. 4. Main emphasis is thereby the influence of the orientation of the disk relative to the observer, in order to study the consequences of anisotropy and beaming effects in super-Eddington accretion flows. To illustrate the impact of the orientation of such a disk relative to the observer, we display the two Seyfert 2 galaxies M51 (*Whirlpool Galaxy*) and M102 (*Spindle Galaxy*) in Fig. 1.1.

Of great interest are not only the continuum spectra of accretion disk systems. Atomic and molecular lines offer the chance to measure rotation/outflow velocities through red- or blueshifted lines. They also allow to constrain temperature, pressure and density, or even strong gravitational effects in the vicinity of a black hole from line profiles and strengths (relative to each other and to the continuum). The potential diagnostic power of discrete line emission and absorption features, which has been attracting theorists and observers for decades, is reviewed in great detail in Miller (2007). In the high energy regime, the iron K lines are of particular importance, not only because iron is the most abundant element in space (about 8% in mass of

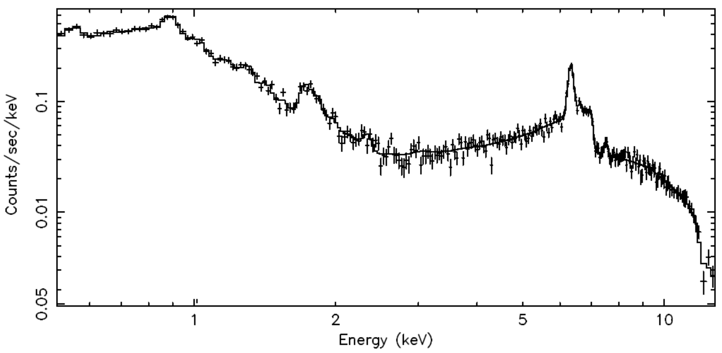

Figure 1.2. Prominent iron K line emission in Mrk 3, observed with *XMM-Newton* (Bianchi et al., 2005).

all metals), but also because its K lines are very strong transitions in a relatively unconfused spectral region between 6 keV and 9 keV. Iron K line observations show a long history, with first detections being reported from rocket observations of the supernova remnant Cas A (Serlemitsos et al., 1973). So it is no wonder, that the availability and accuracy of atomic data is unique among the heavy elements.

With the sensitivity and resolution of modern X-ray telescopes, also iron line observations in black hole accretion disks became possible in the last decade. In particular in the case of supermassive black holes in quasars and Seyfert galaxies, significant progress has been made. The observations vary greatly, showing strong and broad emission lines (e. g., in the Seyfert 2 galaxy Mrk3 (Bianchi et al., 2005), see Fig. 1.2), complex absorption features with broad and narrow emission lines (e. g., in the Seyfert 1.5 galaxy NGC3516 (Markowitz et al., 2008)) and also highly blueshifted and extremely strong emission lines (e. g., in the Seyfert 1 galaxy PG1402+261 (Reeves et al., 2004)). The situation is more complicated in the case of accretion flows around potential low mass black holes (i. e. ULXs), due to their relative weakness. Iron K line observations are therefore limited to a handful of objects, such as M82 X-1 (see below). However, the spectacular progress of each generation of X-ray telescopes over the last decades gives rise to hope that this situation will change in the near future.

In the light of the recent successes in both theory and observation, we extend our investigation of the spectral energy distribution of super-Eddington flows towards a modeling of the iron K lines (Chapt. 5). We thereby take advantage of the existing radiative transfer code from the first stage of the project, which is fully parallelized and therefore can be run on modern cluster computers with high efficiency. We apply the calculations to extended data sets of the original 2D RHD simulations (Ohsuga (2007) and Ohsuga, priv. comm.) with varying accretion rates and different central black hole masses between 10 and 10^8 solar masses. We also extrapolate the available sets of simulation data to the specific case of M82 X-1 and compare our theoretical spectra with observations by *Chandra* and *XMM-Newton* (Sect. 5.6).

Remark. We choose the cgs-system as system of units in all following studies. If not explicitly stated, all numbers are given/displayed in their corresponding cgs-units. The physical constants used on this work are listed in the appendix (Table A.1 on page 129).

2 The diffusion limit and convective feedback in selfgravitating disks

2.1 Introduction

In this chapter, we present a simple accretion disk model to investigate the influence of the turbulent backcoupling on the energy transport in disks, similar to earlier work by Duschl (1983). Since we want to investigate not only disks with negligible masses (compared to the central object), but also with comparable or even dominating masses, we apply the β-viscosity description (Duschl et al., 2000). In standard disk theories, the viscosity parameter β is taken to be constant and in principle only limited by an upper value $\beta_{\rm max} \ll 1$. However, it is well known that for a too high value of β, a diffusion limit has to be applied (c. f., the discussion below and in Duschl et al. (2000)).

To avoid the additional introduction of a diffusion limit, we first investigate disk models where we limit β by an upper value $\beta_{\rm max}$, but allow it to be reduced, if necessary. Subsequently, we discuss the contribution of turbulent backcoupling to the overall energy transport in Sect. 2.5.

2.2 Model setup

The principal disk geometry is displayed in Fig. 2.1 (upper plot), where we also introduce the main geometrical variables. A cylindrical coordinate system is the natural choice for such a system, in particular under the general assumption of azimuthal symmetry. We distinguish between the 3-dimensional radius r and the planar radius s in the disk plane. In the limiting case of a thin disk with disk height $h = h(s) \ll s$, one gets $r \approx s$.

The lower two plots in Fig. 2.1 sketch two standard methods to calculate geometrically thin accretion disks. The simplest approximation is the so-called one-zone approximation, where the problem reduces to a one-dimensional calculation by using only integrated values for the vertical structure. Somewhat more sophisticated is the 1+1-dimensional calculation. Here, one assumes that the vertical structure decouples from the radial one, which splits the two-dimensional problem into two one-dimensional problems. This simplification is only possible as long as the disk is sufficiently thin, which, for example, causes the vertical structure to react instantaneously to changes of the radial disk properties.

We derive the disk equations in this chapter under the following assumptions: (1) stationarity, (2) no relativistic effects, (3) monopole approximation for the disk's gravitational potential Φ, (4) Kramer's opacity as description of the scattering and absorption processes, (5) β-viscosity as introduced by Duschl et al. (2000), (6) geometrically thin disk, (7) one-zone approximation. In that context, the disk equations are given as follows: the continuity equation reduces to

$$\dot{M} = -2\pi s v_s \Sigma\,, \tag{2.1}$$

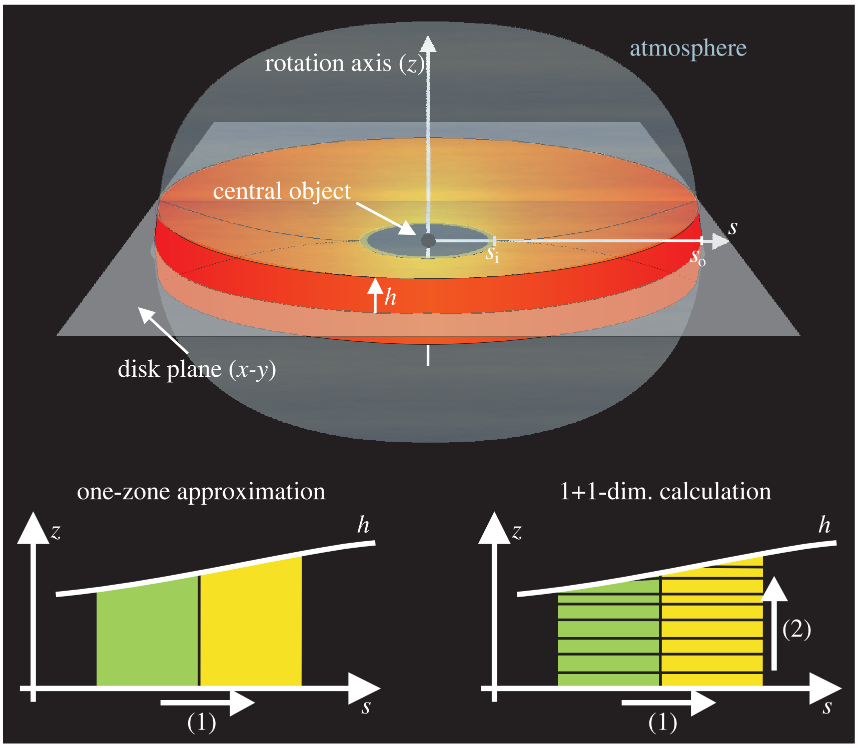

Figure 2.1. Principal disk geometry and the two commonly used methods for simplifying the two-dimensional problem. The general assumption hereby is the azimuthal symmetry of the disk.

where $\dot{M}$ denotes the accretion rate, v_s the radial velocity in the disk and Σ the integrated surface density. The momentum equation – with ω being the angular velocity, M_c the mass of the central object and $M_\mathrm{d}(s)$ the enclosed disk mass – gets

$$\omega^2 = \frac{G(M_\mathrm{c} + M_\mathrm{d}(s))}{s^3} \tag{2.2}$$

The angular momentum equation is given by

$$-\omega\dot{M} = 2\pi s\nu\Sigma\frac{\partial\omega}{\partial s} + \frac{C_1}{s^2}\,, \tag{2.3}$$

where ν stands for the viscosity and C_1 is a constant of integration which remains to be set, for example at the inner boundary s_i. The hydrostatic equilibrium in the monopole approximation becomes

$$p = \frac{G(M_\mathrm{c} + M_\mathrm{d}(s))\rho}{s}\cdot\frac{h^2}{s^2} + \pi G\Sigma^2\,, \tag{2.4}$$

with the total pressure p, while the energy equation can be written as follows:

$$\underbrace{\frac{1}{2}\nu\Sigma s^2\left(\frac{\partial\omega}{\partial s}\right)^2}_{F_+} = \underbrace{\frac{2acT^4}{3\kappa\Sigma}}_{F_-}\,. \tag{2.5}$$

Thus, all energy dissipated in the accretion flow is radiated from the disk, and the internal energy remains unchanged. We use the standard equation of state for gas and radiation:

$$p = p_{\text{gas}} + p_{\text{rad}} = \rho \frac{k_{\text{B}} T}{\mu m_{\text{H}}} + \frac{a_{\text{rad}}}{3} T^4 \,. \tag{2.6}$$

The Kramer's opacity is expressed as

$$\kappa = \kappa_{\text{es}} + \kappa_0 \rho T^{-7/2} = 0.4 \,\frac{\text{cm}^2}{g} + 6.4 \cdot 10^{21}\, T[\text{K}]^{-7/2}\, \rho[\text{g/cm}^3]\, \frac{\text{cm}^2}{g} \,. \tag{2.7}$$

The β-viscosity is given as usual by (for the definition of the “parameter” β, see Sect. 2.2.2):

$$\nu = \beta s^2 \omega \,. \tag{2.8}$$

We further define the disk's mass, inner disk radius and sound speed by

$$\begin{aligned} M_{\text{d}}(s) &= 2\pi \int_{s_{\text{i}}}^{s} s\Sigma \, ds \,, & (2.9)\\ \Sigma &= 2\rho h \,, & (2.10)\\ s_{\text{i}} &= 3 r_{\text{S}} = \frac{6GM_{\text{c}}}{c^2} \,, & (2.11)\\ c_{\text{s}}^2 &= p/\rho \,, & (2.12) \end{aligned}$$

where r_{S} denotes the Schwarzschild radius (we assume a non-rotating Schwarzschild black hole). For the sound speed, the pressure and density are taken from the disk plane as usual. With $M_{\text{d}}(s_{\text{i}}) = 0$ (2.9), we obtain the angular velocity from (2.2) as

$$\omega(s_{\text{i}}) = \omega_{\text{K}}(s_{\text{i}}) = \frac{GM_{\text{c}}}{s_{\text{i}}^3} \tag{2.13}$$

and its derivative as

$$\left.\frac{\partial \omega}{\partial s}\right|_{s=s_{\text{i}}} = -\frac{3}{2} \frac{\omega_{\text{K}}(s_{\text{i}})}{s_{\text{i}}} \,. \tag{2.14}$$

2.2.1 Boundary condition

We set the boundary condition as usual at the inner disk radius s_{i}. The classical boundary condition in thin accretion disk theories is a vanishing torque at the inner boundary of the disk, corresponding to $C_1 = 1 \cdot \dot{M} s_{\text{i}}^2 \omega(s_{\text{i}})$. In this case, the angular momentum equation (2.3) becomes

$$\nu\Sigma = -\frac{\dot{M}}{2\pi s (\partial\omega/\partial s)} \left(\omega(s) - 1 \cdot \frac{s_{\text{i}}^2}{s^2} \omega(s_{\text{i}}) \right) \,.$$

The other extreme case is full Keplerian rotation at the inner boundary, which is realized by $C_1 = 0 \cdot \dot{M} s_{\text{i}}^2 \omega(s_{\text{i}}) = 0$, with a simple angular momentum equation of the form

$$\nu\Sigma = -\frac{\dot{M}\omega(s)}{2\pi s (\partial\omega/\partial s)} \,.$$

The latter case is purely theoretical, since it implies that the accretion process is effectively stopped at s_i if there is no other mechanism to extract angular momentum in the small boundary layer region. But even if there is, a significant amount of energy needs to be transferred from the plunging region into the disk to maintain the overall energy balance (see, e. g., Duschl & Tscharnuter (1991) for a further discussion).

For a general treatment, we define a parameter χ with $C_1 = \chi \cdot \dot{M} s_\mathrm{i}^2 \omega(s_\mathrm{i})$. The angular momentum equation (2.3) is then given by

$$\nu\Sigma = -\frac{\dot{M}}{2\pi s(\partial\omega/\partial s)}\left(\omega(s) - \chi \cdot \frac{s_\mathrm{i}^2}{s^2}\omega(s_\mathrm{i})\right) . \tag{2.15}$$

for $0 \leq \chi \leq 1$. We will investigate the influence of this parameter χ in Sect. 2.3. Nonetheless, we derive a special value for it from the following idea: the value of χ defines which fraction of the Keplerian angular momentum is still carried by the material arriving at the inner boundary. For $\chi = 0$, the material circulates with the local Keplerian angular velocity, $l(s_\mathrm{i}) = l_\mathrm{K}(s_\mathrm{i})$, and therefore cannot be accreted by the central black hole. Contrary, $\chi = 1$ means that the material holds no angular momentum anymore and can fall freely onto the black hole. However, this extreme situation causes numerical problems at the inner boundary, since $\nu\Sigma = 0$ at $s = s_\mathrm{i}$. Therefore, we ask for the minimum value of χ in order to allow the material to reach the central object. In the case of a Schwarzschild black hole, this corresponds to a Keplerian angular momentum at the Schwarzschild radius $r_\mathrm{S} = 2GM_\mathrm{c}/c^2$. With $s_\mathrm{i} = 3r_\mathrm{S}$ and $M_\mathrm{d} = 0$ for $s \leq s_\mathrm{i}$ (see (2.9)),

$$l_K(r_\mathrm{S}) = \sqrt{GM_\mathrm{c} r_\mathrm{S}} = \sqrt{\frac{GM_\mathrm{c} s_\mathrm{i}}{3}} = \frac{l_\mathrm{K}(s_\mathrm{i})}{\sqrt{3}}$$

We define $\chi_* := 1 - 1/\sqrt{3} \approx 0.423$, which will be used as standard value in the following. Although being exact in the simple model considered here, the value of χ_* will change, if, for example, the black hole spin or the magnetic field are included in the description of the disk's inner region. For $\chi_* = 0.423$, the integrated disk luminosity gets 1.08 times the gravitational energy released by the accretion process down to s_i. Thus, a small amount of energy needs to be injected into the disk from the plunging region (between s_i and r_S), where twice as much potential energy is released as in the disk (between s_o and s_i). There is also the fact that the boundary layer in this disk model is assumed to be infinitely small, which is of course not realistic. An extended boundary layer can allow for energy exchange between these regions (Duschl & Tscharnuter, 1991).

2.2.2 Adaptable viscosity parameter β and numerical techniques

The viscosity is given by (2.8). Usually, a diffusion limit is added in the case that the turbulent velocity $v_\mathrm{turb} \approx \sqrt{\beta} v_\varphi$ exceeds the local sound speed c_s.

$$\sqrt{\beta} v_\varphi > c_\mathrm{s} \Longrightarrow \nu_\mathrm{DL} = \eta^2 c_\mathrm{s}^2 \left|\frac{\partial v_\varphi}{\partial s}\right|^{-1} \tag{2.16}$$

with an additional parameter $\eta \lessapprox 1$. For turbulent velocities exceeding the local sound speed, shock fronts would be created, leading to a shock dissipation limited regime. Up to now, no reliable and handsome theory of supersonic turbulence exists that covers these effects.

In the following, we propose a different mathematical mechanism to avoid supersonic turbulent velocities. Before presenting the details, we discuss the main properties of our numerical calculation: for simplicity, we adopt an explicit Eulerian scheme with logarithmic equidistant step size. Since the calculations are quite cheap, a sufficiently small step size can be chosen by default (see below). The boundary conditions are given at the inner radius, therefore we start the calculation at $s = s_\mathrm{i}$ and stop at $s_\mathrm{o} \gg s_\mathrm{i}$. Here, we use $s_\mathrm{o} = 10^3 s_\mathrm{i}$ and divide the calculation into $N_n = 5000$ steps in radii: $s_n = s_\mathrm{i} \cdot 10^{0.0006 \cdot n}$.

We define an upper limit β_max, which is of the order of the usual β parameter (e. g., 10^{-3}). If the condition $\sqrt{\beta_\mathrm{max}} v_\varphi > c_\mathrm{s}$ becomes true during the calculation, we decrease β by $\xi\beta_\mathrm{max}$, $\xi < 1$, and repeat the calculation for step n. This iteration is performed until $\sqrt{\beta} v_\varphi = c_\mathrm{s}$. Thereby, two requirements have to be fulfilled: (a) the behavior of β as a function of radius s has to be sufficiently smooth, and (b) the reduction of β by $\xi\beta_\mathrm{max}$ has to be small, compared to the actual value of the viscosity parameter – these conditions remain to be checked afterwards.

The calculation starts at the inner boundary s_i. By substituting ν with (2.8) in the angular momentum equation (2.15) at the inner boundary and using (2.2) with (2.9), we get an initial equation for Σ:

$$\Sigma_\mathrm{i} = \frac{\dot{M}}{3\pi\beta_\mathrm{i} s_\mathrm{i}^2 \omega_\mathrm{K}(s_\mathrm{i})}(1 - \chi)\,. \tag{2.17}$$

With the aid of the remaining disk equations and definitions, all quantities can be calculated for s_i. In detail, the equations can be reduced to a system of two non-linear equations for T and ρ, which are solved by a Newtonian iterative scheme.

The numerical step $n \to n+1$ is performed by calculating the disk's mass $M_\mathrm{d}(s)$ from (2.9), the angular velocity from the momentum equation (2.2) and its derivative from

$$\left.\frac{\partial\omega}{\partial s}\right|_{s=s_n} \approx \frac{\omega(s_n) - \omega(s_{n-1})}{s_n - s_{n-1}}\,. \tag{2.18}$$

Then, Σ and all other variables can be calculated from the remaining equations. Again, if the turbulent velocity exceeds the sound speed in step n, the parameter β is reduced and the calculation for step n is repeated until $v_\mathrm{turb} = c_\mathrm{s}$.

2.3 Results

In this section, we present the results for our new disk model. We investigate the influence of three parameters in the following subsections: the accretion rate $\dot{M}$ (Sect. 2.3.1), the inner boundary condition χ (Sect. 2.3.2) and the viscosity parameter β_max (Sect. 2.3.3). In all calculations, a standard setup is used:

$$\begin{aligned} M_\mathrm{c} &= 10 M_\odot\,, \\ s_\mathrm{i} &= 8.86 \cdot 10^6\,\mathrm{cm}\,, \\ s_\mathrm{o} &= 10^3 s_\mathrm{i}\,, \\ N_n &= 5 \cdot 10^3\,, \\ \xi &= 10^{-4}\,. \end{aligned} \tag{2.19}$$

$\dot{M}/\dot{M}_\mathrm{E}$	10^{-3}	10^{-2}	10^{-1}	10^{0}	10^{+1}
s_0/s_i	1.000	1.000	8.544	117.8	—

Table 2.1. Radius s_0 of innermost β-correction.

2.3.1 Influence of $\dot{M}$

To explore the influence of the accretion rate, we set $\chi = \chi_* = 0.423$ and $\beta_\mathrm{max} = 10^{-3}$. Figure 2.2 shows the disk properties for varying accretion rates between $10^{-3}\dot{M}_\mathrm{E}$ and $10^{1}\dot{M}_\mathrm{E}$. The Eddington accretion rate for $M_\mathrm{c} = 10M_\odot$ is given by $\dot{M}_E = 1.67 \cdot 10^{19}\mathrm{g/s}$.

The overall expectation of an increasing height of the disk for higher accretion rates can be recovered from the figures. The high accretion rate cases $\dot{M} = \{1, 10\}\dot{M}_\mathrm{E}$ significantly violate the thin disk approximation in the inner part of the disk. The shape of the disk height is influenced by the actual value of β, as are the other disk quantities: while for high accretion rates, the default value $\beta_\mathrm{max} = 10^{-3}$ is always allowed, for lower accretion rates the limit $\sqrt{\beta_\mathrm{max}}v_\varphi = c_\mathrm{s}$ is violated at radius s_0, which is listed in Table 2.1 and which decreases the lower the accretion rates are.

This drop in β is directly translated into smaller radial inflow velocities and higher surface densities Σ for $s \gtrapprox s_0$. This leads to an increase in densities ρ and temperatures T, which results in a rising pressure p by means of the equation of state (2.6).

For even larger radii, the viscosity “parameter” β adopts a minimum value and starts to increase again, while ρ, p and T are decreasing. The behavior of Σ is determined mostly by the density ρ and therefore also shows a significant peak for $s \gtrapprox s_0$.

Since the disk mass M_d remains negligible for all accretion rates, the azimuthal velocity is identical for all accretion rates. As a first guess, this may be due to the small extent of the disk, $s_\mathrm{o} = 10^3 s_\mathrm{i}$. We therefore repeat the calculations for the same physical parameters, but with $s_\mathrm{o} = 10^6 s_\mathrm{i}$ and $N_n = 5 \cdot 10^6$. For all accretion rates between $10^{-3}\dot{M}$ and $10^{1}\dot{M}$, we obtain final disk masses between $10^{-8}M_\mathrm{c}$ and $10^{-5}M_\mathrm{c}$. Thus, the disk mass remains negligible also for extended disks.

Contrary to the azimuthal motion, the sound speed c_s strongly depends on $\dot{M}$: for high accretion rates and small radii (large ratio of h/s), the rotational velocity becomes subsonic, as expected from the thin disk relation $h/s = c_\mathrm{s}/v_\varphi$. Accordingly, for low accretion rates $c_\mathrm{s} \ll v_\varphi$ always holds. At $s = s_0$, the slope of c_s flattens. Due to the decrease in β, the viscosity ν is smaller in the diffusion limited regions. This effect becomes significantly stronger the lower the accretion rate is.

An interesting competition between mass supply by accretion and radial inflow velocities can be seen in the exact profile of M_d: when the accretion rate is decreased, in a first instance the surface density and therefore the disk mass decrease, too. But, as we outlined before, the radial inflow velocities decrease due to the down-correction of β, which forces the disk mass to increase again.

The opacity κ is dominated by electron scattering as long as the temperature is high enough. Only for large radii and small accretion rates, atomic absorption comes into play and increases the opacity up to $1\,\mathrm{cm}^2/\mathrm{g}$. The composition of the total pressure p also depends strongly on the accretion rate. For high $\dot{M}$, radiation pressure dominates p, while for low accretion rates, gas pressure determines the local pressure throughout all radii.

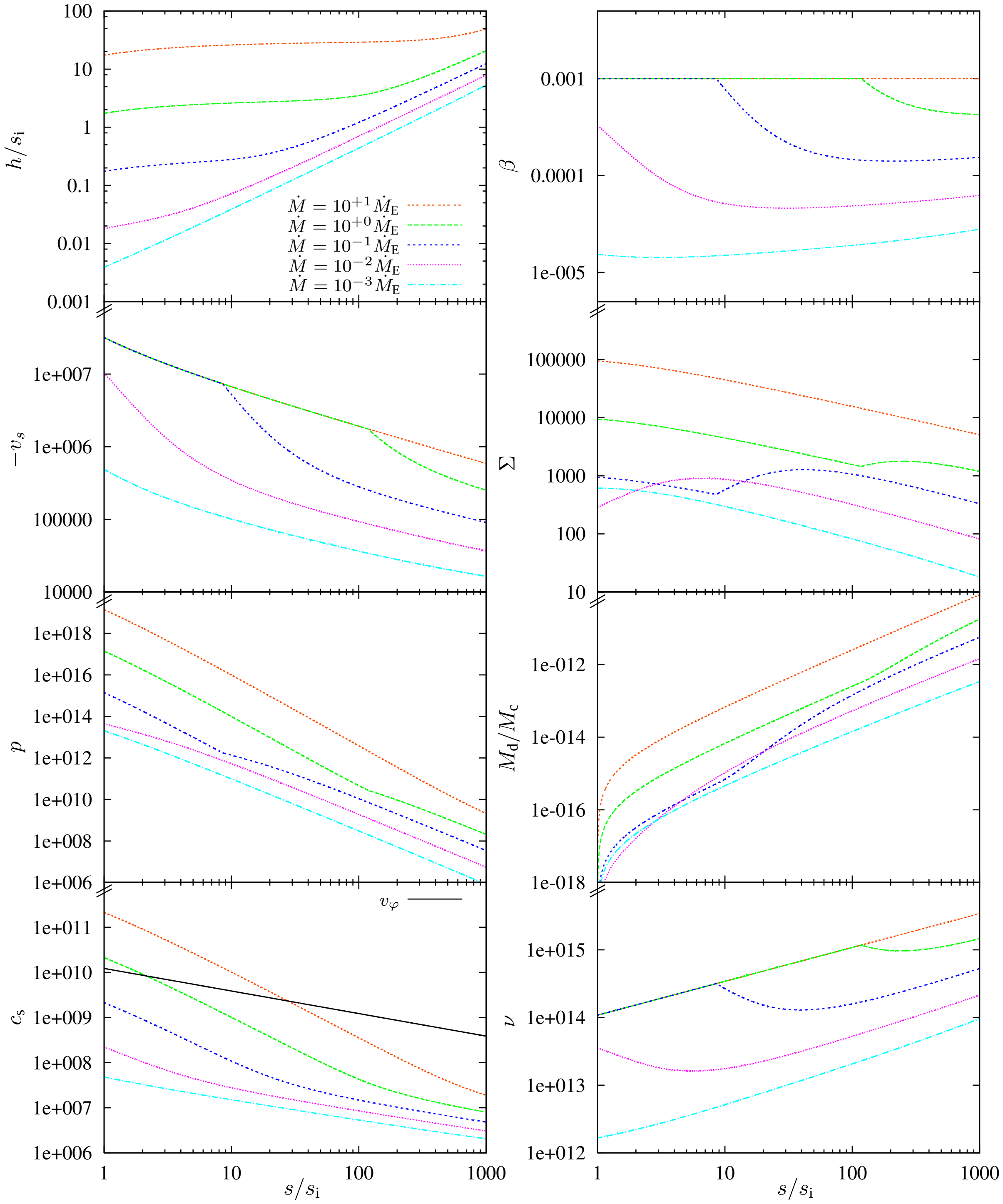

Figure 2.2. Steady state β-disk model for $\dot{M} = \{10^{-3}, 10^{-2}, 10^{-1}, 1, 10\}\dot{M}_\mathrm{E}$.

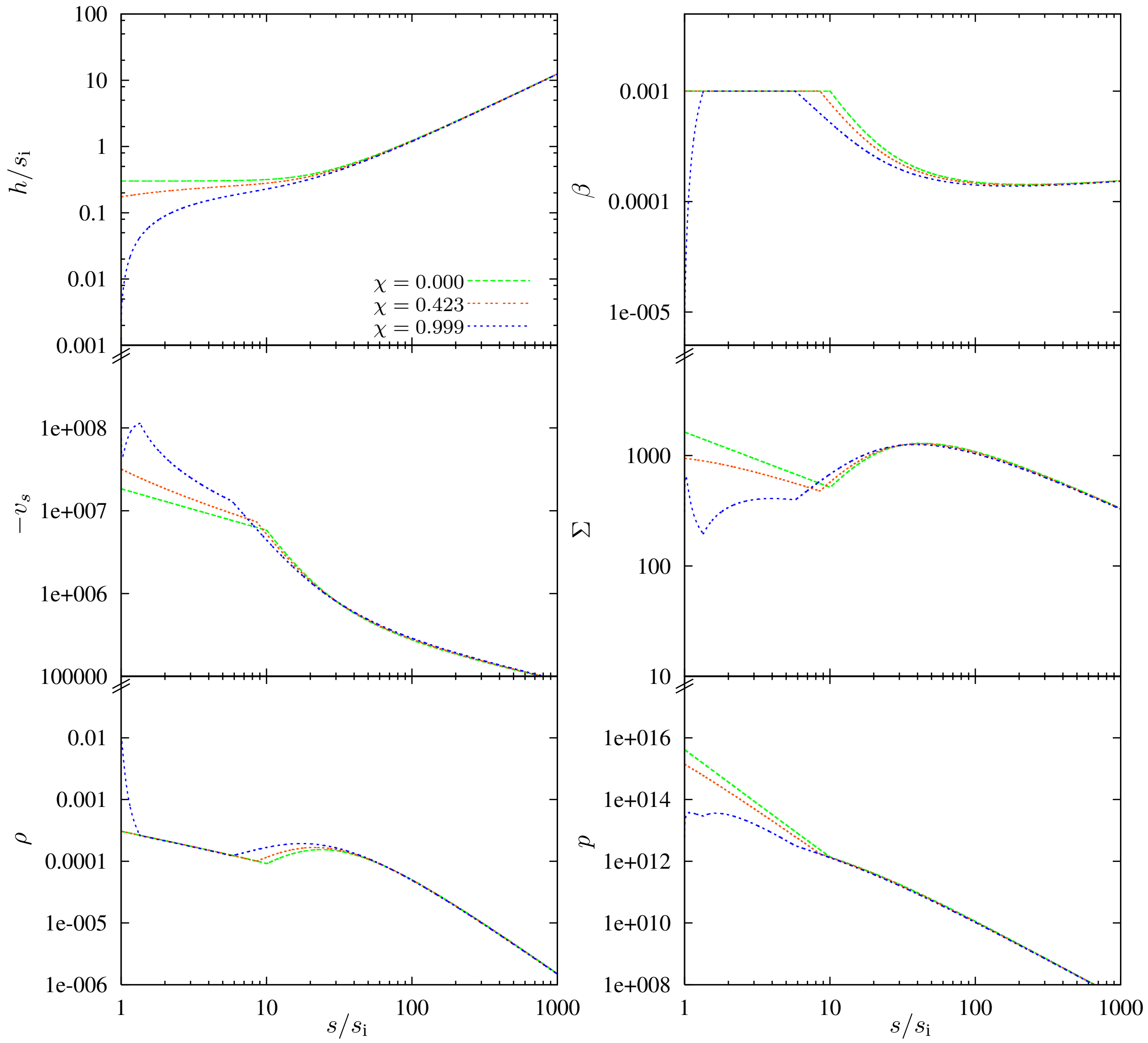

Figure 2.3. Steady state β-disk model for $\chi = \{0.000, 0.423, 0.999\}$.

2.3.2 Influence of χ

In this section, we investigate the effects of the boundary condition at the disk's inner radius s_i with fixed accretion rate $\dot{M} = 10^{-1}\dot{M}_\mathrm{E}$ and $\beta_\text{max} = 10^{-3}$. The parameter χ varies between 0 and 0.999, which is close to the torque-free case. To avoid numerical difficulties, we use $\chi = 0.999$ as the largest χ, instead of 1. The results are displayed in Fig. 2.3.

The shape of the curves is now determined by two effects: firstly, by the decrease in β at $s \geq s_0$, where s_0 varies between $5s_\mathrm{i}$ ($\chi = 0.999$) and $10s_\mathrm{i}$ ($\chi = 0$); secondly, by the different boundary conditions at $s = s_\mathrm{i}$. The latter effect can only be seen in the inner part of the disk, $s \lessapprox 30s_\mathrm{i}$, due to the factor s_i^2/s^2 in the angular momentum equation (2.15).

In the torque-free case, $\chi = 0.999$, the height of the disk decreases sharply for $s \longrightarrow s_\mathrm{i}$. Contrary, for $\chi = 0$, it adopts a constant value. For standard β-disks, one expects that $\nu\Sigma \longrightarrow 0$ for $\chi \longrightarrow 1$ (see (2.15)), and $v_s \longrightarrow \infty$ (see (2.1)). But here, the parameter β is reduced drastically for $s \lessapprox 1.3s_\mathrm{i}$ and $\chi = 1$, which leads to a sharp increase in Σ and ρ and to a rapid drop in v_s

for the same radii. For $1.3s_{\rm i} \leq s \leq 10s_{\rm i}$, the viscosity parameter adopts its maximum value $\beta_{\rm max}$ and the disk models approach each other. Thus, the boundary condition not only has a direct influence on the inner disk structure, but also an indirect one through the onset of the shock dissipation limit for larger values of χ.

Although a change in χ only affects the very inner disk regions, this might be very important: Fukue (2000, 2004) and Heinzeller & Duschl (2007) showed that the innermost disk region is crucial for the determination of an Eddington-type limit for accretion disks. They found a significant decrease in the maximum amount of matter that can be accreted by the black hole (i. e., the critical accretion rate).

2.3.3 Influence of $\beta_{\rm max}$

Of great importance is also the influence of the viscosity parameter on the disk model. Although the value of $\beta_{\rm max}$ can be motivated from hydrodynamic turbulence, it remains an “ad-hoc” parameter. We investigate its effects for the standard setup $\dot{M} = 10^{-1}\dot{M}_{\rm E}$, $\chi = 0.423$, and vary $\beta_{\rm max}$ between 10^{-4} and 10^{-2}. The results are displayed in Fig. 2.4.

The disk height, the sound speed and also the disk mass are hardly influenced by the maximum viscosity parameter. For $\beta_{\rm max} \leq 1.4 \cdot 10^{-4}$, the condition $\sqrt{\beta_{\rm max}} v_\varphi \leq c_{\rm s}$ holds throughout all radii, therefore the results for $\beta_{\rm max} = 10^{-4}$ show a disk which is not affected by our new model for the viscosity. For $\beta_{\rm max} = \{10^{-3}, 10^{-2}\}$, the influence of our viscosity description becomes visible, in particular for the radial velocity, the density and the surface density: in the region where β drops rapidly, the density and surface density are maximal, while the radial inflow velocity decreases.

One interesting point should be mentioned here: as can be seen from Fig. 2.4, the local sound speed $c_{\rm s} = \sqrt{p/\rho}$ is unaffected by the maximum viscosity parameter $\beta_{\rm max}$, although p and ρ depend on its actual value. From the disk equations and the fact that the disk is in a non-selfgravitating state for all values of $\beta_{\rm max}$, we can derive the following scaling laws:

shock dissipation limit	dominant pressure term	scaling of sound speed
no	$p_{\rm rad}$	$c_{\rm s} \propto \beta_{\rm max}^0 = \text{const}$
no	$p_{\rm gas}$	$c_{\rm s} \propto \beta_{\rm max}^{-1/8}$
yes	$p_{\rm rad}, p_{\rm gas}$	$c_{\rm s} \propto \beta_{\rm max}^0 = \text{const}$

The dependence of $c_{\rm s}$ on the upper limit $\beta_{\rm max}$ is (almost) zero in all cases.

2.4 Comparison with the classical diffusion limited case

One could ask for the validity of the iterative calculation of the viscosity parameter β. We therefore investigate its application in comparison with the usually applied diffusion limit introduced in (2.16):

$$\sqrt{\beta_{\rm max}} v_\varphi > c_{\rm s} \Longrightarrow \nu_{\rm DL} = \eta^2 c_{\rm s}^2 \left| \frac{\partial v_\varphi}{\partial s} \right|^{-1} .$$

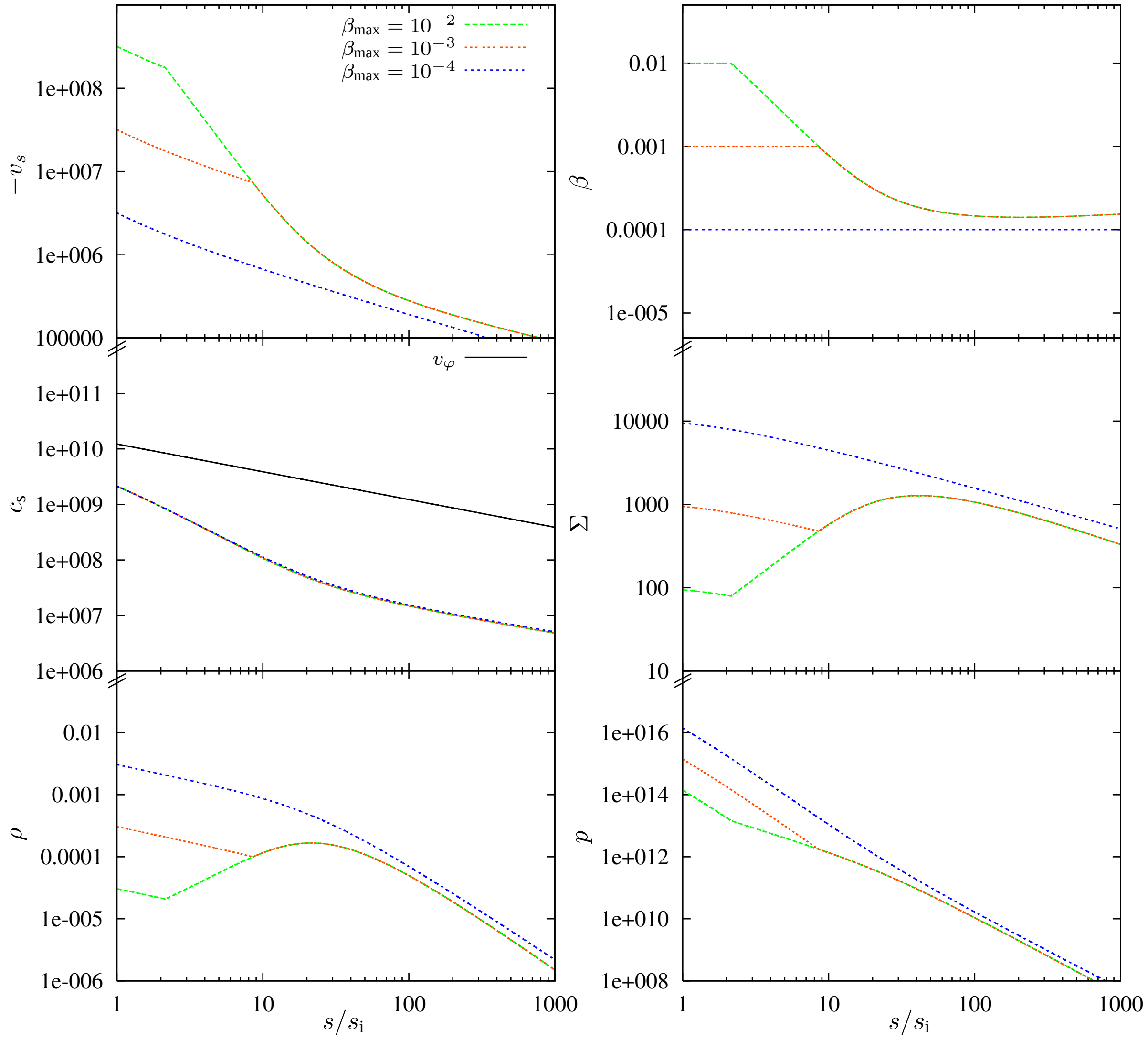

Figure 2.4. Steady state β-disk model for $\beta_{\max} = \{10^{-4}, 10^{-3}, 10^{-2}\}$.

The weakness of (2.16) is, that it requires an additional parameter $\eta \lessapprox 1$, whose value may be chosen somewhat arbitrarily in a first instance. This, however, may lead to discontinuities of the physical variables at the radius s_0. Thus, it needs to be adjusted manually.

In the following, we discuss how this parameter η is related to the value of β when the condition $\sqrt{\beta_{\max}} v_\varphi \leq c_{\mathrm{s}}$ is violated. Suppose that $\sqrt{\beta_{\max}} v_\varphi > c_{\mathrm{s}}$. The actual value of β is decreased in small steps from $\beta_{\max}$ to a value which we may call β^* with

$$\beta^* = c_{\mathrm{s}}^2 / v_\varphi^2 \,. \tag{2.20}$$

By comparing the resulting viscosity (2.8) with the diffusion limit (2.16), we get

$$\beta^* s^2 \omega = \frac{c_{\mathrm{s}}^2}{s^2 \omega^2} \cdot s^2 \omega = \eta^2 c_{\mathrm{s}}^2 \left| \frac{\partial v_\varphi}{\partial s} \right|^{-1} \,. \tag{2.21}$$

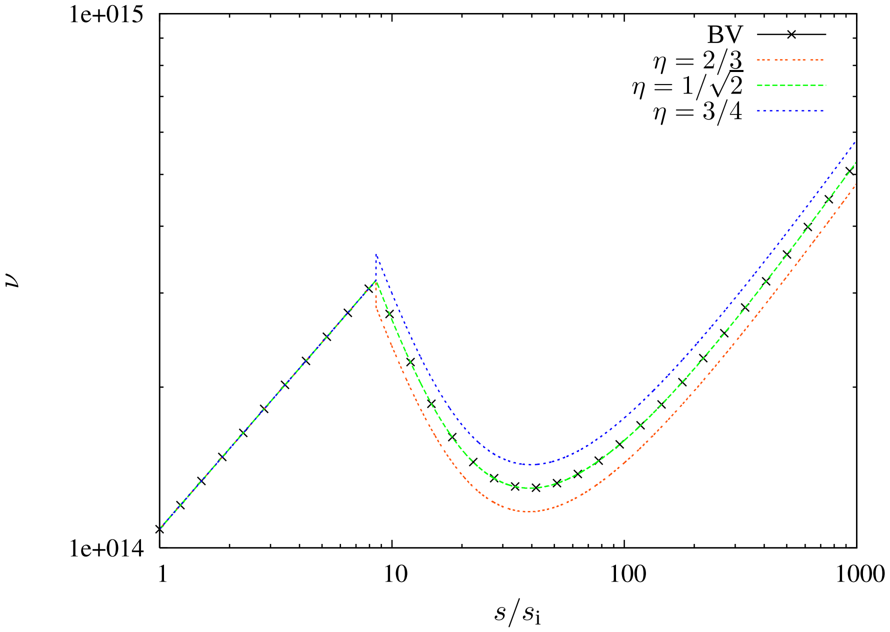

Figure 2.5. Diffusion limited disks (DL) with $\eta = \{2/3, 1/\sqrt{2}, 3/4\}$ and a disk with varying β (BV).

Solving for η^2 and substituting $v_\varphi = s\omega$ leads to

$$\eta^2 = \frac{1}{\omega} \cdot |\omega + s\,\partial\omega/\partial s| \ . \tag{2.22}$$

We discuss two concrete values for special disk cases (NSG: non-selfgravitating, KSG: Keplerian selfgravitating, FSG/Mestel disk: fully selfgravitating):

$$\eta^2 = \begin{cases} \frac{1}{2} & \text{NSG/KSG:} \quad \frac{\partial\omega}{\partial s} = -\frac{3\omega}{2s} \\ 0 & \text{Mestel disks:} \quad v_\varphi = s\omega = \text{const} \Longrightarrow \frac{\partial\omega}{\partial s} = -\frac{\omega}{s} \end{cases} . \tag{2.23}$$

Since $\partial\omega/\partial s < 0 \ \forall \ s$ in the disk models presented here (see (2.3)), it is automatically assured that $\eta < 1$. Interestingly, the „constant“ parameter may become variable in this scenario if, e. g., the outer regions of the diffusion limited zone are self-gravitating, while the inner regions are dominated by the gravitation of the central object. If, on the other hand,

$$\frac{\partial\omega}{\partial s} = A \cdot \frac{\omega}{s}, \qquad A = \text{const}\,, \tag{2.24}$$

the diffusion limit parameter η adopts a constant value – which is unique, since it is given by the requirement of continuity of ν, Σ, … at the radius s_0, where the viscosity parameter β needs to be decreased for the first time. This effect is shown in Fig. 2.5 for the viscosity. Since the disk remains in a non-selfgravitating state for all radii, the diffusion limited disk with $\eta = \text{const} = 1/\sqrt{2}$ gives the same results as a disk with varying viscosity parameter β.

2.5 The influence of turbulence on the energy transport

In this section, we study the influence of turbulence on the energy transport in the sense that we investigate its feedback on the upward energy transport (and not its contribution to it). The latter case will be studied in much more detail in the following chapter. More precisely, we study the following problem.

Consider an accretion disk which is stable with respect to the Schwarzschild criterium (c. f., Sect. 3.7). Then, by definition, convective turbulent motion is shut down. On the other hand, since the accretion process requires viscosity to be at work, this implies that there *must* be some kind of turbulence. Since the stratification is assumed to be Schwarzschild-stable, the turbulent energy transport is formally negative and therefore counteracts the radiative energy transport.

In standard disk theory, all the energy generated by friction (i. e., by viscosity; F_+) is radiated locally (F_-). Thus, if turbulent feedback turns out to transport a non-negligible amount F_turb of energy downwards into the disk, the effective cooling flux F_rad must account for this:

$$F_\text{rad} = F_+ + F_\text{turb} = F_- + F_\text{turb}\,. \tag{2.25}$$

A similar investigation has been carried out by Duschl (1983) in the case of a non-selfgravitating disk with an α-viscosity description. It is straightforward to adapt the method and assumptions to our disk model. Here, we briefly summarize the main aspects of the theory and refer the reader to Duschl (1983) for a detailed explanation.

Based on the mixing length theory, which describes the effects of turbulence on the energy transport (see also Sect. 3.4.1), the author introduces two quantities x and y in the sense that

$$F_\text{rad} = x \cdot \nabla\,, \tag{2.26}$$

$$F_\text{turb} = y \cdot (\nabla - \nabla')\,, \tag{2.27}$$

where $\nabla = d\log T/d\log p$ denotes the average temperature gradient and ∇' the temperature gradient of a falling (or rising) element of matter, both with respect to pressure. From our disk model, the quantities x and y can be calculated as follows:

$$x = 4F_- = 4F_+ = \frac{8acT^4}{3\Sigma\kappa}\,, \tag{2.28}$$

$$y = \frac{1}{2}c_\text{p}\rho T v_\text{turb} = \frac{1}{2}c_\text{p}\rho T\frac{\nu}{h}\,. \tag{2.29}$$

In (2.29), $v_\text{turb} = \nu/h$ stands for the turbulent velocity. The isobaric heat capacity is given by

$$c_\text{p} = \frac{\mathfrak{R}}{\mu} \cdot \frac{32 - 24\gamma - 3\gamma^2}{2\gamma^2}\,, \tag{2.30}$$

where $\gamma = p_\text{gas}/p$ is the ratio of the gas pressure to the total pressure. Based on our assumptions, the radiative energy flux F_rad has to equal or exceed the total flux F_-, since turbulence may generate an energy flux in the opposite direction to the radiative flux. The ratio is given by

$$\frac{F_\text{rad}}{F_-} = 4\frac{\nabla_\text{ad} + \frac{1}{4}\frac{x}{y} + \frac{3}{4}\left(\frac{x}{y}\right)^2}{1 + \frac{x}{y} + 3\left(\frac{x}{y}\right)^2}\,, \tag{2.31}$$

with the adiabatic gradient

$$\nabla_{\text{ad}} = \frac{8-6\gamma}{32-24\gamma-3\gamma^2}\,. \tag{2.32}$$

We discuss the results for a disk with a non-selfgravitating and a self-gravitating region and a β-viscosity description. Therefore, we set the model parameters as follows:

$$\begin{aligned}
M_{\text{c}} &= 10M_{\odot}\,,\\
s_{\text{i}} &= 8.86\cdot 10^{6}\,\text{cm}\,,\\
s_{\text{o}} &= 10^{12}s_{\text{i}}\,,\\
N_n &= 5\cdot 10^{6}\,,\\
\xi &= 10^{-4}\,,\\
\beta_{\text{max}} &= 10^{-3}\,,\\
\dot{M} &= \dot{M}_{\text{E}}\,,\\
\chi &= \chi_{*} \,=\, 1-1/\sqrt{3} = 0.423\,.
\end{aligned} \tag{2.33}$$

The calculations are performed for an adaptable viscosity parameter β (BV) as presented in Sect. 2.2.2, and for a diffusion limited disk with a real calculation of the parameter η (DL) (Sect. 2.4). For comparison, the value of η is calculated also in the non-diffusion limited part of the disk from (2.16). Figures 2.6 and 2.7 show the results of the calculation.

The (identical) disks BV and DL can be divided into several regions by the radial coordinate s, which is summarized in Table 2.2. To understand the increase in F_{rad}/F_{-} in the outer part of the disk, we have to take a closer look at the two figures. In region B, a minimal increase in F_{rad}/F_{-} occurs at the radius where the diffusion limit sets in and where the transition from a pressure dominated to a gas dominated disk takes place. In the outer parts of the disk (regions D and E), the radiation pressure is negligible compared to the gas pressure. Thus, $\gamma = 1$ and

$$c_{\text{p}} = \frac{5}{2}\frac{\mathfrak{R}}{\mu} = \text{const}\,, \tag{2.34}$$

$$\nabla_{\text{ad}} = \frac{2}{5} = \text{const}\,, \tag{2.35}$$

$$\frac{F_{\text{r}}}{F_{-}} = 4\frac{\dfrac{2}{5}+\dfrac{1}{4}\dfrac{x}{y}+\dfrac{3}{4}\left(\dfrac{x}{y}\right)^2}{1+\dfrac{x}{y}+3\left(\dfrac{x}{y}\right)^2}\,. \tag{2.36}$$

The ratio x/y increases from 10^{-5} at the inner radius s_{i} to a value of 3.5 in region B. This value stays constant for a large part of the disk, until it finally drops again to $4\cdot 10^{-3}$ in regions D and E, where self-gravitation comes into play. With $\gamma = 1$ and $\nabla_{\text{ad}} = 2/5$, the ratio of the effective radiative flux F_{rad} is increased by a constant factor of 1.6 with respect to the cooling flux F_{-}.

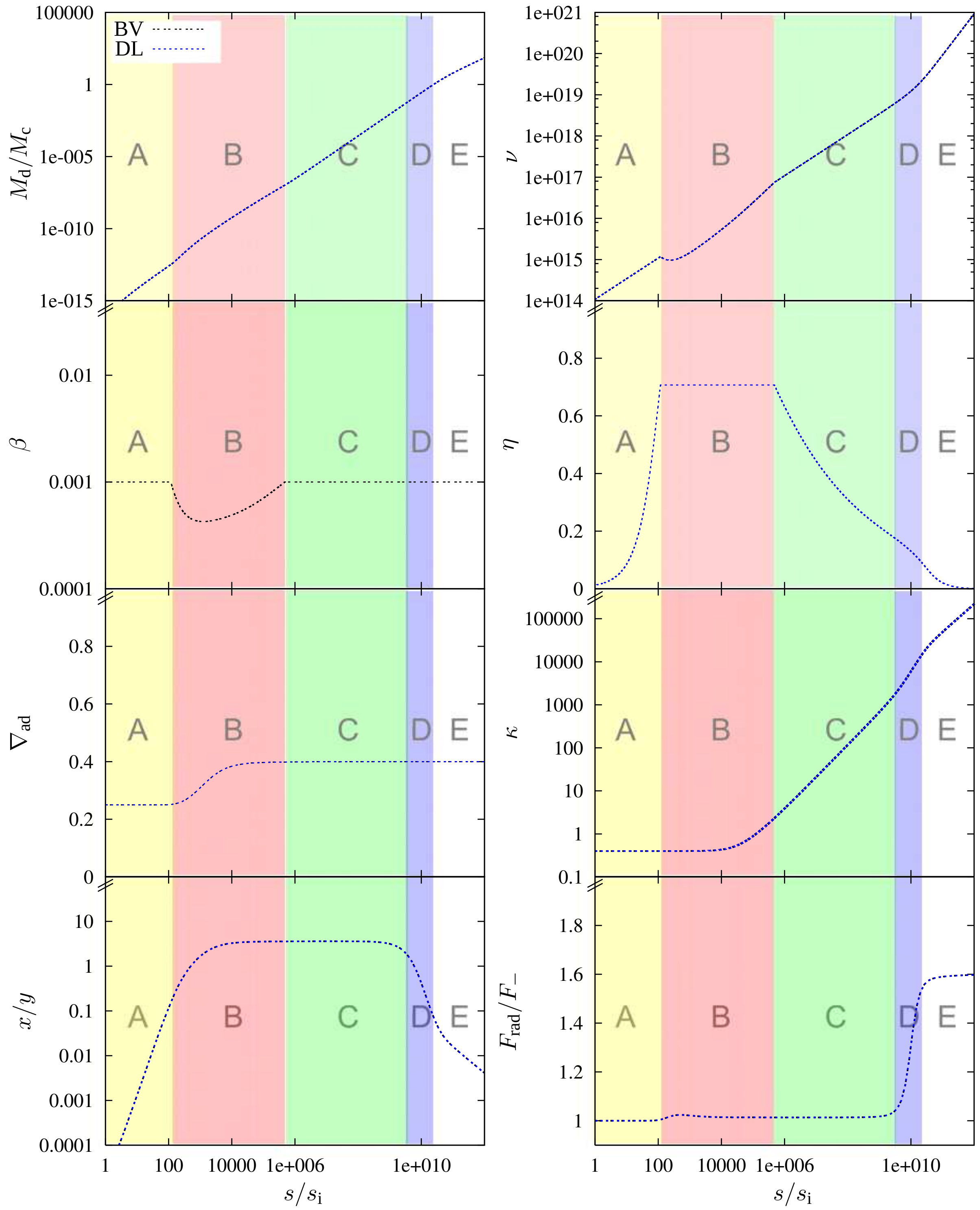

Figure 2.6. The influence of turbulence on the energy transport in steady-state β-disks. BV corresponds to a disk model with adaptable viscosity parameter, DL to a diffusion limited disk. For details, see text.

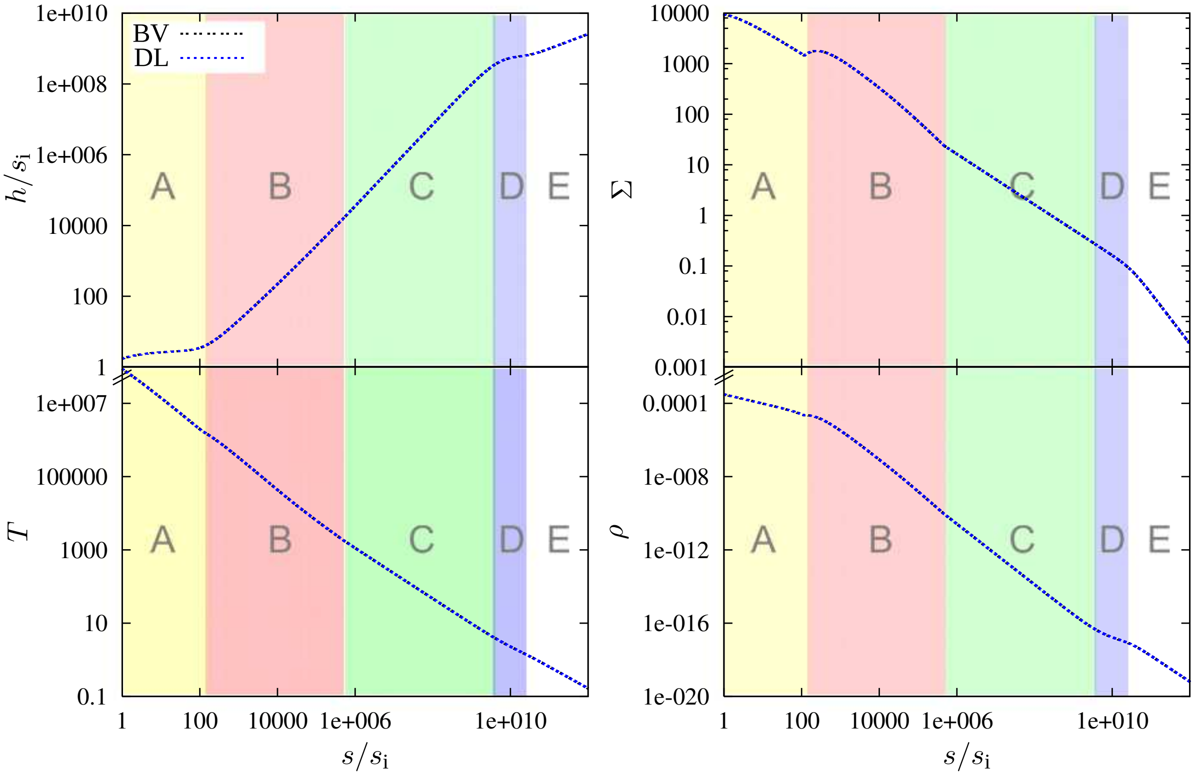

Figure 2.7. Relevant physical variables for the increase in F_rad/F_- in the outer parts of the disk.

2.6 Conclusions

From the study of the impact of turbulence on the overall energy transport, we found that the convective feedback on the upward energy flux becomes non-negligible in two cases.

1. In the region where the disk becomes shock dissipation limited, the turbulence is maximally efficient. Hence, it is to be expected that also the turbulent downward motion is increased. Our results show that this is indeed the case, although this effect is rather small, increasing the effective radiative flux by 2.4% of the cooling flux F_-.

2. In the outskirts of the disk, selfgravitation sets in. In region D, the disk is in a Keplerian selfgravitating state (KSG), which means that selfgravity determines the vertical structure, but not the radial one. Contrary, in the fully selfgravitating state (FSG) in region E, the local gravitational attraction dominates for both directions. In these two regions, the net motion of matter is therefore influenced by the strong gravitational attraction towards the disk plane. Hence, the convective backcoupling has a strong effect, raising the effective radiative flux by 60% of the cooling flux.

We conclude that only in the selfgravitating regime, the convective feedback has to be included in the energy transport equation.

In the first part of this study, we focused on the shock dissipation limit in the disk. Wether a disk runs into a shock dissipation limited state or not, depends strongly on the maximum strength of the viscosity (i. e., on the parameter β_max) and on the accretion rate $\dot{M}$. For lower

Table 2.2. Radial structure of the extended disk models DL and BV. “SG” denotes the status of the disk (NSG, KSG, FSG). The dominant pressure term, either gas or radiation, can be deduced from the adiabatic gradient ∇_{ad} in Fig. 2.6: for $p = p_{\text{rad}}$, $\nabla_{\text{ad}} = 0.25$, while for $p = p_{\text{gas}}$, $\nabla_{\text{ad}} = 0.4$.

Label	s_{min}	s_{max}	BV state	DL state	SG state	pressure
A	s_{i}	$1.2 \cdot 10^2 s_{\text{i}}$	$\beta = \beta_{\text{max}}$	does not apply	NSG	$p = p_{\text{rad}}$
B	$1.2 \cdot 10^2 s_{\text{i}}$	$4.7 \cdot 10^5 s_{\text{i}}$	$\beta < \beta_{\text{max}}$	$\eta = 1/\sqrt{2}$	NSG	transition
C	$4.7 \cdot 10^5 s_{\text{i}}$	$3.8 \cdot 10^9 s_{\text{i}}$	$\beta = \beta_{\text{max}}$	does not apply	NSG	$p = p_{\text{gas}}$
D	$3.8 \cdot 10^9 s_{\text{i}}$	$2.4 \cdot 10^{10} s_{\text{i}}$	$\beta = \beta_{\text{max}}$	does not apply	KSG	$p = p_{\text{gas}}$
E	$2.4 \cdot 10^{10} s_{\text{i}}$	s_{o}	$\beta = \beta_{\text{max}}$	does not apply	FSG	$p = p_{\text{gas}}$

accretion rates, the diffusion limit applies more likely, while it is inhibited for lower values of β_{max}. Taking into account that the disks have to be geometrically thin ($\dot{M} < \dot{M}_{\text{E}}$), we found that for $\beta_{\text{max}} \lessapprox 10^{-4}$, the diffusion limit can be neglected in the disk models.

We also derived an analytical expression for the diffusion limit parameter η, which allows to calculate it directly from the disk quantities rather than to determine it iteratively. This expression depends only on the azimuthal motion (i. e., the angular velocity).

Finally, we investigated in a simple way the influence of the inner boundary condition on the disk. In accordance with earlier work by Duschl & Tscharnuter (1991), who investigated an extended inner boundary region around an accreting star, we found that the temperature and luminosity is decreased for the innermost ring of such a disk. Cao & Xu (2003) studied the case that the matter inside the marginally stable orbit of a black hole accretion disk is magnetically connected to the disk. They found that the structure of the inner edge is altered and that the accretion efficiency can be much higher than in a standard accretion-disk model. This matches nicely with our results. In general, the discussion about the inner boundary condition, in particular about the validity of the torque-free formulation, is still ongoing (see Gammie (1999); Krolik (1999); Paczyński (2000), for example).

3 The role of convection in black hole accretion disks

3.1 Context

We calculate accretion disk models where the viscosity and the transport of energy is supported by convective processes, in addition to a radiative energy transport and an underlying β-viscosity. Convection is treated in the framework of the mixing-length theory, the disks are assumed to be geometrically thin in order to allow for a $1+1$-dimensional treatment of the equations (c. f. Fig. 2.1). The resulting disk models will be compared to standard β-viscosity disks (Duschl et al., 2000) with the goal of evaluating the β-viscosity ansatz against a convective viscosity description.

3.2 Set-up and nomenclature

As in the previous chapter, we use a cylindrical coordinate system with planar radial coordinate $s = \sqrt{x^2+y^2}$, vertical coordinate z and true radius $r = \sqrt{s^2+z^2}$. The disk geometry is determined by an inner and an outer radius s_i and s_o, and the disk's height $h = h(s)$ from the mid-plane. Further quantities apart from the standard ones are defined in Table 3.1.

Table 3.1. Physical quantities used throughout this investigation.

Symbol	meaning	unit
F_z	energy flux in vertical direction at height z	erg/s
F	total energy flux at radius s	erg/s
g_s	acceleration due to gravitational potential in radial direction	$\mathrm{cm/s^2}$
g_z	acceleration due to gravitational potential in vertical direction	$\mathrm{cm/s^2}$
l_conv	convective lengthscale	cm
l_m	mixing length	cm
M_c	mass of central object	g
M_d	disk mass within radius s	g
$\dot{M}$	accretion rate	g/s
ω	angular velocity of disk material	1/s
Σ_z	surface density at height z	$\mathrm{g/cm^2}$
Σ	total surface density	$\mathrm{g/cm^2}$
v_conv	convective velocity	cm/s
v_s	radial velocity in the disk	cm/s

A turbulent viscosity, caused by convective processes, is generally given by

$$\nu_{\text{conv}} = \frac{1}{3} v_{\text{conv}} l_{\text{conv}} \tag{3.1}$$

when assuming isotropy. We replace the isotropy factor $1/3$ by a factor ϖ of the order of unity to account for non-isotropic cases. Since we apply the mixing-length theory for calculating convective processes in the disk, we identify the convective lengthscale l_{conv} with the mixing-length l_{m}, which will be defined later. Therefore, we get

$$\nu_{\text{conv}} = \varpi v_{\text{conv}} l_{\text{m}} \, . \tag{3.2}$$

We assume a permanently supporting viscosity to be present in the disk, which accounts for other sources of viscosity, like differential rotation, … It is parameterized in terms of the standard β-viscosity, given by

$$\nu_\beta = \beta s^2 \omega \, , \tag{3.3}$$

with $\beta \ll 1$ being the viscosity parameter. The total viscosity ν is then given by a combination of these two contributors,

$$\nu = \nu_{\text{conv}} + \nu_\beta \, . \tag{3.4}$$

3.3 Radial structure

For the calculation of the radial structure, we introduce the disk's surface density

$$\Sigma = \int_0^h \rho \, dz \tag{3.5}$$

and

$$\Psi = \int_0^h \nu \rho \, dz \, . \tag{3.6}$$

Only in the special case of $\nu = \text{const}$ can we rewrite (3.6) to $\Psi = \nu\Sigma$. In all other cases, we can apply the mean value theorem to define an average value $\nu^\star$ such that

$$\Psi = \nu^\star \Sigma$$

The individual contributors $\nu^\star$ and Σ remain unknown from the radial structure equations only. They are determined by the vertical structure equations (Sect. 3.4.1).

The radial structure is determined by the conservation of mass, momentum, angular momentum and energy. The corresponding equilibrium equations are

$$\begin{aligned} \dot{M} &= -4\pi s v_s \Sigma \, , && (3.7) \\ \omega^2 &= -\frac{g_s}{s} \, , && (3.8) \\ 2\Psi &= -\frac{\dot{M}\omega}{2\pi s (\partial\omega/\partial s)} f_\chi(s) \, , && (3.9) \\ 2F &= -\frac{\dot{M} s \omega (\partial\omega/\partial s)}{2\pi} f_\chi(s) \, . && (3.10) \end{aligned}$$

Here, $f_\chi(s)$ represents the disk's boundary condition at the inner radius s_i,

$$f_\chi(s) = 1 - \chi \frac{s_\mathrm{i}^2 \omega(s_\mathrm{i})}{s^2 \omega(s)}\,, \tag{3.11}$$

with $0 \leq \chi \leq 1$. The standard free-fall boundary condition, implying a vanishing torque at the disk's inner radius, is generated from setting $\chi = 1$.

Note that the momentum equation (3.8) is simplified by the assumption of Keplerian rotation. The gravitational acceleration in radial direction is assumed to be given by the monopole approximation, assuming a Pseudo-Newtonian gravitational potential (Paczyński & Wiita, 1980):

$$g_s = -\frac{G(M_\mathrm{c} + M_\mathrm{d}(s))}{(r - r_\mathrm{g})^2} \cdot \frac{s}{r}\,. \tag{3.12}$$

The enclosed disk mass at radius s is calculated via

$$M_\mathrm{d}(s) = \int_{s_\mathrm{i}}^{s} 4\pi s' \Sigma \, ds'\,. \tag{3.13}$$

3.4 Vertical stratification

3.4.1 Structure equations

In analogy to Hofmann (2005) and Vehoff (2005), we take the energy flux F_z ($F_z = 0 \ldots F$) as the independent coordinate for the vertical integration since it appears as the natural choice for the solution of the problem. We additionally introduce the surface density at height z

$$\Sigma_z = \int_0^z \rho \, dz\,, \qquad \Sigma_z(z = h) = \Sigma\,, \tag{3.14}$$

and

$$\psi = \int_0^z \nu\rho \, dz\,, \qquad \psi(z = h) = \Psi\,. \tag{3.15}$$

Neither Σ nor h are known *à priori* – they will be a result of the vertical integration. The equations for the vertical structure of the disk are given as follows:

$$\frac{\partial z}{\partial F_z} = \frac{1}{\rho \nu s^2 \left(\frac{\partial \omega}{\partial s}\right)^2}\,, \tag{3.16}$$

$$\frac{\partial T}{\partial F_z} = \frac{1}{\rho \nu s^2 \left(\frac{\partial \omega}{\partial s}\right)^2} \cdot \left\{ -(1 - \zeta) \frac{3\kappa\rho F_z}{4acT^3} - \zeta \frac{(-g_z)Q}{c_\mathrm{p}} \right\}\,, \tag{3.17}$$

$$\frac{\partial \Sigma_z}{\partial F_z} = \frac{1}{\nu s^2 \left(\frac{\partial \omega}{\partial s}\right)^2}\,, \tag{3.18}$$

$$\frac{\partial p}{\partial F_z} = \frac{g_z}{\nu s^2 \left(\frac{\partial \omega}{\partial s}\right)^2}\,. \tag{3.19}$$

For the derivation of (3.19), we assumed hydrostatic equilibrium:

$$\frac{\partial p}{\partial F_z} = \frac{\partial p}{\partial z} \cdot \frac{\partial z}{\partial F_z} = \rho g_z \cdot \frac{1}{\rho \nu s^2 \left(\frac{\partial \omega}{\partial s}\right)^2} \,. \tag{3.20}$$

Using (3.17), (3.19) and the equation of state,

$$p = p_{\text{gas}} + p_{\text{rad}} = \frac{\rho k_{\text{B}} T}{\mu m_{\text{H}}} + \frac{4\sigma_{\text{SB}}}{3c} T^4 \,, \tag{3.21}$$

we transform (3.19) into an equation for the mass density ρ:

$$\rho \;=\; \frac{\mu m_{\text{H}}}{k_{\text{B}}} \left(\frac{p}{T} - \frac{4\sigma_{\text{SB}}}{3c} T^3 \right) \tag{3.22}$$

$$\Downarrow$$

$$\begin{aligned}
\frac{\partial \rho}{\partial F_z} &= \frac{\mu m_{\text{H}}}{k_{\text{B}} T} \cdot \frac{\partial p}{\partial F_z} - \frac{\mu m_{\text{H}}}{k_{\text{B}}} \left(\frac{p}{T^2} + \frac{4\sigma_{\text{SB}}}{c} T^2 \right) \cdot \frac{\partial T}{\partial F_z} \\
&= \frac{-\mu m_{\text{H}}}{k_{\text{B}} \nu s^2 \left(\frac{\partial \omega}{\partial s}\right)^2} \cdot \left[\frac{(-g_z)}{T} + \left(\frac{p}{\rho T^2} + \frac{4\sigma_{\text{SB}} T^2}{\rho c} \right) \cdot \left\{ -(1-\zeta) \frac{3\kappa \rho F_z}{4acT^3} - \zeta \frac{(-g_z) Q}{c_{\text{p}}} \right\} \right] \\
&= \frac{-\mu m_{\text{H}}}{k_{\text{B}} \nu s^2 \left(\frac{\partial \omega}{\partial s}\right)^2} \cdot \aleph \,.
\end{aligned} \tag{3.23}$$

We introduce

$$\begin{aligned}
\wp &= \left\{ -(1-\zeta) \frac{3\kappa \rho F_z}{4acT^3} - \zeta \frac{(-g_z) Q}{c_{\text{p}}} \right\} \,, \\
\aleph &= \frac{(-g_z)}{T} + \left(\frac{p}{\rho T^2} + \frac{4\sigma_{\text{SB}} T^2}{\rho c} \right) \cdot \wp
\end{aligned}$$

for a better reading of the lengthy expressions in the next sections. We further introduce the constants

$$\Xi = \frac{\mu m_{\text{H}}}{k_{\text{B}}}, \qquad a_{\text{rad}} = \frac{4\sigma_{\text{SB}}}{c}, \qquad \text{and} \qquad \Upsilon = \left(s^2 (\partial\omega/\partial s)^2\right)^{-1} \,, \tag{3.24}$$

where Υ is constant for the vertical integration at every radial position s, to obtain the final set of differential equations:

$$\frac{\partial z}{\partial F_z} = \frac{\Upsilon}{\rho \nu} \,, \tag{3.25}$$

$$\frac{\partial T}{\partial F_z} = \frac{\Upsilon}{\rho \nu} \cdot \wp \,, \tag{3.26}$$

$$\frac{\partial \Sigma_z}{\partial F_z} = \frac{\Upsilon}{\nu} \,, \tag{3.27}$$

$$\frac{\partial \rho}{\partial F_z} = -\frac{\Xi \Upsilon}{\nu} \cdot \aleph \,. \tag{3.28}$$

Additional assumptions are required to provide the necessary physical quantities for the numerical solution of the vertical stratification: the opacity $\kappa = \kappa(\rho, T)$ can be calculated either from tables or interpolation formulae. We provide several methods to compute its value, ranging from fast and simple Thomson-scattering to slow, but much more precise tabulated values (see Sect. 3.4.3 for details).

Like g_s in (3.12), the gravitational acceleration in vertical direction g_z is provided by the monopole approximation:

$$g_z = -\frac{G(M_\mathrm{c} + M_\mathrm{d}(s))}{(r - r_\mathrm{g})^2} \cdot \frac{z}{r} - 4\pi G \Sigma_z \,. \tag{3.29}$$

In order to solve the vertical structure equations, a model for the convection must be chosen. Here, we apply the mixing-length theory (Cox & Giuli, 1968), which is used successfully in stellar evolution as well as in previous accretion disk calculations (cf., Hofmann (2005) and Vehoff (2005)). The mixing-length theory expresses the efficiency of convective energy transport relative to the radiative transport processes by the variable ζ, where $0 \leq \zeta \leq 1$. A vanishing ζ implies no convective transport, while in the case $\zeta = 1$ all energy is transported by convection. Its value can be calculated from the cubic equation

$$\zeta^{1/3} + B \cdot \zeta^{2/3} + a_0 B^2 \zeta - a_0 B^2 = 0 \,, \tag{3.30}$$

with a numerical factor $a_0 = 9/4$ and further quantities defined as

$$\begin{aligned}
B &= \left[\frac{A^2}{a_0} \cdot (\nabla_\mathrm{rad} - \nabla_\mathrm{ad})\right]^{1/3} \,, \\
A^2 &= \frac{Q(c_\mathrm{p}\kappa(-g_z))^2 \rho^5 l_\mathrm{m}^4}{288 a^2 c^2 p T^6} \,, \\
Q &= \frac{4 - 3\gamma}{\gamma} \,, \\
c_\mathrm{p} &= \frac{\mathfrak{R}}{\mu} \cdot \frac{32 - 24\gamma - 3\gamma^2}{2\gamma^2} \,, \\
\gamma &= \frac{p_\mathrm{gas}}{p} \,, \\
\nabla_\mathrm{rad} &= \frac{3\kappa\rho\lambda_\mathrm{p} F_z}{4acT^4} \,, \\
\nabla_\mathrm{ad} &= \frac{8 - 6\gamma}{32 - 24\gamma - 3\gamma^2} \,, \\
l_\mathrm{m} &= \min(\lambda_\mathrm{p}, h) \,, \\
\lambda_\mathrm{p} &= \frac{p}{-g_z \rho} \,.
\end{aligned}$$

The mixing length l_m is usually of the order of the pressure scale height λ_p. However, in analogy to the stellar case, it is limited by simple geometric effects. While in the stellar case, it usually cannot exceed the actual radial distance from the center due to symmetry requirements, we adopt as upper limit the actual height $h = h(s)$ of the disk. This overrides the symmetry of the disk with respect to the disk plane and also the strict upper barrier for the convective elements (i. e., the disk surface), but provides a simple method of taking into account the overshooting effects and a more realistic, smooth transition between the disk and the atmosphere. We anticipate that the results differ only slightly from the more restrictive case $l_{\mathrm{m}} = \min(\lambda_{\mathrm{p}},h - z)$, so that our conclusions are not changed by this assumption.

From the above definitions, the cubic equation (3.30) can be solved numerically. Once a value for ζ has been found, the convective viscosity can be calculated from

$$v_{\mathrm{conv}} = c_{\mathrm{s}} \cdot \frac{Q^{1/2}\alpha_{l_{\mathrm{m}}}}{2\sqrt{2}\Gamma_1^{1/2}} \left(\frac{\nabla_{\mathrm{rad}} - \nabla_{\mathrm{ad}}}{a_0 A}\right)^{1/3} \zeta^{1/3}\,, \tag{3.31}$$

where c_{s} denotes the sound speed at the actual coordinate (s,z) in the disk. In the non-relativistic regime, it is given by

$$c_{\mathrm{s}} = \sqrt{\Gamma_1\, p/\rho}\,. \tag{3.32}$$

The constant Γ_1 stands for the polytropic index, which in the case of a non-relativistic, ideal gas is given by $5/3$. The parameter $\alpha_{l_{\mathrm{m}}}$ relates the typical distance traveled by the convective elements to the pressure scale height and is generally of the order of unity (Cox & Giuli, 1968). To be consistent with our definition of the mixing-length, it has to be calculated from

$$\alpha_{l_{\mathrm{m}}} = \frac{l_{\mathrm{m}}}{\lambda_{\mathrm{p}}} \leq 1\,. \tag{3.33}$$

The derivation of the mixing-length theory assumes a purely subsonic motion of the convective elements (*Eddies*), $v_{\mathrm{conv}} \leq c_{\mathrm{s}}$. This inequality cannot be assured by the definition of the convective velocity in (3.31). Since there is currently no supersonic convective theory which is as simple and successful as the mixing-length theory, one usually defines the sound speed c_{s} as an upper limit for the convective velocity. Thus, in the case of (3.31) resulting in $v_{\mathrm{conv}} > c_{\mathrm{s}}$, one has to set $v_{\mathrm{conv}} = c_{\mathrm{s}}$, which lowers the actual value of ζ from its original value, given by (3.30), to

$$\zeta = \frac{8\sqrt{8}\Gamma_1^{3/2} a_0^{3/2} A}{Q^{3/2}\alpha_{l_{\mathrm{m}}}^3 (\nabla_{\mathrm{rad}} - \nabla_{\mathrm{ad}})}\,. \tag{3.34}$$

We calculate the anisotropy parameter ϖ (which measures the ratio of the convective turbulence in vertical direction relative to all directions) from

$$\varpi = \frac{v_{\mathrm{conv}}}{c_{\mathrm{s}}} \leq 1\,. \tag{3.35}$$

This relation is based on the following idea: that the maximum (3-dimensional) velocity of an Eddie is given by the local sound speed c_{s}. The individual velocities in directions (s,φ,z) are normally not identical, since they depend on the energy gradients in their direction. We assume for simplicity that in the convective regions, the convection for all three dimension together is maximally efficient, i. e., that the 3-dimensional convective velocity of the Eddies is given by c_{s}. We then approximate the fraction in the vertical direction z from (3.35).

3.4.2 Boundary conditions

For the four differential equations (3.25)–(3.28), we need to define four boundary conditions at either the disk's midplane ($F_z = 0$) or surface ($F_z = F$). These are:

$$z_{\mathrm{mp}} = z(F_z = 0) = 0\,, \tag{3.36}$$

$$T_{\mathrm{eff}} = T(F_z = F) = \left(\frac{F}{\sigma_{\mathrm{SB}}}\right)^{1/4}, \tag{3.37}$$

$$\Sigma_{z,\mathrm{mp}} = \Sigma_z(F_z = 0) = 0\,, \tag{3.38}$$

$$\rho_{\mathrm{eff}} = \rho(F_z = F) = \rho_{\mathrm{eff,input}}\,. \tag{3.39}$$

The boundary condition on ρ cannot be determined from the radial structure equations or from simple geometric arguments. It requires the addition of an atmosphere above the surface of the disk, which allows us to determine the effective density consistently with the height h, the surface density Σ and the effective temperature T_{eff}. The model and numerical method for calculating the atmosphere will be given in Sect. 3.4.4 and 3.5.2.

Remark. At first, it seems that (3.9) provides the missing boundary condition and that (3.39) is not only dispensable, but may even be wrong. This is not the case, since (3.9) is automatically fulfilled for the correct solution for any ρ_{eff}, as the following short calculation shows.

$$\begin{aligned}
\Psi &= \int_{-h}^{+h} \nu\rho\, dz \\
&= 2 \cdot \int_{0}^{+h} \nu\rho\, dz \\
&\overset{(3.25)}{=} 2 \cdot \int_{F_z(z=0)}^{F_z(z=+h)} \nu\rho \cdot \left(\frac{\Upsilon}{\rho\nu}\right) dF_z \\
&\overset{(3.24)}{=} 2 \cdot \frac{1}{s^2\,(\partial\omega/\partial s)^2} \cdot \int_{F_z(z=0)}^{F_z(z=+h)} dF_z \\
&\overset{(3.10)}{=} \frac{1}{s^2\,(\partial\omega/\partial s)^2} \cdot \frac{-\dot{M} s\omega\,(\partial\omega/\partial s)}{2\pi} f_\chi(s) \\
&= -\frac{\dot{M}\omega}{2\pi s(\partial\omega/\partial s)} f_\chi(s) \equiv \text{rhs(3.9)}
\end{aligned}$$

3.4.3 Opacity κ

Numerous possibilities exist to approximate the opacity κ which, in general, depends on the density ρ and temperature T of the medium.

Thomson scattering The easiest approximation is given by pure electron scattering,

$$\kappa_{\mathrm{es}} = 0.4\,\mathrm{cm}^2/\mathrm{g}\,. \tag{3.40}$$

Kramer's opacity The simplest approach, apart from solely assuming Thomson scattering, is to use Kramer's opacity description

$$\kappa_{\rm kr} = \kappa_{\rm es} + \kappa_0 \rho T^{-7/2} \tag{3.41}$$

with $\kappa_0 = 6.4 \cdot 10^{22}\,\mathrm{cm^5 K^{7/2}/g^2}$. The Kramer's opacity is only valid in the optical thick regime.

Analytic interpolation formula We allow for opacity sources other than Thomson scattering and free-free absorption by using an analytic interpolation formula (Gail, priv. comm.; for a similar approach, see also Bell & Lin (1994)) for Rosseland opacities. Thus, this interpolation formula is also valid only in the optically thick regions.

$$\begin{aligned} \frac{1}{\kappa_{\rm in}} &= \left[\frac{1}{\kappa_{\rm ice}^4} + \frac{T_0^{10}}{T_0^{10}+T^{10}} \cdot \frac{1}{\kappa_{\rm ice,\,evap}^4 + \kappa_{\rm dust}^4}\right]^{1/4} \\ &\quad + \left[\frac{1}{\kappa_{\rm dust,\,evap}^4 + \kappa_{\rm mol}^4 + \kappa_{\rm H^-}^4} + \frac{1}{\kappa_{\rm atom}^4 + \kappa_{\rm e^-}^4}\right]^{1/4} \end{aligned} \tag{3.42}$$

The individual contributors κ_l are approximated by

$$\kappa_l = \kappa_{0,l} \cdot T^{\kappa_{T,l}} \cdot \rho^{\kappa_{\rho,l}} \tag{3.43}$$

and are compiled in Table 3.2. The parameter T_0 needs to be set by hand under the requirement that it is sufficiently large. An adequate value is, for example, $T_0 = 3000\,\mathrm{K}$. Note that the definition of the individual contributors is such that the total interpolation formula fits the real values; they cannot be used on their own as a physical description of the corresponding process.

Table 3.2. Interpolation of the opacity: set of parameters (in cgs-units).

Contributor l	**Symbol**	$\kappa_{\mathrm{l},\mathbf{0}}$	$\kappa_{\mathrm{l},\rho}$	$\kappa_{\mathrm{l},\mathbf{T}}$
Dust with ice mantles	$\kappa_{\rm ice}$	$2.0 \cdot 10^{-4}$	0	2
Evaporation of ice	$\kappa_{\rm ice,\,evap}$	$1.0 \cdot 10^{16}$	0	-7
Dust particles	$\kappa_{\rm dust}$	$1.0 \cdot 10^{-1}$	0	$1/2$
Evaporation of dust particles	$\kappa_{\rm dust,\,evap}$	$2.0 \cdot 10^{81}$	1	-24
Molecules	$\kappa_{\rm mol}$	$1.0 \cdot 10^{-8}$	$2/3$	3
Negative hydrogen ion	$\kappa_{\rm H^-}$	$1.0 \cdot 10^{-36}$	$1/3$	10
Bound-free and free-free-transitions	$\kappa_{\rm atom}$	$1.5 \cdot 10^{20}$	1	$-5/2$
Electron scattering	$\kappa_{\rm e^-}$	0.348	0	0

Tabulated values Various databases exist that offer tables of numerically calculated opacities for different temperature and density ranges. Given that we want to cover a large domain in temperature and density, multiple sources have to be included in our model. The presence of a disk and an atmosphere requires not only Rosseland opacities, but also Planck opacities, which are valid in the optical thin regime.

The selection of opacity databases is therefore restricted to those sources offering mean Rosseland *and* Planck opacities. In the high-temperature limit, we adopt the tables from the TOPS project (TOPS, 2008). We compile tables for Rosseland and Planck opacities on a $\log T$–$\log \rho$ grid. For the TOPS opacities, $\log \rho$ and $\log T$ are in the range of

$$\begin{aligned} \log \rho &= [-12.5 \ldots + 10.5] \,, \\ \log T &= [+4.5 \ldots + 9.1] \,. \end{aligned}$$

The number of data points is 47 on an equidistant scale for $\log \rho$ and 41 for $\log T$, respectively.

In the low-temperature regime, we include the Ferguson opacities (Ferguson et al., 2005; Ferguson, 2008). Contrary to the TOPS opacities, they provide tables for Rosseland and Planck opacities on a $\log T$–$\log R$ grid. For historical reasons, in astrophysical applications the R parameter is often used instead of the density ρ. It is defined by

$$\begin{aligned} R &= \frac{\rho}{T_6^3} \,, \qquad \rho = \rho[\mathrm{g\,cm^{-3}}], \quad T_6 = T[\mathrm{K}]/10^6 \,, && (3.44) \\ \log R &= \log \rho + 18 - 3 \log T \,. && (3.45) \end{aligned}$$

The ranges for the Ferguson opacities are

$$\begin{aligned} \log R &= [-8.0 \ldots + 1.0] \,, \\ \log T &= [+2.7 \ldots + 4.5] \,. \end{aligned}$$

These ranges correspond to minimum and maximum mass densities of $\log\ \rho = -17.9$ and $+6.5$, with a resolution of 19 equidistant points in $\log R$ and 85 in $\log T$.

For a consistent approach, we choose identical chemical abundances with mass fractions $X = 0.7$, $Y = 0.28$, $Z = 0.02$, and the chemical mixture of Grevesse & Sauval (1998).

Opacity mixture In order to get smooth transitions and a broad coverage of the T-ρ range, we use a combination of the tabulated opacities (TOPS, Ferguson) and the interpolation formula 3.42: the transition between TOPS and Ferguson opacities takes place at $\log T = 4.5$. We therefore use a linear interpolation of the opacities from both sources in the range $\log T = [4.0 \ldots 5.0]$.

At the “outer” boundaries of the TOPS- and Ferguson-opacities, we use the same kind of linear transition in a range of $\delta \log \rho = 1$ and $\delta \log T = 1$ between the tabulated values and the interpolation formula 3.42. The resulting opacities are defined on a $\log T$–$\log \rho$ grid with 150 data points in each direction and

$$\begin{aligned} \log \rho &= [-15.0 \ldots + 10.0] \,, \\ \log T &= [+1.0 \ldots + 9.0] \,, \end{aligned}$$

which is sufficient for our purposes. Figures 3.1a,b show the resulting opacities on the $\log T$–$\log \rho$ grid, while Figs. 3.1c,d display opacity curves as a function of temperature for certain fixed densities.

3.4.4 Atmosphere

In this investigation, the only purpose of the atmosphere is to provide a value for the mass density at the surface of the accretion disk at each radial position s, which is consistent with the actual effective temperature, geometrical height and surface density.

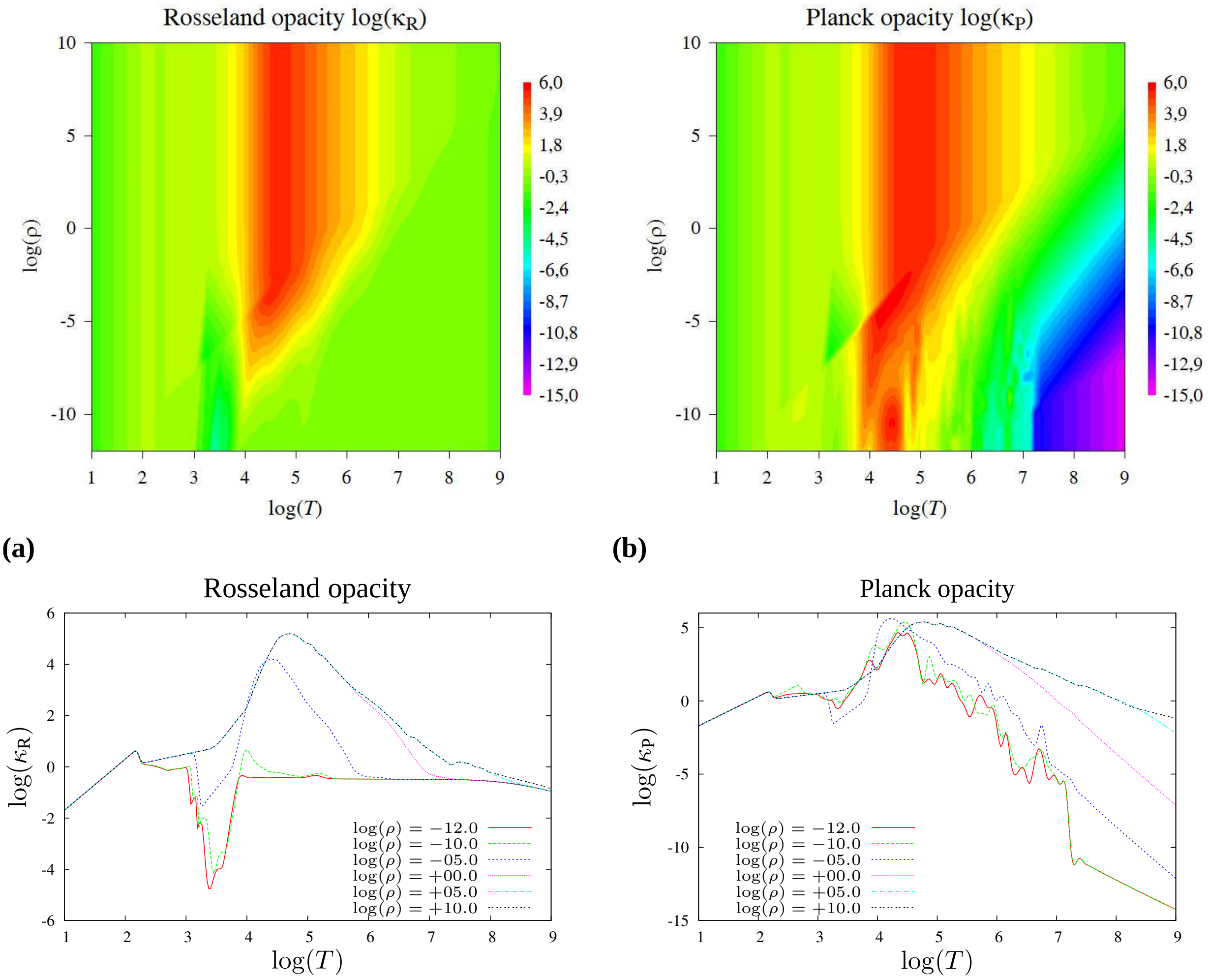

(a) **(b)**

(c) **(d)**

Figure 3.1. **(a)** Rosseland and **(b)** Planck opacities for the opacity mixture on a $\log T$–$\log \rho$ grid; temperature dependency of **(c)** Rosseland and **(d)** Planck opacities for fixed densities.

Therefore, it is sufficient to calculate a simple grey atmosphere in the Milne-Eddington way, where the temperature distribution is given as a function of the optical depth τ by

$$T(\tau)^4 = C_{1,\text{atm}} T_{\text{eff}}^4 \cdot (\tau + C_{2,\text{atm}}) \,. \tag{3.46}$$

The constants $C_{1,\text{atm}}$ and $C_{2,\text{atm}}$ depend on the transition point τ_{eff} between the atmosphere (optically thin) and the disk (optically thick) and the final value for the temperature at the “upper” end of the atmosphere ($\tau = 0$). The most common values are

$$T^4(\tau = 0) = (1/2) \cdot T_{\text{eff}}^4 \qquad \text{and} \qquad \tau_{\text{eff}} = 2/3 \,.$$

We keep the upper value for the temperature, but use $\tau_{\text{eff}} = 1$ for a simple reason: in the optical thin atmosphere, the equation of state (3.21) has to be modified such that the radiation pressure term tends to zero for $\tau \to 0$. This is necessary because the coupling between radiation and matter becomes negligible by definition in the optical thin regime. With the correct expression for the radiation pressure in an optical thin medium,

$$p_{\text{rad, atm}} = \frac{4\sigma_{\text{SB}}}{3c} \tau T^4 \,, \tag{3.47}$$

we get a smooth transition at the disk's surface only for $\tau_{\text{eff}} = 1$. This is consistent with the requirements on the value of τ, which has to be such that it is characteristic for a transition between optically thin and optically thick domains.

The constants $C_{1,\text{atm}}$ and $C_{2,\text{atm}}$ then become

$$C_{1,\text{atm}} = \frac{1}{2}, \qquad C_{2,\text{atm}} = 1 \,. \tag{3.48}$$

Therefore, the temperature in the atmosphere is given by

$$T(\tau)^4 = \frac{1}{2} T_{\text{eff}}^4 \cdot (\tau + 1) \,. \tag{3.49}$$

The remaining equations are given as follows: from the definition of the optical depth,

$$d\tau = -\kappa\rho \, dz \,,$$

we get an expression for $\partial z / \partial\tau$. The differential expression for the surface density

$$d\Sigma_z = \rho \, dz$$

is then transformed into $\partial\Sigma_z / \partial\tau$. The remaining equation for either the mass density, gas pressure or total pressure is derived from assuming hydrostatic equilibrium (cf., (3.20)) and inserting the temperature stratification from (3.49). We choose the gas pressure as the fourth dependent variable and obtain the following set of differential equations for the structure of the atmosphere:

$$\frac{\partial z}{\partial\tau} = -\frac{1}{\rho\kappa} = -\frac{T}{\Xi\kappa p_{\text{gas}}} \,, \tag{3.50}$$

$$\frac{\partial\Sigma_z}{\partial\tau} = -\frac{1}{\kappa} \,, \tag{3.51}$$

$$\frac{\partial T}{\partial\tau} = T_{\text{eff}} \cdot \left(\frac{1}{2}\right)^{9/4} \cdot (\tau + 1)^{-3/4} \,, \tag{3.52}$$

$$\frac{\partial p_{\text{gas}}}{\partial\tau} = \left(\frac{-g_z}{\kappa} - \frac{4\sigma_{\text{SB}}}{3c} T_{\text{eff}}^4 \cdot \left(\tau + \frac{1}{2}\right)\right) \,. \tag{3.53}$$

The mass density ρ in (3.50) is given as usual by $\rho = \dfrac{\mu m_{\text{H}} p_{\text{gas}}}{k_{\text{B}} T}$.

Boundary conditions Again, we have to solve a set of four differential equations, this time with the independent variable τ and the dependent variables z, Σ_z, T and p_{gas}. This requires four boundary conditions which have to be set at either the lower boundary (corresponding to $\tau = \tau_{\text{eff}} = 1$) or the upper boundary (corresponding to $\tau = \tau_{\text{min}} \ll 1$; due to numerical reasons, it is not possible to set $\tau_{\text{min}} = 0$).

Three of these boundary conditions are provided by the solution of the vertical disk structure:

$$h = z(F_z = F) = z(\tau = \tau_{\text{eff}})\,, \tag{3.54}$$

$$\Sigma = \Sigma_z(F_z = F) = \Sigma_z(\tau = \tau_{\text{eff}})\,, \tag{3.55}$$

$$T_{\text{eff}} = T(F_z = F) = T(\tau = \tau_{\text{eff}})\,. \tag{3.56}$$

The fourth boundary condition on the gas pressure has to be set at the upper boundary of the atmosphere by the following line of argumentation: the properties of the disk surface will change as a function of the radial distance from the central object. In particular, the effective temperatures and densities will drop outwards. The first attempt could be to set a constant minimum value on the gas pressure at the upper boundary of the atmosphere. However, since the effective temperature and therefore also the minimum temperature at τ_{min} will decrease with radial distance, a constant $p_{\text{gas,min}}$ then implies that the mass density ρ_{min} at τ_{min} has to increase with radius. At the same time, however, we expect the mass density at the disk surface ρ_{eff} to decrease.

Another possibility is to define a constant minimum value for the mass density

$$\rho_{\text{min}} = \rho(\tau = \tau_{\text{min}}) = \text{const} \tag{3.57}$$

and to calculate the corresponding value $p_{\text{gas,min}}$ at every radial position from T_{min} and ρ_{min}.

3.5 Numerical solution of the vertical stratification

To solve the set of differential equations numerically, we use two separate methods for the disk and the atmosphere. The disk equations are obviously more complicated to solve and as such they are more prone to numerical issues like steep gradients, truncation errors, … Therefore, we use a Henyey algorithm for solving the set of differential equations in the disk. The Henyey method looks back on a successful history of applications in stellar structure and evolution codes, being able to deal with steep gradients by its relaxation method nature. The atmospheric equations, however, are much easier to solve and do not require a powerful, yet expensive algorithm like the Henyey method. We use a simple shooting algorithm to solve the atmospheric structure in a simple and quick way.

In Sect. 3.5.1, we present the set of discretized equations for the vertical disk structure that is generated by applying the Henyey method. A detailed description of this numerical scheme is given in the appendix (Sect. A.2), where we also elaborate how the original differential equations are transformed into their discretized counterparts. There, we further discuss how the set of linear equations is stored and solved in an efficient way.

Subsequently, Sect. 3.5.2 briefly introduces the shooting method and its implementation for solving the atmospheric structure. In Sect. 3.5.3, we discuss how the tabulated opacities are incorporated in the numerical analysis of both the disk and the atmosphere.

3.5.1 Set of discretized equations

We introduce a discretization in the vertical direction by transferring the continuous variables F_z, z, T, Σ_z, ρ to discrete values $F_{z,i}, \ldots$ with $i = 1, \ldots, N_i$. Thereby, $F_{z,1} = 0$ and $F_{z,N_i} = F$. The mean value of any quantity x for grid points i and $i-1$ is abbreviated with $x_{i-1/2} = (x_i + x_{i-1})/2$.

In the framework of the Henyey method, the set of differential equations (3.25)–(3.28) transforms into four linear equations $G_i^{(j)}$, $j = 1, \ldots, 4$ at every grid point i. Thereby, $j = 1$ corresponds to the differential equation for z, etc. Analogous, the four boundary conditions (3.36)–(3.39) allow us to rewrite these equations partially for $i = 1$ and $i = N_i + 1$.[1]

We now repeat the individual differential equations for the vertical stratification (3.25)–(3.28) and give the corresponding discretized Henyey equations.

For the geometric coordinate z, we get:

$$\begin{aligned} \frac{\partial z}{\partial F_z} &= \frac{\Upsilon}{\rho\nu} \\ &\Downarrow \\ G_i^{(1)} &= (z_i - z_{i-1})\rho_{i-1/2}\,\nu_{i-1/2} - \Upsilon(F_{z,i} - F_{z,i-1}) = 0\,. \end{aligned} \tag{A.12}$$

The temperature stratification is given as follows:

$$\begin{aligned} \frac{\partial T}{\partial F_z} &= \frac{\Upsilon}{\rho\nu} \cdot \wp \\ &\Downarrow \\ G_i^{(2)} &= (T_i - T_{i-1})\rho_{i-1/2}\,\nu_{i-1/2} - \Upsilon(F_{z,i} - F_{z,i-1})\wp_{i-1/2} = 0\,. \end{aligned} \tag{A.13}$$

The surface density equation converts to:

$$\begin{aligned} \frac{\partial \Sigma_z}{\partial F_z} &= \frac{\Upsilon}{\nu} \\ &\Downarrow \\ G_i^{(3)} &= (\Sigma_{z,i} - \Sigma_{z,i-1})\nu_{i-1/2} - \Upsilon(F_{z,i} - F_{z,i-1}) = 0\,. \end{aligned} \tag{A.14}$$

Finally, the Henyey equation for the density becomes:

$$\begin{aligned} \frac{\partial \rho}{\partial F_z} &= -\frac{\Xi\Upsilon}{\nu} \cdot \aleph \\ &\Downarrow \\ G_i^{(4)} &= (\rho_i - \rho_{i-1})\nu_{i-1/2} + \Xi\Upsilon(F_{z,i} - F_{z,i-1})\aleph_{i-1/2} = 0\,. \end{aligned} \tag{A.15}$$

From the four boundary conditions (3.36)–(3.39), we get:

$$G_1^{(1)} = z_1 = 0\,, \tag{A.16}$$

$$G_{N_i+1}^{(2)} = T_{N_i} - T_{\text{eff}} = 0\,, \tag{A.17}$$

$$G_1^{(3)} = \Sigma_{z,1} = 0\,, \tag{A.18}$$

$$G_{N_i+1}^{(4)} = \rho_{N_i} - \rho_{\text{eff}} = 0\,. \tag{A.19}$$

---

[1] The additional grid point $i = N_i + 1$ is introduced by the Henyey method for a purely numerical reason. See the detailed description in the appendix (Sect. A.2) for a further explanation.

Normalization of Henyey equations Theoretically, the Henyey equations (A.12)–(A.15) and their boundary conditions (A.16)–(A.19) can be evaluated and solved directly via the matrix inversion presented before. However, the numerical analysis requires a proper scaling of these equations; otherwise, they may differ by orders of magnitude and round-off errors are inevitable when matrix manipulations are performed. We therefore scale all equations and the corresponding derivatives in the matrix to the order of $(F_{z,i} - F_{z,i-1})/F_{z,i}$ by dividing them by

$$\Upsilon F_{z,i}, \qquad \Upsilon F_{z,i}\wp_i, \qquad \Upsilon F_{z,i}, \qquad \Xi\Upsilon F_{z,i}\aleph_i,$$

for $G_i^{(1)}$, $G_i^{(2)}$, $G_i^{(3)}$, $G_i^{(4)}$, or, in the case of the boundary conditions, by

$$1, \qquad T_{\text{eff}}, \qquad 1, \qquad \rho_{\text{eff}},$$

for $G_1^{(1)}$, $G_{N_i+1}^{(2)}$, $G_1^{(3)}$, $G_{N_i+1}^{(4)}$.

Convergence criteria A key point in every iterative scheme is to determine if the iteration has converged to the exact solution and to define an acceptance limit for an iterative solution. We use three different criteria to evaluate the accuracy of one iterative solution.

1. The variations $\delta z_i, \ldots, \delta\rho_i$ at each grid cell i have to be smaller than a certain fraction of their actual values $z_i, \ldots, \rho_i$ over a given number of successive iterations. We impose an accuracy limit of

   $$\delta y_i \overset{!}{\leq} \epsilon_1 \cdot y_i \,. \tag{3.58}$$

   for a minimum of n_{it} successive iterations.

2. The absolute deviation of the solution, measured by the sum of the absolute values of all entries in $\mathcal{G}$, has to be smaller than a given number G_{max} over the same number of successive iterations n_{it}. The average minimum accuracy for one variable in one grid cell, y_i, is then $G_{\text{max}}/(4N_i)$.

3. The quality of the solution is also checked by the relation

   $$\Psi - \int_{-h}^{+h} \nu\rho \, dz \overset{!}{\leq} \epsilon_2 \Psi \,, \tag{3.59}$$

   which ideally is zero for the real solution of the set of equations.

Automatic mesh refinement One problem of the numeric solution, especially when convective viscosity comes into play, is that the required grid resolution may vary considerably. We therefore start each iterative run with a lower grid resolution $N_{i,\text{start}}$, let the solution relax towards the true solution and then refine the grid by checking the changes in ρ – which turns out to be the crucial quantity for the solution to converge to the correct one – between adjacent grid cells. We allow for a maximum difference of ρ between two grid cells of

$$|\rho_i - \rho_{i-1}| \overset{!}{\leq} \epsilon_3 \min\{\rho_i,\rho_{i-1}\} \,. \tag{3.60}$$

If this condition is violated, the interval is split into two intervals. This is done recursively until (3.60) holds or $N_i = N_{i,\rho}$ is reached.

A certain number of iterations are then performed to let the solution adjust to the new grid, before the same type of condition is imposed on the changes of ζ, which measures the efficiency of convective processes in one grid cell. Since $0 \le \zeta \le 1$, an absolute limit must be given (instead of a relative one as in the case of ρ):

$$|\zeta_i - \zeta_{i-1}| \overset{!}{\le} \epsilon_4 \,. \tag{3.61}$$

Again, if this condition is violated, the interval is split recursively into two intervals until (3.61) holds or $N_i = N_{i,\zeta}$ is reached.

3.5.2 Atmosphere

The structure of the atmosphere is calculated using a fast and simple shooting method. The solver for the atmosphere receives as input the values of $z_{\text{eff}} = h$, T_{eff}, $\Sigma_{z,\text{eff}} = \Sigma$ and ρ_{eff} at the disk surface from the Henyey solver. While the first three quantities remain unchanged for the atmospheric calculations, the density is subject to successive iterations until the vertical structure of the atmosphere is solved.

Lock and load

The numerical integration of the atmosphere involves quantities like the mass density changing over orders of magnitude between the disk's surface and the upper end of the atmosphere. At the same time, the surface density Σ_z for example increases only slightly. It is therefore advisable to rewrite the equations (3.50)–(3.53) and introduce logarithmic quantities.

$$\frac{\partial \log z}{\partial \log \tau} = -10^{\log\tau + \log T - \log\kappa - \log z - \log\Xi - \log p_{\text{gas}}}, \tag{3.62}$$

$$\frac{\partial \log \Sigma_z}{\partial \log \tau} = -10^{\log\tau - \log\kappa - \log z}, \tag{3.63}$$

$$\frac{\partial \log T}{\partial \log \tau} = 10^{\log\tau - \log 4 - \log(\tau+1)}, \tag{3.64}$$

$$\frac{\partial \log p_{\text{gas}}}{\partial \log \tau} = 10^{\log\tau - \log p_{\text{gas}}} \cdot \left(\frac{-g_z}{\kappa} - \frac{4\sigma_{\text{SB}}}{3c} T_{\text{eff}}^4 \cdot \left(\tau + \frac{1}{2}\right)\right) \,. \tag{3.65}$$

In (3.65), g_z and κ are then functions of $\log T$ and $\log p_{\text{gas}}$.

Even in logarithmic variables, shooting from the disk's surface to the upper boundary is problematic, since tiny changes in the starting value $p_{\text{gas,eff}}$ result in highly different values p_{gas} at the upper boundary. Therefore, we reverse the integration path by starting from the upper boundary with iteratively determined upper values of $z_{\max} = z(\tau_{\min})$ and $\Sigma_{z,\max} = \Sigma_z(\tau_{\min})$ and shoot "downwards" to τ_{eff}. This is repeated until the resulting values for z and Σ_z fit to the input from the Henyey solver.

Shooting method

The course of action of one iteration follows the routine `shoot` of Press et al. (2001) and is divided into three phases.

Phase 1: *load* Using the upper boundary condition on p_{gas}, the known temperature T and two iteration values for z and Σ_z, we set up the starting values for the numerical integration of (3.62)–(3.65).

Phase 2: *target* With the remaining boundary conditions (3.54), (3.55) at $\tau = \tau_{\text{eff}}$, the targets of the numerical integration are defined.

Phase 3: *shoot* The numerical integration is performed using an explicit fourth order Runge-Kutta scheme with automatic step refinement (see Sect. 4.2.5 for details about the integration method). Depending on the quality of the solution, either new starting values for the z_{max} and $\Sigma_{z,\text{max}}$ are derived and the shooting process is repeated, or the corresponding value for ρ_{eff} is returned to the Henyey solver. In Sect. 3.5.2, more details will be given on that phase.

The *shoot* phase

Quality of the solution To evaluate the quality of one iteration, and by that the veracity of the "guessed" value ρ_{eff} at the disk surface, the values of the geometrical height $z_{\text{final}} = z(\tau_{\text{max}})$ and surface density $\Sigma_{z,\text{final}} = \Sigma_z(\tau_{\text{max}})$ from the numerical integration are compared with the boundary values z_{eff}, $\Sigma_{z,\text{eff}}$ and accepted iff

$$|z_{\text{final}} - z_{\text{eff}}| \leq \epsilon_5 \min\{z_{\text{final}}, z_{\text{eff}}\}\,, \tag{3.66}$$

$$|\Sigma_{z,\text{final}} - \Sigma_{z,\text{eff}}| \leq \epsilon_5 \min\{\Sigma_{z,\text{final}}, \Sigma_{z,\text{eff}}\}\,. \tag{3.67}$$

In the case of a non-acceptance, new values for z_{max}, $\Sigma_{z,\text{max}}$ have to be generated. In the same way as for the Henyey method, successive corrections are calculated from

$$z_{\text{final}}^{\{k-1\}} + \left(\frac{\partial z_{\text{final}}}{\partial z_{\text{max}}}\right)^{\{k-1\}} \delta z_{\text{max}}^{\{k-1\}} + \left(\frac{\partial z_{\text{final}}}{\partial \Sigma_{z,\text{max}}}\right)^{\{k-1\}} \delta \Sigma_{z,\text{max}}^{\{k-1\}} = 0\,, \tag{3.68}$$

$$\Sigma_{z,\text{final}}^{\{k-1\}} + \left(\frac{\partial \Sigma_{z,\text{final}}}{\partial z_{\text{max}}}\right)^{\{k-1\}} \delta z_{\text{max}}^{\{k-1\}} + \left(\frac{\partial \Sigma_{z,\text{final}}}{\partial \Sigma_{z,\text{max}}}\right)^{\{k-1\}} \delta \Sigma_{z,\text{max}}^{\{k-1\}} = 0\,, \tag{3.69}$$

where the derivatives are again determined numerically and the new solutions are obtained by solving this "system of equations" and by

$$z_{\text{max}}^{\{k\}} = z_{\text{max}}^{\{k-1\}} + \delta z_{\text{max}}^{\{k-1\}}\,, \tag{3.70}$$

$$\Sigma_{z,\text{max}}^{\{k\}} = \Sigma_{z,\text{max}}^{\{k-1\}} + \delta \Sigma_{z,\text{max}}^{\{k-1\}}\,. \tag{3.71}$$

Discretized grid and scaling The default grid is determined by logarithmic equidistant grid points τ_i with $\tau_0 = \tau_{\text{eff}}$ and $\tau_{N_{i,\text{atm}}} = \tau_{\text{min}}$. The standard grid resolution is the same as for the disk calculation, $N_{i,\text{atm}} = N_{i,\text{start}}$. The automatic refinement by the Runge-Kutta integrator is unlimited.

Additionally to the refinement by the integration scheme, the dependent variables are allowed to change only for a certain fraction of their actual value, otherwise the stepsize is reduced. Since the values along the integration path are not stored, this operation is not costly compared to the mesh-refinement for the Henyey solver.

3.5.3 Numerical implementation of κ

Depending on the description of the opacity (see Sect. 3.4.3), a numerical treatment is necessary. While the calculation of the opacities for Thomson-scattering, Kramer's opacity and the interpolation formula is straightforward, the tabulated values have to be interpolated.

The interpolation on the regular $\log T$–$\log R$ grid is done by using the cubic spline method `spline` from Press et al. (2001): while reading the opacity tables at the beginning of the program, tables of second derivatives are calculated and stored together with the values for the opacities. During the numerical calculation, these tables allow a fast interpolation of the required values $\kappa(\rho,T)$.

3.5.4 Agreement of disk and atmosphere solution

The solution for the vertical stratification of the disk and atmosphere at one radial position is accepted once the iteratively determined values h, T_{eff}, Σ, ρ_{eff} at the disk's surface solve both systems of equations:

$$\left|\rho_{\text{eff,disk}} - \rho_{\text{eff,atm}}\right| \overset{!}{\leq} \epsilon_6 \cdot \min\left\{\rho_{\text{eff,disk}},\rho_{\text{eff,atm}}\right\} \ . \tag{3.72}$$

Then, from (3.9), the average viscosity $\nu^\star$ can be calculated. The disk mass is updated by the obtained value of Σ and the calculation proceeds radially outwards until the outer boundary is reached. This path of calculation is mandatory, since the monopole approximation (3.12), (3.29) requires the enclosed disk mass to be known. Obviously, this is the case *à priori* only for $s = s_{\text{i}}$ where $M_{\text{d}} = 0$.

3.6 Results

3.6.1 Parameters, simulation characteristics

The results presented below were obtained for the following set of parameters:

Central black hole mass	M_{c}	$10M_\odot$
Accretion rate	$\dot{M}$	$0.1\dot{M}_{\text{E}}$
Inner disk radius	s_{i}	$3r_{\text{S}} = 6r_{\text{g}}$
Outer disk radius	s_{o}	$500r_{\text{S}}$
Grid points in radial direction	N_s	100
Default grid points in vertical direction	$N_{i,\text{start}}$	100
Standard β-viscosity parameter	β	$10^{-4}\dots10^{-7}$
Inner boundary condition parameter	χ	1
Optical depth at upper end of atmosphere	τ_{min}	10^{-4}
Density at upper end of atmosphere	ρ_{min}	10^{-12}

Due to the free-fall inner boundary condition ($\chi = 1$), we start the radial calculation at $s = 6r_{\text{S}}$ to avoid numerical difficulties. From the values for the surface density obtained at $s = 2s_{\text{i}}$, we can estimate the enclosed disk mass for $s_{\text{i}} \leq s < 2s_{\text{i}}$. Since its contribution is more than ten orders of magnitude smaller than the central mass in all cases, we can safely neglect the contribution to the disk mass from this innermost ring.

The required accuracies for accepting the solutions are given in the notation of Sect. A.2.2:

Maximum variation of variables	ϵ_1	0.1
Minimum number of successful iterations	n_{it}	2
Maximum deviation from true solution	G_{max}	$0.01 \cdot 4N_i$
Maximum deviation of integral equation (3.59)	ϵ_2	0.01
Threshold for mesh refinement for ρ	ϵ_3	0.1
Maximum mesh refinement for ρ	$N_{i,\rho}$	300
Threshold for mesh refinement for ζ	ϵ_4	0.01
Maximum mesh refinement for ζ	$N_{i,\zeta}$	400
Required accuracy for shooting method (Sect. 3.5.2)	ϵ_5	0.01
Maximum deviation of disk and atmosphere solution	ϵ_6	0.01

3.6.2 Disk properties

Standard disk Our main purpose is to investigate the contribution and efficiency of convection in transporting energy and providing viscosity. We therefore use a standard setup with $M_{\text{c}} = 10M_{\odot}$ and $\dot{M} = 0.1\dot{M}_{\text{E}}$ for which we vary the β-parameter of the underlying β-viscosity. We plot the radial structure of these disks in the following Figs. 3.2–3.4 as a function of radius in units of the Schwarzschild-radius $r_{\text{S}} = 2.95 \cdot 10^6$cm.

Common values for the viscosity parameter β are in the range of $10^{-4} \ldots 10^{-2}$ (Duschl et al., 2000). Since we want to investigate if the turbulence caused by convection can account partly for the total viscosity, we perform disk calculations with $\beta = [10^{-7}; 10^{-4}]$. We limit β to this range for the following two reasons.

1. For $\beta > 10^{-4}$, the standard β-viscosity prescription runs into the dissipation limit because the turbulent velocity $v_{\text{turb},\beta} = \sqrt{\beta} s\omega$ exceeds the sound speed c_{s}. In that case, a diffusion limit would have to be introduced. As we showed in the previous chapter, this results in an effective decrease of β. In the particular example of a $10M_{\odot}$ black hole accreting at 10% of the Eddington rate, the diffusion limit sets in for $\beta > 1.4 \cdot 10^{-4}$.

2. For $\beta < 10^{-7}$, hardly any solutions can be found for the required accuracies and the radial range considered here. The reason for this will be given by our results presented below.

In Fig. 3.2, we display the efficiency of convection in the energy transport, measured by the dimensionless quantity ζ. At each radial position, $\zeta = \zeta(s,z)$ is averaged vertically by

$$\zeta_{\text{avg}} = h^{-1} \int_0^h \zeta dz \,.$$

For $\beta = [10^{-5}; 10^{-4}]$, we find that a significant amount of the total energy is transported by convection in the inner part of the disk; close to the inner disk radius, $\zeta \approx 0.98$. Radiative energy transport dominates in the outer part of these disks, with a transition zone expanding from $[10r_{\text{S}}; 80r_{\text{S}}]$ for $\beta = 10^{-4}$ to $[10r_{\text{S}}; 180r_{\text{S}}]$ for smaller β. While the curves show a smooth behavior for $\beta \geq 10^{-5}$, this picture changes when β is decreased further: radial variations of ζ of about 0.1 can be seen in these cases. While the outer end of the transition zone is the same as in the $\beta = 10^{-5}$ case, the characteristic shape changes completely in the inner disk region,

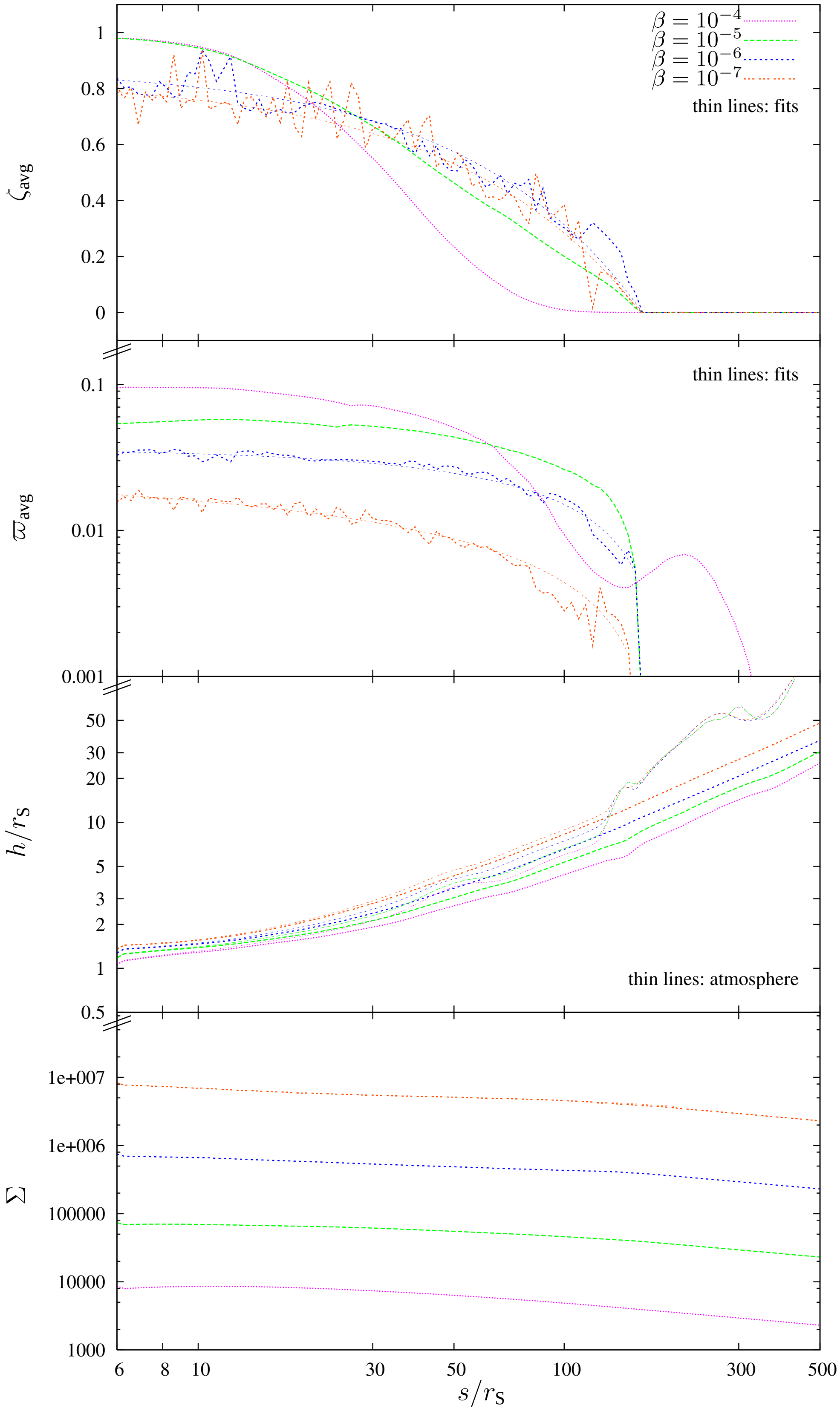

Figure 3.2. Solutions for the standard disk with $\beta = [10^{-7}; 10^{-4}]$, part 1.

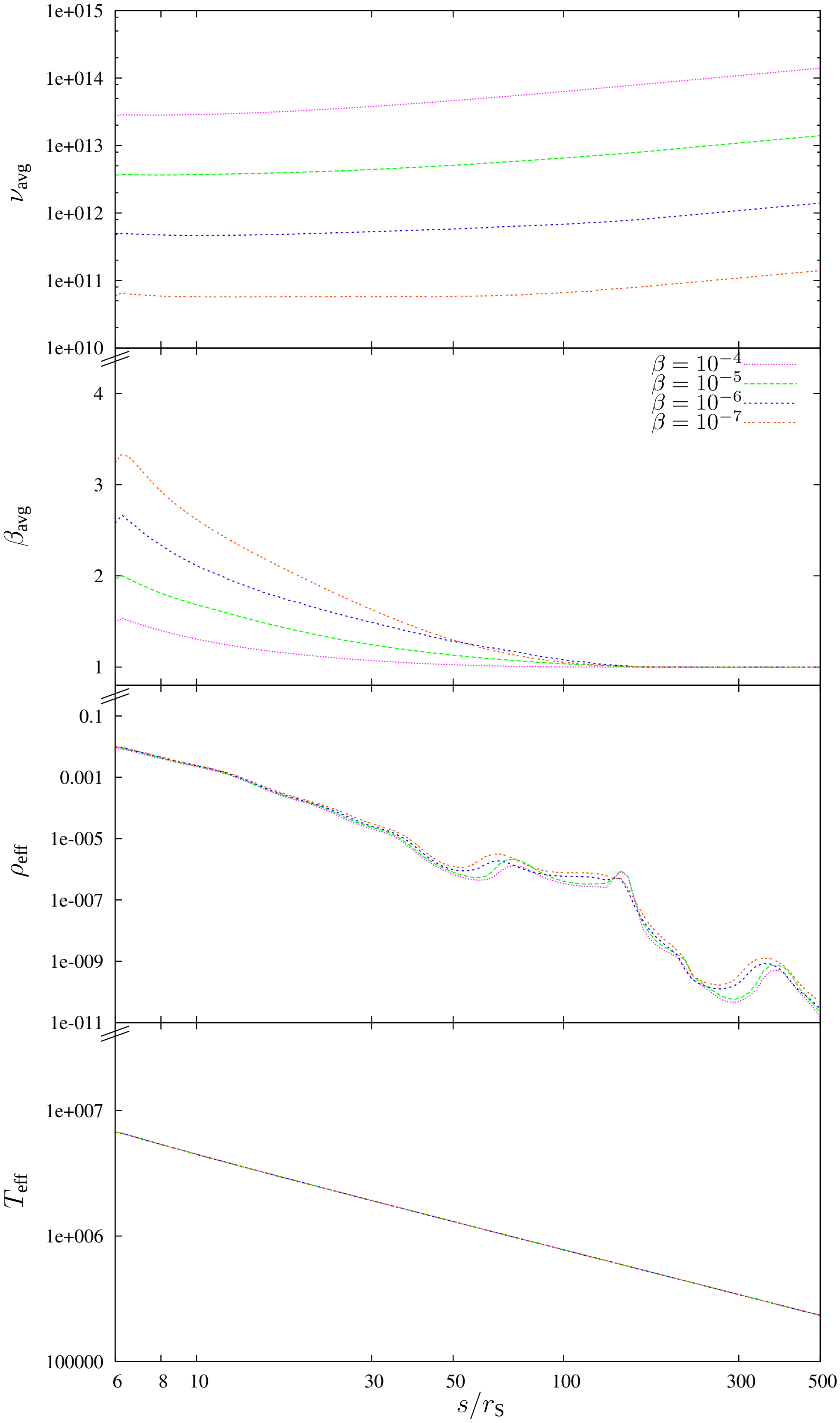

Figure 3.3. Solutions for the standard disk with $\beta = [10^{-7}; 10^{-4}]$, part 2.

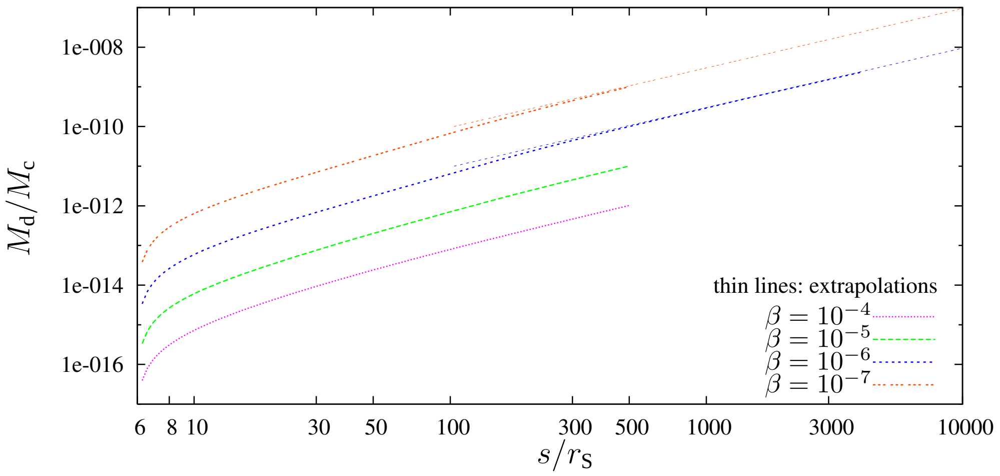

Figure 3.4. Solutions for the standard disk with $\beta = [10^{-7}; 10^{-4}]$, part 3.

and the maximum efficiency is decreased to about 0.8. In addition to the real results, we plot fitting curves (thin lines) to the cases $\beta = \{10^{-6}, 10^{-7}\}$, which were obtained by averaging over 20 successive solutions of the vertical stratification and by smoothing the curves afterwards.

For each β, the anisotropy factor $\varpi_\mathrm{avg} = (v_\mathrm{conv}/c_\mathrm{S})_\mathrm{avg}$ adopts a roughly constant value in the innermost, convective region, ranging from 0.1 ($\beta = 10^{-4}$) down to 0.02 ($\beta = 10^{-7}$). Thus, convection appears as radial drums rather than vertically elongated structures. The oscillations in ζ are reflected relatively weakly in the anisotropy factor (Fig. 3.2). In the non-convective outer parts of the disk, the convective viscosity and therefore the anisotropy factor vanish by definition.

A proper explanation of the possible reasons for these variations in ζ can be given only by investigating further disk quantities such as the disk height h, which is plotted in units of r_S in Fig. 3.2 (thick lines). Additionally, we plot the height of the atmosphere by thin lines. In all cases, the disks are geometrically thin, with a maximum ratio of $h/s \approx 0.25$. With decreasing β, the disk puffs up slightly. The atmosphere is negligibly thin in the inner region, but expands for larger radii. Contrary to ζ and ϖ, no instabilities can be detected for the low-β case for both the disk and the atmosphere.

The same is true for the surface density Σ of the disk (Fig. 3.2). We observe smooth curves for all values of β, with a linear increase at each radius with β^{-1}. The mass contained in the atmosphere is completely negligible in all cases.

In Fig. 3.3, we plot the vertically averaged viscosity

$$\nu_\mathrm{avg} = h^{-1} \int_0^h \nu \, dz$$

and $\beta_\mathrm{avg} = \nu_\mathrm{avg}/\nu_\beta$, where ν_β is constant for the vertical stratification. For all β, the total viscosity decreases less than linearly with β, which is due to the contribution from convective viscosity. We find that in the low-β case, the convective viscosity ν_conv can become twice as large as the underlying β-viscosity. It is important to note that although the convective viscosity becomes *relatively stronger* for lower supporting viscosities, its absolute value decreases as well. Thus, the total viscosity generated in the disk becomes lower and lower with decreasing β. Again, in both plots no instabilities can be detected, although the influence of ζ is definitely strong. The small peak seen in β_avg at the innermost radii is caused by the inner boundary condition.

The density ρ_{eff} at the disk's surface is also shown in Fig. 3.3, together with the effective temperature T_{eff}. Since the disk mass is negligible for all disk runs (see below), the radial structure equations give the same results for the total flux and therefore for the temperature T_{eff} at the disk surface. Looking at the corresponding densities, we find that their values lie very close for all solutions with a clear decreasing trend towards larger radii. A certain irregular structure can be seen for all results, an effect of the opacity model, which itself is very sensitive to the densities and temperatures in this region of the disk.[2] The instabilities in ζ are also not detectable, neither in temperature, nor in density.

Finally, Fig. 3.4 displays the resulting disk mass in units of the central mass. As expected, the disk mass increases with decreasing β, since the disk gets thicker and the surface density increases. For all cases, the enclosed disk mass is completely negligible compared to the central black hole mass. We estimate the equality radius s_{equ} where $M_{\text{d}}(s) = M_{\text{c}}$ by extending the radial calculation towards larger radii for the $\beta = 10^{-6}$ disk case. A linear fit to the outer region in the $\log$-$\log$ plot gives

$$M_{\text{d}}(s)/M_{\text{c}} = 3 \cdot 10^{-10} \left(\frac{s}{10^3 r_{\text{S}}}\right)^{3/2}, \qquad \beta = 1 \cdot 10^{-6}\,, \tag{3.73}$$

$$M_{\text{d}}(s)/M_{\text{c}} = 3 \cdot 10^{-9} \left(\frac{s}{10^3 r_{\text{S}}}\right)^{3/2}, \qquad \beta = 1 \cdot 10^{-7}\,, \tag{3.74}$$

which in turn leads to

$$s_{\text{equ}} = 2.2 \cdot 10^9 r_{\text{S}}, \qquad \beta = 1 \cdot 10^{-6}\,, \tag{3.75}$$

$$s_{\text{equ}} = 4.8 \cdot 10^8 r_{\text{S}}, \qquad \beta = 1 \cdot 10^{-7}\,. \tag{3.76}$$

Thus, self-gravity is safely negligible in our disk calculations.

Extended parameter space We extend the disk calculations towards varying accretion rates and central masses in order to see how general properties and, in particular, the instabilities in ζ, depend on the input parameters.

In a first step, we investigate the dependence of the results on the accretion rate while keeping a constant $\beta = 10^{-5}$ and a constant $M_{\text{c}} = 10 M_{\odot}$. We perform disk calculations with accretion rates of $\dot{M} = [0.01; 0.2] \dot{M}_{\text{E}}$. Higher rates are not included, since the disks become too thick for the thin-disk approximation to be valid: for $\dot{M} = 0.2$, the ratio h/s reaches values larger than 0.3 in the inner disk region, while it does not exceed 0.03 for the lower limit $\dot{M} = 0.01$, see Fig. 3.5. The figure also shows that the disk mass and the surface density scale almost linearly with the accretion rate, as expected. The contribution of convective turbulence is naturally higher the higher the accretion rate, up to $\nu_{\text{conv}} = 1.5 \nu_{\beta}$, with the convective zone reaching outwards to $20 r_{\text{S}}$ for low accretion rates, and $250 r_{\text{S}}$ for high accretion rates, respectively. The anisotropy factor in the convective zones is not influenced by the accretion rate (not displayed).

In Fig. 3.6, we see that the density and the temperature at the disk's surface also increase with $\dot{M}$, although the dependence is weaker than linear, $\rho_{\text{eff}} \propto \dot{M}^{0.3}$ and $T_{\text{eff}} \propto\propto \dot{M}^{0.25}$. The solutions also show a clear dependency of ζ on the accretion rate (Fig. 3.7): beside the standard case $\dot{M} = 0.1 \dot{M}_{\text{E}}$, also the low accretion rate calculation produces a stable solution, but with

---

[2] When dropping the sophisticated opacity description and using simple formulas like, e. g., the Kramer's opacity, the structure disappears and a linear decrease is found in the $\log$-$\log$ plot.

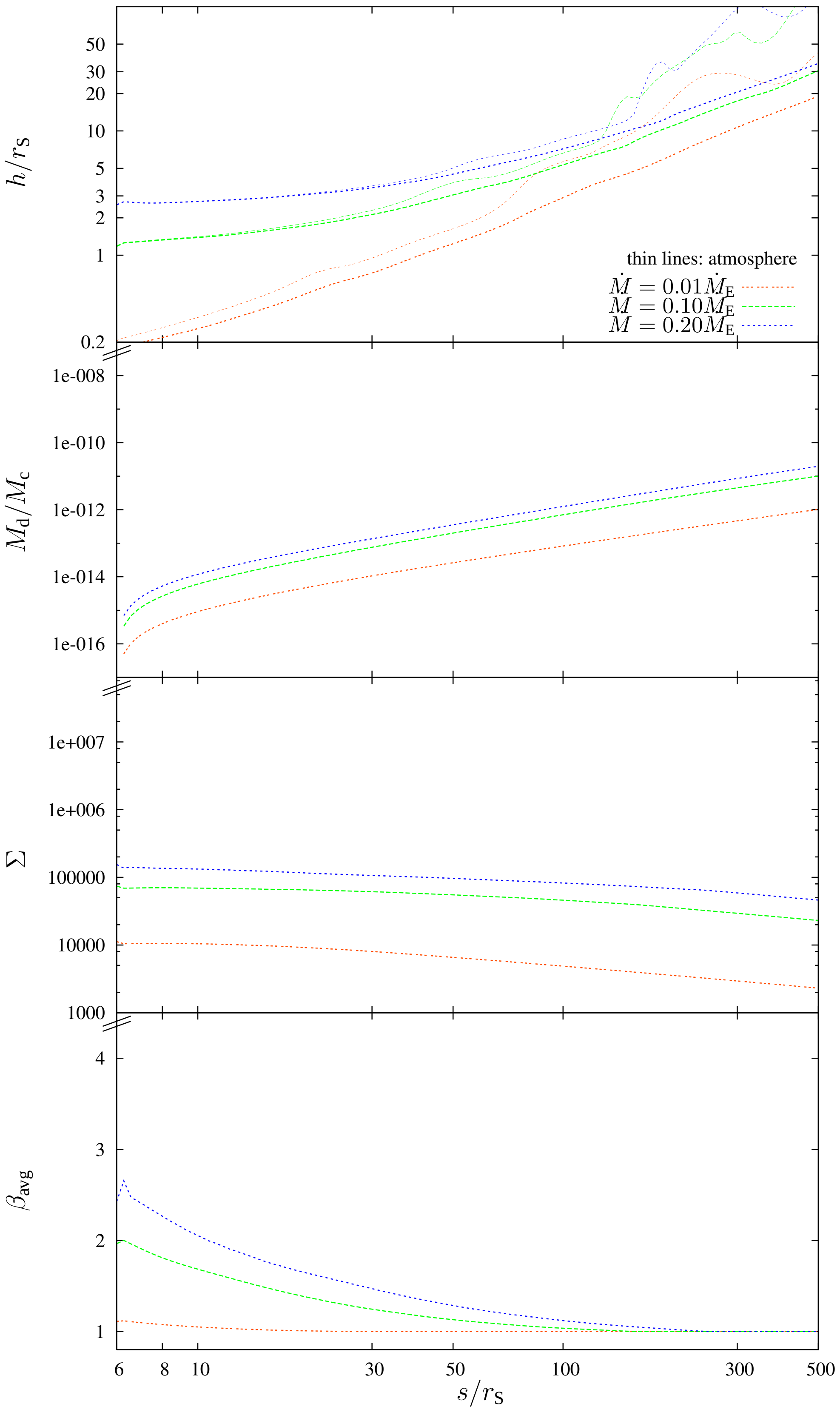

Figure 3.5. Solutions for varying accretion rates with $M_c = 10M_\odot$ and $\beta = 10^{-5}$, part 1.

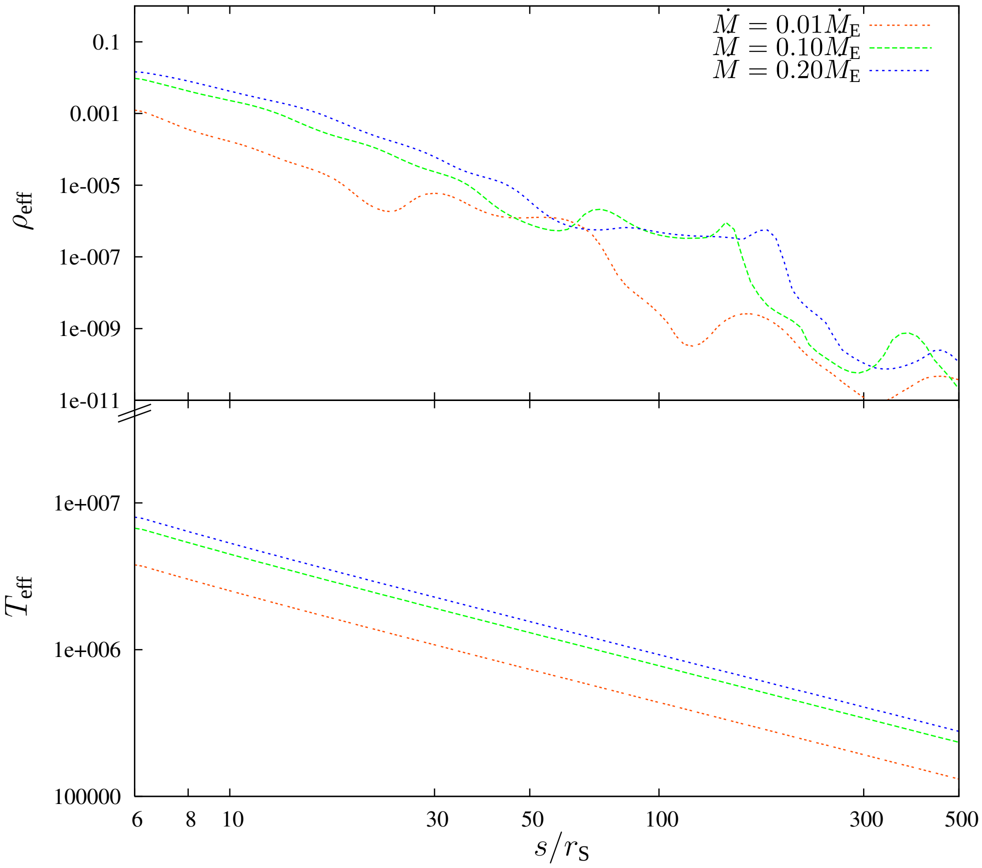

Figure 3.6. Solutions for varying accretion rates with $M_{\rm c} = 10M_\odot$ and $\beta = 10^{-5}$, part 2.

a significant reduction of the relative contribution from convection. Given that both the total energy and the angular momentum that have to be transported through the disk depend linearly on the accretion rate (compare (3.10), (3.33)), the standard β-viscosity is almost large enough to account for both requirements. On the contrary, higher accretion rates lead to the same type of instabilities of ζ as lower β-values $< 10^{-6}$ do for the standard setup.

Secondly, we focus on varying central masses for a constant $\beta = 10^{-5}$ and a constant absolute value $\dot{M}$ such that it corresponds to $0.1\dot{M}_{\rm E}$ for a $10M_\odot$ black hole. *Thus, the Eddington ratio* $\dot{M}/\dot{M}_{\rm E}$ *scales with* $M_{\rm c}^{-1}$. We limited the parameter range to $M_{\rm c} = [5; 100]M_\odot$, which corresponds to Eddington ratios of $\dot{M} = [0.2; 0.01]\dot{M}_{\rm E}$. For lower central masses, the disks get too thick (c. f., Fig. 3.8), while for higher central masses, the density at the disk surface reaches our boundary condition $\rho_{\rm min} = 10^{-12}{\rm g/cm}^3$ at the upper end of the atmosphere too early. This is also why we stop the $M_{\rm c} = 100M_\odot$ calculation at $s \approx 120r_{\rm S}$, see Fig. 3.8. The disk height h, the density $\rho_{\rm eff}$ and the effective temperature $T_{\rm eff}$ are all very sensitive to the Eddington ratio and hereby to $M_{\rm c}$.

We also find that the surface density Σ scales with $M_{\rm c}^{-1}$ in the outer part of the disk, while this scaling law changes slightly in the inner part of the disk where convection plays an important role. Thus, the disk mass scales with $M_{\rm c}$ and $M_{\rm d}/M_{\rm c} = {\rm const}$ (not displayed).

As in the previous case of varying $\dot{M}$, the underlying viscosity is large enough to allow for a significant reduction of convective processes in the high mass case, because $F \propto M_{\rm c}^{-2}$,

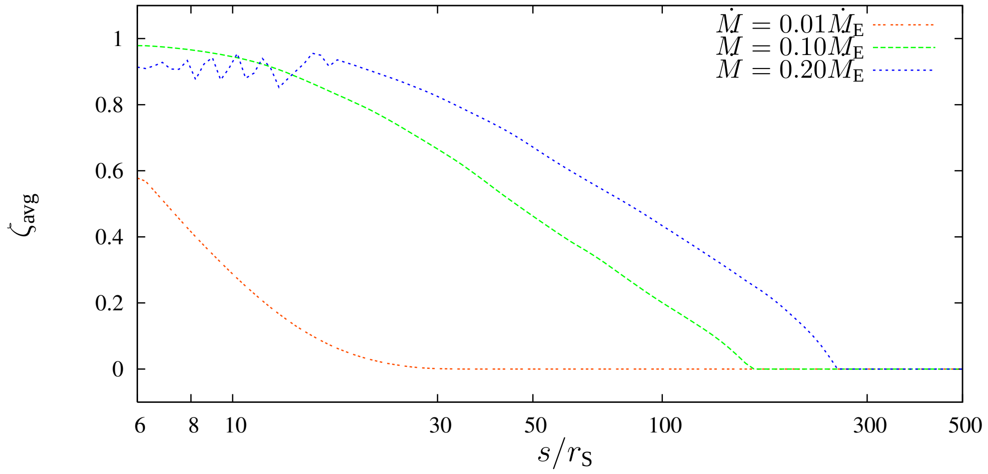

Figure 3.7. Solutions for varying accretion rates with $M_c = 10M_\odot$ and $\beta = 10^{-5}$, part 3.

$\Psi = \text{const}$ and $\nu_\beta \propto M_c$. This is reflected in β_{avg} as well as in the vertically averaged convective efficiency ζ_{avg}, which shows a stable and smooth solution for the higher central mass cases, while instabilities occur for the low mass case (Fig. 3.9).

In a last step, we vary the mass of the central black hole in the range of $M_c = [1; 100]M_\odot$ while keeping a constant $\beta = 10^{-5}$ and a constant Eddington ratio $\dot{M} = 0.1\dot{M}_E$ for the accretion rate. *This means that the absolute value of the accretion rate in* g/s *is implicitly scaled with* M_c. It turns out that both the ratio h/r_S and the surface density Σ do not change for varying central masses (not displayed). For this fact to hold, the mass density ρ has to scale with M_c^{-1}, which is reflected very nicely in Fig. 3.10. Then, given that the disk's mass scales only with $s^2 \propto M_c^2$, the ratio M_d/M_c scales with M_c. Note that the calculation for the $M_c = 100M_\odot$ case terminates at $s \approx 250r_S$, because the density ρ_{eff} decreases towards 10^{-12}g/cm^3, which is already the upper boundary condition (i. e., the lowest value of the density) in the atmosphere.

The effective temperature, also plotted in Fig. 3.10, clearly shows a decrease for higher central masses. From the energy equation (3.10), we derive that $F \propto M_c^{-1} \implies T_{eff} \propto M_c^{-0.25}$ and $\nu_\beta \propto M_c$. Thus, less energy has to be transported through the vertical layers, while at the same time the supporting viscosity is increased for higher central masses. We expect that the larger the central mass, the lower the default β-parameter can be before the radial variations in ζ set in. This is confirmed by our results; the variations appear only for the low mass case, while the standard and high mass cases are stable in the inner region. It is worth mentioning that the convective zone reaches further outwards for the high central mass case, although radiative processes dominate the energy transport. For completion, we would like to add that neither the ratio β_{avg}/β_{std}, nor the anisotropy factor ϖ are influenced significantly by a varying central mass when the Eddington ratio is kept constant.

Radial variations in the convection efficiency ζ An important point in this discussion is the origin of the instabilities in ζ for certain disk solutions. We have seen that they occur if the underlying viscosity is decreased under a threshold value, which itself depends on the parameters central mass and accretion rate. Interestingly, these instabilities appear only in ζ and ϖ, two artificial quantities introduced for a better understanding of the ongoing processes.

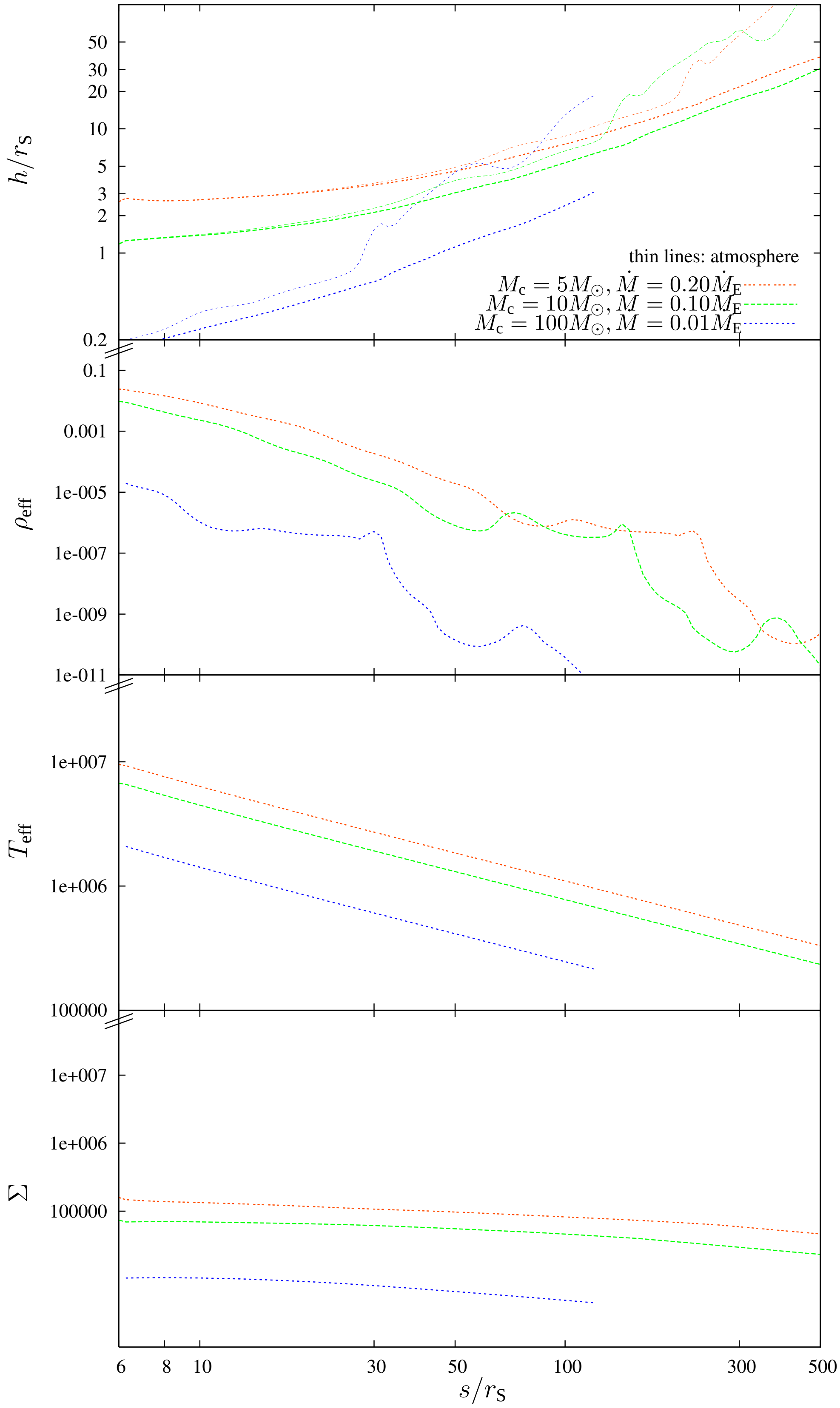

Figure 3.8. Solutions for varying central masses with constant $\dot{M}$ – corresponding to $0.10\dot{M}_\mathrm{E}$ for a central black hole mass $M = 10M_\odot$ – and $\beta = 10^{-5}$, part 1.

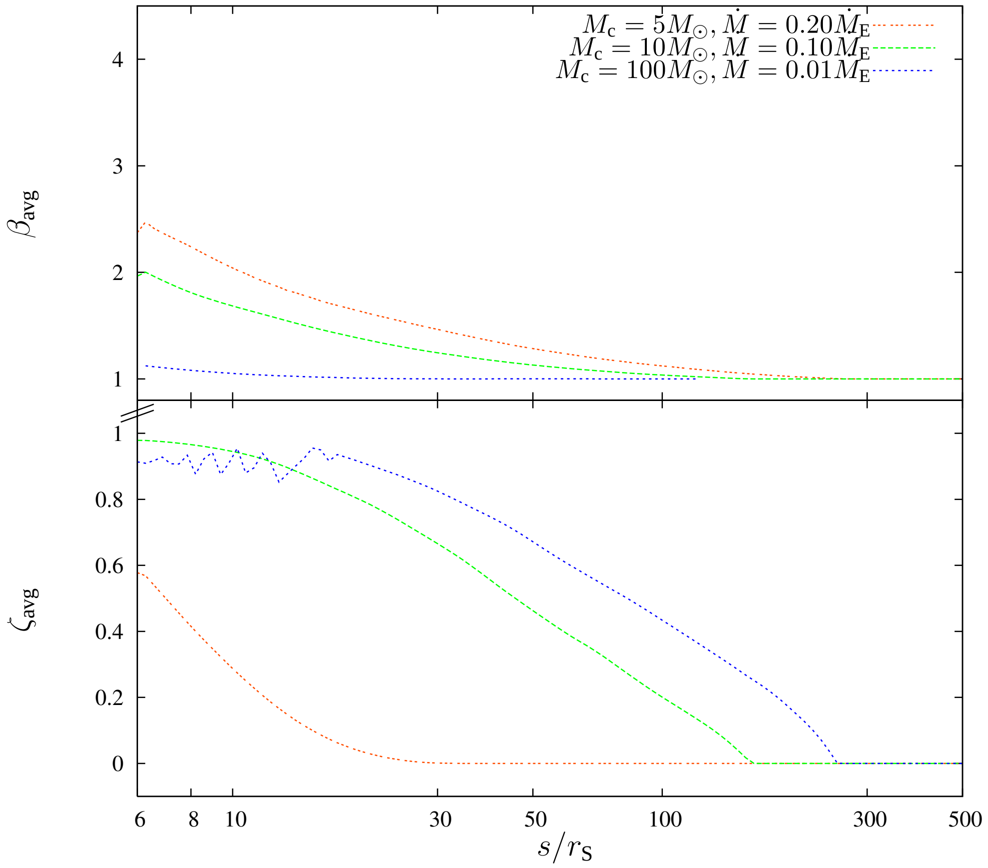

Figure 3.9. Solutions for varying central masses with constant $\dot{M}$ – corresponding to $0.10\dot{M}_\mathrm{E}$ for a central black hole mass $M = 10M_\odot$ – and $\beta = 10^{-5}$, part 2.

None of the physically relevant quantities such as density, temperature and pressure reflect these instabilities, reducing the importance of the fluctuations for a physical interpretation of these disks.

Nevertheless, we can understand their occurrence by taking a closer look on the vertical structure in the instable zone of the disk. We therefore plot the vertical stratification of the pressure, the convection efficiency ζ and the two gradients ∇_rad, ∇_ad at a radial position close to the black hole ($s = 8r_\mathrm{S}$) for our standard setup disk (Fig. 3.11). The x-axis is hereby given by the heat flux F_z in units of the total flux F, fixed by the energy equation (3.10). The data is taken from a single solution of the vertical structure without any smoothing or averaging.

Close to the black hole, radiation pressure dominates over gas pressure by about one order of magnitude. Since the two pressure contributions show smooth curves for all β, ρ and T must also adopt such a smooth structure. Therefore, the instabilities in ζ are not caused by numerical noise in the density or temperature.

Let us now have a look at the vertical layering of the convective efficiency ζ in the instable cases $\beta = \{10^{-6}, 10^{-7}\}$. We detect narrow "convective cells" for small $F_z \approx 0.1F$, which do not occur for larger β. These small cells are fluctuating for successive iterations, with the vertical layers close to the mid plane being either fully convective or non-convective. On the contrary, the vertical structure retains a stable, almost fully convective state for $\beta = \{10^{-4}, 10^{-5}\}$. The reason for these fluctuations can be found in the lower plots of Fig. 3.11, where we display the

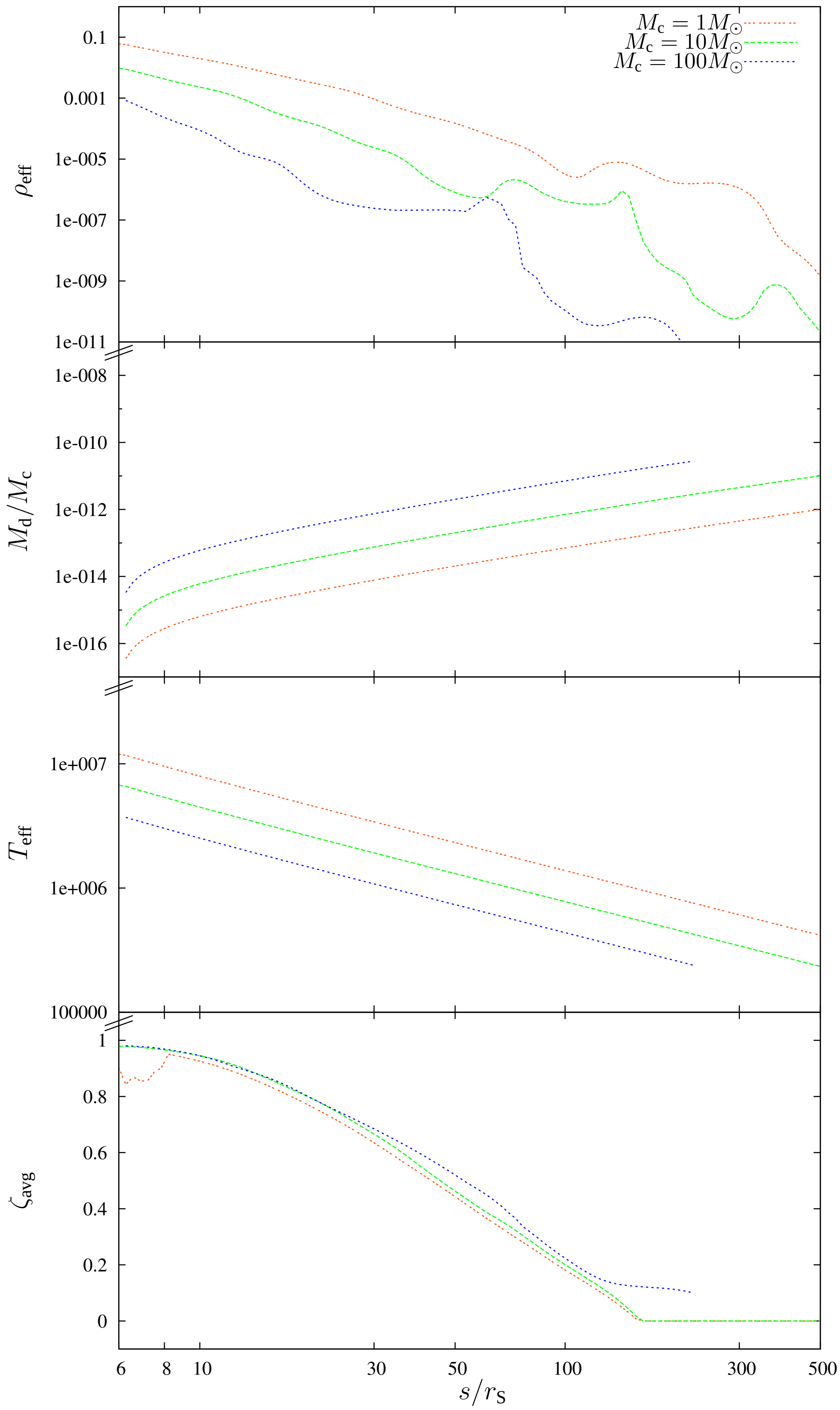

Figure 3.10. Solutions for varying M_c, constant Eddington ratio $\dot{M} = 0.10\dot{M}_E$ and $\beta = 10^{-5}$.

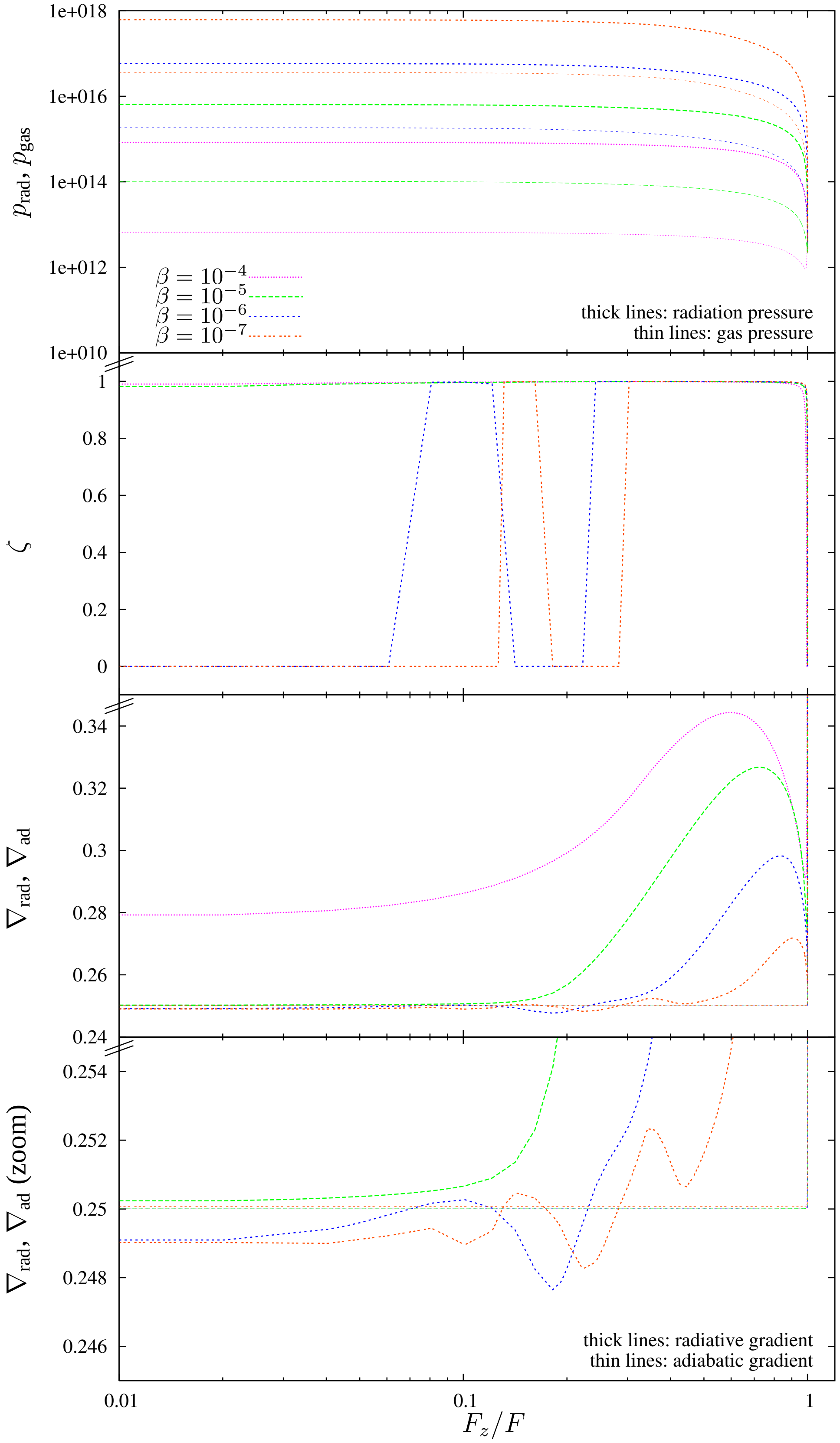

Figure 3.11. Vertical structure for the standard disk close to the central black hole at $s = 8r_{\rm S}$.

two gradients $\nabla_{\rm rad}$ and $\nabla_{\rm ad}$, which determine if convection occurs or not. The quantity ζ is determined by the cubic equation (3.30), which depends strongly on B, with $\zeta \to 0$ for $B \to 0$ and $\zeta \to 1$ for $B \to \infty$. The key point is that B reflects the Schwarzschild criterium, meaning that if the radiative gradient is less or equal to the adiabatic one, the stratification is stabilized and no convection occurs:

$$\nabla_{\rm rad} \leq \nabla_{\rm ad} \implies B = 0, \qquad \zeta = 0\,.$$

In the opposite case, even a small positive difference $\nabla_{\rm rad} - \nabla_{\rm ad}$ is multiplied by $A^2 \approx 10^{10}$ and therefore $B \gg 1$ and $\zeta \lessapprox 1$. Thus, fluctuations in $\nabla_{\rm rad} - \nabla_{\rm ad}$, regardless of being of physical or numerical nature, will cause fluctuations in ζ. These fluctuations can not be seen in the physical quantities, because they occur only for small values of F_z and therefore have little effect on the total structure. For an interpretation of the overall physics and a relation to observable quantities, these instabilities play only a minor role and can be replaced by smoothed values. However, a further investigation of the nature of these fluctuations is necessary, but beyond the scope of this work.

3.7 Conclusions

Lower limit on the β-parameter In the light of the above results, we derive that convection alone cannot account for viscosity in accretion disks. It requires an underlying viscosity, produced by some other process, which is parameterized by ν_β in our model. The reason for this can be understood by the following line of argumentation: convection works towards establishing an adiabatic vertical stratification of the disk. Assuming that there exists an additional source of viscosity in the disk, the convective elements are decelerated by this inherent friction as well and an equilibrium state is established where energy is transported steadily by both radiation and convection, and where the total viscosity is given by the sum of the underlying and the convective viscosity. A good example therefore is the $\beta = 10^{-5}$ case in Fig. 3.11, where $\nabla_{\rm rad}$ exceeds $\nabla_{\rm ad}$ only slightly, but in a stable manner.

If, however, the underlying viscosity is too weak, convection is unchecked and very efficient in building an adiabatic stratification in the disk with $\nabla_{\rm rad} \lessapprox \nabla_{\rm ad}$. Such a state is also called *marginally Schwarzschild-stable* (Cox & Giuli, 1968). Physically, such a state means that no energy is transported and convection ceases. Thus, convective turbulence and viscosity vanish. In addition, given that the supporting β-viscosity is too low, the total viscosity becomes very small in the vertical disk calculations. This contradicts the requirements from the radial structure equations: that the total amount of energy, released by the accretion process and given by (3.10), has to be transported away. Furthermore, viscosity must be present to fulfill the angular momentum transport equation (3.9). From this argumentation, the underlying viscosity can also be regarded as the “driving force” for convection.

Influence of central mass and accretion rate The results and the discussion given above show that the effects of a varying central mass with fixed accretion rate are very similar to those of an inversely varying accretion rate with fixed central mass. With increasing $\dot{M}/\dot{M}_{\rm E}$, the required amount of energy and angular momentum which have to be transported through the disk increase, leading to larger threshold values for the total viscosity. Since convection can only partly account for the required increase, the supporting viscosity needs to be larger as well.

More interesting, however, is the study of an varying central mass while the Eddington ratio is kept constant. Here, variations of M_c have a strong influence on the resulting convective disks, in particular on the occurrence of the ζ-variations and the importance of self-gravity: since we can assume that the scaling law $M_\mathrm{d}/M_\mathrm{c}$ holds for higher central black hole masses, the estimated disk mass at $s = 500 r_\mathrm{S}$ increases from $10^{-11} M_\mathrm{c}$ to $10^{-4} M_\mathrm{c}$ for a supermassive black hole with $10^8 M_\odot$, and the equality radius s_equ shrinks by a factor $(10^7)^{2/3} \approx 5 \cdot 10^4$. Furthermore, we demonstrated that higher central masses in principle allow for lower supporting viscosities, leading to relatively higher disk masses. But, as we showed in the previous chapter, convection also produces a negative feedback on the energy transport in the self-gravitating regions of the disk. The interesting question of when and how self-gravity enters the game and changes the disk structure will be investigated in future work.

Convective turbulence, differential rotation and magneto-rotational instability: a speculative viscosity-mixture Our results show that disk solutions do only exist if there is viscosity produced by effects other than convection. Convection itself can contribute significantly to the total viscosity, but needs a driving force to establish an equilibrium in energy transport in the vertical direction.

In our investigation, we parameterize the supporting viscosity by a permanent β-viscosity, where the threshold value of the standard β-parameter depends on the central mass and the accretion rate. Originally, the β-viscosity was motivated by differential rotation, a physical interpretation of friction in Keplerian disks. As we discussed already in Chapt. 1, differential rotation was first excluded from being a possible solution in accretion disks, because early laboratory experiments resulted in discouragingly low viscosities. However, Richard & Zahn (1999) showed that differential rotation can give rise to turbulence with the analogue of the β-parameter being as large as 10^{-5}.

In this work, we completely ignored the turbulence due to magnetic effects, the well-known MRI (Balbus & Hawley, 1991). This effect is regarded as the primary explanation for the high viscosity in accretion disks, although some aspects remain to be clarified (see, e. g., Begelman & Pringle (2007); King et al. (2007)). Machida et al. (2004) investigated how the effects of magnetic turbulence translate into the classical α-parameterization in the case of a $10 M_\odot$ black hole and found that the corresponding α is not constant, but approximately decreases linearly with radius:

$$\alpha \propto \exp\left\{\frac{1}{2s/r_\mathrm{S}}\right\} - 0.99, \qquad \alpha \to 0.01 \text{ for } s \gg r_\mathrm{S}\,.$$

Their results have to be used carefully since the absolute values in the fitting formula depend strongly on the disk corona – a high-temperature and low-density region, put artificially to prevent disk material to evaporate (Machida, priv. comm.). Also, the general question if the MRI effects can be translated into an α- or β-type viscosity (as a rule of thumb, $\beta \approx \alpha^2 \ldots \alpha$) remains to be answered (see, e. g., Pessah et al. (2008)).

A particular problem of the MRI are the so-called *dead zones*, where the growth rate of magneto-rotational instabilities is strongly suppressed. For the MRI to be efficient, the magnetic field needs to couple to the rotating material. If the ionization of the disk material is too low, the coupling is weak (Gammie, 1996). This affects mainly the middle regions of accretion disks, which are sufficiently cool and dense at the same time.

Let us assume for the moment that a parameterization is possible and that the s^{-1} behavior of the MRI viscosity is roughly valid. Then, we can draw the following picture involving differential rotation, convection, and magnetic turbulence: in the inner disk region, we saw that convection and differential rotation with a corresponding β-parameter of $\sim 10^{-5}$ do not produce enough viscosity for the low central mass and/or high accretion rate case. However, close to the central black hole, the magnetic turbulence is strong, resulting in a large viscosity due to the magneto-rotational instability. In the intermediate disk region, a weaker MRI effect adds to convection and differential rotation to account for the required total viscosity. Finally, in the outer disk region, both magnetic effects and convection become negligible, but differential rotation is sufficient in generating the less demanding values of the total viscosity. It would be of great importance and interest to combine these three sources of viscosity in a sophisticated project in the near future and to see if the required viscosity can be generated for a large variety of disk parameters.

4 Spectral energy distribution of super-Eddington flows I – continuum processes

4.1 Context

Numerous theoretical investigations have shown that the classical Eddington limit, which has been derived for a spherical symmetric object such as a star, does not apply in accretion disks (see also the introductory remarks in Chapt. 1). Along with these studies, also the emerging disk spectra of various types of accretion disk models have been investigated widely in the past, since a correct interpretation of observational data needs to stand comparison with theoretical models.

Standard blackbody or modified blackbody spectra for supercritical accretion disks have been calculated (Szuszkiewicz et al., 1996; Wang & Zhou, 1999; Mineshige et al., 2000; Watarai et al., 2000). Furthermore, slim accretion disk spectra, including self-irradiation and self-occultation for self-similar solutions have been studied by Fukue (2000), while Watarai et al. (2005) investigated the implications of geometrical effects and general relativistic effects on the disk spectra. Further, Kawaguchi (2003) considered Comptonization effects in spectral calculations, finding significant spectral hardening occurring at large accretion rates. In these approaches, however, anisotropy in radiation fields is not taken into account, although we naively expect mild beaming effects, i. e., radiation is likely to escape predominantly in the direction perpendicular to the disk plane. Moreover, the influence of the environment of the disk, e. g. its atmosphere, is not considered. It is well known that accretion disks have extended atmospheres, which indeed have a strong influence on the emerging spectra. The photoionization of the accretion disk surface by incident X-rays has been investigated by Reynolds et al. (1999), while Dörrer et al. (1996) calculated disk spectra for thin α-disks around a Kerr black hole, surrounded by a hydrogen atmosphere.

In this study, we focus on the question of wether supercritical accretion is not only allowed, but also actually present in black hole accretion disks. Therefore, we calculate the spectral energy distribution of supercritical accretion flows based on the radiation hydrodynamic (RHD) simulations computed by Ohsuga et al. (2005). *Supercritical accretion* is often used as a synonym for super-Eddington accretion, which means that accretion takes place with rates above the classical Eddington rate as it is derived from the stellar case: one usually assumes that half of the gravitational energy, released by the accretion process, goes into radiation, while the other half adds to the kinetic energy to maintain the (nearly) Keplerian rotation. Assuming a non-rotating central black hole with mass M_c and equating the total disk luminosity with the classical Eddington luminosity $L_\mathrm{E} = (M_\mathrm{c}/M_\odot) \cdot 1.2 \cdot 10^{38}\,\mathrm{erg/s}$, one gets

$$\dot{M}_\mathrm{E} = \frac{L_\mathrm{E}}{\iota c^2} = 2.6 \cdot 10^{-8} \left(\frac{M_\mathrm{c}}{M_\odot}\right) \frac{M_\odot}{\mathrm{yr}} \,. \tag{4.1}$$

In (4.1), the dimensionless factor ι parameterizes the efficiency of converting gravitational energy into radiation and is set to unity for simplicity.

In Sect. 4.2, we describe the methods of calculation used in this investigation. Main aspects of the subjacent simulation data will also be briefly summarized there. We then present our spectral calculations in Sect. 4.3. Discussion will be given in Sect. 4.4, while Sect. 4.5 is devoted to conclusions. The results presented in this chapter have been published in the Monthly Notices of the Royal Astronomical Society (Heinzeller et al., 2006).

4.2 Model setup

4.2.1 RHD simulations

In this study, we account for both a sophisticated disk model and the disk's surroundings, computed in a self-consistent way within RHD simulations: we apply our calculations to the 2D RHD simulation data from Ohsuga et al. (2005). Starting with an empty disk and continuously injecting mass through the outer disk boundary, the authors simulated the structure of a supercritical accretion flow, until it reaches the quasi-steady state. The central object is given by a non-rotating stellar mass black hole ($M_\mathrm{c} = 10 M_\odot$), generating a pseudo-Newtonian potential (Paczyński & Wiita, 1980). The viscosity is given by the classical α-prescription with $\alpha = 0.1$. The mass input rate at the outer boundary ($500 r_\mathrm{S}$, r_S: Schwarzschild radius) strongly exceeds the Eddington limit, $\dot{M}_\mathrm{ext} = 1000 \dot{M}_\mathrm{E}$. The authors considered energy transport through radiation and advection and included relativistic effects in the radiation part. Note that photon trapping effects were automatically incorporated in the simulations. A gray computation of the radiative transfer in the flux limited approximation (Levermore & Pomraning, 1981) was used.

They found that the supercritical flow is composed of two parts: the disk region and the outflow regions above and below the disk. Within the disk region, circular motion as well as patchy density structures are observed. The mass accretion rate decreases inwards (i. e. as matter accretes), roughly in proportion to the radius, and the remaining part of the disk material leaves the disk to form an outflow. In particular, only 10% of the inflowing material finally reaches the inner boundary ($3 r_\mathrm{S}$), while the remaining 90% gets stuck in the dense, disk-like structure around the midplane or transforms into moderately high-velocity outflows with wide opening angles. The outflows are accelerated up to $\sim 0.1c$ via strong radiation pressure force. Figure 4.1 displays key quantities of the simulation data on a two-dimensional grid in directions $s = \sqrt{x^2 + y^2}$ and z, which reflect the powerful outflow from the disk with high velocities, high gas temperatures and low mass densities. By comparing gas and radiation temperatures, it can be seen that an equilibrium between matter and the radiation field is only established in the dense, disk-like structure close to the x-y plane.

From the simulation data, the gas density ρ, its temperature T_gas and its velocity v are taken as input parameters, as well as the radiation energy density E. The methods of calculating other quantities, such as the radiation temperature T_rad, the source function S_ν and the radiation pressure tensor $\mathcal{P}_\nu$, will be given in the following subsections.

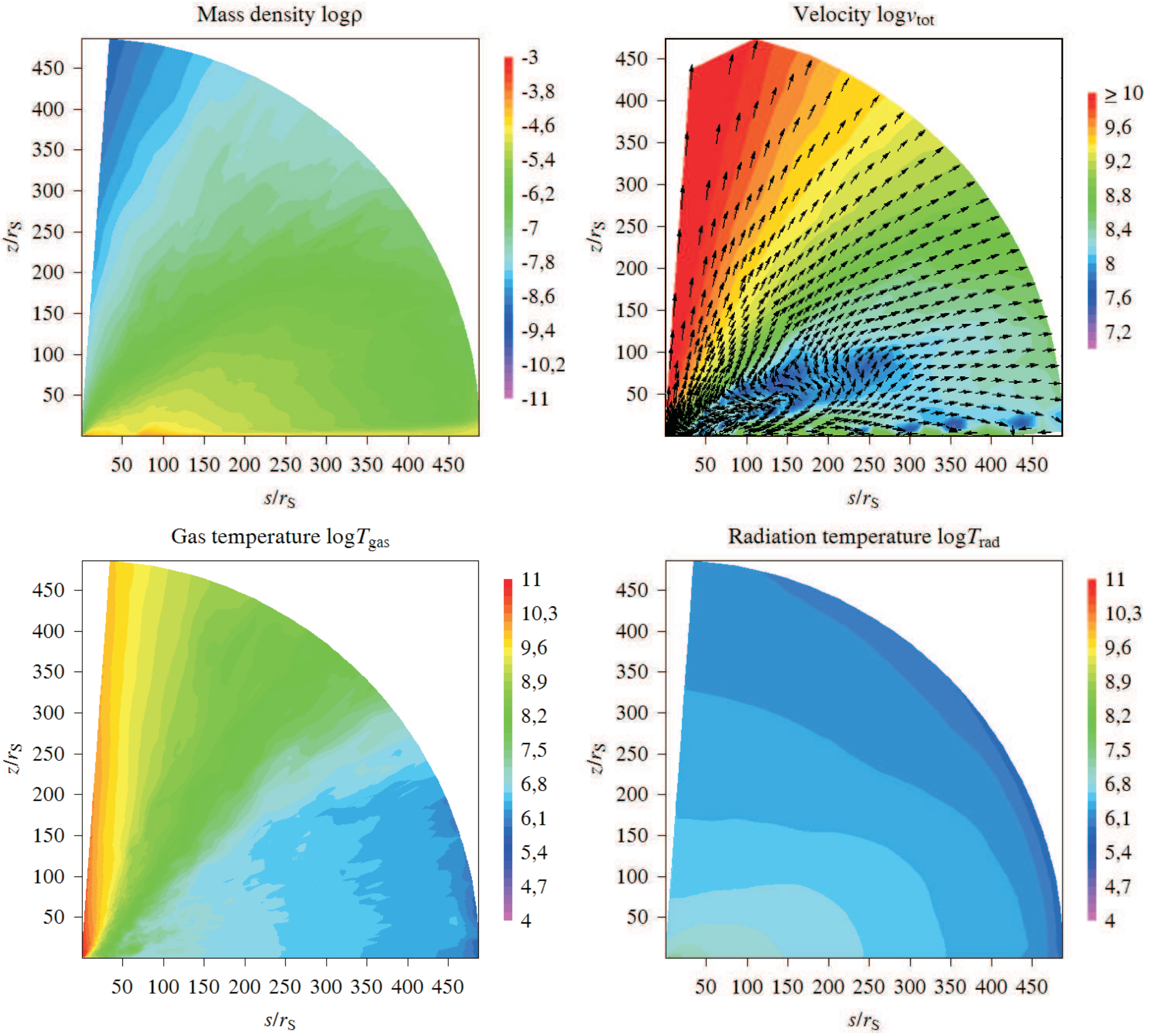

Figure 4.1. Key quantities of the simulation data for $M_\mathrm{c} = 10 M_\odot$ and $\dot{M}_\mathrm{ext} = 1000 \dot{M}_\mathrm{E}$. Upper left: mass density ρ; upper right: absolute velocity v_tot; lower left: gas temperature T_gas; lower right: radiation temperature T_rad.

4.2.2 Equation of radiative transfer

Under the assumption of an observer being located at infinite distance from the object, we calculate the emerging flux/luminosity as a function of the observer's inclination angle Θ and azimuthal angle Φ. Here, Θ and Φ refer to the spherical coordinate system that describes the computational box.[1]

More precisely, we adopt a parallel line of sight calculation on a two-dimensional grid on the projected surface, seen by the observer (see Fig. 4.2 for a better understanding). We start the line of sight calculation at a sufficiently high optical depth $\tau_{\nu,\mathrm{start}}$ from the projected surface with initial intensity $I_\nu = 0$ and with fixed direction cosine vector $\mathbf{l} = \mathbf{l}(\Theta, \Phi)$. This is achieved by a

---

[1] Note that the equatorial plane of the computational box is defined by the injection point of gas and its angular momentum vector.

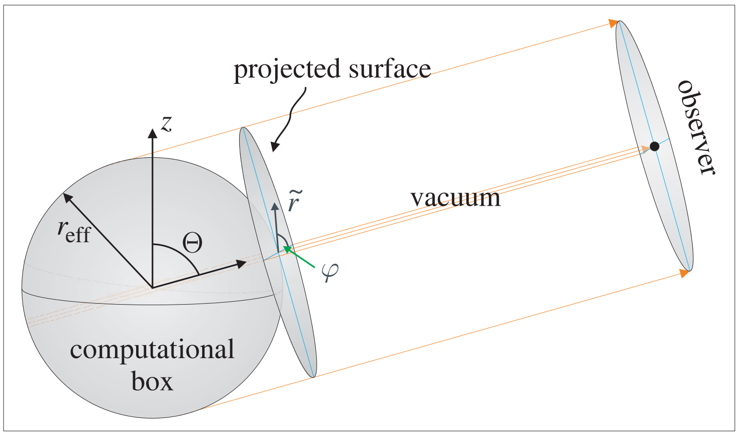

Figure 4.2. Sketch of the line of sight calculation.

two-way integration. In a first step, the integration proceeds inwards from $r = r_{\text{eff}}$ where $\tau_\nu = 0$, to a position $\mathbf{r}_{\nu,\text{start}}$ with $\tau_\nu = \tau_{\nu,\text{start}}$. During this integration, only the optical depth is calculated while the radiative transfer equation does not need to be solved. In a second step, the integration then proceeds outwards from $\tau_{\nu,\text{start}}$ to the outer boundary of the computational box where the radiative transfer equation is solved using an initial value of $I_{\nu,\text{start}} = 0$.[2]

We focus on solving the radiative transfer equation numerically by a Runge-Kutta algorithm, considering hereby the relativistic corrections due to the high velocities of the gas. General relativistic effects such as gravitational lensing and gravitational redshift are not taken into account. We have to distinguish between two different coordinate systems: we describe the system in which the observer and the computational area are at rest with I_ν, $\mathbf{l}$, ..., while the same quantities are tagged with 0 in the frame comoving with the local gas velocity $\mathbf{v}$. Since the gas velocity strongly varies, the comoving frame depends on the position in the simulation box.

In this framework, the relativistic equation of radiative transfer is given by

$$(\mathbf{l}\cdot\nabla)I_\nu \quad = \quad \left(\frac{\nu}{\nu_0}\right)^2 \cdot \left\{ \kappa^{\text{abs}}_{\nu_0} S_{\nu_0} - \chi_{\nu_0} I_{\nu_0} + \frac{3}{4}\kappa^{\text{sca}}_{\nu_0}\frac{c}{4\pi}\left(E_{\nu_0} + l_{0i} l_{0j} P^{ij}_{\nu_0}\right) \right\}, \tag{4.2}$$

while, in the non-relativistic case, it reduces to

$$(\mathbf{l}\cdot\nabla)I_\nu \quad = \quad \left\{ \kappa^{\text{abs}}_{\nu} S_{\nu} - \chi_{\nu} I_{\nu} + \frac{3}{4}\kappa^{\text{sca}}_{\nu}\frac{c}{4\pi}\left(E_{\nu} + l_{i} l_{j} P^{ij}_{\nu}\right) \right\}. \tag{4.3}$$

It is important to note that all quantities on the right hand side of (4.2) are evaluated in the comoving frame, while those on the left hand side are given in the rest frame. In the equation of radiative transfer, S_ν denotes the source function for matter, E_ν the radiation energy density and P^{ij}_ν the components of the radiation pressure tensor $\mathcal{P}_\nu$. The total extinction is given by $\chi_\nu = \kappa^{\text{abs}}_\nu + \kappa^{\text{sca}}_\nu$.

In this first approach, we restrict ourselves to frequency-dependent absorption coefficients for free-free absorption processes and totally neglect bound-free absorption processes, $\kappa^{\text{abs}}_\nu = \kappa^{\text{ff}}_\nu$. This holds as a good approximation, since the gas temperature is mostly above 10^5 K, and, hence, hydrogen is fully ionized. For simplicity, we do not consider metal opacities. We adopt the formula given in Rybicki & Lightman (1979),

---

[2] Since the starting point $\tau_{\nu,\text{start}}$ has to be sufficiently large such that the calculations saturate, the starting value $I_{\nu,\text{start}}$ can be chosen arbitrarily without changing the results.

$$\kappa_\nu^{\mathrm{ff}} = 3.7 \cdot 10^8 T^{-1/2} \left(\frac{\rho}{m_{\mathrm{p}}}\right)^2 \nu^{-3} \left(1 - e^{-h\nu/kT}\right) \ \mathrm{cm}^{-1} \,. \tag{4.4}$$

For the scattering processes, we only consider electron scattering, given by

$$\kappa^{\mathrm{sca}} = \sigma_{\mathrm{es}} \left(\frac{\rho}{m_{\mathrm{p}}}\right) \mathrm{cm}^{-1}, \qquad \sigma_{\mathrm{es}} = 6.652 \cdot 10^{-25} \mathrm{cm}^2. \tag{4.5}$$

The relativistic transformation rules are

$$\begin{aligned}
\nu_0 &= \nu\Gamma\left(1 - \frac{\mathbf{v}\cdot\mathbf{l}}{c}\right), && (4.6)\\
\mathbf{l}_0 &= \frac{\nu}{\nu_0}\left[\mathbf{l} + \left(c\frac{\Gamma-1}{v^2}\mathbf{v}\cdot\mathbf{l} - \Gamma\right)\frac{\mathbf{v}}{c}\right], && (4.7)\\
I_{\nu_0} &= \left(\frac{\nu_0}{\nu}\right)^3 I_\nu \,, && (4.8)
\end{aligned}$$

with Γ being the Lorentz factor.

4.2.3 Frequency-dependent radiation quantities

Special attention is needed when deriving the quantities S_ν and E_ν and, therefore, when applying the flux limited diffusion approximation (see Sect. 4.2.4). As the radiative transfer in the 2D RHD simulation is calculated in a gray approximation, the simulation data provides only frequency-integrated values for the radiation energy density. The matter distribution is described by the gas density and gas temperature. We assume local thermal equilibrium for the matter distribution and for the radiation field separately:

$$\begin{aligned}
S_\nu &= B_\nu(T_{\mathrm{gas}}) = \frac{2h\nu^3}{c^2} \cdot \frac{1}{\exp\left(\frac{h\nu}{k_B T_{\mathrm{gas}}}\right) - 1}, && (4.9)\\
T_{\mathrm{rad}} &= \left(\frac{E}{a_{\mathrm{rad}}}\right)^{1/4} \quad a_{\mathrm{rad}} = \text{ radiation constant}\,, && (4.10)\\
E_\nu &= \frac{4\pi}{c} B_\nu(T_{\mathrm{rad}})\,. && (4.11)
\end{aligned}$$

While (4.9) generally holds as a good approximation, (4.10) and (4.11) have to be treated carefully: in a scattering dominated domain, as it is the case in the underlying simulation data here, photons undergo multiple scattering and therefore expand in space – accordingly, the radiation field is diluted and the photon number decreases. This implies that the average photon temperature will be underestimated by (4.10) and (4.11), which will be discussed later (Sect. 4.2.6). Therefore, we henceforth focus our discussion on the relative changes of the flux, photon energy and photon number due to the variations of the inclination angle Θ.

4.2.4 Flux limited diffusion approximation

To calculate the radiation pressure tensor, we apply the frequency-dependent flux limited diffusion (FLD) approximation (Levermore & Pomraning, 1981) to the quantities in the comoving frame. In this context, the radiation pressure tensor can be expressed by

$$\mathcal{P}_{\nu,0} = \mathcal{F}_\nu \, E_{\nu,0} \,, \tag{4.12}$$

where $\mathcal{F}$ is called the Eddington-tensor. Its components are given by

$$F_\nu^{ij} = \frac{1}{2}(1 - f_\nu)\delta^{ij} + \frac{1}{2}(3f_\nu - 1)n_\nu^i n_\nu^j \,. \tag{4.13}$$

Here, n^i denotes the normalized energy density gradient,

$$n_\nu^i = \frac{\left(\nabla E_\nu\right)^i}{\left|\nabla E_\nu\right|} \,. \tag{4.14}$$

Following Kley (1989), n_ν^i and subsequent quantities can be expressed as functions of the energy density in the inertial frame.

To close the resulting equations, the Eddington factor f_ν has to be determined. From the momentum equations, the relation between f_ν and λ_ν is given by

$$f_\nu = \lambda_\nu + \lambda_\nu^2 \mathcal{R}_\nu^2 \,, \qquad \mathcal{R}_\nu = \frac{\left|\nabla E_\nu\right|}{\chi_\nu E_\nu} \,. \tag{4.15}$$

The flux limiter λ_ν itself cannot be determined from the equations of radiative transfer, but has to be defined manually. In order to do so, two conditions have to be fulfilled. In the case of $\chi_\nu \rightarrow \infty$, the equations have to reduce to the classical diffusion limit, i. e. $\lambda_\nu \rightarrow \frac{1}{3}$. In the case of $\chi_\nu \rightarrow 0$, the flux limiter must tend towards $1/\mathcal{R}_\nu$ to ensure $|\mathbf{F}_\nu| \leq cE_\nu$.

Naturally, there exist multiple possibilities to describe the flux limiter λ_ν. We adopt the common formulation from Levermore & Pomraning (1981):

$$\lambda_\nu(\mathcal{R}_\nu) = \frac{2 + \mathcal{R}_\nu}{6 + 3\mathcal{R}_\nu + \mathcal{R}_\nu^2} \,. \tag{4.16}$$

4.2.5 Numerics

In this investigation, we choose a *single* snapshot of the RHD simulation data after the simulation has settled down into a quasi-steady structure. In this stadium, the structure does not change anymore in time in a significant way, giving rise to the consideration that our results are characteristic properties of such a system. The calculation of the disk spectra is performed as presented above with and without relativistic corrections. As the simulation data is symmetric with respect to the azimuthal angle Φ, we compute the spectra only in terms dependent on the inclination angle Θ.

Optical depth We investigate the results of the computation for different starting points (i. e., optical depths $\tau_{\nu,\text{start}}$) for the line of sight calculation. For $\tau_{\nu,\text{start}} \approx 8$, the results begin to saturate, leading to changes below one percent when starting at higher optical depths. We used $\tau_{\nu,\text{start}} = 10$ throughout and validated the results with several integrations from higher optical depths.

The reason why such a low $\tau_{\nu,\text{start}}$ reveals the same results as higher optical depths can be understood from the two extreme cases listed below.

1. Either the gas is dense and cool with $T_\text{gas} \approx T_\text{rad}$ and small contributions of the gas to the total emissivity, or
2. it is diluted such that $\kappa_\nu^\text{abs} \ll \kappa_\nu^\text{sca}$ and the total emission along the line of sight is completely dominated by the radiation field.

For all calculations it turns out that increasing gas temperatures go hand in hand with dropping gas densities so that opacity and total emission are governed by the radiation field.

Discretization We divide the projected surface seen by the observer in a polar grid with coordinates $(\tilde{r},\varphi)$, see Fig. 4.2. Both for the radial and the polar coordinate, we adopt a linear grid with $N_{\tilde{r}} = 100$ and $N_\varphi = 200$ grid points. The discretization in frequency is taken to be logarithmic with $N_\nu = 200$ frequency values between 10^{14} Hz (0.5 eV) and 10^{22} Hz (50 MeV).

Step size During the numerical integration, the step size along the integration path is limited by three different requirements to ensure numerical accuracy.

1. The geometric distance Δr must not exceed $C_1 \cdot r_\text{S}$ with $C_1 = 0.1$.
2. The optical depth $\Delta\tau_\nu$ of each step must be smaller than $C_2 = 0.1$.
3. The gradient of the total extinction is limited by $(\partial\chi_\nu/\partial r)\,\Delta r \le C_3 = 1\,\text{cm}^{-1}$. This last requirement is necessary to enable the handling of drastic changes in the optical depth during inward integration with the explicit Runge-Kutta scheme.

For each integration step, the default step size is calculated from these requirements and is input into the Runge-Kutta integrator.

Runge-Kutta method The integration of the differential equations (4.2), (4.3) is performed by a fourth order explicit Runge-Kutta algorithm with automatic step size control. We calculate the subsequent value I_ν^{k+1} from the given intensity I_ν^k and the default step size Δr in two ways:

$$\begin{aligned} I_{\nu,1}^{k+1} &= \Delta r \cdot \Big((\mathbf{l} \cdot \nabla) I_\nu \Big)_{\text{position } k} , \qquad (4.17) \\ I_{\nu,2}^{k+1/2} &= \frac{1}{2}\Delta r \cdot \Big((\mathbf{l} \cdot \nabla) I_\nu \Big)_{\text{position } k} , \\ I_{\nu,3}^{k+1} &= \frac{1}{2}\Delta r \cdot \Big((\mathbf{l} \cdot \nabla) I_\nu \Big)_{\text{position } k+1/2} . \qquad (4.18) \end{aligned}$$

The step size Δr is accepted if the difference between $I_{\nu,1}^{k+1}$ and $I_{\nu,3}^{k+1}$ is sufficiently small:

$$\begin{aligned} \text{est} &= \frac{I_{\nu,3}^{k+1} - I_{\nu,1}^{k+1}}{15}\,, \\ I_{\nu,3}^{k+1} &= I_{\nu,3}^{k+1} + \text{est}\,, \\ \text{error} &= \frac{|\text{est}|}{10^{-3} + |I_{\nu,3}^{k+1}|}\,, \\ \text{error} &\overset{!}{\leq} \text{maxtol} = 10^{-5}\,. \end{aligned} \tag{4.19}$$

The numerical constants in this error estimation are taken from Plonka-Hoch (2004) and depend on the order of the Runge-Kutta scheme and the required accuracy of the problem.

In the case (4.19) is not fulfilled, the stepsize is reduced by a factor of $1/2$ and the calculation is repeated until (4.19) holds.

Interpolation on the grid Along the line of sight integration, the physical quantities ρ, T_{rad}, $T_{\text{gas}}, \ldots$ need to be calculated from the grid data by an interpolation method. For a 3-dimensional problem, the best accuracy is achieved by a volume interpolation (see Fig. 4.3): given a point X, a physical quantity Y, and surrounding grid points $X_1, \ldots, X_8$ with $Y_1, \ldots, Y_8$, its value is given by

$$Y = \sum_{i=1}^{8} V_i Y_i \Big/ \sum_{i=1}^{8} V_i\,. \tag{4.20}$$

The implementation of the interpolation displayed in Fig. 4.3 is straightforward as long as the poles of the computational box ($\Theta = \{0,\pi\}$) are not touched. Otherwise, special attention is necessary for determining the correct surrounding grid points $X_1, \ldots, X_8$.

This interpolation is applied to all physical quantities except the energy density gradient, which is necessary for the correct calculation of the FLD contribution (see (4.14)). In this case, two additional points are calculated by surface interpolation (in the same way as the volume interpolation (4.20)), which in turn are used to interpolate the energy density gradient at point X by linear interpolation (see Figs. 4.3 and 4.4 for a better explanation).

Parallelization Radiative transfer calculations put strong demands on computational power. For a quick computation of the continuum spectra and – even more – for a further extension towards line emission and absorption processes, the line of sight integration is parallelized using MPI (*Message Passing Interface*, ANL (2008)).

Within MPI, the processes have their private memory and communicate by sending messages to each other. The reason for choosing MPI and not a shared-memory system is that the parallel line of sight calculation involves very little communication, since the individual rays are independent.

The code is parallelized like a ticketing system for N_{p} processes: one process, acting as the server, offers single jobs (single rays for a specific combination of $\tilde{r}$ and φ) to $N_{\text{p}} - 1$ clients. The clients are served in a queue in a first-come-first-serve principle. After receiving a job, the client leaves the queue, performs the calculation and queues up again to deliver its results and to

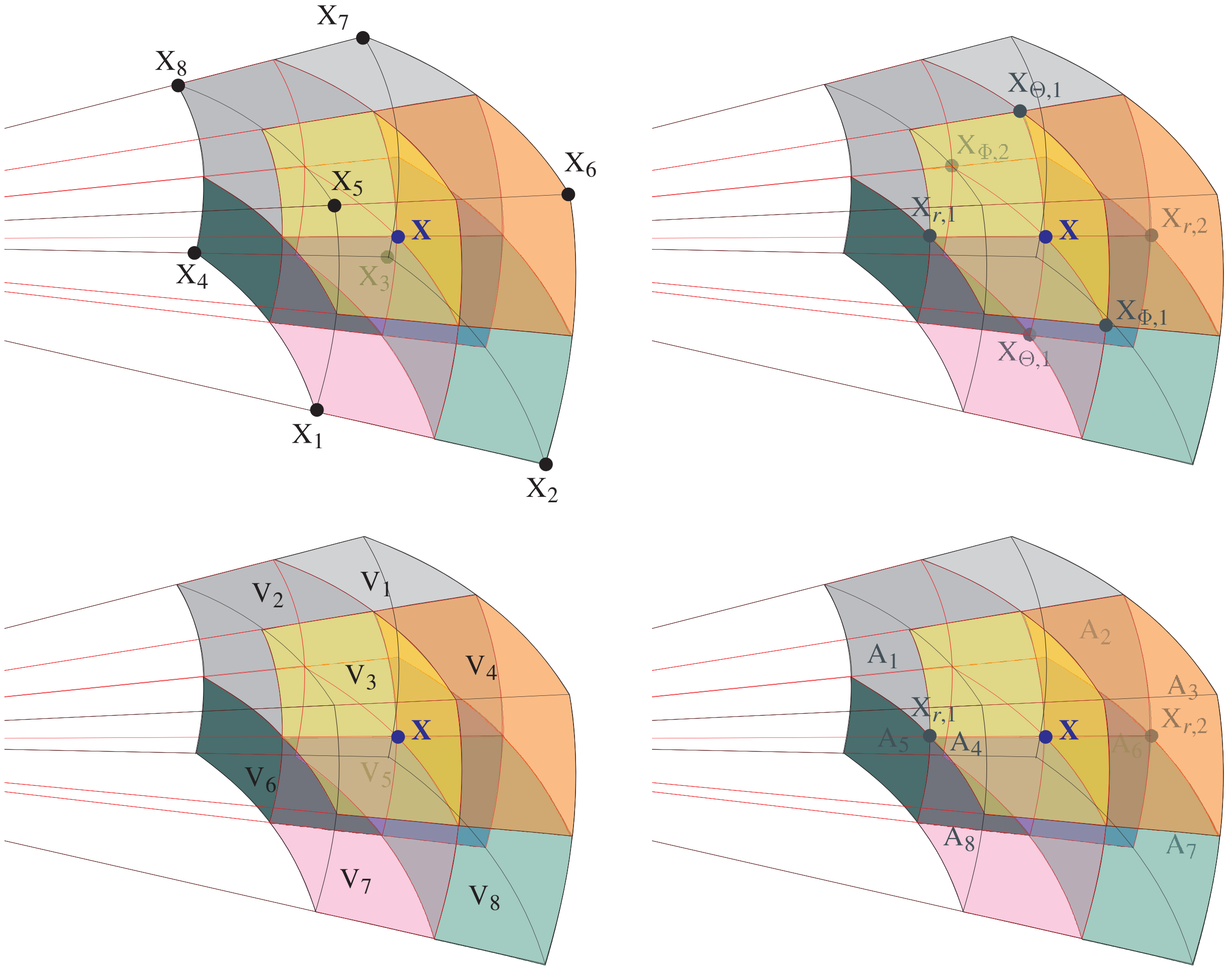

Figure 4.3. Visualisation of the volume interpolation method. Upper left: for the interpolation of X, the surrounding eight grid points $X_1, \ldots, X_8$ are considered; lower left: their relative contributions are determined by the volumes $V_1, \ldots, V_8$; upper right: the energy density gradient $\nabla_y E_\nu$ in direction $y = \{r, \Theta, \Phi\}$ is interpolated linearly from two points $X_{y,1}, X_{y,2}$ which are calculated by surface interpolation from the surrounding grid points $X_1, \ldots, X_8$; lower right: example of the interpolation $\nabla_r E_\nu$.

Figure 4.4. Visualisation of the linear interpolation for the example $\nabla_r E_\nu$.

get new work to do. This process is repeated until all work is done, the results are collected and merged for the final spectral data on the server.

Starting at the innermost radial point on the projected surface ($\tilde{r} = 0$), the line of sight calculation is performed for all N_φ rays before increasing the polar radius until the outermost ring ($\tilde{r} = 500 r_\mathrm{S}$) is calculated. After each radial step, the clients are held until all N_φ calculations are finished and a temporary data file is written to enable the computation to be resumed at that radius.

This ticketing system approach also ensures the efficiency of the parallelization for different clients with varying computational power. The overhead for the parallel calculation is minimal, consisting only of delivering N_ν values for the intensity $I_\nu(\Theta,\tilde{r},\varphi)$ and the client rank, and of receiving two values $\tilde{r}$ and φ for the subsequent step. This justifies the usage of MPI.

4.2.6 Color-corrected temperatures

As mentioned above, due to (4.10) and (4.11), the resulting fit temperatures underestimate the real temperature of the radiation field. Strictly speaking, the temperature of the radiation field should be determined at $\tau^* \approx 1$ ($\tau^* \sim \sqrt{\kappa^\mathrm{sca}\kappa^\mathrm{abs}}$) and not at $\tau \approx 1$ (in a scattering dominated domain, $\tau \sim \kappa^\mathrm{sca}$). Hence, the radiation energy density E_ν will resemble more a shifted blackbody distribution with a color-corrected temperature T_col,

$$E_\nu \sim B_\nu(T_\mathrm{col})\sqrt{\kappa^\mathrm{sca}/\kappa_\nu^\mathrm{abs}}\,, \tag{4.21}$$

rather than (4.11), where $E_\nu \sim B_\nu(T_\mathrm{fit})$. From the requirement of energy conservation,

$$E = \int B_\nu(T_\mathrm{fit})\,d\nu = \int B_\nu(T_\mathrm{col})\sqrt{\frac{\kappa^\mathrm{sca}}{\kappa_\nu^\mathrm{abs}}}\,d\nu\,. \tag{4.22}$$

To get a rough idea on how much the derived temperatures are underestimated, we solve (4.22) numerically for T_col in the main emanating region of radiation ($\tau \approx 10$).

4.3 Results

4.3.1 Overall spectral properties

Figure 4.5 shows the resulting spectrum νL_ν for inclination angles $\Theta = 0, \pi/4$ and $\pi/2$ with and without relativistic corrections. The luminosity is given by

$$L_\nu(\Theta) = 4\pi \int_A I_\nu(\Theta,\tilde{r},\varphi)\,dA\,, \tag{4.23}$$

where A denotes the projected surface of the computational area, as it is seen by the observer. For low frequencies, the spectra only weakly depend on the viewing angle. Also, relativistic corrections are unimportant for energies $\lessapprox 400\,\mathrm{eV}$ ($\nu \lessapprox 10^{17}\,\mathrm{Hz}$). Contrarily, for higher energies, the dependency on the viewing angle becomes stronger. For high inclinations, i. e. for an edge-on view of the system, relativistic corrections still remain unimportant, while they become drastically visible for low inclinations, i. e. for a nearly face-on view of the disk. For both the relativistic and the non-relativistic cases, an enhancement of the peak frequency and luminosity

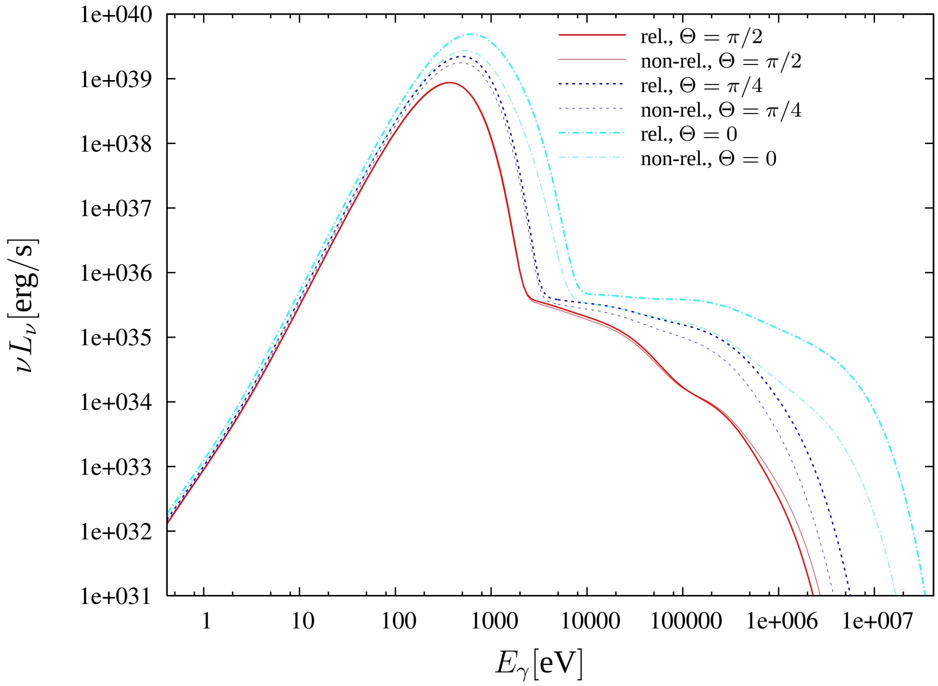

Figure 4.5. Disk spectra νL_ν for inclination angles $\Theta = 0, \pi/4, \pi/2$ with and without relativistic corrections.

is observable for small inclination angles; although, this boost is much stronger when considering relativistic corrections. Furthermore, instead of a rapid drop of νL_ν for high energies, a slower decline to a plateau-like structure can be seen in all cases.

Figure 4.6 illustrates again the spectrum for $\Theta = 0$. To show that the observed plateau in Figs. 4.5 and 4.6 is a result of the thermal emission $\kappa^{\text{abs}} S_\nu$ from the hot gas in the photosphere, we calculate the spectrum without gas contribution, i. e. we set $S_{\nu,\text{gas}} = 0$ everywhere. As it can be seen from the figure, the high-energy plateau disappears completely when neglecting the contribution from the hot gas, confirming our hypothesis. We want to make the following remarks.

1. This structure may be altered significantly if Compton scattering is taken into account, since this provides an effective cooling mechanism for the gas. However, the inclusion of Compton scattering and calculation of the decrease in T_{rad} is beyond the scope of this work.

2. Observation of this plateau is unlikely, since the overall emission in this energy range is considerably low and the spectrum is dominated by the peak emission.

To illustrate the influence of the disk's environment in the face-on case in Fig. 4.6, we calculate the spectrum for a "screened" central region (for $r \leq 100 r_{\text{S}}$, we set all physical quantities to zero) and for the core region only (for $r \geq 100 r_{\text{S}}$, all physical quantities are set to zero). Here, r denotes the radial coordinate in the spherical coordinate system describing the computational box. The former case corresponds to a system where the inner $100 r_{\text{S}}$ are entirely evacuated and so emission, absorption and scattering processes only exist outside the core region. Contrarily, the latter case means that no emission, no absorption and no scattering takes place for $r \geq 100 r_{\text{S}}$,

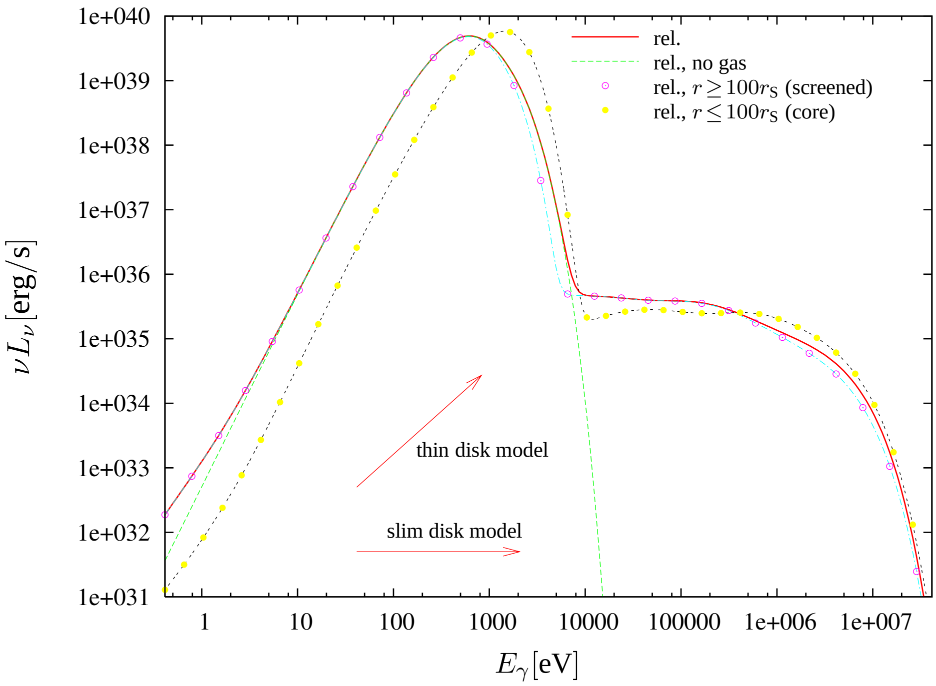

Figure 4.6. Disk spectra νL_ν for $\Theta = 0$ with relativistic corrections. Beneath the normal spectrum (as in Fig. 4.5), we plot the spectra without gas contributions, for the core region only ($r \leq 100 r_S$) and for a screened inner region ($r \geq 100 r_S$). Additionally, theoretical spectral shapes for thin and slim accretion disks are sketched.

yielding an unaltered emission from the core region only. Obviously, the environment of the disk has a rather strong influence on the emerging spectrum.

Furthermore, the theoretical spectral shapes for a standard thin α-disk (Shakura & Sunyaev, 1973) and for a standard slim disk (Abramowicz et al., 1988) are indicated in Fig. 4.6, each time without consideration for self-irradiation, atmosphere, relativistic effects. If we just take into account the surface temperature T_{eff} for these disk models and take advantage of the face-on view (no self-occultation), the theoretical predictions are $\nu L_\nu \propto \nu^{4/3}$ for the thin disk case, and $\nu L_\nu \propto \nu^0$ for the slim disk case (see, e. g., Kato et al. (1998, Sect. 3.2.5)). These shapes do not coincide with our results, although they should be valid at least for the peak intensity region of the spectrum. This reveals a weak point of our investigation, which is the need to assume a spectral distribution for the emission of the radiation field and the gas component from the given gray quantities (see Sect. 4.2.3).

4.3.2 Angular dependence of the luminosity

In Fig. 4.7, we show the dependency of the total luminosity

$$L_{\text{tot}}(\Theta) = \int L_\nu(\Theta)\, d\nu \tag{4.24}$$

on the viewing angle for both the relativistic and the non-relativistic calculation by dividing the resulting luminosities by its edge-on value $L_{\text{tot}}(\pi/2)$. The energy boost for small inclination

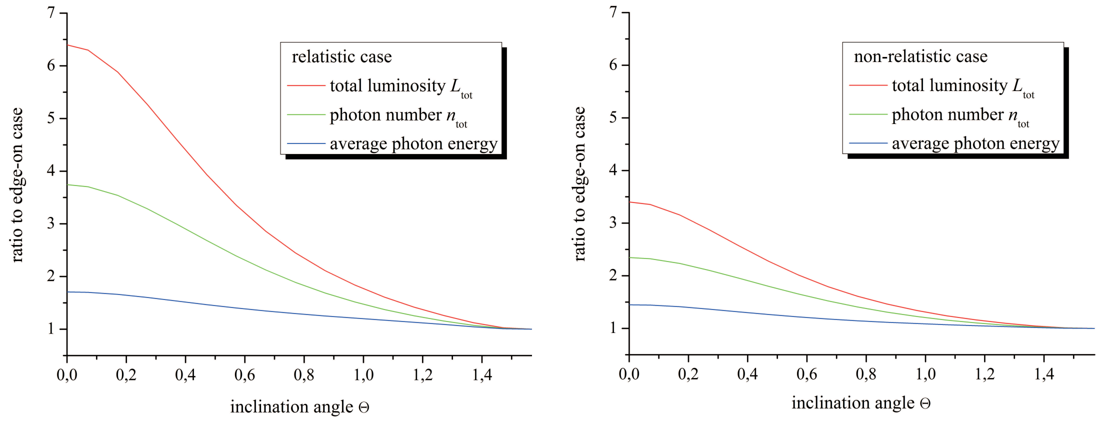

Figure 4.7. Total luminosity L_{tot}, total photon number n_{tot} and average photon energy $\langle h\nu \rangle$ as a function of the viewing angle Θ for the relativistic (left) and non-relativistic (right) calculation. The quantities are normalized by their corresponding edge-on values.

angles appears in both cases, although it is stronger for the relativistic calculation. Due to relativistic effects, the gain in luminosity compared to the non-relativistic calculation $L_{\text{tot}}^{\text{rel}}/L_{\text{tot}}^{\text{non-rel}}$ varies between 1.0 for $\Theta = \pi/2$ and 1.9 for $\Theta = 0$.

We find that L_{tot} is enhanced by a factor of ~ 6.4, at most, for a face-on observer, compared with an edge-on observer. In absolute values, $L_{\text{tot}} = [1.3 \cdot 10^{39}\text{erg/s}; 8.4 \cdot 10^{39}\text{erg/s}]$. The increase in total luminosity may be due either to an increase in photon number or an increase in average photon energy. Which one is more important?

To answer this question and to outline the relativistic effects more explicitly, we also display in Fig. 4.7 the total photon number density n_{tot} and the average photon energy $\langle h\nu \rangle$ as a function of the inclination angle, again normalized by their edge-on values. From our SEDs, we calculate the photon number density using

$$n_{\text{tot}}(\Theta) = \int n_\nu(\Theta)\, d\nu = \int \frac{L_\nu(\Theta)}{h\nu c}\, d\nu \qquad (4.25)$$

and from that, the average photon energy by $\langle h\nu \rangle(\Theta) = L_{\text{tot}}(\Theta)/(c n_{\text{tot}}(\Theta))$. While relativistic effects become more or less unimportant in the edge-on case, they cause an additional increase both in the total number of photons originating from the system and in the average photon energy in the face-on case. Table 4.1 summarizes the gain in total luminosity, photon number and average photon energy compared to the edge-on case. These results can be explained physically as follows. Starting from the *non-relativistic* calculation, we find that:

- Lower densities and, therefore, less effective absorption and scattering in the photosphere allow a deeper look into the hotter region for the face-on case, compared to the edge-on case. Hence, the average photon energy $\langle h\nu \rangle$ is increased by a factor of 1.45.

- Photons can escape more easily through the diluted medium along the polar axis, while they get stuck in the dense disk-like structure concentrated in the midplane. The outflow is therefore collimated and the number of escaping photons is raised by a factor of 2.35.

At the same time, the (outflow) velocities of the gas close to the black hole ($r \lessapprox 100 r_\mathrm{S}$) and around the polar axis are higher, which becomes important for the *relativistic* calculation.

- The frequency of the escaping photons is shifted from ν to $\nu_0 \geq \nu$ by the relativistic Doppler effect, increasing the average photon energy additionally by a factor of about $1.71/1.45 = 1.18$, when comparing the face-on view with the edge-on view.
- Given that the relativistic invariant is I/ν^3, the emerging intensity in the relativistic calculation compared to the non-relativistic case is given by $I_0/I \sim (\nu_0/\nu)^3$. One factor of ν_0/ν directly goes into $\langle h\nu \rangle$ via the relativistic Doppler effect, the remaining factor of $(\nu_0/\nu)^2$ applies to the emerging photon number $n_\nu \sim I_\nu / \langle h\nu \rangle$, raising it once more by factor of $3.74/2.35 = 1.59$, when Θ decreases from $\pi/2$ to 0.

An observer located at $\Theta = \pi/2$ only sees the emission from the outer part of the optically thick disk-like structure, which itself screens the relativistic effects in the inner region of the system. The radial velocities and also the azimuthal velocities are relatively low ($v_\varphi \approx 0.01c$). For the mainly contributing part to the spectrum, the azimuthal velocity is (almost) perpendicular to the line of sight, therefore the already weak relativistic effects are not detectable for an edge-on observer. In the face-on case, the highly relativistic flow ($v_\mathrm{s} \lessapprox 0.3c$) can by observed due to the optically thin atmosphere above the disk. At the same time, the radial velocity is pointing in the direction of the observer, leading to strong enhancements of the radiative flux at low inclinations.

4.3.3 Blackbody fitting

When spectral data of black hole sources are obtained, it is usual to fit them with blackbody (or disk blackbody) spectra. We thus attempt a similar spectral fitting to our theoretically calculated spectra: we apply a non-linear least square fit to the emerging intensity I_ν using a blackbody spectrum with temperature T_fit, altered by a spectral hardening factor ε (Soria & Puchnarewicz, 2002). The fitting function is then given by

$$f = f(\nu, \varepsilon, T_\mathrm{fit}) = \varepsilon^{-4} \cdot \frac{2h\nu^3}{c^2} \cdot \frac{1}{\exp\left(\frac{h\nu}{\varepsilon k_B T_\mathrm{fit}}\right) - 1} \, . \tag{4.26}$$

Note that the factor ε^{-4} is introduced to ensure the same radiation energy loss:

$$\int f(\nu, \varepsilon, T_\mathrm{fit}) \, d\nu = \varepsilon^{-4} \sigma (\varepsilon T_\mathrm{fit})^4 = \sigma T_\mathrm{fit}^4 \, . \tag{4.27}$$

Table 4.1. Gain in total luminosity, photon number and average photon energy compared to the edge-on case (see text for details).

Θ	L_tot		n_tot		$\langle h\nu \rangle$	
	relativistic	non-relativistic	relativistic	non-relativistic	relativistic	non-relativistic
$\pi/2$	1.00	1.00	1.00	1.00	1.00	1.00
$\pi/3$	1.66	1.26	1.41	1.17	1.18	1.08
$\pi/4$	2.40	1.59	1.86	1.39	1.29	1.14
$\pi/6$	3.63	2.14	2.53	1.72	1.43	1.24
0	6.40	3.40	3.74	2.35	1.71	1.45

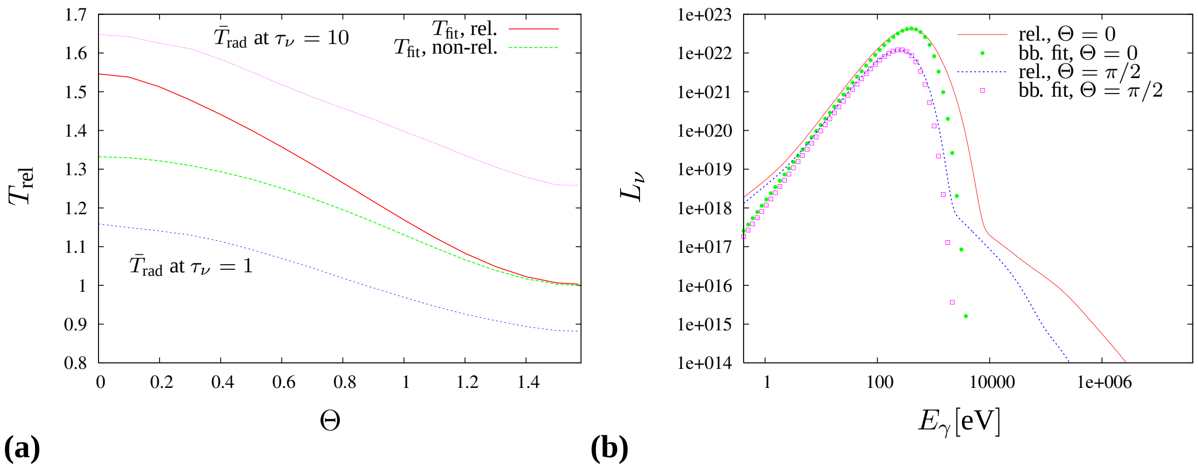

Figure 4.8. **(a)** fitted blackbody temperatures for the relativistic and non-relativistic calculation as a function of the viewing angle Θ. Additionally, mean temperatures at $\tau_\nu = 1$ and $\tau_\nu = 10$ are shown. All temperatures are scaled by $T_{\rm fit}$ at $\Theta = \pi/2$. **(b)** luminosity L_ν and the corresponding blackbody fits.

In order to account for stochastic fluctuations, we weigh the fitting coefficients by their relative intensity. So, the weight-function is given by

$$w(\nu) = \frac{I_\nu}{I_{\rm tot}}, \qquad I_{\rm tot} = \int I_\nu \, d\nu \,. \tag{4.28}$$

Figure 4.8a shows the results for the fitting temperatures $T_{\rm fit}$ as a function of the inclination angle. Additionally, we plot the surface-averaged radiation temperatures

$$\bar{T}_{\rm rad} = \frac{1}{A} \int_A T_{\rm rad} \, dA \tag{4.29}$$

at optical depths $\tau_\nu = 1$ and $\tau_\nu = 10$. As mentioned earlier, the temperature of the radiation field will be underestimated by (4.10) and (4.11). We therefore concentrate on its relative changes for different inclinations and scale all temperatures to the fitting temperature $T_{\rm fit}$ at $\Theta = \pi/2$, where it is basically the same for the relativistic and for the non-relativistic calculation.

If neglecting relativistic corrections, the fitted blackbody temperature is given roughly by the radiation temperature at a *constant* optical depth between 1 and 10. The blackbody temperature rises by a factor of 1.3 when switching from an edge-on to a face-on case. The spectrum is only weakly hardened compared to a Planck distribution at the same temperature $T_{\rm fit}$: the spectral hardening factor ε adopts an almost constant value close to unity, $\varepsilon \approx 1.15$, for all inclinations.

When accounting for relativistic corrections, no surface of constant optical depth can be defined any more: while the fitting temperatures resemble those of the non-relativistic case for high inclinations, they differ significantly for low inclinations, mirroring the above statement of stronger relativistic effects for the face-on seen system. While the blackbody temperature rises by a factor of 1.6, the hardening factor ε stays almost constant around 1.15, like in the non-relativistic calculation.

Finally, Fig. 4.8b shows the luminosity L_ν for the face-on view and the edge-on view and the corresponding blackbody fits in the relativistic case. Due to the weighting function, the peak intensity region is fitted quite well, while there are large deviations in the low-energy and high-energy regions.

4.4 Discussion

The results presented in Sect. 4.3 permit us to draw several conclusions about the observational appearance of supercritical accretion disk systems.

It is clearly not sufficient to consider only the disk and neglect its surroundings like its hot photosphere, outflow regions, etc. Their influence becomes most important in the high-energetic part of the spectrum ($h\nu \gtrapprox 4\,\mathrm{keV}$). We find a plateau-like structure, independent of relativistic effects and of the viewing angle, which can be ascribed directly to the high gas temperature in the corona. Therefore, neither the basic thin disk spectrum, nor the basic slim disk spectrum fit our results.

Our results also confirm that the Eddington-Barbier approximation, a common simplification of radiative transfer calculations for stellar atmospheres, cannot be applied in accretion disks: in this approximation, one generally assumes that the emergent intensity along the line of sight is equal to the source function at constant optical depth $\tau = 2/3$. In our calculation, the main contribution to the emerging flux is produced at higher optical depths $\tau_{\text{eff}} > 2/3$; moreover, the exact value of τ_{eff} depends on the inclination angle.

We observe an enhanced luminosity for more and more face-on seen systems, which is due to both enhanced average photon energy and total photon number. Relativistic effects alter the total photon number much more significantly (almost twice the non-relativistic treatment) than the average photon energy. This can be identified as *mild relativistic beaming*.

As outlined in Sect. 4.2.6, due to (4.10) and (4.11), the resulting fit temperatures underestimate the real temperature of the radiation field. The correction derived from (4.22) reveals that the fit temperatures are underestimated by one order of magnitude. With

$$T_{\text{fit}} = \left[9.4 \cdot 10^5\mathrm{K} \ldots 1.4 \cdot 10^6\mathrm{K}\right] \tag{4.30}$$

for $\Theta = [\pi/2 \ldots 0]$, this leads to color-corrected temperatures in the range of

$$T_{\text{col}} = \left[9.4 \cdot 10^6\mathrm{K} \ldots 1.4 \cdot 10^7\mathrm{K}\right] \ . \tag{4.31}$$

These temperatures would be consistent with the observed high temperatures of several ULX sources (Makishima et al., 2000) that can not be explained in terms of intermediate mass black hole systems with sub-Eddington accretion rates. However, our approach is certainly too simplified to answer this “too hot accretion disk” puzzle in a satisfactory way.

For our results, spectral hardening turns out to be negligible. This may be due in parts to the assumption of Thomson scattering: Comptonization effects are expected to harden the spectrum significantly (Czerny & Elvis, 1987; Ross et al., 1992; Kawaguchi, 2003). Then, if only the peak of the spectrum is observed, the absolute scale and therefore the spectral hardening factor ε remains unknown and the observed temperature $T_{\text{obs}} = \varepsilon T_{\text{col}}$ overestimates the color temperature T_{col}. Moreover, bulk motion Compton scattering is known to alter photon energies due to the angular redistribution of the scattered photons (Psaltis & Lamb, 1997). Socrates et al. (2004) showed that turbulent Comptonization produces a significant contribution to the far-UV and X-ray emission of black hole accretion disks.

Another possible weak point in our investigation is the application of the flux limited diffusion approximation instead of solving the full momentum equations: in this approximation, several terms in the equation of radiative transfer (4.2), like $1/c^2\,(DF/Dt)$ with F being the absolute value of the flux, are dropped. These terms are of the order of v/c and may contribute to the relativistic effects we find in our spectral calculations. By calculating the emerging spectra under the classical diffusion limit (i. e. complete isotropy, $\lambda = 1/3$), we find only little influence of the FLD approximation at all. Thus, the inconsistencies invoked by applying the flux limited diffusion approximation do not affect our results in a significant way.

4.5 Conclusions

Our radiative transfer calculations, based on the 2D RHD simulation of highly accreting supercritical disks including the photon trapping mechanism, show that the interpretation of observed disk spectra is not a straightforward task. Especially, we find moderate beaming effects when the system is viewed from nearly face-on, i. e., the average photon energy is larger by a factor of ~ 1.7 in the face-on case than in the edge-on case due mainly to Doppler boosting. Likewise, the photon number density is larger by a factor of ~ 3.7 because of anisotropic matter distribution around the central black hole. Interpreting observations thus has to be done in a more sophisticated way than one may expect from basic disk models: it requires a careful treatment of the radiative transfer with consideration of the disk's surroundings.

We assume that both the gas and the radiation field separately stay in local thermal equilibrium. Although the weak coupling of matter and radiation ($\kappa_{\text{abs}} \ll \kappa_{\text{sca}}$) supports this assumption, it remains questionable and also underestimates the temperature of the radiation field. It is important to note that previous investigations by Wang et al. (1999); Fukue (2000); Watarai et al. (2005) also rely on this approximation; nevertheless, their results differ in a significant way. Solving the crux of assuming LTE for the gas and for the matter distribution at the present stage is not possible, because it requires frequency-dependent RHD simulations. As a general warning, we remark that the gas temperatures of the simulation data are high, sometimes exceeding 10^9 K in the dilute photosphere of the disk. Such high temperatures are usually not expected and also not treated consistently in the RHD simulations, since they imply that nuclear reactions should be considered in the energy equation.

In further steps, Compton scattering has to be included as well as frequency-dependent absorption for both continuum (bound-free absorption may become relevant in the low-energetic tail of the SED) and line processes: from the observational side, emission lines, especially the K-shell transitions of iron, are a prominent feature in accretion disk system and comprise many details about the observed object (see Reynolds et al. (1999); Reynolds (2006) and the introductory remarks in Chapt. 1). Beneath the effects on the high-energetic part of the spectrum mentioned before, Compton scattering will provide an efficient cooling mechanism for the hot gas.

As pointed out by Watarai et al. (2005), also general relativistic effects should be considered in the vicinity of the black hole, which will primarily affect the spectra of face-on seen systems.

5 Spectral energy distribution of super-Eddington flows II – the iron K line complex

5.1 Context

In the previous chapter, we calculated the observational appearance of supercritical accretion flows onto stellar mass black holes (see also the published version: Heinzeller et al. (2006)). Accounting for continuum processes solely, we solved the relativistic radiative transfer equation along the line of sight and analyzed the continuum spectral features, e. g., bolometric luminosities as a function of the orientation of the observer relative to the accretion disk system. The underlying simulation data was provided by Ohsuga et al. (2005).

In the case of a stellar mass black hole (ten solar masses) accreting at a thousand times the classical Eddington rate, we found that the observational appearance of the system depends strongly on the inclination angle. Also, relativistic effects become important for small inclinations. This is due to the lower densities in the photosphere of the disk, which allow a deeper look into the central black hole region (see Fig. 5.1).

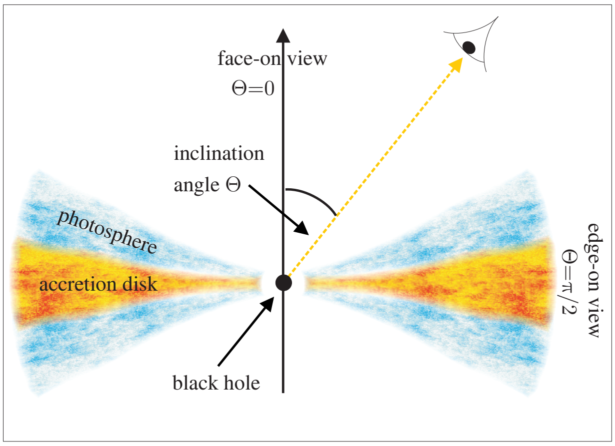

Figure 5.1. Sketch of observer's orientation towards the disk.

Since 2005, Ohsuga extended his simulations towards varying accretion rates and central black hole masses (Ohsuga (2007) and Ohsuga, priv. comm.). Also on the observational side, there was significant progress in the quantity and quality of available data. In particular, current X-ray satellites like *Chandra*, *XMM-Newton* and *Suzaku* revealed the presence of strong iron emission and absorption lines in many black hole accretion disks, from ULXs to AGN (see Fig. 5.2 for some illustrative examples). Because their properties vary significantly, they may illuminate the accretion process in the vicinity of the black hole.

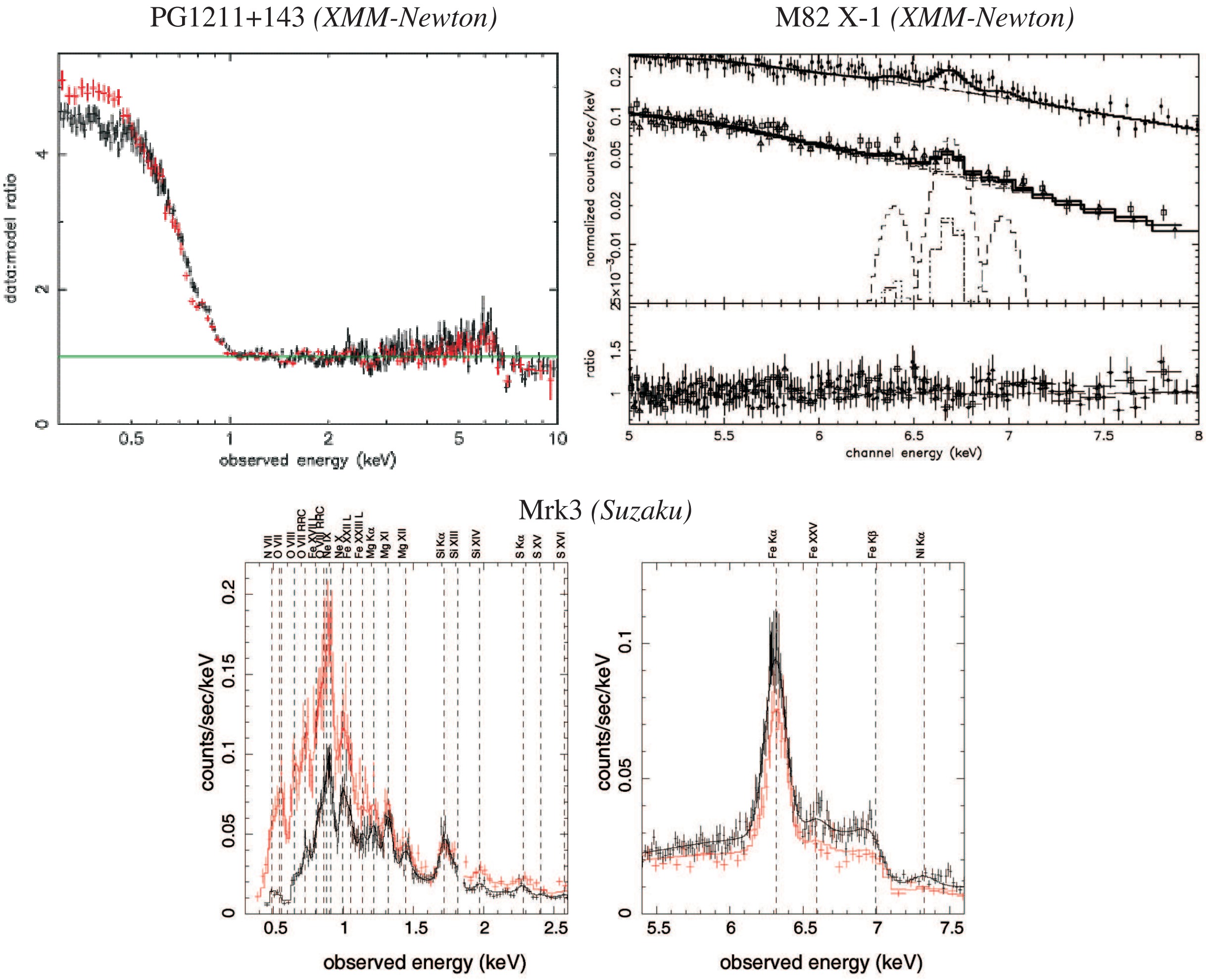
PG1211+143 *(XMM-Newton)*

M82 X-1 *(XMM-Newton)*

Mrk3 *(Suzaku)*

Figure 5.2. Numerous observations of iron lines can be found in the literature. Among them, prominent and illustrative examples are the quasar PG1211+143 (Pounds et al., 2003), the Seyfert 2 galaxy Mrk3 (Awaki et al., 2007) and the ultraluminous X-ray source M82 X-1 (Strickland & Heckman, 2008). Their masses are $M_{\rm c} = \{4 \cdot 10^7 M_\odot, 4.5 \cdot 10^8 M_\odot, 20 - 700 M_\odot\}$, respectively. The *Suzaku* observation of Mrk3 shows beautifully the advantage of observing the iron K lines, which lie in a relatively unconfused spectral region. The remarkable Fe K emission line of Mrk3 has also been observed with *XMM-Newton*, which we showed earlier in Fig. 1.2.

Based on our previous work on the observational appearance of super-Eddington accretion flows, we extend the radiative transfer calculations towards the calculation of the iron K line emission and absorption. To achieve this, the ionization equilibrium has to be calculated as well, providing the number density of free electrons and the electronic pressure. As a side-effect, this allows us to include bound-free absorption of the most abundant elements (H, He) in the radiative transfer calculation.

Since the radiation energy density in the simulation data is considerably high, Compton scattering effects of high-energy photons may become important as well. We start with an extension of the simple Thomson scattering used previously in Sect. 5.2, before we describe our model of the bound-free absorption processes in Sect. 5.3. We proceed to the actual goal of the present investigation, the observational appearance of the iron K lines, in Sect. 5.4.

While this project evolved, we discovered that the size of the computational domain of the RHD simulations is too small for a proper interpretation of the iron line features. We therefore model an extended atmosphere around the computational domain in Sect. 5.5 and discuss the results in Sect. 5.6. There, we also try to fit our data to actual observations of the ultraluminous X-ray source M82 X-1. Final conclusions are given in Sect. 5.7.

5.2 Compton scattering

A comprehensive and realistic description of Compton scattering effects is beyond the scope of this work. We apply the Klein-Nishina correction for unpolarized radiation to the integrated Thomson scattering coefficient $\kappa_{\text{Th}}^{\text{sca}} = \sigma_{\text{Th}} \cdot (\rho/m_{\text{H}})$:

$$\kappa_{\nu,\text{KN}}^{\text{sca}} = \kappa_{\text{Th}}^{\text{sca}} \cdot \left[\frac{1+x}{x^3} \left\{ \frac{2x(1+x)}{1+2x} - \ln(1+2x) \right\} + \frac{1}{2x} \ln(1+2x) - \frac{1+3x}{(1+2x)^2} \right] . \quad (5.1)$$

where $x = (h\nu)/(m_{\text{e}}c^2)$ (Rybicki & Lightman, 1979). The principal effect of the Klein-Nishina correction is to tend towards the classical Thomson coefficient for $x \ll 1$, while it reduces its value for $x \gg 1$ (see Fig. 5.3 for an illustration).

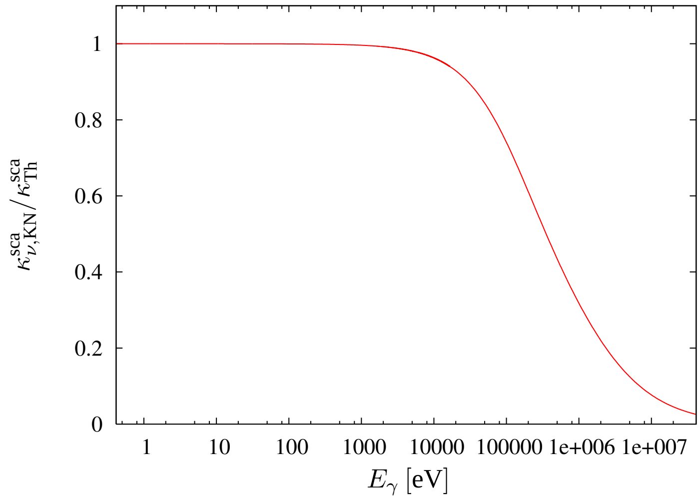

Figure 5.3. $\kappa_{\nu,\text{KN}}^{\text{sca}}/\kappa_{\text{Th}}^{\text{sca}}$ as a function of the incident photon energy.

5.3 Frequency-dependent bound-free absorption

To incorporate bound-free absorption in our calculations, a simplified approach is used and then combined with the analytic approximation formula of the free-free absorption coefficient, taken from Rybicki & Lightman (1979),

$$\kappa_\nu^{\text{ff}} = 3.7 \cdot 10^8 T^{-1/2} \left(\frac{\rho}{m_{\text{p}}} \right)^2 \nu^{-3} \left(1 - e^{-h\nu/kT} \right) \text{ cm}^{-1} . \quad (5.2)$$

In the following, we present the general definition for the bound-free absorption in Sect. 5.3.1. The theory presented below is applied to the contributions of hydrogen and helium, as these two elements represent roughly 98% of the material when assuming solar abundances.

5.3.1 Bound-free absorption coefficients

In general, the bound-free absorption processes for each element A can be expressed as

$$\kappa_\nu^{\text{bf, A}} = \sum_{i=0}^{Z^\text{A}} \sum_{l=1}^{\infty} n_{i,l}^\text{A} \cdot \sigma_{i,l}^{\text{bf, A}} \,, \tag{5.3}$$

where l enumerates the excitation state of the ionized state i ($i = 0$: A I, $i = 1$: A II, …; Z^A: atomic number) of the atom ($l = 0$: ground state, $l > 0$: excited states), $n_{i,l}^\text{A}$ the corresponding absolute number density and $\sigma_{i,l}^{\text{bf, A}}$ its bound-free absorption cross section. Their units are $[n_{i,l}^\text{A}] = \text{cm}^{-3}$, $[\sigma_{i,l}^{\text{bf, A}}] = \text{cm}^2$ and therefore $[\kappa_\nu^{\text{bf, A}}] = \text{cm}^{-1}$.

In the following, $\chi_{i,\text{ion}}^\text{A}$ denotes the ionization energy of state i, while $\chi_{i,l}^\text{A}$ stands for the energy of the excited state (i,l) with respect to the ground state $(i,0)$. To evaluate the contribution of bound-free absorption of each element, its cross sections $\sigma_{i,l}^{\text{bf, A}}$ and number densities $n_{i,l}^\text{A}$ need to be computed.

5.3.2 Number densities

To calculate the number density for an element with ionization degree i and excitation level l, several quantities have to be computed: first, the partition function has to be evaluated. Second, the ionization degree of the element is computed by means of the Saha equation. Together with the given total number density of the element, the population of each level is determined.

Partition functions

An approximate calculation of the partition function W_i^A for one ionization degree i of element A is straightforward for hydrogen and hydrogenic atoms. Hydrogenic atoms are elements other than hydrogen in an ionized state with only one electron left. In this case, the partition function is given by

$$W_{Z-1}^\text{A} = \sum_{k=1}^{\infty} 2k^2 \cdot \exp\left\{ -(Z^\text{A})^2 \frac{Ry \cdot h}{k_\text{B} T} \cdot \left(1 - k^{-2}\right) \right\} . \tag{5.4}$$

This is also a good approximation for more-electron systems like He I in high excitation states, where inner shell electrons effectively screen the nuclear charge, so that the outermost electron “sees” a hydrogen-like atom with an effective nuclear charge $z = i + 1$.

Problems arise when calculating the partition function for high temperatures: as $T \rightarrow \infty$, the partition function also diverges. From a physical point of view, the element ionizes completely (c. f. the Saha equation below) and therefore the diverging partition function becomes meaningless. A common approach to ensure the computability for all temperatures reflects this fact by treating all states above a particular (high) state k_max (with excitation energies close to the ionization energy) as quasi-ionized. Formally,

$$\chi_{Z^\text{A}-1,\text{ion}}^\text{A} = (Z^\text{A})^2 \cdot Ry \cdot h \cdot \left(1 - \frac{1}{(k_\text{max}+1)^2}\right) \lessapprox (Z^\text{A})^2 \cdot 13.6\,\text{eV} \,, \tag{5.5}$$

$$W_{Z^\text{A}-1}^\text{A} = \sum_{k=1}^{k_\text{max}} 2k^2 \cdot \exp\left\{ -(Z^\text{A})^2 \frac{Ry \cdot h}{k_\text{B} T} \cdot \left(1 - k^{-2}\right) \right\} . \tag{5.6}$$

However, this method of calculating the partition function is only an approximation and not applicable for more-electron systems in lower excitation states. In particular, it cannot be used in the case of iron, where most of the excitation levels correspond to non-hydrogenic states. Another quite common approach is to use the ground states of the individual ionization levels only. Although this is a valid approach in the low ionization regime, it is invalid in our investigation. The gas temperature reaches sufficiently high values such that even iron becomes highly ionized.

We therefore refrain from these simple approaches and perform a full calculation of the partition functions, since this gives accurate results and is valid in all cases: for each element, we take into account “all” excitation states per ionization level. The partition functions W_i^{A} are calculated from

$$W_i^{\mathrm{A}} = \sum_{l=0}^{l_{\mathrm{max},i}} g_{i,l}^{\mathrm{A}} \exp\left\{-\frac{\chi_{i,l}^{\mathrm{A}}}{k_{\mathrm{B}}T}\right\} , \qquad i = 0,\ldots,Z^{\mathrm{A}}-1 , \qquad W_{Z^{\mathrm{A}}}^{\mathrm{A}} = 1 , \tag{5.7}$$

where $g_{i,l}^{\mathrm{A}}$ stands for the statistical weight of the excitation state and $l_{\mathrm{max},i}$ for the number of levels incorporated in the calculation. We use the atomic data from the National Institute of Standards and Technology (NIST, 2006): for each ionization level i, the statistical weights $g_{i,l}^{\mathrm{A}}$, the energies of the ground state and all available excitation states $\chi_{i,l}^{\mathrm{A}}$, and also the ionization energy $\chi_{i,\mathrm{ion}}^{\mathrm{A}}$ are taken from the atomic spectra database. We compile tables for hydrogen and helium, including 166 levels for H I, 187 levels for He I, and 239 levels for He II.

Ionization degree

To calculate the ionization degrees of element A, the Saha equation is used:

$$\frac{n_{i+1}^{\mathrm{A}} n_{\mathrm{e}}}{n_i^{\mathrm{A}}} = \frac{2W_{i+1}^{\mathrm{A}}}{W_i^{\mathrm{A}}} \cdot \frac{(2\pi m_{\mathrm{e}})^{3/2}}{h^3} (k_{\mathrm{B}}T)^{3/2} \cdot \exp\left\{-\frac{\chi_{i,\mathrm{ion}}^{\mathrm{A}}}{k_{\mathrm{B}}T}\right\} . \tag{5.8}$$

The number density for ionization degree i represents the sum over all excitation levels l, $n_i^{\mathrm{A}} = \sum_l n_{i,l}^{\mathrm{A}}$. The total number density of free electrons, n_{e}, couples the Saha equation for all elements involved:

$$n_{\mathrm{e}} = \sum_{\text{Elements A}} \sum_{i=1}^{Z^{\mathrm{A}}} i \cdot n_i^{\mathrm{A}} . \tag{5.9}$$

The partition functions of fully ionized elements are $W_{Z^{\mathrm{A}}}^{\mathrm{A}} = 1$, the spin of the free electron is considered by the factor 2 in the r. h. s. of (5.8). For known temperatures T, the remaining partition functions W_i^{A} can be evaluated. Together with the known *total* number densities of all elements

$$n^{\mathrm{A}} = \sum_i n_i^{\mathrm{A}} = \frac{X^{\mathrm{A}}}{\mu^{\mathrm{A}}} \cdot \frac{\rho}{m_{\mathrm{at}}} , \tag{5.10}$$

the coupled Saha equations can be solved numerically. Here, X^{A} denotes the mass fraction of element A with atomic weight μ^{A} in the gas; m_{at} the atomic mass unit. Thus, $\sum_{\text{Elements A}} X^{\mathrm{A}} = 1$. Since hydrogen and helium provide most of the free electrons in the plasma, we simplify the computation by assuming that the electron pressure is determined solely by these two elements.

Table 5.1. Solar abundances (mass fractions) of important elements, Unsöld & Baschek (2002, p. 203).

Z		element	atomic weight μ	mass fraction X
1	H	hydrogen	1.008	0.73
2	He	helium	4.003	0.25
11	Na	sodium	23.00	$3.02 \cdot 10^{-5}$
12	Mg	magnesium	24.31	$4.61 \cdot 10^{-4}$
14	Si	silicon	28.09	$6.77 \cdot 10^{-4}$
19	K	potassium	39.10	$2.54 \cdot 10^{-6}$
20	Ca	calcium	40.08	$5.85 \cdot 10^{-5}$
26	Fe	iron	55.85	$1.63 \cdot 10^{-3}$

This assumption can be justified easily: taking solar abundances (see Table 5.1), and assuming that all iron atoms are completely ionized, the number of free electrons from iron relative to those from hydrogen and helium is

$$\frac{1.63 \cdot 10^{-3} \cdot \frac{26}{55.85}}{0.73 \cdot \frac{1}{1.008} + 0.25 \cdot \frac{2}{4.003}} = 8.9 \cdot 10^{-4}$$

and thus negligible. After this preparative work, the number densities can be calculated from

$$n_{i,l}^{\mathrm{A}} = n_i^{\mathrm{A}} \cdot \frac{g_{i,l}^{\mathrm{A}}}{W_i^{\mathrm{A}}} \cdot \exp\left\{ -\frac{\chi_{i,l}^{\mathrm{A}}}{k_{\mathrm{B}}T} \right\} . \tag{5.11}$$

5.3.3 Cross-sections

Hydrogen and hydrogenic atoms

We first focus on hydrogenic atoms, as the results are applicable as “exact” solutions to hydrogen and single-electron atoms and at least as an approximation to more-electron systems like He I in high excitation states. Following Mihalas (1970), the cross section for hydrogenic atoms is given by

$$\sigma_{i,k}^{\mathrm{bf,\,A}} = z^4 \frac{64\pi^4 m_{\mathrm{e}} e^{10}}{3\sqrt{3} c h^6} \cdot \frac{g_{i,\mathrm{bf}}^{\mathrm{A}}(k,\nu)}{k^5 \nu^3} = z^4 K \cdot \frac{g_{i,\mathrm{bf}}^{\mathrm{A}}(k,\nu)}{k^5 \nu^3} \tag{5.12}$$

with the constant factor $K = 2.81540 \cdot 10^{29}\,\mathrm{cm}^2\,\mathrm{s}^{-3}$ (in cgs-units), effective nuclear charge $z = i + 1$ and the bound-free gaunt factor $g_{i,\mathrm{bf}}^{\mathrm{A}}$ which depends on the excitation level and on the frequency of the radiation. The elementary charge is given by $e = 4.8032 \cdot 10^{-10}\,\mathrm{g}^{1/2}\,\mathrm{cm}^{3/2}\,\mathrm{s}^{-1}$ (in cgs-units). For hydrogen and single-electron atoms, the main/effective quantum number k can be identified with the number of the excitation state plus one, $k = l + 1$. For more-electron systems in the hydrogenic approximation, it can be calculated from (see Traving et al. (1966))

$$k = \left\lfloor (1+i)\sqrt{\frac{Ry \cdot h}{\chi_{i,\mathrm{ion}}^{\mathrm{A}} - \chi_{i,l}^{\mathrm{A}}}} + 1 \right\rfloor , \qquad \lfloor \ldots \rfloor = \text{floor function}. \tag{5.13}$$

Other cases

For more-electron systems in low excitation states, the assumption of effective shielding by the remaining inner electrons becomes inaccurate. A full quantum mechanic calculation is very costly and beyond the scope of this work. Therefore, approximate solutions and interpolation formulae are taken from the literature for low excitation states.

He I Beneath hydrogen, helium is the most abundant element in space. Hence, we expect its contribution to the bound-free absorption to be important. The ionization energy of neutral helium is $\chi_{0,\text{ion}}^{\text{He I}} = 24.58$ eV, corresponding to temperatures of $2.8 \cdot 10^5$ K and photon frequencies of $5.9 \cdot 10^{15}$ Hz, which lie both in the achievable range of our simulation. We apply interpolated cross sections (c. f. Mihalas (1970)) for the inner two shells $k = 1$ and 2 (states $l = 0, \ldots, 6$ in the NIST database) and adopt the hydrogenic approximation for higher excitation levels $l > l^* = 6$ ($k > k^* = 2$). The interpolated values are taken from Gingerich (1964) and given in Table 5.2, together with the statistical weights $g_{i,l}^{\text{He}}$ needed for the calculation of these low excitation states.

Table 5.2. Bound-free absorption for He I and $l = 0, \ldots, 4$.

l	State	$\chi_{0,l}^{\text{He}}$[eV]	$g_{0,l}^{\text{He}}$	$\sigma_{0,k}^{\text{bf, He}}$[cm^2]	ν[s^{-1}] at edge
0	1^1S	0	1	$2.95 \cdot 10^{14} \cdot \nu^{-2.00}$	$5.94 \cdot 10^{15}$
1	2^3S	19.72	3	$2.90 \cdot 10^{-7} \cdot \nu^{-0.775}$	$1.18 \cdot 10^{15}$
2	2^1S	20.51	1	$4.47 \cdot 10^{11} \cdot \nu^{-1.91}$	$9.84 \cdot 10^{14}$
3,4,5	2^3P	20.86	9	$3.72 \cdot 10^{26} \cdot \nu^{-2.90}$	$8.99 \cdot 10^{14}$
6	2^1P	21.11	3	$2.04 \cdot 10^{35} \cdot \nu^{-3.50}$	$8.39 \cdot 10^{14}$

Bound-free Gaunt factors

The gaunt factor is a slowly varying function of the order of unity. As a first approach, we set $g_{i,\text{bf}}^{\text{A}}(l,\nu) \equiv 1$ for all elements, ionization states and excitation levels. For a more sophisticated calculation, these quantities have to be treated more carefully: one possibility would be to interpolate them from tabulated values, e. g. given in Karzas & Latter (1961), or use approximation formulae at least for the inner shells.

5.3.4 Upper limits on the contribution of excitation levels

From the number densities and cross-sections, the bound-free absorption contribution $\kappa_\nu^{\text{bf, A}}$ of each element A can be computed with (5.3). In the above derivation, we used a hydrogenic approximation for high excitation levels $l > l^*$ ($k > k^*$). In the hydrogenic approximation, the contribution of one excitation state $n_{i,l}^{\text{A}}$ to the bound-free absorption depends strongly on k, where k is the main quantum number which corresponds to the excitation level l:

$$n_{i,l}^{\text{A}} \cdot \sigma_{i,l}^{\text{bf, A}} \propto k^2 \cdot k^{-5} = k^{-3} \,.$$

It is therefore sufficient to consider only states l with $k \leq k_{\text{bf}}$, where k_{bf} has to be chosen sufficiently large. From intensive parameter investigations, we found that $k_{\text{bf}} = 15$ is acceptable.

5.4 Line transitions

In the following, we discuss a simplified description of the bound-bound processes. The goal is to provide a sufficiently fast and easy method to calculate the line emission from selected atoms, like Fe K$_\alpha$.

In general, line emission and absorption is described by spontaneous emission, induced emission and absorption. It is a common way to treat induced emission as negative absorption in order to retain the classical structure for the emission/absorption coefficients:

$$\begin{aligned} j_\nu &= j_\nu^{\text{cont}} + j_\nu^{\text{lines}} , \\ \kappa_\nu &= \kappa_\nu^{\text{cont}} + \kappa_\nu^{\text{lines}} . \end{aligned}$$

A characteristic property of heavy metals is that ionization energies vary extremely for different ionization stages. As an example, consider iron. The ionization energy of neutral iron is 7.9 eV, while it requires 9.3 keV to ionize hydrogenic iron. The environmental conditions in our simulation data vary considerably, depending on the central mass, accretion rate, radial distance from the black hole and inclination angle from the vertical direction. We therefore expect significantly different ionization equilibria in the computational domain. While in a high energy regime, line transitions by spontaneous/induced emission and absorption are known to be dominant, in a low energy regime they become outbalanced by secondary effects like fluorescence lines and radiation-less Auger transitions.

We assume LTE to be established throughout the computational domain. Thus, the ionization equilibrium is determined by the gas temperature and density only. For an investigation of emission and absorption line features, we therefore do not have to bother about Auger transitions. Besides line emission and absorption caused by collisions, we only have to incorporate iron fluorescence lines in our calculation:

$$\begin{aligned} j_\nu^{\text{lines}} &= j_\nu^{\text{collision}} + j_\nu^{\text{fluorescence}} , \\ \kappa_\nu^{\text{lines}} &= \kappa_\nu^{\text{collision}} + \kappa_\nu^{\text{fluorescence}} . \end{aligned}$$

The full equation of radiative transfer gets

$$\begin{aligned} (\vec{l}\cdot\vec{\nabla})I_\nu \;=\; & \left(\frac{\nu}{\nu_0}\right)^2 \cdot \Bigg\{ \kappa_{\nu_0}^{\text{abs, cont}} S_{\nu_0} + \frac{3}{4}\kappa_{\nu_0}^{\text{sca, cont}} \frac{c}{4\pi}\left(E_{\nu_0} + l_{0i} l_{0j} P_{\nu_0}^{ij}\right) + j_{\nu_0}^{\text{lines}} \\ & - \left(\kappa_{\nu_0}^{\text{abs, cont}} + \kappa_{\nu_0}^{\text{sca, cont}} + \kappa_{\nu_0}^{\text{lines}}\right) I_{\nu_0} \Bigg\} . \end{aligned} \tag{5.14}$$

where the conversion rules for ν_0, $\vec{l}_0$ and I_{ν_0} are given by (4.6)–(4.8). The line contribution from collisional excitation for a transition $j \to i$ ($j > i$) with line frequency ν_0 is generally defined by

$$j_{\nu_0}^{\text{coll.}} = h\nu_0 A_{ji} n_j \psi_{\nu_0} \qquad \text{and} \qquad \kappa_{\nu_0}^{\text{coll.}} = h\nu_0 \left(B_{ij} n_i - B_{ji} n_j\right) \phi_{\nu_0} , \tag{5.15}$$

where the Einstein coefficients for spontaneous emission (A_{ji}), induced emission (B_{ji}) and absorption (B_{ij}) are related under the assumption of LTE by

$$A_{ji} = \frac{2h\nu_0^3}{c^2} B_{ji} \qquad \text{and} \qquad B_{ij} = \frac{g_j}{g_i} B_{ji} . \tag{5.16}$$

Table 5.3. Number of excitation levels per ionization degree i of iron.

$i =$	0	1	2	3	4	5	6	7	8	9	10	11	12	13	14	15	16	17	18	19	20	21	22	23	24	25
$l_{\text{max},i} =$	492	577	566	276	180	93	154	41	34	64	66	76	49	71	71	79	66	70	63	62	49	60	72	49	43	25

The line profile functions are defined such that $\int \psi_{\nu_0} d\nu_0 = \int \phi_{\nu_0} d\nu_0 = 1$. To calculate the bound-bound contributions, these line profile functions have to be computed (Sect. 5.4.4) along with the level populations n_i, n_j. The level populations require the computation of the partition function (Sect. 5.4.2) and a subsequent application of the Saha equation (Sect. 5.4.3). Both calculations are simplified using Debye's theory (Sect. 5.4.1). In Sect. 5.4.5, we present the set of lines considered in our computations and provide the necessary physical quantities. Finally, in Sect. 5.4.6, we discuss the iron K-shell fluorescence lines.

5.4.1 Atomic population calculations and Debye's theory

The calculation of the number densities for metals is highly simplified by the fact that the number of free electrons, and therefore the electron pressure, is given by hydrogen and helium. This means that we do not have to include all 26 ionization states of iron in the coupled system of equations determining the number of free electrons.

However, an increasing number of free electrons leads to an increasing electron pressure which alters the ionization equilibrium of *all* elements. This is taken into account in the subsequent deduction by applying Debye's theory (see, e. g., Traving et al. (1966)), which incorporates this effect by a reduction of the ionization energy of the individual ionization states n_i^{A}, $i = 0, \ldots, Z^{\text{A}}$ of element A:

$$\Delta\chi_i = 4.98 \cdot 10^4 \,\text{eV}\; \cdot (i+1) \cdot \frac{5040}{T_{\text{gas}}[\text{K}]} \cdot P_{\text{e}}[\text{erg/cm}^3]\,, \qquad P_{\text{e}} = n_{\text{e}} k_{\text{B}} T_{\text{gas}}\,. \tag{5.17}$$

5.4.2 Partition functions for metals

For calculating the partition functions, we use the same method as for hydrogen and helium by taking into account all available excitation states per ionization level. Contrary to before, the complexity of calculating "all" internal states of iron is still a serious task. For the present investigation, we use a comprehensive set of data, again from NIST (2006): like in the case of hydrogen and helium, all relevant data is taken from the atomic spectra database. The number of levels is given in Table 5.3.

The corrected partition functions W_i^{A} are now calculated from

$$W_i^{\text{A}} = \sum_{l=0}^{l_{\text{max},i}} g_{i,l}^{\text{A}} \exp\left\{-\frac{\chi_{i,l}^{\text{A}} - \Delta\chi_i}{k_{\text{B}}T}\right\}\,, \qquad i = 0, \ldots, Z^{\text{A}} - 1\,, \qquad W_{Z^{\text{A}}}^{\text{A}} = 1\,. \tag{5.18}$$

In all cases, the ionization energies are larger than the reduction $\Delta\chi_i$ due to the electron pressure.

5.4.3 Saha equation for metals

The original Saha equation (5.8) is modified by the reduction of the ionization energy and therefore becomes

$$\frac{n_{i+1}^{\mathrm{A}} n_{\mathrm{e}}}{n_i^{\mathrm{A}}} = \frac{2W_{i+1}^{\mathrm{A}}}{W_i^{\mathrm{A}}} \cdot \frac{(2\pi m_{\mathrm{e}})^{3/2}}{h^3} (k_{\mathrm{B}}T)^{3/2} \cdot \exp\left\{ -\frac{\chi_{i,\mathrm{ion}}^{\mathrm{A}} - \Delta\chi_i}{k_{\mathrm{B}}T} \right\} . \tag{5.19}$$

Since the electron density (pressure) is determined by the previously calculated ionization degrees of hydrogen and helium solely, n_{e} is known and constant. Combining this set of equations with the conservation of the total number density (5.10), it can easily be solved for the individual n_i^{A}. The level populations are again computed from (5.11).

5.4.4 Line profile functions

The line profile function generally consists of three different contributions: natural line width, pressure/collisional broadening, Doppler broadening. Since the environmental conditions in our simulation box (temperatures, pressure, …) are highly varying and since the transitions considered here (Fe K$_\alpha$, K$_\beta$) are very strong transitions with Einstein coefficients A_{ji} up to $10^{14}\,\mathrm{s}^{-1}$, the usually neglected natural line width also has to be taken into account. Contrary to pressure broadening, with its strong dependence on the element and its ionization state, Doppler broadening is a universal feature. In this investigation, we assume that the profile functions for spontaneous emission and absorption equal each other, $\psi_\nu = \phi_\nu$.

Doppler broadening

The Doppler width of a spectral line of frequency ν_0 is given by

$$\Delta\nu = \frac{\nu_0}{c} \sqrt{\frac{2k_{\mathrm{B}}T}{m_i^{\mathrm{A}}}} , \tag{5.20}$$

where m_i^{A} is the ion mass. A purely Doppler broadened line can be described by a Gaussian profile function

$$D(\nu) = \frac{1}{\sqrt{\pi}\,\Delta\nu} \exp\left\{ -\frac{(\nu-\nu_0)^2}{\Delta\nu^2} \right\} , \qquad \int D(\nu)\,d\nu = 1 . \tag{5.21}$$

Natural line width

Due to the finite life time of excited states and the Heisenberg uncertainty principle, the line is broadened by a Lorentzian shape:

$$L(\nu) = \frac{1}{\pi} \cdot \frac{\gamma}{(\nu-\nu_0)^2 + \gamma^2} , \qquad \int L(\nu)\,d\nu = 1 . \tag{5.22}$$

Its only parameter $\gamma = \gamma_{\mathrm{rad}}$ (*radiation damping coefficient*) is given by the coefficient of spontaneous emission, $\gamma_{\mathrm{rad}} = A_{ji}/2$.

Pressure broadening

In most cases, pressure broadening also produces a Lorentzian shape of the profile function and is parameterized by a damping constant γ_{pr} analogous to natural line broadening. An exception to this pattern is broadening of lines by ions due to the linear Stark effect, which results in a Holtsmark profile with distinctive broad line wings. We neglect this particularity of the linear Stark effect and assume that pressure broadening produces a Lorentzian profile with damping constant γ_{pr}. A discussion of this assumption is given at the end of this subsection.

Combining pressure broadening and radiation damping is then straightforward due to the additivity of the Lorentz profile function. It is achieved by replacing the radiation damping constant γ_{rad} by a combined damping constant γ, which is the sum of the broadening mechanisms that are involved:

$$\gamma = \gamma_{\text{rad}} + \gamma_{\text{pr}}\,. \tag{5.23}$$

Similar to stellar structure calculations, main contributions to the pressure damping term originate from Stark broadening by electrons (γ_4, quadratic Stark effect) for all ionization degrees of iron and by electrons and ions (γ_2, linear Stark effect) for Fe XXVI. Finally, van der Waals interaction with neutral hydrogen and helium atoms is acting on neutral iron atoms (γ_{vdw}) (Traving et al., 1966):

$$\gamma_{\text{pr}} = \begin{cases} \gamma_{\text{vdw}} & \text{Fe I} \\ \gamma_4 & \text{Fe I–XXVI} \\ \gamma_2 & \text{Fe XXVI} \end{cases}\,. \tag{5.24}$$

Van der Waals broadening We consider pressure broadening for low-temperatures, presumably in the outer part of our simulation box, in the approximation of Unsöld (1955) and Traving et al. (1966).

Van der Waals broadening acts on neutral iron atoms and is caused by the presence of neutral hydrogen and helium atoms. In the temperature and pressure ranges where γ_{vdw} becomes important, we may neglect the differences in excitation and ionization of H and He:

$$\gamma_{\text{vdw}} = \gamma^{\text{H}}_{\text{vdw}} + \gamma^{\text{He}}_{\text{vdw}} = \gamma^{\text{H}}_{\text{vdw}}\left(1 + \varsigma\frac{\varepsilon^{\text{He}}}{\varepsilon^{\text{H}}}\right)\,. \tag{5.25}$$

The constant ς is determined approximately by the polarizability $\mathcal{P}$ and atomic weight μ,

$$\varsigma = \left(\frac{\mathcal{P}^{\text{He}}}{\mathcal{P}^{\text{H}}}\right)^{2/5} \cdot \left(\frac{\mu^{\text{H}}}{\mu^{\text{He}}}\right)^{3/10} = \frac{1}{2.4192}\,. \tag{5.26}$$

By introducing the interaction constant C_6, the van der Waals damping mechanisms can by expressed as

$$\log \gamma^{\text{H}}_{\text{vdw}}[10^8\,\text{s}^{-1}] = \frac{2}{5}\log C_6 + 8.6735 + \frac{7}{10}\log\Theta + \log P_{\text{H}}\,, \tag{5.27}$$

where P_{H} is the partial pressure of neutral hydrogen atoms,

$$P_{\text{H}} = X^{\text{H}} \cdot (P_{\text{gas}} - P_{\text{e}}) \cdot \frac{n^{\text{H}}_{i=0}}{n^{\text{H}}}\,. \tag{5.28}$$

We base the calculation of C_6 on Unsöld's hydrogenic approximation (Unsöld, 1955) and apply a correction factor for non-alkali metals (Wehrse & Liebert, 1980). We explicitly account for the different polarizabilities of neutral iron and hydrogen (Schweitzer et al., 1996) and get

$$\begin{aligned} C_6 &= C_6^{\rm corr} \times C_6^0 \\ &= 10^{1.8} \times \frac{\mathcal{P}^{\rm Fe}}{\mathcal{P}^{\rm H}} 1.01 \cdot 10^{-32} (Z^{\rm Fe}+1)^2 \cdot \left[\frac{{\chi^{\rm H}_{0,\rm ion}}^2}{(\chi^{\rm Fe}_{0,\rm ion} - \chi^{\rm Fe}_{0,i})^2} - \frac{{\chi^{\rm H}_{0,\rm ion}}^2}{(\chi^{\rm Fe}_{0,\rm ion} - \chi^{\rm Fe}_{0,j})^2} \right] . \end{aligned} \tag{5.29}$$

Here, $Z^{\rm Fe} = 26$. We recall that the level energy of the upper level of iron K line transitions ($\chi^{\rm Fe}_{0,j} \approx 6.4\,$keV) is much higher than the ionization energy of hydrogen ($\chi^{\rm H}_{0,\rm ion} = 13.6\,$eV) and neutral iron ($\chi^{\rm Fe}_{0,\rm ion} = 7.90\,$eV), while the lower level energy of iron K line transitions $\chi^{\rm Fe}_{0,i} = 0$. Hence, this may be simplified to

$$C_6 = \frac{\mathcal{P}^{\rm Fe}}{\mathcal{P}^{\rm H}} 6.37 \cdot 10^{-31} (Z^{\rm Fe}+1)^2 \cdot \frac{{\chi^{\rm H}_{0,\rm ion}}^2}{{\chi^{\rm Fe}_{0,\rm ion}}^2} . \tag{5.30}$$

We adopt the polarizabilities given in Schweitzer et al. (1996), $\mathcal{P}^{\rm Fe}/\mathcal{P}^{\rm H} \approx 12.58$.

Quadratic Stark effect Line broadening by electrons is treated in terms of the quadratic Stark effect caused by electrons in the present investigation[1]. An exact treatment of the pressure widths requires a quantum mechanical approach, involving sophisticated calculations for each line. Since this is unrealistic in astrophysical applications, previous calculations used a semi-empirical approximation (Gonzalez et al., 1995):

$$\gamma_4 = \frac{\iota}{2} \cdot \frac{n_l^4 + n_u^4}{(Z_i^{\rm Fe}+1)^2} \cdot \frac{n_{\rm e}}{\sqrt{T_{\rm gas}}} . \tag{5.31}$$

Here, n_l and n_u are the principal quantum numbers of the lower and upper levels ($n_l = 1$ and $n_u \in \{2{,}3\}$ for $\mathrm{K}_{\{\alpha,\beta\}}$ transitions), $Z_i^{\rm Fe}$ is the charge of the ion, and ι is a numerical constant in the range of $1.6 \cdot 10^{-6}$ (Michaud et al., 1976) to $2.0 \cdot 10^{-5}$ (Cox, 1965). We adopt the latter value, $\iota = 2.0 \cdot 10^{-5}$, in order to simulate sensitive iron lines.

Linear Stark effect For highly ionized Fe XXVI, the linear Stark effect dominates over the quadratic one. Following Cox (1965), we consider it by raising the quantum numbers n_l and n_u to the fifth power instead of the fourth:

$$\gamma_2 = \frac{\iota}{2} \cdot \frac{n_l^5 + n_u^5}{(Z_i^{\rm Fe}+1)^2} \cdot \frac{n_{\rm e}}{\sqrt{T_{\rm gas}}} . \tag{5.32}$$

Remark. In fact, the environmental conditions in the simulation box vary between two extreme ranges. For low temperatures and densities, natural line widths dominate the broadening of the lines; for high temperatures and densities, the Doppler effect is the most important mechanism for line broadening. Van der Waals broadening is negligible throughout the computational domain.

---

[1] The Stark effect produced by the corresponding ions is lower by a factor of ≈ 6 due to its higher mass (Kusch, 1957) and therefore neglected here.

In all cases, pressure broadening by the quadratic Stark effect is lower than the leading contribution by 2–4 orders of magnitude. Also, the usually prominent linear Stark effect is weak for the K_α and K_β transitions considered here: examining the semi-empirical fitting formula (5.32), we find that the principle quantum numbers n_l and n_u are small, while at the same time the ionic charge is large for Fe XXVI, $Z_i^{\mathrm{Fe}} = 25$.

To further justify our assumption of neglecting the Holtsmark shape of lines broadened by the linear Stark effect, we note that the ionization energies of Fe XXV and Fe XXVI lie very close together ($\chi^{\mathrm{Fe}}_{24,\mathrm{ion}} = 8.8\,\mathrm{keV}$, $\chi^{\mathrm{Fe}}_{25,\mathrm{ion}} = 9.3\,\mathrm{keV}$), while Fe XXIV is ionized at significantly lower temperatures ($\chi^{\mathrm{Fe}}_{24,\mathrm{ion}} = 2.0\,\mathrm{keV}$). Thus, we expect that either Fe XXV is dominant with a small contribution of Fe XXVI, or that completely ionized iron dominates over the hydrogenic iron. Hence, the contribution of single-electron iron will be small in any case.

Therefore, assuming a Lorentz-shape profile is acceptable in our calculations. Additionally, since pressure broadening by the Stark and the van der Waals effect plays only a minor role, we can safely neglect the small line shifts which are caused by these two mechanisms.

Combined broadening mechanisms

In general, a combination of Doppler broadening and collisional/radiative broadening influences the line shape, resulting in a Voigt profile

$$V(\nu) = \int_{-\infty}^{\infty} \frac{e^{-\frac{(\nu'-\nu_0)^2}{\Delta\nu^2}}}{\sqrt{\pi}\Delta\nu} \cdot \frac{\gamma}{\pi\left((\nu-\nu'-\nu_0)^2+\gamma^2\right)}\,d\nu'\,, \qquad \int L(\nu)\,d\nu = 1\,. \tag{5.33}$$

In principle, the values of $V(\nu)$ could be taken from tables. However, there are many methods to evaluate the Voigt profile function more precisely. We henceforth focus on a subtle approach utilizing the complex error function (Klim, 1981).

Although the convolution (5.33) cannot be solved analytically, it can be expressed as the real part of the complex error function $w(z)$ for which numerical approximations are available at high precision:

$$V(\nu) = \frac{\mathfrak{Re}[w(z)]}{\Delta\nu\sqrt{\pi}}\,, \qquad z = \frac{\nu + i\gamma}{\Delta\nu}\,. \tag{5.34}$$

We adopt a standard code (Poppe & Wijers, 1990) to evaluate $w(z)$ quickly and precisely.

5.4.5 Standard line transition data

The prominent and strong iron K lines lie in a deserted part of the spectrum, meaning that only few or weak transitions of other elements influence this spectral range. The line energy and frequency ranges of the iron K_α and K_β lines are summarized in Table 5.4.

Assembling all necessary data of the iron line transitions is not a straightforward task: results from numerical computations and experimental measurements are spread widely over the literature during the last decades.

Fe K_α Line data for neutral iron (Fe I) is taken from the NIST database (NIST, 2006). A comprehensive set of transition data for Fe II–XXV excluding Fe X is taken from the XSTAR

Table 5.4. Iron line transitions overview.

Spectral line	λ_0 [Å]	ν_0 [s^{-1}]	E_{ij} [eV]	Reference
Fe K$_\alpha$				
Fe I K$_\alpha$	1.94	$1.55 \cdot 10^{18}$	$6.40 \cdot 10^{3}$	NIST (2006)
Fe XXVI K$_\alpha$	1.78	$1.69 \cdot 10^{18}$	$6.97 \cdot 10^{3}$	Shirai et al. (2000)
Fe K$_\beta$				
Fe I K$_\beta$	1.76	$1.70 \cdot 10^{18}$	$7.04 \cdot 10^{3}$	NIST (2006)
Fe XXVI K$_\beta$	1.50	$1.99 \cdot 10^{18}$	$8.25 \cdot 10^{3}$	QM calculation

database (XSTAR, 2007), missing data for Fe X is added from Mendoza et al. (2004). Finally, Fe XXVI data is provided by the compilation of Shirai et al. (2000). In total, 1336 lines are taken into account.

Fe K$_\beta$ Significantly fewer data is available for the iron K$_\beta$ line. For the neutral state (Fe I), data is taken again from NIST (2006). XSTAR (2007) provides a basic set of data for Fe II–XVII (176 lines). Presently, no data for Fe XVIII–Fe XXIV can be found in the literature. The reason for this lack of data is that these iron ions consist of just K- and L-shell electrons in the ground state. Realistic electron densities and photon intensities are too low to produce significant population in the M-shell *at the same time* as producing a K-shell hole (Badnell, priv. comm.), minimizing the importance of (and also the interest of atomic physic research in) the K$_\beta$ lines of these ions.

For almost completely ionized iron, Fe XXV data can be found in Fuhr et al. (1988) and Fe XXVI data can be calculated from quantum mechanic approximation of hydrogenic atoms. Altogether, 181 lines for K$_\beta$ enter our radiative transfer calculations.

5.4.6 Fluorescence lines

The fluorescence absorption coefficient is determined by the photoionization cross-section of the iron K-shell. We use resonance-averaged photoionization cross-sections (Bautista et al., 1998), having several advantages compared to the usage of standard cross-sections.

Firstly, realistic cross-sections involve heavy quantum-mechanical calculations and often show extremely narrow but strong resonance peaks, therefore requiring very high frequency resolution. We avoid this demand by using resonance-averaged cross-sections. Additionally, the smearing-out by the averaging process roughly accounts for broadening processes like Doppler broadening.

Secondly, the authors provide an elegant routine to calculate the resonance-averaged K-shell photoionization cross-sections for elements $1 \leq Z^{\mathrm{A}} \leq 26$ and all their ionization degrees: given an ionization state i with nuclear charge Z^{Fe} and $N_{\mathrm{e}} = Z^{\mathrm{Fe}} - i$ bound electrons, and an energy of the ejected electron $E_{\mathrm{e}} = h\nu - \chi^{\mathrm{Fe}}_{i,\mathrm{ion}}$ in eV (*not* in Ry as it is stated mistakenly in Bautista et al. (1998)), this routine calculates the K-shell photoionization cross-section $\sigma^{\mathrm{Fe\,K\text{-}fl.}}_{i,\nu}$ in Mb $= 10^{-18}$cm^2. Multiplying this with the number density of the corresponding ion n^{Fe}_i results in the K-shell fluorescence absorption coefficient

$$\kappa^{\mathrm{Fe\,K\text{-}fl.}}_{i,\nu} = \sigma^{\mathrm{Fe\,K\text{-}fl.}}_{i,\nu} \cdot n^{\mathrm{Fe}}_i \,, \qquad \left[\kappa^{\mathrm{Fe\,K\text{-}fl.}}_{i,\nu}\right] = \mathrm{cm}^{-1}.$$

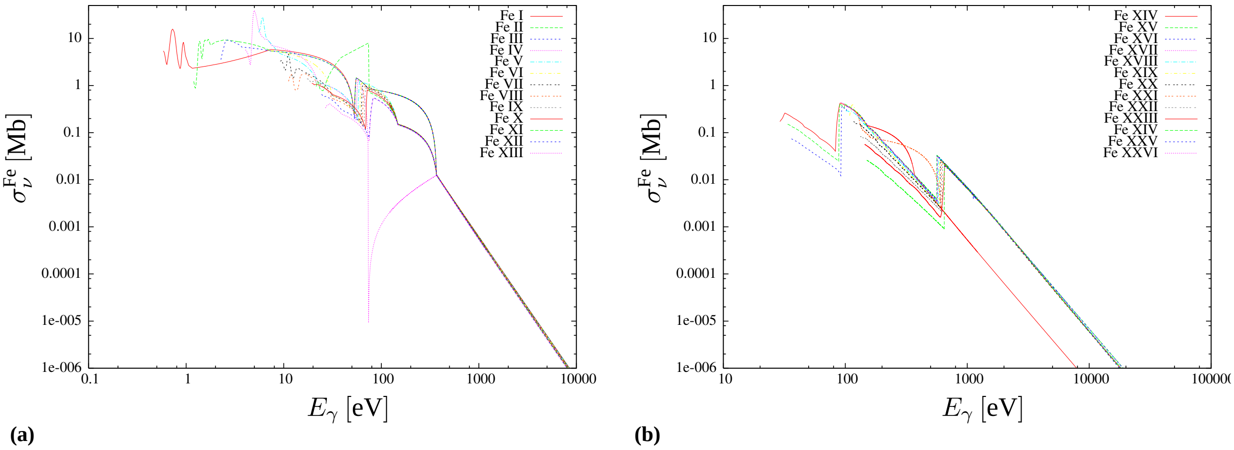

Figure 5.4. Photoionization cross-sections as function of photon energy. **(a)** Fe I-XIII **(b)** Fe XIV-XXVI.

Figure 5.4 shows the K-shell photoionization-cross section for all ionization states of iron as a function of the incident photon energy. Having the fluorescence absorption coefficients at hand, we proceed with the calculation of the total number of photoionization events per volume and time (for comparison, see van Teeseling et al. (1995)):

$$\eta_i^{\rm Fe\,K\text{-}fl.} = \int_{\nu_{{\rm K},i}}^{\infty} \frac{\kappa_{i,\nu}^{\rm Fe\,K\text{-}fl.} S_\nu(T_{\rm rad})}{h\nu}\, d\nu\,, \qquad [\eta_i^{\rm Fe\,K\text{-}fl.}] = {\rm Hz\,cm^{-3}}\,. \tag{5.35}$$

The mean intensity of the radiation field is given by the Planck-function $B_\nu(T_{\rm gas})$ in our calculation, assuming isotropy and LTE for the gas and the radiation separately (see Sect. 4.2.3). Finally, the K-shell fluorescence line emission contribution for one specific $\rm K_\alpha$ or $\rm K_\beta$ line is calculated from

$$j_\nu^{\rm Fe\,K\text{-}fl.} = \sum_{i=0}^{25} Y_i \eta_i^{\rm Fe\,K\text{-}fl.} h\nu\, \psi_{\nu_i}\,, \tag{5.36}$$

with Y_i being the fluorescence yield and ν_i the corresponding line frequency. We take the fluorescence line data (Y_i, ν_i) from Kaastra & Mewe (1993). The line profile function is calculated as outlined in the previous sections. We note that natural line widths (i. e., radiative transition rates) could not be found or unambiguously identified for the fluorescence lines. However, since pressure broadening is generally small compared to the dominant broadening mechanisms (see discussion in Sect. 5.4.4), we approximate the natural line widths $\gamma_{\rm rad}$ by typical values for strong iron K lines. The data used for the K-shell fluorescence calculation is summarized in Table A.3 in the appendix (page 137). We note that the fluorescence yields for highly ionized iron are extremely small, especially for $\rm K_\beta$ transitions. This is due to strong competing effects that inhibit iron K line emission, e. g., autoionization channels (Bautista, priv. comm.).

5.4.7 Supplement to the numerical calculation

The principal method of calculation remains the same as in the previous investigation of the continuum features. However, the addition of line emission and absorption makes the calculation

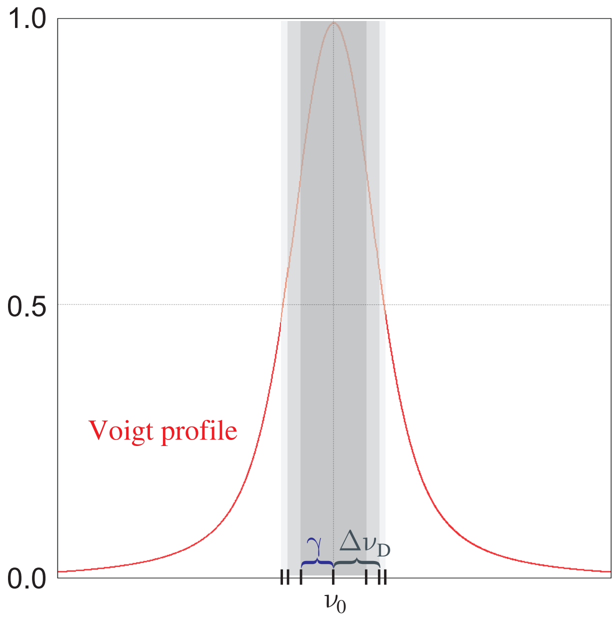

Figure 5.5. Illustration of line profile calculation for the case that Doppler broadening (Doppler width $\Delta\nu_\mathrm{D}$) dominates over pressure broadening (damping constant γ). Outside the line core ($|\nu-\nu_0| > \Delta\nu_\mathrm{D}$), the standard resolution is used. Inside the Doppler-, but outside the Lorentz-core ($\Delta\nu_\mathrm{D} \geq |\nu-\nu_0| > \gamma$), the resolution is increased by a factor of 10, and inside both cores ($|\nu-\nu_0| \leq \gamma$) by a factor of 100, respectively. The case $\gamma > \Delta\nu_\mathrm{D}$ is analog.

of the opacity coefficient for absorption very costly. Before, the opacity contributions κ_sca and κ_abs and the emission coefficients were calculated *after* the volume interpolation from the interpolated densities ρ and temperatures T_gas, T_rad. Unfortunately, this method is not practicable at all. We therefore split the calculation into two distinct steps.

1. For each grid point of the simulation data, we precompile the scattering/absorption coefficients and the emission coefficients and store the resulting data in binary data files. This process is parallelized in the simplest way by dividing the number of grid points by the number of available nodes. In fact, also this step is composed of two processes in order to cope with the key problem of opacity calculations: the frequency resolution. The problem consists of the fact that even for the high temperatures and velocities in the inner region of our simulation data, and even more for the lower values in the outer regions, the line profiles of the individual lines are very narrow. This, however, is only true for the collisional (de-)excitation and not for the fluorescence lines, since in the latter case resonance averaged line profiles are used (c. f., Sect. 5.4.6).

   A discretization of the frequency with a reasonable resolution of $N_\nu \leq 1000$ in the iron K line range $\nu = [4 \cdot 10^{17}; 4 \cdot 10^{18}]$ Hz (for comparison, the total resolution in our previous investigation was $N_\nu = 200$ for $\nu = [10^{14}; 10^{22}]$ Hz) often leads to

   $$\int_0^\infty \phi_\nu \, d\nu \rightarrow \sum_{i=1}^{N_\nu} \phi_{\nu_i} \Delta\nu_i = 0\,,$$

   since the separation of the discrete frequencies is larger than the line widths. To circumvent this, we first calculate the line emission and absorption coefficients on a high resolution frequency array with $N_\nu = 12000$ points in the iron K line range. Even in this case, a further refinement is necessary, which is demonstrated in Fig. 5.5. The high resolution data is then written to the disk as binary data, requiring about 12 GB of disk space.

   Next, we produce lower resolution data by downsampling the high resolution data to $N_\nu = 600$ in the line range. Again, the data is stored on the hard disk in binary format, which

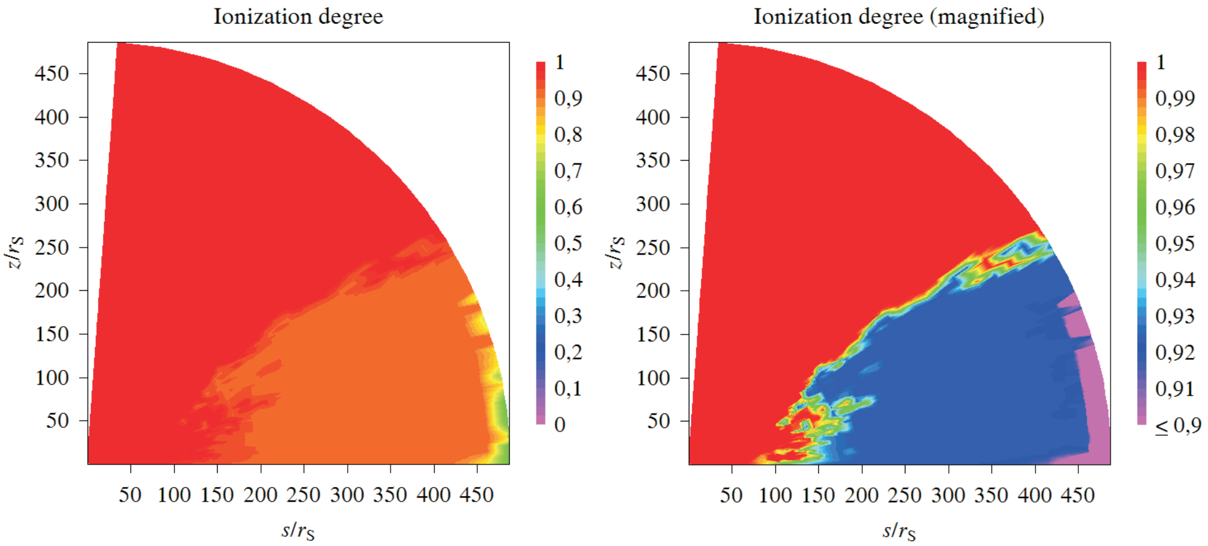

Figure 5.6. Average ionization degree in the simulation data for $M_\mathrm{c} = 10M_\odot$ and $\dot{M}_\mathrm{ext} = 1000\dot{M}_\mathrm{E}$; left: full scale from Fe I–Fe XXVII, right: magnification from Fe XXIII–Fe XXVII. For details, see text.

takes about 600 MB. The advantages of this two-step approach are that different lower resolutions can be calculated very quickly once the high resolution data is available, and that in general the opacity calculation needs to be done only once per simulation data set.

2. The real radiative transfer calculation starts with checking if the opacity data is available for the required resolution. The frequency resolution is typically $N_\nu = 700$, where 100 grid points are taken to be outside the line frequency range, and 600 grid points inside the line frequency range. The complete low resolution opacity data is then read by each node and interpolated like all other physical quantities by volume interpolation on the grid.

One may argue that this method of calculating the opacities is less accurate than a direct calculation from the interpolated densities and temperatures. However, we note that the intrinsic accuracy of the data – and therefore of the opacities – is not better than the grid resolution from the RHD simulations.

5.5 Atmosphere

Before we discuss the results of the numerical computation, we anticipate that we will find unusually strong emission lines and no absorption features for all the different sets of simulation data and inclination angles. This is not wrong necessarily, but we would expect to find signatures of absorption in some cases and generally weaker lines in most cases. This is also supported by the observational data presently available.

One possible explanation for finding no absorption and very strong emission lines is that the size of the computational domain is too small. The temperatures, in particular the gas temperature, are still at such a high level that iron is almost fully ionized. For illustration, see Fig. 4.1 and Fig. 5.6 for the simulation data with $M_\mathrm{c} = 10M_\odot$ and $\dot{M} = 10^3\dot{M}_\mathrm{E}$. The latter figure describes the ionization degree of the material by color coding: a value of 0 corresponds to neutral

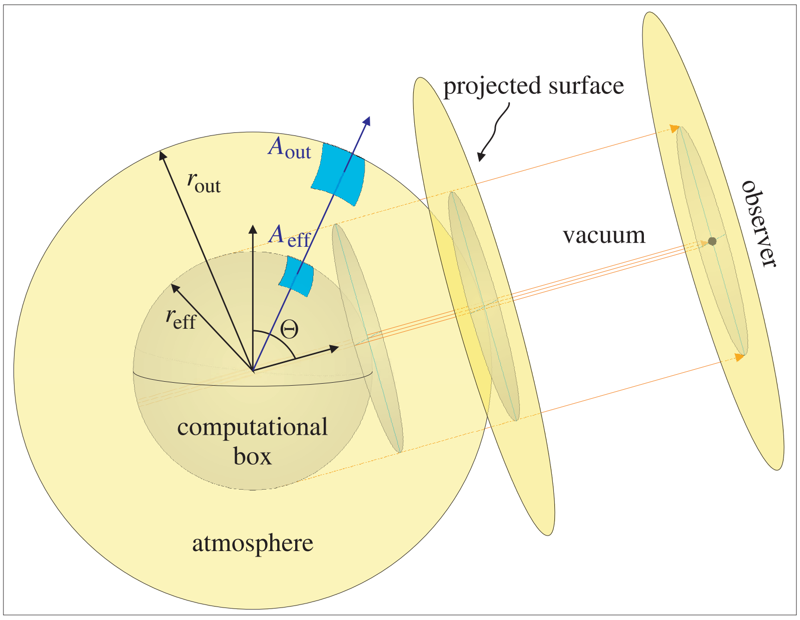

Figure 5.7. Simple sketch of the computational box and its surrounding atmosphere.

iron, $1/26$ to Fe II, $\dots$, and 1 to fully ionized Fe XXVII. The resulting color is then calculated from the average ionization degree at the corresponding grid point. We can see from the figure that the dilute outflow region is completely ionized, while Fe XXIII–Fe XXIV are dominating at lower altitudes and larger radii, reaching out to almost $500 r_{\rm S}$. There, the ionization degree drops to lower values of about 0.5, corresponding to Fe XIII.

However, it is unnatural to assume that such a system is truncated at an outer boundary $r_{\rm eff}$ (see Fig. 5.7) where temperatures and densities are still very high. In reality, there must be an extended outer region (*atmosphere*), where densities and temperatures decrease towards outer-space values. Certainly, the emergent spectrum will be altered by such an additional structure.

In the following, we describe our simple model for the surrounding atmosphere. We denote quantities at the outer radius (*surface*) of the computational box with the subscript “eff” and quantities at the outer boundary of the atmosphere (*outer space*) with the subscript “out”. If not explicitly stated otherwise, the radius r is assumed to be in the range of $[r_{\rm eff}; r_{\rm out}]$. Our radiative transfer calculations require the following data for the atmosphere: mass density ρ, radiation temperature $T_{\rm rad}$ (or radiation energy density E), gas temperature $T_{\rm gas}$ (or gas energy density e), velocity field $\mathbf{v} = (v_r, v_\Theta, v_\Phi)$.

Please note that in the following approach the zenithal and azimuthal velocities already include the scaling factors due to the spherical coordinate system. Thus, if $v_{\Theta,\rm real}$ and $v_{\Phi,\rm real}$ are given in radians, we use $v_\Theta = r v_{\Theta,\rm real}$ and $v_\Phi = r \sin\Theta\, v_{\Phi,\rm real}$ in units of centimeters instead.

5.5.1 Basic assumption

In order to derive a simple model for an extended atmosphere around the computational box, we consider the radial profile of the mass density ρ in the outer part of the computational domain. We therefore investigate one set of simulation data with a larger computational box, where $r_{\rm eff} \approx 2700 r_{\rm S}$ instead of $r_{\rm eff} = 500 r_{\rm S}$. The grid resolution is too low to use this data for our radiative transfer calculations, but it allows us to estimate the radial profile of the physical quantities for $r > 500 r_\mathrm{S}$.

In Fig. 5.8a, we plot the mass density as a function of radius for three distinct inclination angles Θ between $\pi/8$ (face-on case) and $3\pi/8$ (edge-on case). As one can see from the figure, there exists a clear trend towards a quadratic decrease of the density with radius for larger radii $r/r_\mathrm{S} \gtrapprox 500$. Therefore, we get a first relation for the atmosphere:

$$\rho(r) = \left(\frac{r_\mathrm{eff}}{r}\right)^2 \rho_\mathrm{eff} \,. \tag{5.37}$$

5.5.2 Atmosphere model

The disk-like structure in the computational domains settles to a quasi-static state after a certain time. We assume the atmosphere to be in such a quasi-static state as well. Consider a surface element A_eff at the outer boundary of the computational box. The outflow (or inflow) mass rate in radial direction through that surface at any time is given by

$$\frac{\Delta M}{\Delta t} = \rho_\mathrm{eff} v_r A_\mathrm{eff} \,.$$

Due to azimuthal symmetry and the fact that the radial motion dominates over the zenithal motion for all inclination angles except for the very edge-on case (c. f., Fig. 4.1, upper right), we can assume that this outflow rate is the same through all surface elements $A = A(r)$ along the radial vector:

$$\frac{\Delta M}{\Delta t} = \rho_\mathrm{eff} v_r A_\mathrm{eff} = \rho(r) v_r(r) A(r) \,. \tag{5.38}$$

Since $A(r) \propto r^2$, we can solve (5.38) for the radial velocity v_r using (5.37):

$$v_r = v_{r,\mathrm{eff}} = \mathrm{const} \,. \tag{5.39}$$

This constant behavior can also be found in the radial profile of the velocities, especially for small inclination angles (see Fig. 5.8b). The corresponding values for the zenithal velocity v_Θ (Fig. 5.8c) are slightly decreasing and can be fitted adequately by the following expression:

$$v_\Theta = \left(\frac{r_\mathrm{eff}}{r}\right)^{1/2} v_{\Theta,\mathrm{eff}} \,. \tag{5.40}$$

In a highly diluted atmosphere, we expect that the viscous stresses vanish in the outskirts of the system. Thus, the angular momentum is conserved and the azimuthal velocity should decrease linearly with radius:

$$v_\Phi = \frac{r_\mathrm{eff}}{r} v_{\Phi,\mathrm{eff}} \quad \Longrightarrow \quad l = l(r) = l_\mathrm{eff} = \mathrm{const} \,. \tag{5.41}$$

We find such a trend in the corresponding radial profile (see Fig. 5.8d), although the curve shows a slightly flatter decrease.[2]

---

[2] We also performed calculations where we assumed a Keplerian rotation ($v_\Phi \propto r^{-1/2}$), leading to the same results. Given that the transversal Doppler effect is negligible in our calculations, the azimuthal velocity plays only a minor role.

Additionally to the vanishing of the viscous stresses, the interaction between matter and the radiation field becomes negligible, since the average absorption opacities drop drastically. This is true for both the free-free opacity $\kappa_{\rm ff}$ (Rybicki & Lightman, 1979) and the bound-free opacity $\kappa_{\rm bf}$ (Hayashi et al., 1962) scale with ρ^2 and thus with r^{-4}. This greatly simplifies the treatment of the gas energy density and the gas temperature: the original energy equation for matter from inside the computational box (equation (7) in Ohsuga et al. (2005)) reduces in our case to

$$\nabla \cdot (e\mathbf{v}) = -p\nabla \cdot \mathbf{v} \, . \tag{5.42}$$

Again, we can take advantage of considering the outflow domain to reduce (5.42) further to

$$\frac{1}{r^2}\frac{\partial}{\partial r} r^2 e v_r = -p\frac{1}{r^2}\frac{\partial}{\partial r} r^2 v_r \, . \tag{5.43}$$

The definitions of the energy density and the pressure are

$$e = \frac{k_{\rm B}}{(\gamma-1)\mu m_{\rm H}}\rho T_{\rm gas} \, , \tag{5.44}$$

$$p = (\gamma-1)e \, , \tag{5.45}$$

where $\gamma = 5/3$ is the polytropic index for a non-relativistic gas and $\mu = 1/2$ is the mean molecular weight. Using these definitions and our previous scaling law for the radial velocity (5.39), we get

$$\begin{aligned}
\frac{\partial}{\partial r} r^2 e &= -p\frac{\partial}{\partial r} r^2 \\
\frac{k_{\rm B}}{(\gamma-1)\mu m_{\rm H}}\frac{\partial}{\partial r} r^2 \rho T_{\rm gas} &= -2r\frac{k_{\rm B}}{\mu m_{\rm H}}\rho T_{\rm gas} \\
\frac{\partial}{\partial r} r^2 \rho T_{\rm gas} &= -2r(\gamma-1)\rho T_{\rm gas} \\
\frac{\partial}{\partial r} r\left(\frac{r_{\rm eff}}{r}\right)^2 \rho_{\rm eff} T_{\rm gas} &= -2r(\gamma-1)\left(\frac{r_{\rm eff}}{r}\right)\rho_{\rm eff} T_{\rm gas} \\
\frac{\partial}{\partial r} T_{\rm gas} &= -2(\gamma-1)\frac{T_{\rm gas}}{r} \\
\frac{\partial T_{\rm gas}}{T_{\rm gas}} &= -2(\gamma-1)\frac{\partial r}{r} \, ,
\end{aligned}$$

and finally

$$T_{\rm gas} = \left(\frac{r_{\rm eff}}{r}\right)^{2(\gamma-1)} T_{\rm gas,eff} \, , \tag{5.46}$$

from which we recover the expected conservation of entropy:

$$p \propto \rho T_{\rm gas} \propto r^{-2} r^{-4/3} = r^{-10/3} \propto \rho^{5/3} \, . \tag{5.47}$$

A comparison of the scaling law (5.46) for the gas temperature with the radial profile in Fig. 5.8e shows that the curve in the computational box is slightly flatter than the scaling law predicts. This is no surprise, since viscous stresses are still at work in the computational box. For the outermost part around $2000 r_\mathrm{S}$, the asymptotic behavior of the gas temperature tends towards the scaling law (5.46).

Finally, we calculate the radiation energy density (or radiation temperature) profile in the atmosphere. If we repeat our previous argument, the energy equation (Ohsuga et al. (2005), equation (8)) becomes

$$\nabla \cdot (E_0 \mathbf{v}) = 0 \, . \tag{5.48}$$

For the radiation field in the outflow region of the atmosphere, we get:

$$\begin{aligned} 0 &= \frac{1}{r^2}\frac{\partial}{\partial r} r^2 E_0 v_r \\ &= \frac{\partial}{\partial r} r^2 E_0 \, . \end{aligned}$$

Thus,

$$E_0 = \left(\frac{r_\text{eff}}{r}\right)^2 E_{0,\text{eff}} \, . \tag{5.49}$$

With the definition of the radiation energy density

$$E_0 = a_\text{rad} T_\text{rad}^4 \, , \tag{5.50}$$

we get an expression for the radiation temperature profile:

$$T_\text{rad} = \left(\frac{r_\text{eff}}{r}\right)^{1/2} T_\text{rad,eff} \, . \tag{5.51}$$

This result fits remarkably with the radial profile in the computational box (Fig. 5.8f). To summarize, the radial profile of the physical quantities in the atmosphere is given as follows:

$$\rho \propto r^{-2}, \quad v_r = \text{const}, \quad v_\Theta \propto r^{-1/2}, \quad v_\Phi \propto r^{-1}, \quad T_\text{gas} \propto r^{-4/3}, \quad T_\text{rad} \propto r^{-1/2} \, .$$

The functional forms (5.37), (5.39), (5.40), (5.41), (5.46), and (5.51) guarantee a steady transition from the computational box to the atmosphere at $r = r_\text{eff}$. The outer boundary r_out has to be defined manually by imposing a lower limit on either the mass density or the gas temperature, for example. We decide to set a lower limit on the gas temperature, since we are interested in iron absorption line features. By defining

$$T_\text{gas,out} = 10^4 \text{K} \lessapprox 1 \, \text{eV} \, , \tag{5.52}$$

it is obvious that in the outer region of the atmosphere, iron is completely neutral (the lowest ionization energy for iron is $\chi_\text{Fe I} \approx 7.9$ eV). The corresponding outer radius r_out is

$$r_\text{out} = r_\text{eff} \cdot \left(\frac{T_\text{gas,eff}}{T_\text{gas,out}}\right)^{1/(2\gamma-2)} \, . \tag{5.53}$$

In Fig. 5.9, we show the resulting radial profiles for the mass density and the gas temperature for both the computational box and the atmosphere. We see that the density at the outer boundary of the computational box is very small, justifying the decision to cut the atmosphere at $r_\text{out} = 10^7 r_\mathrm{S}$. Note that the atmosphere is huge, compared to the computational box, and that in its inner region ($500 r_\mathrm{S} < r \lessapprox 5000 r_\mathrm{S}$) the densities still exceed 10^{-10} g/cm^3. This will be relevant in Sect. 5.6.

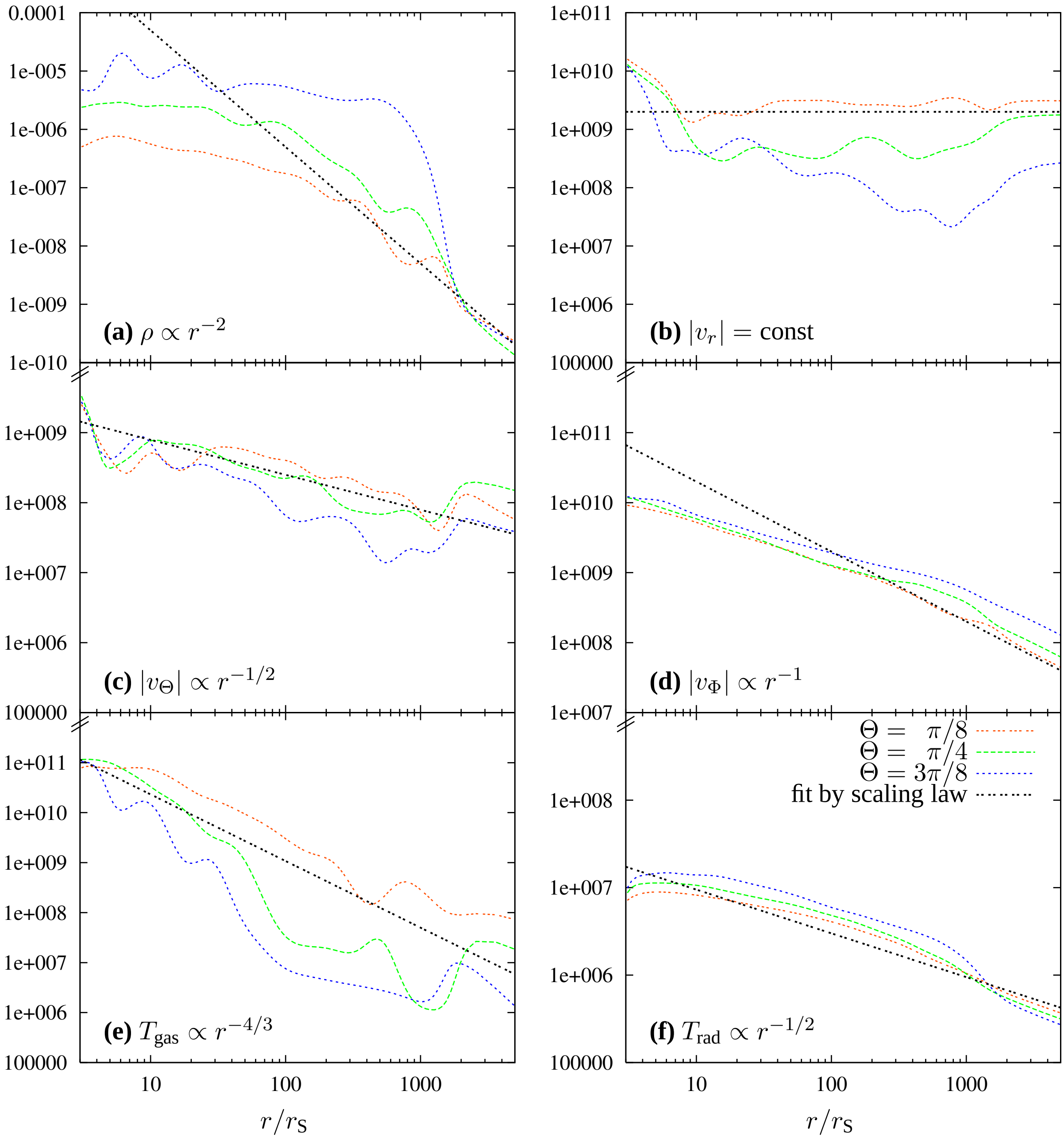

Figure 5.8. Radial profiles of the relevant physical quantities in the atmosphere and their corresponding fits. The colors correspond to different inclination angles. The fit is plotted in black.

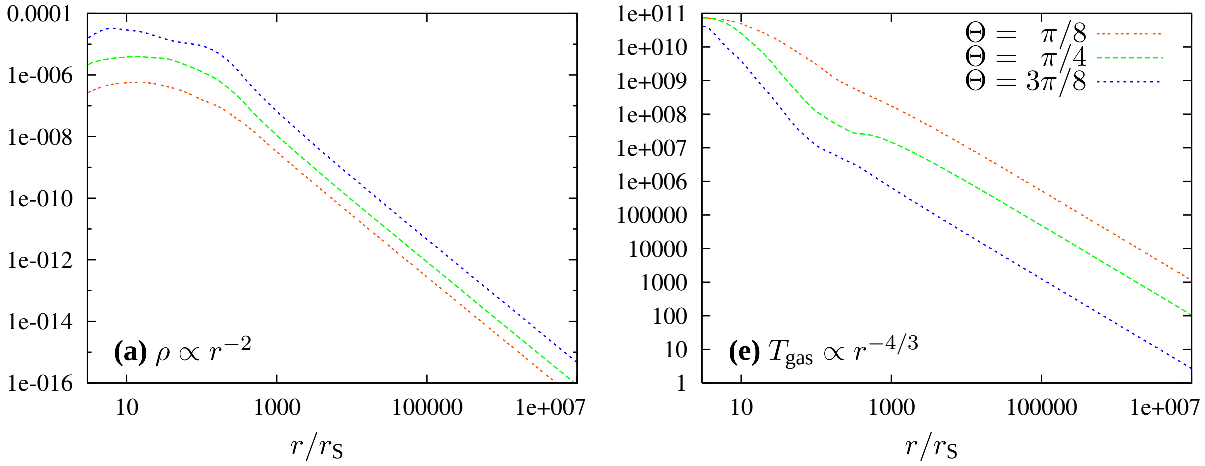

Figure 5.9. Radial profiles of the density and gas temperature in the computational box ($r \leq 500 r_\mathrm{S}$) and in the extended atmosphere. The colors correspond to different inclination angles.

5.5.3 Modification of the radiative transfer equation

Our model for the atmosphere is highly simplified. Therefore, we do not attempt to produce realistic continuum spectra by processing the emergent continuum radiation from the surface of the computational box through the atmosphere.

Also, the emitted intensity from continuum processes is derived by assuming blackbody emission for the radiation field and the gas. While this assumption is generally acceptable in the optical thick computational box, it is clearly not viable in an optical thin atmosphere. Moreover, in such an optical thin environment, the interaction between the radiation field and the gas weakens by definition and therefore radiation and matter decouple.

Hence, it is sufficient to investigate the effects of line emission and absorption on the emanating spectrum from the computational box and neglect all contributions from the continuum on the equation of radiative transfer (5.14). In the atmosphere, it therefore reduces to

$$(\vec{l} \cdot \vec{\nabla}) I_\nu = \left(\frac{\nu}{\nu_0}\right)^2 \cdot \left\{ j_{\nu_0}^{\mathrm{lines}} - \kappa_{\nu_0}^{\mathrm{lines}} I_{\nu_0} \right\} . \tag{5.54}$$

5.6 Results

5.6.1 Data sets

We calculate spectral energy distributions for five different sets of data. In the case of a stellar mass black hole with $M_\mathrm{c} = 10 M_\odot$, we investigate the influence of the accretion rate by considering the three cases $\dot{M} = \{300,1000,3000\} \dot{M}_\mathrm{E}$. Additionally, we analyze the effect of the central black hole mass for the IMBH case, $M_\mathrm{c} = 10^4 M_\odot$, and the SMBH case, $M_\mathrm{c} = 10^8 M_\odot$.

As a general warning, we want to outline that the RHD simulations by Ohsuga et al. (2005) and Ohsuga (2007) were designed for the case of a stellar mass black hole, focussing on the influence of super-Eddington accretion through a disk-like structure. Therefore, the resulting simulation data for the IMBH and the SMBH cases have to be treated very carefully. Their temperatures and densities lie in ranges for which the RHD code has not been designed and for which additional physical processes such as cooling terms are important. We regard the results for the higher mass scenarios as guidelines for how the general picture changes and not as resilient statements.

In our previous investigation, we intensively discussed the ULX case where $M_\mathrm{c} = 10 M_\odot$, $\dot{M} = 10^3 \dot{M}_\mathrm{E}$, thereby concentrating on the overall continuum features. Keeping in mind the importance of the inclination angle on the continuum emission, we concentrate on the iron K line features in the following. As before, the input simulation data is based on a spherical grid with azimuthal symmetry and a resolution of 96 radial and zenithal grid points in the range of $r = [3; 500] r_\mathrm{S}$ and $\Theta = [0; \pi/2]$. The data is taken from the most recent RHD simulations (Ohsuga (2007) and Ohsuga, priv. comm.), but the basic properties and the physics remain unchanged from the previous version (Ohsuga et al., 2005). The simulation data is time averaged, meaning that once the simulation reaches a quasi-steady state, the data is smoothed over a few steps to reduce the numerical fluctuations. For a detailed discussion of the recent RHD simulations, we refer the reader to Ohsuga (2007). Nevertheless, we want to note that a quasi-steady state of the simulation data could only be obtained for accretion rates in the above given range. For lower values of $\dot{M}$, limit cycle oscillations set in, preventing the formation of a quasi-steady disk state.

For a better understanding of the resulting spectra, we compare the physical key quantities ρ, T_rad, T_gas, v_r, for the different data sets. We infer empirical scaling laws for varying central masses and accretion rates separately. These scaling laws in general do not reflect a physical mechanism, but give a rough idea on how densities and temperatures evolve in the M_c-$\dot{M}$ parameter space. The comparison is done by relating the values at every grid point to the reference data set with $M_\mathrm{c} = 10 M_\odot$ and $\dot{M} = 10^3 \dot{M}_\mathrm{E}$ and by taking the arithmetic mean afterwards. The results shown in Fig. 5.10 let us derive the following relations:

$$\begin{aligned}
\rho(\dot{M}) &\propto \dot{M}\,, & \rho(M_\mathrm{c}) &\propto M_\mathrm{c}^{-1}\,,\\
T_\mathrm{rad}(\dot{M}) &\propto \dot{M}^{1/5}\,, & T_\mathrm{rad}(M_\mathrm{c}) &\propto M_\mathrm{c}^{-1/4}\,,\\
T_\mathrm{gas}(\dot{M}) &\propto \dot{M}^{-1/10}\,, & T_\mathrm{gas}(M_\mathrm{c}) &= \mathrm{const}\,,\\
v_r(\dot{M}) &\propto \dot{M}^{-2/3}\,, & v_r(M_\mathrm{c}) &\propto M_\mathrm{c}^{2/30}\,.
\end{aligned} \tag{5.55}$$

The scaling law for the mass density fits nicely with our expectations (the higher the accretion rate, the more material is in the disk and its surroundings) and the standard accretion disk solution, where $\rho \propto M_\mathrm{c}^{-1}$. As in the previous investigation of convective accretion disks (Chapt. 3), the radiation temperature increases with the accretion rate (the more material that is accreted, the higher the amount of gravitational energy which is released). The radiation temperature decreases with the central mass due to the scaling of the Schwarzschild radius r_S with M_c (see also Sect. 3.6).

The reaction of the gas temperature on $\dot{M}$ and M_c depends on the scaling of the gas energy density e and the mass density ρ. If, in the simplest case, the gas energy density scaled like the radiation energy density, the gas temperature would scale with $\dot{M}^{-1/5}$ and should be independent of the central mass. The actual scaling laws show a slightly flatter decrease with $\dot{M}$ and a roughly constant behavior with M_c. In reality, however, one would expect that the gas temperature decreases with the central mass as well. As mentioned above, the original RHD code was not designed for the case of higher central masses, meaning that important physical mechanisms are not included. With the strong decrease of $\rho \propto M_\mathrm{c}^{-1}$, the coupling between matter and radiation gets very weak and the gas cannot be cooled any more.

Finally, we discuss the dependency of the radial velocity on $\dot{M}$ and M_c. Given that the material in the disk and its surroundings is denser for higher accretion rates, the outflow is obstructed. The same mechanism acts vice versa in the case of higher central masses.

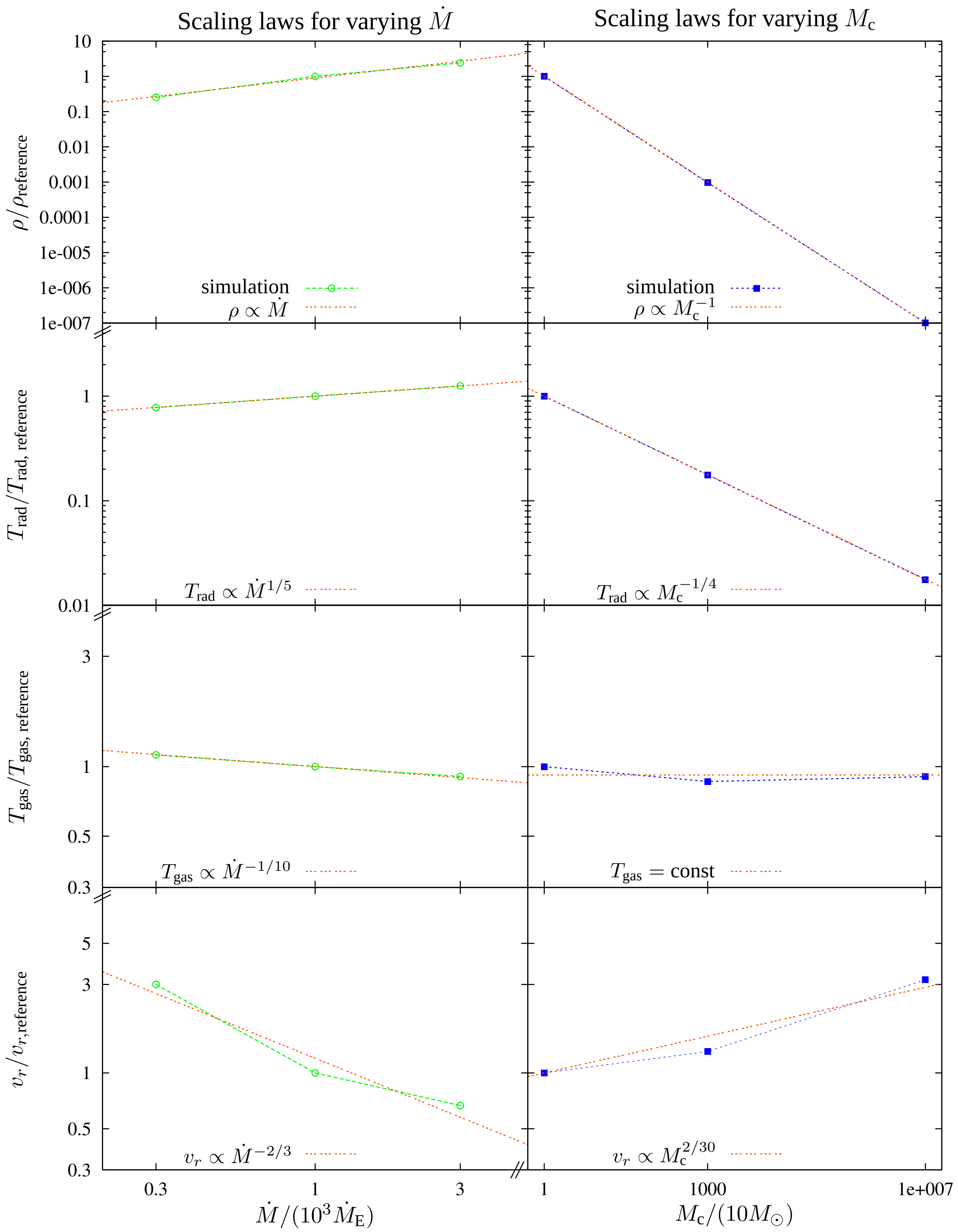

Figure 5.10. Empirical scaling laws for varying accretion rates and central masses. The averaged values are derived by relating the physical values at each grid point and taking the average afterwards. These scaling laws are purely empirical and do not necessarily reflect any physical mechanism.

5.6.2 Spectra

We present the spectra of the five different sets of simulation data in Figs. 5.11–5.16. Additionally, in Table 5.5(a), we summarize the iron K line features at the boundary of the computational box (i. e., before processing the spectrum through the atmosphere) for the individual data sets: the peak intensities of the individual contributors to the K_α and K_β emission lines relative to the continuum are given, as well as their ratios to each other. We also list the equivalent widths of the integrated K_α and K_β lines. Key results are highlighted in red. In Table 5.5(b), we detail the equivalent widths of the resulting absorption lines outside the atmosphere. We do not list their individual peaks, nor do we investigate the emission lines here. We believe – and also find from our results – that our simplified atmosphere does not allow us to draw resilient conclusions on the emission line features.

Table 5.5(c) gives the integrated quantities bolometric luminosity L_{tot}, photon number density $n_{\gamma,\mathrm{tot}}$ and average photon energy $\langle h\nu \rangle$ for the five data sets. The photon number density is calculated as in (4.25). Those values are taken from the boundary of the computational box without considering the atmosphere. Key results are highlighted in blue. Before we investigate the individual spectra, it is worth having a look at those overall quantities: from the stellar mass black hole cases, we can nicely examine the dependencies of the total luminosity.

- For a given inclination angle, the luminosity increases with the accretion rate. The increase in luminosity is roughly proportional to $\log \dot{M}$, as predicted in Watarai et al. (2000); Fukue (2004) for highly super-Eddington disks.
- For a given accretion rate, the luminosity is higher for lower inclination angles, confirming our previous results (Sect. 4.3).

The photon number density and the average photon energy follow the same trend as the luminosity. These nice agreements disappear when looking at the higher black hole mass data: empirically, one would assume that the luminosity of a super-Eddington accretion disk scales with the central black hole mass if the Eddington ratio is unchanged, since $L \propto L_{\mathrm{E}} \propto M_{\mathrm{c}}$ (Fukue, 2004). While this assumption holds for the IMBH case, it breaks down for the SMBH case, where $L_{\mathrm{total}}(10^8 M_\odot) \approx 10^{10} L_{\mathrm{total}}(10 M_\odot)$. Thus, the overall luminosity is higher than expected by a factor of 1000. An equal disagreement can be found for the photon number density and the average photon energy. Thus, we repeat our warning that the high mass data set may be far from a realistic scenario for a SMBH accretion disk, especially considering the constancy of the gas temperature.

Standard setup We start our analysis with the standard case of a stellar mass black hole, $M_{\mathrm{c}} = 10 M_\odot$, and an accretion rate of $10^3 \dot{M}_{\mathrm{E}}$. The spectrum is shown in Fig. 5.11. The upper panels display the overall spectrum at the boundary of the computational box (i. e., inside the atmosphere) for a photon energy range of $[10^{-2}; 10^2]$ keV, corresponding to frequencies of $[2 \cdot 10^{15}; 2 \cdot 10^{19}]$ Hz. The orientation of the observer is taken to be almost face-on ($\Theta = \pi/8$) for the panels on the left, and almost edge-on ($\Theta = 3\pi/8$) for the panels on the right, respectively. In black, we plot a reference spectrum, given by a blackbody emitter with $T_{\mathrm{bb}} = 1.3 \cdot 10^6$ K, altered by a spectral hardening factor $\varepsilon = 1.2$ (compare to (4.26)). The peak intensity in the face-on case is fitted quite well by the reference spectrum, while there exists a clear X-ray excess for higher photon energies.

Table 5.5. Ratios of the emission line strength (i. e., peak intensity) relative to the continuum for the fully resolved lines. $\mathcal{E}_{\alpha/\beta,\mathrm{I}}$: low velocity emission from Fe I–XXIII; $\mathcal{E}_{\alpha/\beta,\mathrm{II}}$: high velocity emission from Fe I–XXVI. The equivalent widths (EW) for the integrated K_α and K_β lines are given in keV, where positive values correspond to absorption lines and negative values to emission lines, respectively. **(a)** at the boundary of the computational box; **(b)** outside the atmosphere; **(c)** total/mean values at the boundary of the comp. box. Key quantities are highlighted in red and blue.

(a) at the boundary of the computational box

Data set	Θ	$\mathcal{E}_{\alpha,\mathrm{I}}$	$\mathcal{E}_{\alpha,\mathrm{II}}$	$\mathcal{E}_{\beta,\mathrm{I}}$	$\mathcal{E}_{\beta,\mathrm{II}}$	$\mathcal{E}_{\alpha,\mathrm{I}}/\mathcal{E}_{\alpha,\mathrm{II}}$	$\mathcal{E}_{\beta,\mathrm{I}}/\mathcal{E}_{\beta,\mathrm{II}}$	$\mathcal{E}_\beta/\mathcal{E}_\alpha$	EW K_α	EW K_β	EW K_β/EW K_α
$10M_\odot, 3\cdot10^2\dot{M}_\mathrm{E}$	$\pi/8$	61	1105	12	195	0.055	0.061	0.18	-166	-35.0	0.211
	$3\pi/8$	94	875	29	115	0.11	0.25	0.13	-211	-23.9	0.113
$10M_\odot, 1\cdot10^3\dot{M}_\mathrm{E}$	$\pi/8$	47	1825	6.0	220	0.026	0.027	0.12	-314	-38.6	0.123
	$3\pi/8$	140	2875	8.4	338	0.049	0.025	0.12	-696	-74.8	0.107
$10M_\odot, 3\cdot10^3\dot{M}_\mathrm{E}$	$\pi/8$	95	1740	11	210	0.055	0.052	0.12	-383	-51.4	0.134
	$3\pi/8$	695	4260	98	492	0.16	0.20	0.12	-1120	-117	0.104
$10^4M_\odot, 1\cdot10^3\dot{M}_\mathrm{E}$	$\pi/8$	607	14430	27	808	0.042	0.033	0.056	-2260	-134	0.059
	$3\pi/8$	358	19579	22	1147	0.018	0.019	0.059	-4300	-253	0.059
$10^8M_\odot, 1\cdot10^3\dot{M}_\mathrm{E}$	$\pi/8$	10426	168100	46	3722	0.062	0.012	0.022	-28600	-549	0.019
	$3\pi/8$	45520	286500	63	5310	0.159	0.010	0.019	-76600	-1250	0.016

(b) outside the atmosphere

Data set	Θ	EW K_α	EW K_β	EW K_β/EW K_α
$10M_\odot, 3\cdot10^2\dot{M}_\mathrm{E}$	$\pi/8$	$+0.034$	$+0.106$	3.12
	$3\pi/8$	$+0.032$	$+0.099$	3.09
$10M_\odot, 1\cdot10^3\dot{M}_\mathrm{E}$	$\pi/8$	$+0.167$	$+0.074$	0.44
	$3\pi/8$	$+0.080$	$+0.063$	0.79
$10M_\odot, 3\cdot10^3\dot{M}_\mathrm{E}$	$\pi/8$	$+0.258$	$+0.111$	0.43
	$3\pi/8$	$+0.131$	$+0.137$	1.05
$10^4M_\odot, 1\cdot10^3\dot{M}_\mathrm{E}$	$\pi/8$	$+0.068$	$+0.127$	0.54
	$3\pi/8$	$+0.162$	0.115	0.71
$10^8M_\odot, 1\cdot10^3\dot{M}_\mathrm{E}$	$\pi/8$	$+0.070$	$+0.099$	1.18
	$3\pi/8$	$+0.344$	$+0.291$	0.71

(c) total/mean quantities at the boundary of the comp. box

Dataset	Θ	L_tot [erg/s]	$n_{\gamma,\mathrm{tot}}$ [1/(cm s)]	$\langle h\nu\rangle$ [eV/cm^2]
$10M_\odot, 3\cdot10^2\dot{M}_\mathrm{E}$	$\pi/8$	4.36E+39	7.16E+38	0.42
	$3\pi/8$	1.23E+39	3.02E+38	0.28
$10M_\odot, 1\cdot10^3\dot{M}_\mathrm{E}$	$\pi/8$	5.50E+39	8.52E+38	0.45
	$3\pi/8$	1.47E+39	3.56E+38	0.29
$10M_\odot, 3\cdot10^3\dot{M}_\mathrm{E}$	$\pi/8$	7.07E+39	1.00E+39	0.49
	$3\pi/8$	2.01E+39	4.56E+38	0.31
$10^4M_\odot, 1\cdot10^3\dot{M}_\mathrm{E}$	$\pi/8$	5.55E+42	4.78E+42	0.081
	$3\pi/8$	1.63E+42	2.06E+42	0.055
$10^8M_\odot, 1\cdot10^3\dot{M}_\mathrm{E}$	$\pi/8$	6.26E+49	3.14E+49	0.14
	$3\pi/8$	9.50E+49	5.04E+49	0.13

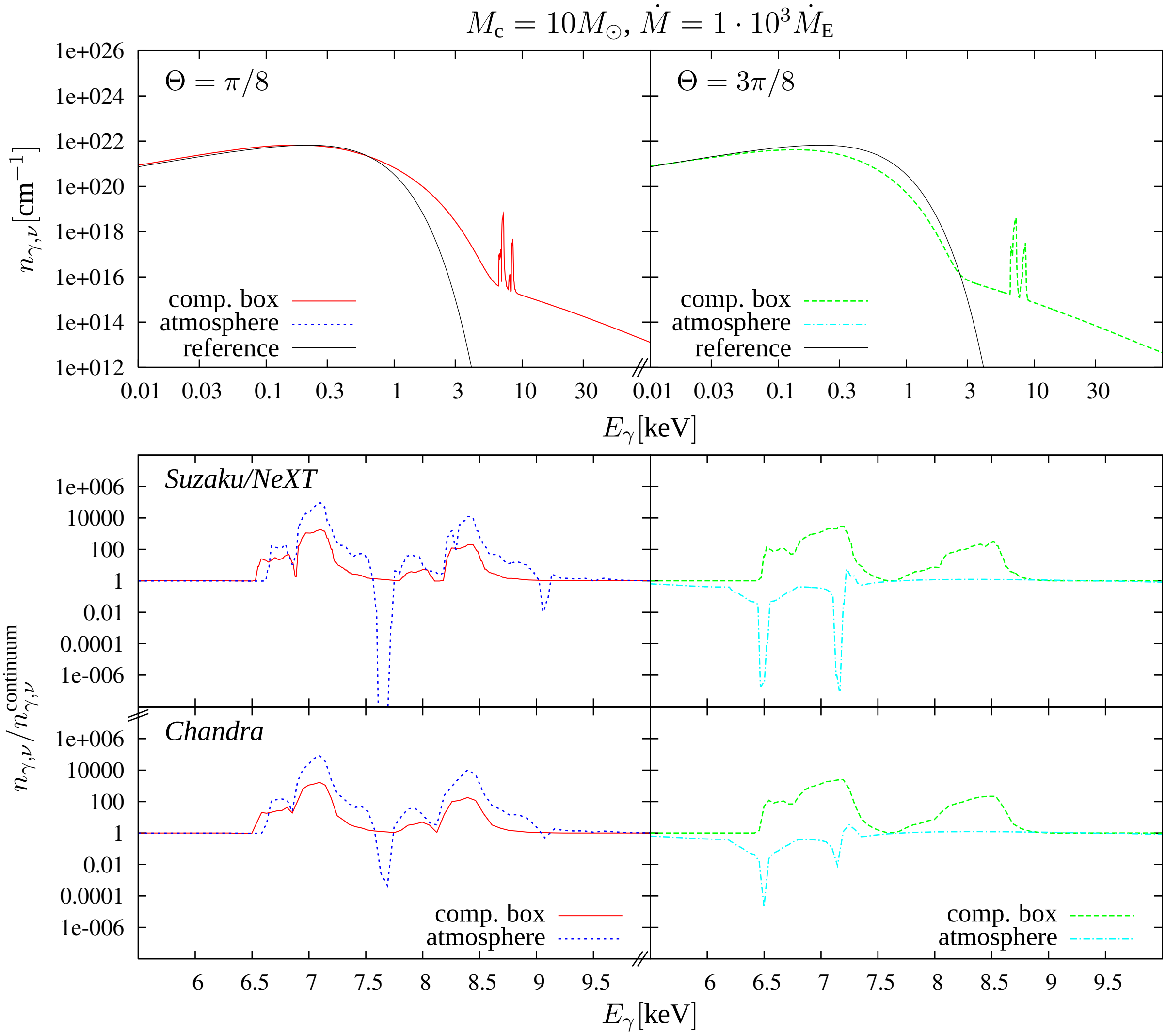

Figure 5.11. Emerging spectrum for $M_\mathrm{c} = 10M_\odot$ and $\dot{M} = 1 \cdot 10^3 \dot{M}_\mathrm{E}$ and inclination angles $\Theta = \pi/8$ (face-on view, left) and $\Theta = 3\pi/8$ (edge-on view, right). Upper panels: emanating photon number density for continuum and lines at the boundary of the computational box; lower panels: ratio of line emission relative to the continuum at the boundary of the computational box and after processing the lines through the atmosphere as seen by *Suzaku*/*NeXT* and *Chandra*. Please note that we do not consider photon count errors (i. e., fluctuations due to the limited number of X-ray photons observed by the instrument).

The first detail we notice is that the line shapes are very different for the two orientations. For high inclinations, the lines are broader, their widths are reduced for lower inclinations.

The *typical* line of sight velocities of the gas in the outer region of the computational box (and thereby in the atmosphere, since $v_{r,\mathrm{atm}} = \mathrm{const}$) are $0.1c$ in the face-on case and $0.01c$ in the edge-on case. This corresponds to Doppler shifts and line energies in the face-on case of:

$$\left.\begin{array}{lllllll}\Delta\nu_{\mathrm{min},\alpha} & = & 0.64\,\mathrm{keV} & \nu_{\mathrm{min},\alpha} & = & 7.0\,\mathrm{keV} & \mathrm{Fe\,I\,K_\alpha} \\ \Delta\nu_{\mathrm{max},\alpha} & = & 0.70\,\mathrm{keV} & \nu_{\mathrm{max},\alpha} & = & 7.7\,\mathrm{keV} & \mathrm{Fe\,XXVI\,K_\alpha} \\ \Delta\nu_{\mathrm{min},\beta} & = & 0.73\,\mathrm{keV} & \nu_{\mathrm{min},\beta} & = & 7.8\,\mathrm{keV} & \mathrm{Fe\,I\,K_\beta} \\ \Delta\nu_{\mathrm{max},\beta} & = & 0.83\,\mathrm{keV} & \nu_{\mathrm{max},\beta} & = & 9.1\,\mathrm{keV} & \mathrm{Fe\,XXVI\,K_\beta}\end{array}\right\} \text{(face-on case)}$$

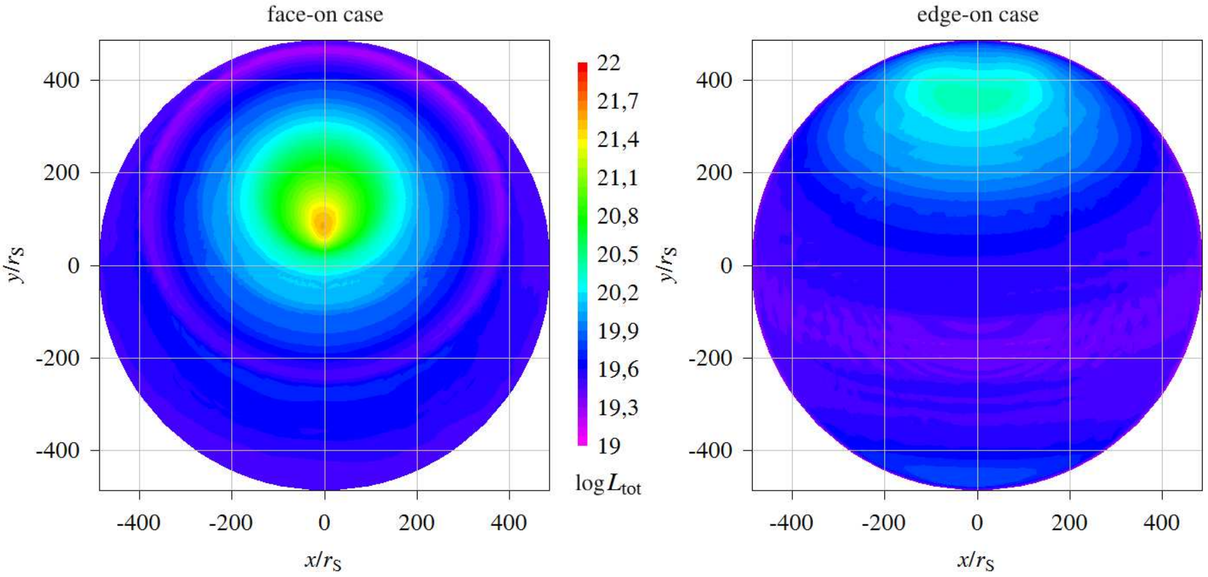

Figure 5.12. Map of the emerging luminosity $\log L_{\mathrm{tot}}[\mathrm{erg/s}]$ at the boundary of the computational box, seen by an observer at inclinations $\pi/8$ (left) and $3\pi/8$ (right) for the standard data with $M_{\mathrm{c}} = 10M_{\odot}$, $\dot{M} = 10^3\dot{M}_{\mathrm{E}}$. x and y denote the coordinates on the projected surface, and r_{S} the Schwarzschild radius.

The line of sight velocities vary for different positions on the projected surface, thereby reaching maximum values of $0.25c$ in the face-on case. From the temperature and velocity distribution in Fig. 4.1 and the projected surface shown in Fig. 5.12 for both inclinations, we conclude that these extreme velocity and high temperature regions occupy only a very small area.

The second important detail to note is the extreme strength of the emission lines and the complete lack of absorption. This becomes even more evident when looking at the lower panels of Fig. 5.11, where we divide the emanating photon number density by the corresponding continuum. In order to account for the limited instrumental resolution, we convolve the emerging lines with the resolutions of *Chandra* and *Suzaku*. The former one, launched in 1999, provides the *Chandra High Energy Transmission Grating (HETG) spectrometer* with an energy resolution of $E/\Delta E = 1000$ at $E = 1\,\mathrm{keV}$, decreasing to $E/\Delta E = 100$ at $E = 10\,\mathrm{keV}$. For details about *Chandra* and the *HETG*, we refer the reader to the excellent review and summary by Canizares et al. (2005). From Canizares et al. (2005, Fig. 30), we find that the resolution curve can be approximated as

$$\Delta E_{\mathit{Chandra}} = 10^{-3+2\log(E\,[\mathrm{keV}]/1\,\mathrm{keV})} = 10^{-3}\dots10^{-1}\,\mathrm{keV}\,, \qquad E = [1;10]\,\mathrm{keV}\,.$$

The Japanese X-ray satellite *Suzaku*, launched in 2005, was originally equipped with the *XRS*, a high-resolution X-ray spectrometer. The *XRS* used an array of X-ray micro-calorimeters and foil mirrors to achieve an unprecedented combination of high resolution and large collecting area (ISAS, 2005): its energy resolution was as low as $7\,\mathrm{eV}$ throughout the range $[0.3;12]\,\mathrm{keV}$ (Kelley et al., 2007). For the line widths of our simulation data, *Suzaku* therefore would have been able to provide a full resolution of the spectral features. Unfortunately, due to a leak in the cooling system, *Suzaku* lost the use of its primary instrument shortly after launch (August 7, 2005). Nevertheless, a similar instrument is planned to be on board the Japanese follow-up mission *NeXT* (*New X-ray Telescope*), which will be launched in 2011.

Leaving aside the instrumental influence for the moment, we first concentrate on the appearance of the lines for different inclinations and on the influence of the atmosphere. Comparing the fully resolved lines at the boundary of the computational box in the left and in the right figure, two peaks can be identified for both inclination angles and both the K_α and the K_β line.

Face-on view: the lower peak ($=: \mathcal{E}_{\alpha/\beta,\mathrm{I}}$) corresponds to slightly blueshifted ($v/c \approx 0.02$) line emission from Fe I–Fe XXIII. The higher peak ($=: \mathcal{E}_{\alpha/\beta,\mathrm{II}}$) is produced by stronger blueshifted emission ($v/c \approx 0.08$) from the same ionization degrees, but with a small contribution of helium- and hydrogen-like iron. The ratios of their relative strengths and the corresponding equivalent widths of the K_α and K_β lines are listed in Table 5.5. We find that $\mathcal{E}_{\alpha,\mathrm{I}}/\mathcal{E}_{\alpha,\mathrm{II}} \approx \mathcal{E}_{\beta,\mathrm{I}}/\mathcal{E}_{\beta,\mathrm{II}}$, suggesting that the temperatures in the low and high velocity outflows are not too different.

Edge-on view: in this case, it is harder to distinguish the two peaks, especially for the K_β lines. However, we still find contributions from a low velocity outflow ($\mathcal{E}_{\alpha/\beta,\mathrm{I}}$) and a broad line from the high velocity outflow ($\mathcal{E}_{\alpha/\beta,\mathrm{II}}$) with about the same Doppler shifts as in the face-on case. The strength of $\mathcal{E}_{\alpha,\mathrm{I}}$ is increased relatively to the other lines. This is due to the lower temperatures in the edge-on case, where fluorescence effects set in and increase the K_α emission from low ionization degrees.

Interestingly, the peak ratio of the K_β line to the K_α line is the same for both inclinations, but the equivalent widths are twice as large for the edge-on case. The absolute values of the equivalent widths are very large and exceed any line widths that have been observed previously. Because of this, and because we do not see any sign of absorption at the boundary of the computational box, we conclude that the simulation box is truncated at too small radii.

The similarity in the line emission for both inclinations, especially the mean outflow velocities, strengthen our conclusion that the emission is dominated by the hot material in and around the disk. Since the disk is cut artificially by the boundary of the computational box, it shows high gas temperatures even close to the disk plane. Therefore, let us now inspect the influence of the atmosphere on the lines.

In the face-on case, we find an increase in the emitted lines for all four peaks. Additionally, we see a broadening of the ($\mathcal{E}_{\alpha/\beta,\mathrm{II}}$) emission lines towards higher photon energies. The most interesting feature, however, is the appearance of two strong dips. They are caused by absorption of the highest ionization degrees of iron in the violent outflow pointing towards the observer ($v/c \approx 0.1$ on average). The broadening of these absorption lines is due to varying outflow velocities on the projected surface and to the combined contribution of Fe XXIV–XXVI. Why do we see absorption features only from the highest ionization degrees? The answer is simple: with decreasing temperatures, the ionization degree of iron drops, changing the emission signatures from helium- and hydrogen-like iron into absorption while Fe I–Fe XXIII can still be seen in emission.[3] As temperatures and densities drop further, absorption and emission due to collisional excitation is outclassed by fluorescence line emission, which itself is only efficient up to Fe XXI (see Sect. 5.4.6).

In the edge-on case, the emission lines disappear completely. We only find two deep absorption features, caused by Fe I–V. The outflow velocities are lower and more turbulent (c. f., Figs. 4.1,5.8) than in the face-on case, so that no Doppler shifts can be detected. For both the

---

[3] The ionization energy of Fe XXIII is only $2\,\mathrm{keV}$, while Fe XXIV has an ionization threshold of $8.8\,\mathrm{keV}$.

face-on and the edge-on case, we list the absorption line equivalent widths in Table 5.5. They are much more reasonable than those of the emission lines. This is mainly due to the definition of the equivalent width,

$$\mathrm{EW} = \int \frac{F_{\text{cont}} - F_{E_\gamma}}{F_{\text{cont}}} dE_\gamma \, . \tag{5.56}$$

We exclude the emission lines in the atmosphere from further discussion, because they are dominated by fluorescence emission, which itself depends heavily on the model of the underlying radiation field (c. f., (5.35)). The ratio of the K_β to the K_α equivalent width is only slightly exceeding 10% in the computational box for the emission lines, but increased to 40%–80% in the atmosphere for the absorption lines.

Influence of the accretion rate After this comprehensive analysis of the standard simulation data, we briefly discuss the influence of varying accretion rates for the same central black hole mass. In Fig. 5.13, we plot the results for the case $\dot{M} = 3 \cdot 10^2 \dot{M}_\mathrm{E}$. The line strengths, line ratios and equivalent widths are listed in Table 5.5 as before.

From the blackbody reference, we find that the continuum spectrum does not change significantly compared to the $10^3 \dot{M}_\mathrm{E}$ case. Also the principal structure of the lines at the outer boundary of the computational box is retained. Compared to the standard case, the strength of the K_β emission lines is slightly increased relative to the K_α lines. This can be seen also in the ratio of the equivalent widths.[4] This reflects the higher gas temperatures for the $3 \cdot 10^2 \dot{M}_\mathrm{E}$ data. The Doppler shift of the emission lines is nearly unchanged, because the dependence of the mean radial velocity v_r on the accretion rate is weak.

The influence of the atmosphere is different than in the previous case, in particular for the face-on case. The emanating photon number density from the computational box remains almost unchanged for the emission lines, since the densities are lower. The absorption lines are also much weaker, but strongly blueshifted ($v/c \approx 0.17$). They show a very weak absorption feature from low ionization K_β fluorescence, additionally to the absorption lines from helium- and hydrogen-like iron seen previously. The same three absorption lines appear much stronger and without being Doppler shifted in the edge-on case. But here, the densities in the atmosphere are too low to completely cancel the emission lines, which leads to absorption features overlaid on emission lines, making it harder to disentangle the equivalent widths. While the EWs of the K_β lines are still smaller than those of the K_α lines in the computational box, this relation is inverted by the atmosphere. Let us consider the effect of the limited instrumental resolution in the case of *Chandra*. The strong and broad emission lines still can be resolved to full detail, but the narrow absorption dips are softened significantly and partly disappear.

In the next step, we discuss the high accretion rate case with $\dot{M} = 3 \cdot 10^3 \dot{M}_\mathrm{E}$, whose spectra are shown in Fig. 5.14. The first thing we note for the spectra at the boundary of the computational box is that the fully resolved spectral lines now show three peaks for the K_α lines in the face-on case. This is due to the increase in density in the computational box. Also the high temperature regions are dense enough to contribute to the line emission. Hence, the left and middle peaks represent the emission of the low velocity outflow. Also the high velocity outflow profits

---

[4] However, we believe that the equivalent width of the K_α line in the face-on calculation is overestimated. This might be due to the fact that the RHD simulations are just at the transition between quasi-steady disks for $\dot{M}_\mathrm{E} \geq 3 \cdot 10^2 \dot{M}_\mathrm{E}$ and limit cycle oscillations for lower values of $\dot{M}$, see Ohsuga (2007).

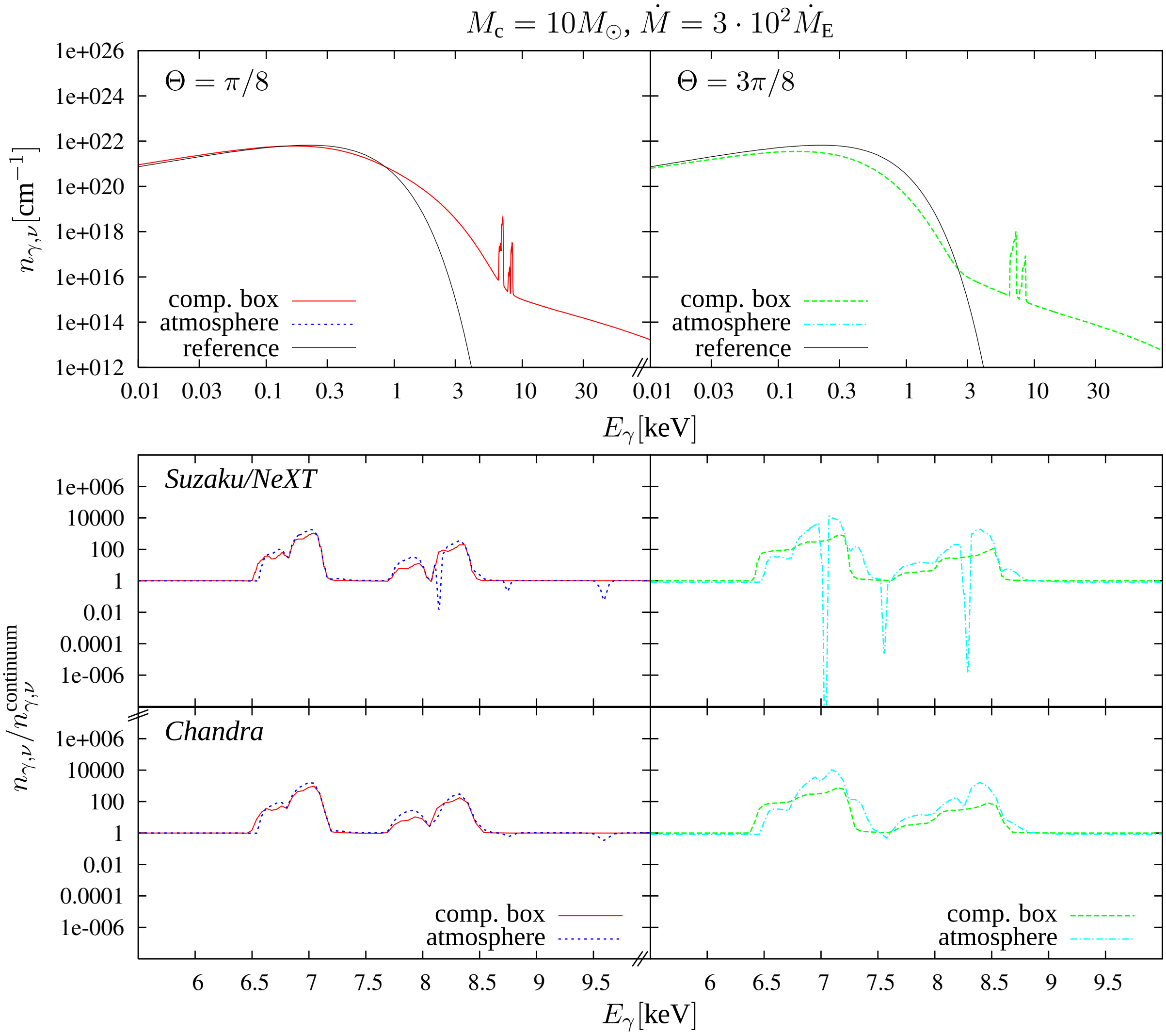

Figure 5.13. Same as Fig. 5.11, but for $M_c = 10M_\odot$ and $\dot{M} = 3 \cdot 10^2 \dot{M}_E$.

from that increase in temperature, showing a broader right wing from a stronger contribution of Fe XXV and Fe XXVI.

An overall increase of the lines relative to the continuum can be seen not only for the face-on case, but also for the edge-on case. Here, we find a strong mixture of the individual contributions to the K lines. The ratio of the peak strength from K_β to K_α is identical with the one from the standard case ($\dot{M} = 10^3 \dot{M}_E$). This is also true for the ratio of the equivalent widths.

Again, the atmosphere has a strong influence on the line features. In the face-on case, absorption from the highest ionization degrees of iron produces strong dips in the emission lines, which are significantly less blueshifted than in the standard setup ($v/c \approx 0.04$ compared to $v/c \approx 0.1$). The atmospheric emission lines are increased further with respect to the computational box values, showing an even broader wing towards higher energies. In the edge-on case, the density is now even higher than in the standard setup case. This causes a complete absorption of the emission lines from the inner regions. The velocities are comparable to the $10^3 \dot{M}_E$ case, so no Doppler shift can be seen in the absorption lines.

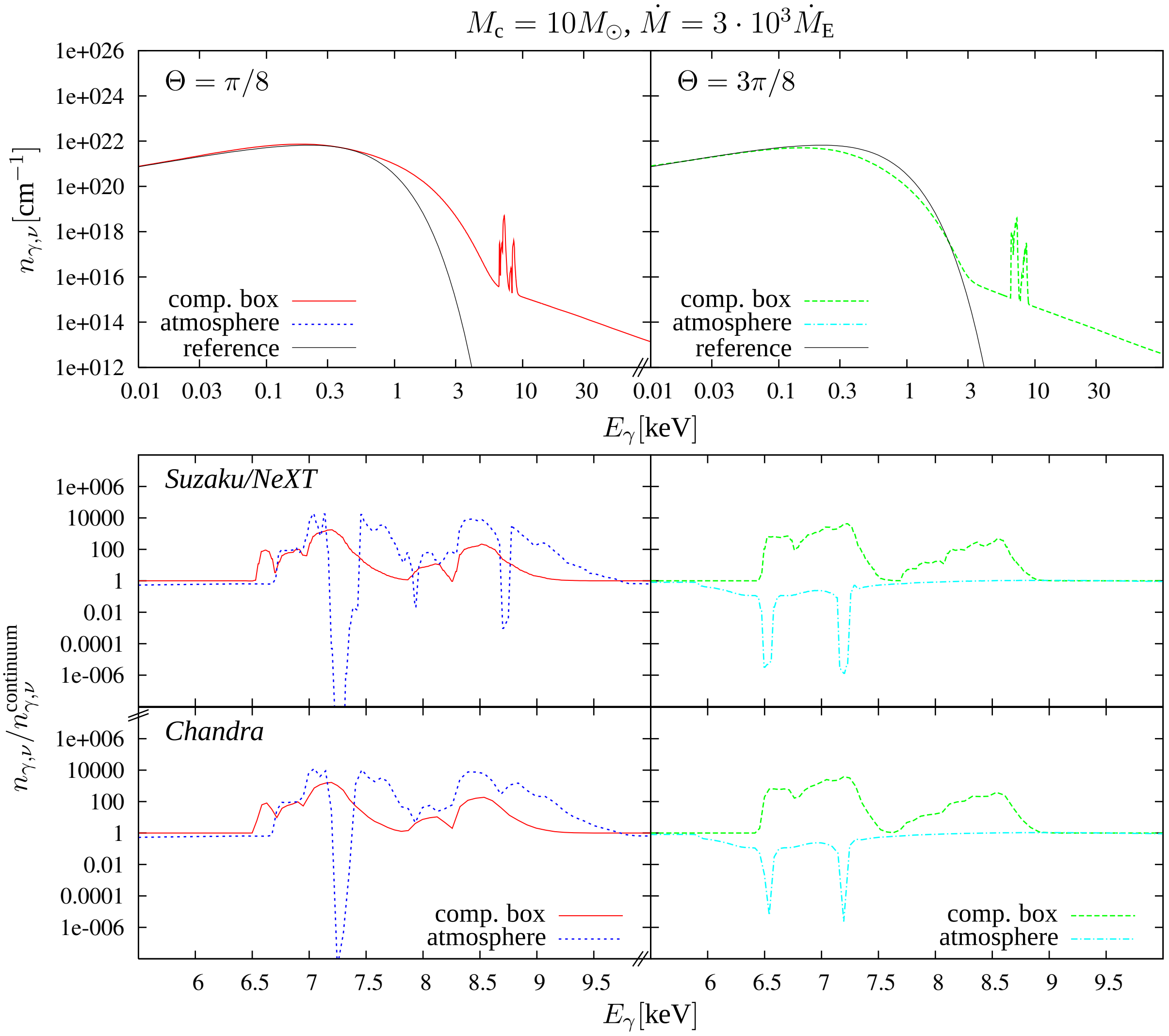

Figure 5.14. Same as Fig. 5.11, but for $M_c = 10M_\odot$ and $\dot{M} = 3 \cdot 10^3 \dot{M}_E$.

Varying central black hole masses We now investigate the influence of the central black hole mass M_c on the spectral energy distribution. We keep a constant Eddington ratio $\dot{M}/\dot{M}_E = 10^3$ and calculate the IMBH ($M_c = 10^4 M_\odot$) and SMBH ($M_c = 10^8 M_\odot$) cases.

The results of the radiative transfer calculations are presented in Table 5.5 and Figs. 5.15, 5.16. As discussed previously, the data must be treated very carefully, particularly in the SMBH case. In order to compare the reference spectrum from the stellar mass black hole case to these spectra, it needs to be increased by several orders of magnitude: we already discussed the increase in total luminosity, which should give a factor of 10^3 for the IMBH case, and 10^7 for the SMBH case, respectively. Given that we plot the curves for the photon number density rather than for the luminosity, an additional factor is necessary. Assuming that the mean photon energy is roughly determined by the temperature of the radiation field and taking into account the scaling law derived in Fig. 5.10, we find

$$n_{\gamma,\mathrm{tot}} \propto \frac{L_{\mathrm{tot}}}{\langle h\nu \rangle} \propto \frac{M_c}{M_c^{-1/4}} = M_c^{5/4}\,.$$

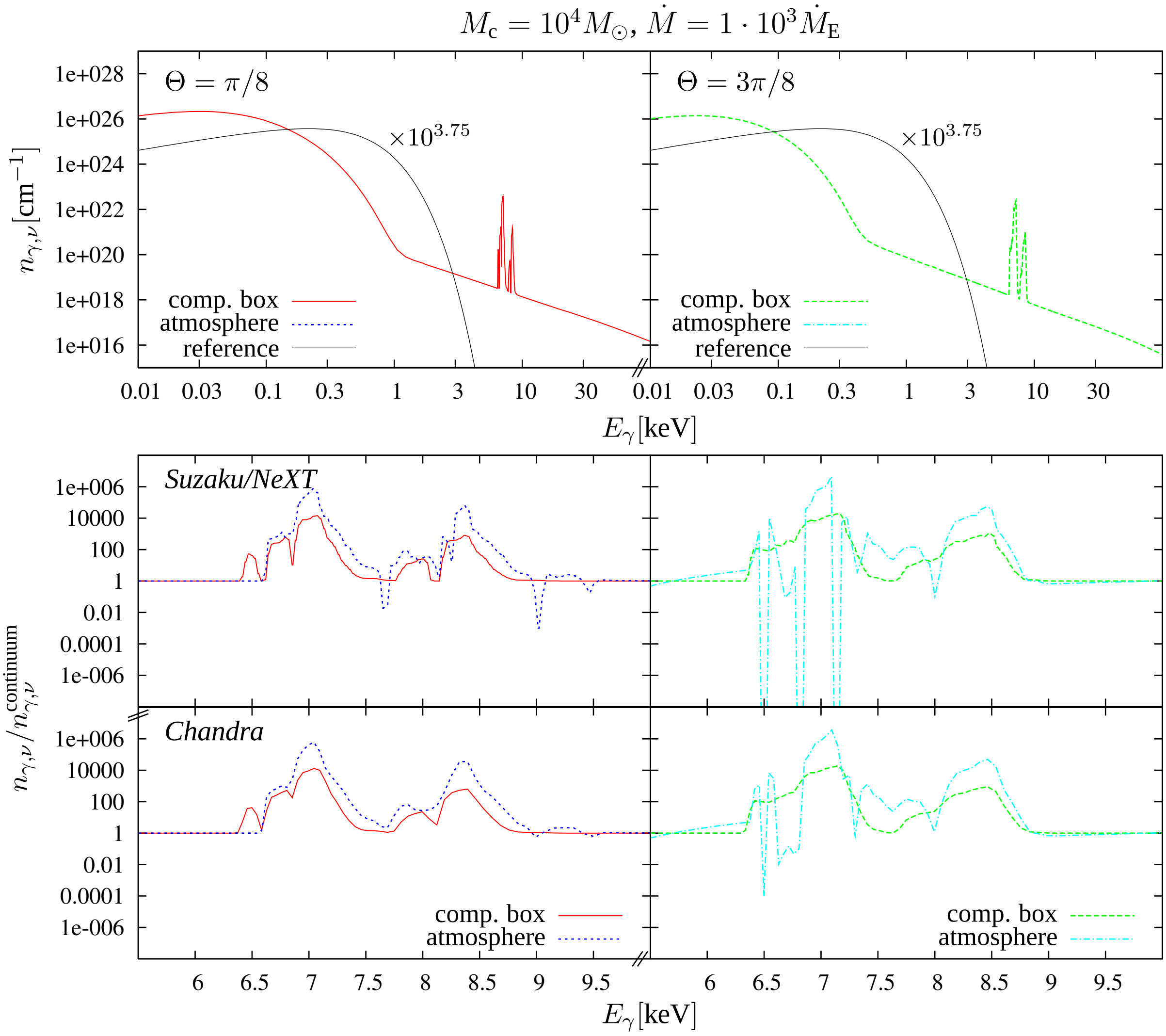

Figure 5.15. Same as Fig. 5.11, but for $M_c = 10^4 M_\odot$ and $\dot{M} = 1 \cdot 10^3 \dot{M}_E$.

We first analyze the IMBH case, displayed in Fig. 5.15. The upscaling of the reference spectrum leads to the correct order of photon number densities. From the high resolution plots of the iron K line region, we can see a further increase of the line strengths relative to the continuum at the boundary of the computational box, when compared to the stellar mass black hole case. Besides this overall increase, the shape and composition of the K_α and K_β lines do not change significantly with respect to the stellar mass cases. An interesting detail, however, is the fact that the low velocity peaks show a slightly redshifted (i. e., left) wing for both inclinations. At the same time, the position of the line centers do not change, compared to the previous results. But, since the density in the computational box decreases by a factor of 1000 on average, we can now see a small part of the material on the far side of the computational box, pointing away from the observer. The equivalent widths and peak ratios listed in Table 5.5 are unnaturally large, but they show that the K_β lines become significantly weaker in relation to the K_α lines. This reflects our expectations from the lower temperatures of the gas and the radiation field in the simulations.

The atmospheric modeling becomes definitely questionable for the IMBH case: the emission lines become even stronger for both inclination angles, overlaid by very narrow and strong

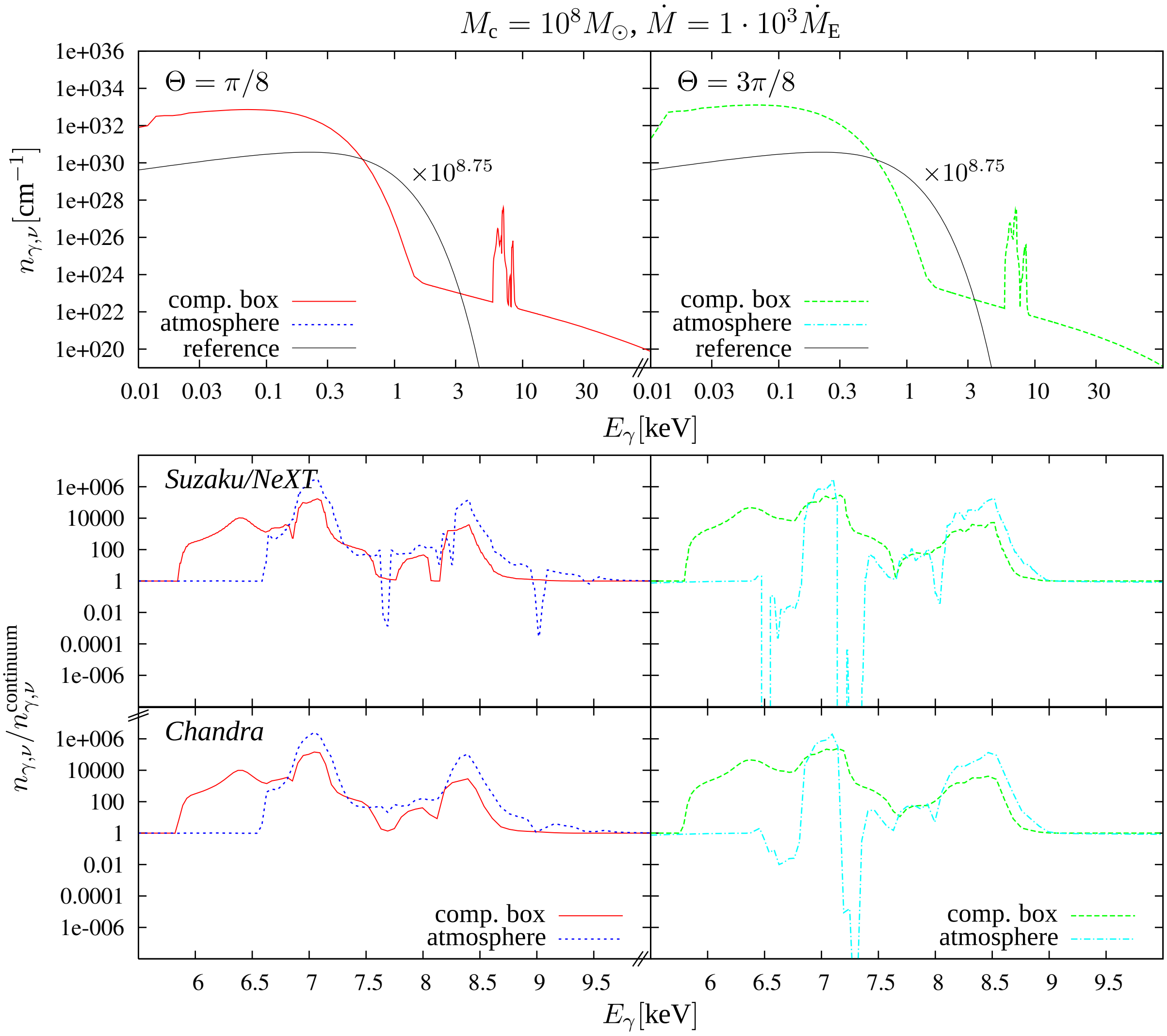

Figure 5.16. Same as Fig. 5.11, but for $M_c = 10^8 M_\odot$ and $\dot{M} = 1 \cdot 10^3 \dot{M}_E$.

absorption dips. However, the ratio of the equivalent widths of the K_β to the K_α line is in a reasonable range, suggesting that only the absolute scaling is off-beat. The influence of a limited instrumental resolution becomes crucial for such narrow and deep absorption lines, as can be seen clearly from the lower panels of Fig. 5.15.

Finally, we consider the SMBH case. The overestimation of the integrated luminosity and photon number density can be found again in the upper plots of Fig. 5.16: the reference spectrum, although amplified by $10^{8.75}$, is still two orders of magnitude too small. The iron lines are unacceptably strong, so that we definitely rule out the validity of this simulation data set. However, the decreasing trend of the equivalent width ratio EW K_β/EW K_α is continued for the spectra at the boundary of the computational box. The simplified model of the atmosphere breaks down completely, and so we omit a further analysis.

We conclude that the simulation data – but not the atmospheric model – for the IMBH case is still acceptable. At the same time, the SMBH data is definitely rejected. A proper investigation of such large scale accretion disk systems requires the consideration of different physical processes such as additional cooling terms. Also, a more accurate treatment of the radiative transfer calculations in both the 2D RHD simulations and our radiative transfer code are necessary (for a discussion of the weak points of the flux limited diffusion approximation used here, see Sect. 4.4).

Confrontation with reality – the case of M82 X-1 Finally, we want to compare our theoretical spectra with observational data. The situation is complicated by the fact that very few iron line detections have been made thus far for potential low mass ultraluminous X-ray sources. Contrary, a lot of observational data is available for highly accreting systems with large central black hole masses such as quasars and Seyfert galaxies. They show a large variety of line features, reaching from strong and broad emission lines to narrow absorption lines or significantly broadened absorption bands: for example, the type 2 Seyfert galaxy Mrk 3, observed with *XMM-Newton* by Bianchi et al. (2005), shows a prominent iron K emission line, while the *Suzaku* observation of the Seyfert 1.5 galaxy NGC 3516 shows a complex absorption feature, and both broad and narrow Fe K emission lines (Markowitz et al., 2008). The remarkable emission line of Mrk 3 has been shown in Figs. 5.2, 1.2.

As we concluded in the last section, our simulation data cannot be extended that easily to higher central masses. Thus, at present it is not possible to compare any of these observations with our theoretical spectra. We therefore concentrate on one of the very few observations of iron K line emission in low mass ULXs, M82 X-1. Particular interest has been paid to the starburst galaxy M82: Matsumoto et al. (2001) analyzed observational data taken with the *High-Resolution Camera* on board the *Chandra X-Ray Observatory* in 1999 and 2000 and detected nine X-ray sources in the central $1.1\,\mathrm{kpc} \times 1.1\,\mathrm{kpc}$ region, but not in the galactic center itself. Among them, M82 X-1 (source 7 in Matsumoto et al. (2001), see Fig 5.17), located about $170\,\mathrm{pc}$ off the dynamical center, is the brightest source with a bolometric luminosity of $L_{\mathrm{bol}} \approx (2.4\text{–}16) \cdot 10^{40}\mathrm{erg/s}$ (Patruno et al., 2006). First iron line detections have been reported by Strohmayer & Mushotzky (2003) from follow-up observations with the *European Photon Imaging Camera (EPIC)* on board *XMM-Newton* in 2001, who also detected a $54\,\mathrm{mHz}$ QPO behavior in M82 X-1. Since then, numerous investigations have been carried out based on this data, making M82 X-1 the prototype for the stellar-mass-black-hole-intermediate-mass-black-hole debate. Mass estimates are ranging from $1000 M_\odot$ (Fiorito & Titarchuk, 2004) down to $19 M_\odot$ (Okajima et al., 2006), all on solid physical basis, and yet no agreement could be found. In the following, we briefly present the analysis of Okajima et al. (2006) and refer the reader to the comprising literature (e. g., Strohmayer & Mushotzky (2003); Fiorito & Titarchuk (2004); Agrawal & Misra (2006); Dewangan et al. (2006); Okajima et al. (2006); Patruno et al. (2006)) for a more detailed discussion.

Okajima et al. (2006) analyzed archival *XMM-Newton* data of M82 X-1 when it was in the steady/low state (April 2001). Applying a “p-free” disk model (p in $T(r) \propto r^{-p}$, Mineshige et al. (1994); Kubota et al. (2006) and references therein), they found $p = 0.61^{+0.03}_{-0.02}$ and concluded that M82 X-1 is in an intermediate thin disk–slim disk state. Thus, energy is transported through the disk partly by advection and the disk flow is radiatively inefficient. From that, they estimated the central black hole mass to be $19\text{–}32 M_\odot$, accreting at $320\text{–}560 \dot{M}_{\mathrm{E}}$ and shining at $4\text{–}6$ times the Eddington luminosity. In the following, we will test their hypothesis with our numerical computations.

Before we start fitting the observed spectrum with our models, we must address another detail. It has been shown (Ohsuga et al., 2002) that the slim disk model does not properly account for

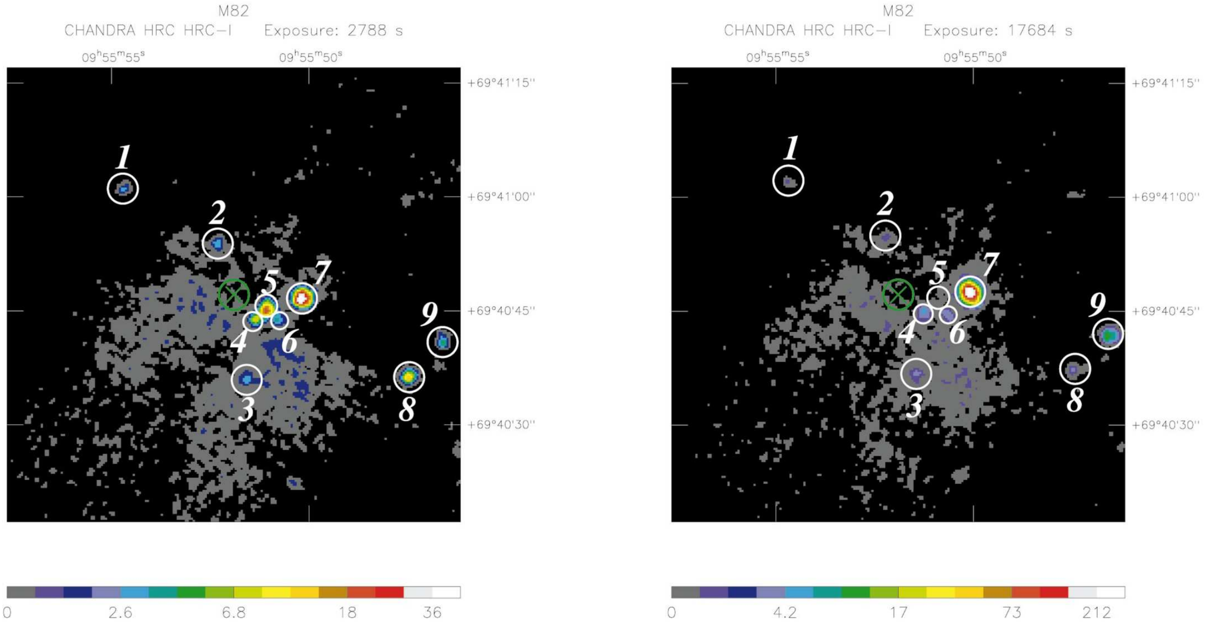

Figure 5.17. Central 1.1 kpc $\times$ 1.1 kpc region of M82; *Chandra* observations from 1999 (left) and 2000 (right). The radio kinematic center is marked with a green cross, M82 X-1 corresponds to source 7. The color scale shows the total counts per pixel. Figure taken from Matsumoto et al. (2001).

the photon trapping effects which occur in the central region of a highly accreting black hole disk. By that effect, high energetic photons from the midplane of the disk are swallowed by the black hole before being able to escape through the optically thick disk. While the 2D RHD simulations by Ohsuga et al. (2005); Ohsuga (2007) incorporate this effect explicitly, Okajima et al. (2006) based their investigation on the standard slim disk model. For an accretion rate of $10^2 - 10^3 \dot{M}_\mathrm{E}$, the slim disk model overestimates the disk luminosity by a factor of 2–3 (Ohsuga et al., 2002, Fig. 1), which means that we should base our computation on an accretion rate of about $1000 \dot{M}_\mathrm{E}$.

From our experiences so far, the resulting luminosities from the simulation data depend on the inclination angle between the disk's rotation axis and the observer. The Eddington luminosity is given as $L_\mathrm{E} = (M_\mathrm{c}/M_\odot) \cdot 1.2 \cdot 10^{38}$ erg/s. We infer from Table 5.5 that the almost face-on case $\Theta = \pi/8$ corresponds to $L/L_\mathrm{E} \approx 5$ for both the stellar mass and the intermediate mass black hole case, while $L/L_\mathrm{E} \approx 1$ for the nearly edge-on case $\Theta = 3\pi/8$. The inclination of M82 X-1 is completely undetermined (the disk cannot be resolved at a distance of about 3 Mpc), so we set the inclination angle to $\pi/8$.[5]

Thus far, we only have simulation data sets for 10 and 10^4 solar masses with accretion rates of $10^3 \dot{M}_\mathrm{E}$. We use the scaling laws from Fig. 5.10 to extrapolate ρ, T_gas, T_rad and v_r from the $10 M_\odot$ data to a $25 M_\odot$ setup. For the missing zenithal and azimuthal velocities v_Θ and v_Φ, which are expressed in geometrical units rather than in radians, we assume them to be constant on the grid. Since the grid points all scale with the radius and therefore with the central mass, this is the expected behavior for at least the azimuthal velocity:

---

[5] For smaller inclinations, the highly relativistic, optically thin jet region has to be considered. At present, this is not covered properly by our radiative transfer calculations.

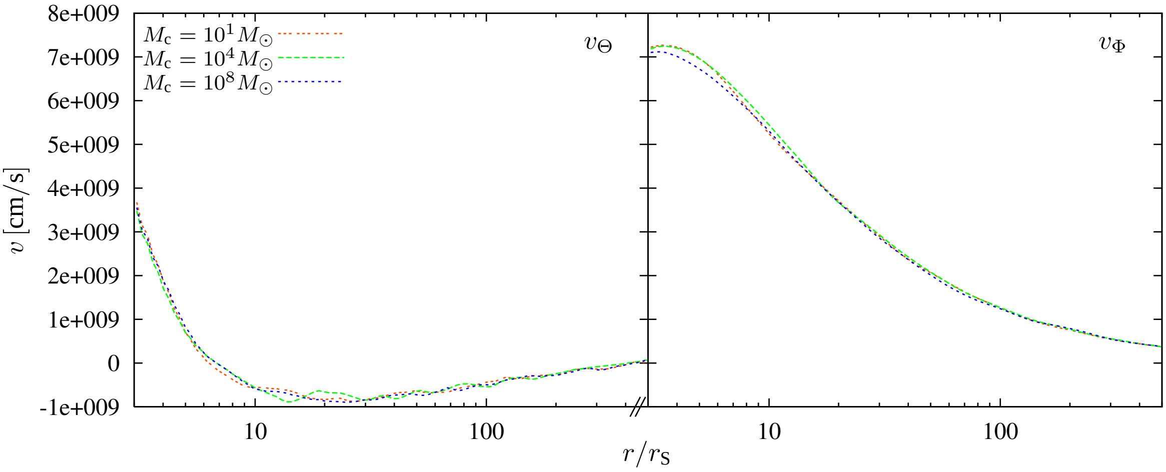

Figure 5.18. Zenithal velocity v_Θ (left) and azimuthal velocity v_Φ (right) for the simulation data sets $M_c = \{10, 10^4, 10^8\} M_\odot$, $\dot{M} = 10^3 \dot{M}_E$.

$$v_\Phi \propto \sqrt{\frac{GM_c}{r}} = \text{const} \,.$$

To see if this assumption holds for v_Φ and also for v_Θ, we plot the radial dependency of both velocities for $\Theta = \pi/8$ in Fig. 5.18. It confirms nicely our expectations by showing constant velocities on the r/r_S grid, even for the supermassive black hole case.

We further have to specify the metallicity of M82 X-1. Since M82 is a classical starburst galaxy, its metal abundances vary greatly. Strickland & Heckman (2008) analyzed the properties of the diffuse hard X-ray emission from observations by *Chandra ACIS-I* (September 1999) and *ACIS-S* (June 2002), as well as by *XMM-Newton EPIC* (May 2001 and April 2004). The authors derived a metallicity of the starburst region of $Z_{\text{Fe},\star} = 5.2 Z_{\text{Fe},\odot} \pm 50\%$. In a previous investigation, Origlia et al. (2004) investigated near-infrared absorption spectra of M82 and derived detailed stellar abundances in the nuclear region of the galaxy. They found $[\text{Fe}/\text{H}] = -0.35$ dex, which corresponds to $Z_{\text{Fe, nuc}} = 0.43 Z_{\text{Fe},\odot}$. It is reasonable to assume that the metal abundance in M82 X-1 is more related to this value. We therefore follow Origlia et al. (2004) and apply the sub-solar abundances, but we remark that these values imply a high uncertainty.

Strickland & Heckman (2008) also found a 6.7 keV emission line from highly ionized iron in the central region of M82 in all observations at high statistical significance, in addition to a marginally significant 6.4 keV Fe K_α emission line (from weakly ionized iron). Only in the May 2001 *XMM-Newton* observation did they detect significantly higher iron line fluxes and an additional 6.9 keV emission line. They attributed the excess to M82 X-1 being in its high state.

We summarize the main parameters of M82 X-1 and our model in Table 5.6. The resulting spectra are plotted in Fig. 5.19. Beside an almost perfect agreement of the bolometric luminosity with the slim disk model of Okajima et al. (2006), we find that it exceeds the classical Eddington luminosity by a factor of 5.2. We also recover the decreasing trend of the ratio of the equivalent widths with increasing black hole mass, from 0.12 for $M_c = 10 M_\odot$ to 0.08 for $M_c = 25 M_\odot$.

Observational data show line widths of the order of -50 eV to -90 eV for the 6.7 keV emission line of the central nuclear region (Okajima et al., 2006; Strickland & Heckman, 2008), while

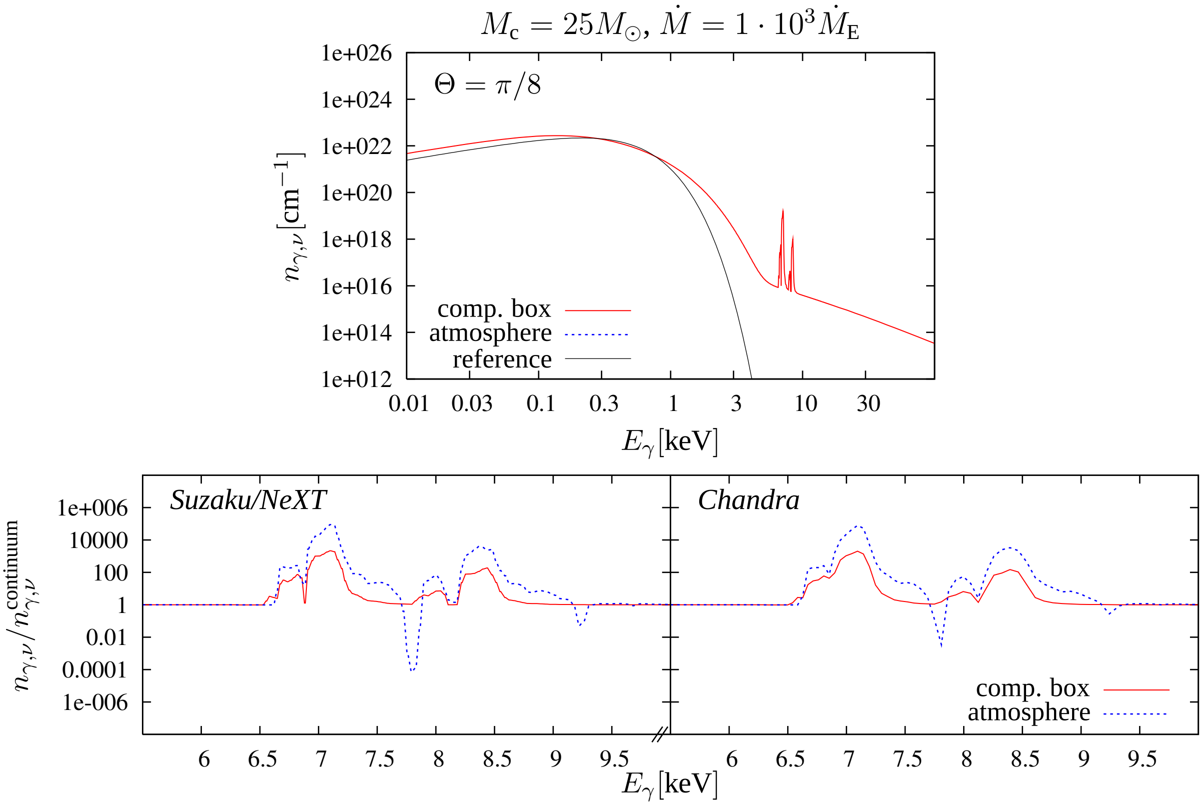

Figure 5.19. Emerging spectrum for $M_c = 25M_\odot$, $\dot{M} = 1 \cdot 10^3 \dot{M}_E$ and inclination angle $\Theta = \pi/8$. Upper panels: emanating photon number density for continuum and lines at the boundary of the computational box; the reference is generated by a blackbody spectrum with temperature $T_{bb} = 1.1 \cdot 10^6$K and a spectral hardening factor $\varepsilon = 1.4$. Lower panels: ratio of line emission relative to the continuum at the boundary of the computational box and after processing the lines through the atmosphere.

they are significantly smaller for the 6.4 keV and 6.9 keV emission lines. For M82 X-1 in its steady/low state, they are almost not detectable with $\mathrm{EW}_{6.4\,\mathrm{keV}} = -9$ eV and $\mathrm{EW}_{6.7\,\mathrm{keV}} = -2$ eV. This is also the data on which Okajima et al. (2006) based their analysis. In the high state, these values are increased to $\mathrm{EW}_{6.4\,\mathrm{keV}} = -23$ eV and $\mathrm{EW}_{6.7\,\mathrm{keV}} = -28$ eV, respectively. Thus far, no absorption lines have been detected. We definitely overestimate the strength of the emission lines, regardless of whether we include the atmosphere in the calculation or not. Even more, like in the previous section, the emission lines are increased by our atmospheric toy model. At the same time, two highly blueshifted, narrow absorption dips are generated. Only considering for the absorption features outside the atmosphere, we find reasonable equivalent widths (c. f. Table 5.6). They are generated by helium- and hydrogen-like iron K line absorption, moving towards the observer with $v/c = 0.12$.

Hence, we conclude that our simulations overestimate the line emission by almost three orders of magnitude! Possible reasons for this are the limited size of the computational box (resulting in an artificial cutoff of the disk and the corona), the oversimplified model of the atmosphere, or the fact that the gas temperatures in the simulation data are extremely high, exceeding 10^9 K in the disk's surroundings. As discussed earlier, these temperatures are neither expected, nor observed thus far. They would also require to incorporate nuclear reactions in the energy equation of the RHD simulations.

Table 5.6. Main properties of the ULX M82 X-1 from Okajima et al. (2006) and adapted to our radiative transfer model. The line widths of our model are calculated at the boundary of the computational box (emission lines, EW< 0) and outside the atmosphere (absorption lines, EW> 0).

	Okajima et al. (2006)	Our model
Central black hole mass	19-32$M_\odot$	$25M_\odot$
Accretion rate	320–$560\dot{M}_\mathrm{E}$	$1000\dot{M}_\mathrm{E}$
Distance	2.7 Mpc	2.7 Mpc
Bolometric luminosity	$1.4\cdot10^{40}\mathrm{erg/s} =$ 4–$6L_\mathrm{E}$	$1.6\cdot10^{40}\mathrm{erg/s} = 5.2L_\mathrm{E}$
X-ray luminosity ($[3;10]$ keV)	$8.4\cdot10^{39}\mathrm{erg/s}$	$1.5\cdot10^{37}\mathrm{erg/s}$
Metallicity (Origlia et al., 2004)	—	$Z_\mathrm{Fe} = 0.43Z_{\mathrm{Fe},\odot}$
Inclination angle	—	$\pi/8$
Scaling of ρ_{25}	—	$0.40\rho_{10}$
$T_{\mathrm{rad},25}$	—	$0.80T_{\mathrm{rad},10}$
$T_{\mathrm{gas},25}$	—	$1.00T_{\mathrm{gas},10}$
$v_{r,25}$	—	$1.06v_{r,10}$
$v_{\Theta,25}$	—	$1.00v_{\Theta,10}$
$v_{\Phi,25}$	—	$1.00v_{\Phi,10}$
Line center K_α emission	6.6 keV	7.1 keV
Equivalent width K_α emission	-85 eV	-449 keV
Line center K_β emission	—	8.4 keV
Equivalent width K_β emission	—	-37 keV
EW K_β/EW K_α emission	—	0.08
Line center K_α absorption	—	7.8 keV
Equivalent width K_α absorption	—	$+160$ eV
Line center K_β absorption	—	9.3 keV
Equivalent width K_β absorption	—	$+77$ eV
EW K_β/EW K_α absorption	—	0.48

Another possibility is revealed by Fig. 5.20, where we compare our modeled spectra with the observational data of *XMM-Newton* when the source was in its low state (Okajima et al., 2006) and in its high state (Strickland & Heckman, 2008). The photon energy range in this figure is limited to $E_\gamma = [3;10]$ keV and the spectrum is given in counts$/(\mathrm{s\,keV})$, where a distance of 2.7 Mpc was assumed. Although the integrated bolometric luminosity of our model – which is dominated by the UV peak emission – is in good agreement with the observations, the X-ray continuum is not. Strickland & Heckman (2008) concluded that the X-ray excess in the galaxy M82 is generated by the nucleus region, the ULX point sources and a dominating diffuse continuum, which cannot be separated from each other. Thus, the observational data overestimates the X-ray continuum flux from M82 X-1. Nevertheless, the discrepancy between our results and the observations is too large to simply attribute it to the diffuse continuum. Instead, we recall that the 2D RHD simulation data provide only gray values for the radiation energy density and the gas density. From these, we derive blackbody temperatures and Planckian energy distributions for the radiation field and the gas, assuming that they are in separate local thermal equilibria.

Contrarily, a power law spectrum $L_\nu \propto \nu^{-\alpha}$ is commonly used *and usually required* to fit the observation of X-ray spectra. M82 X-1 shows an extremely flat continuum in its low state that

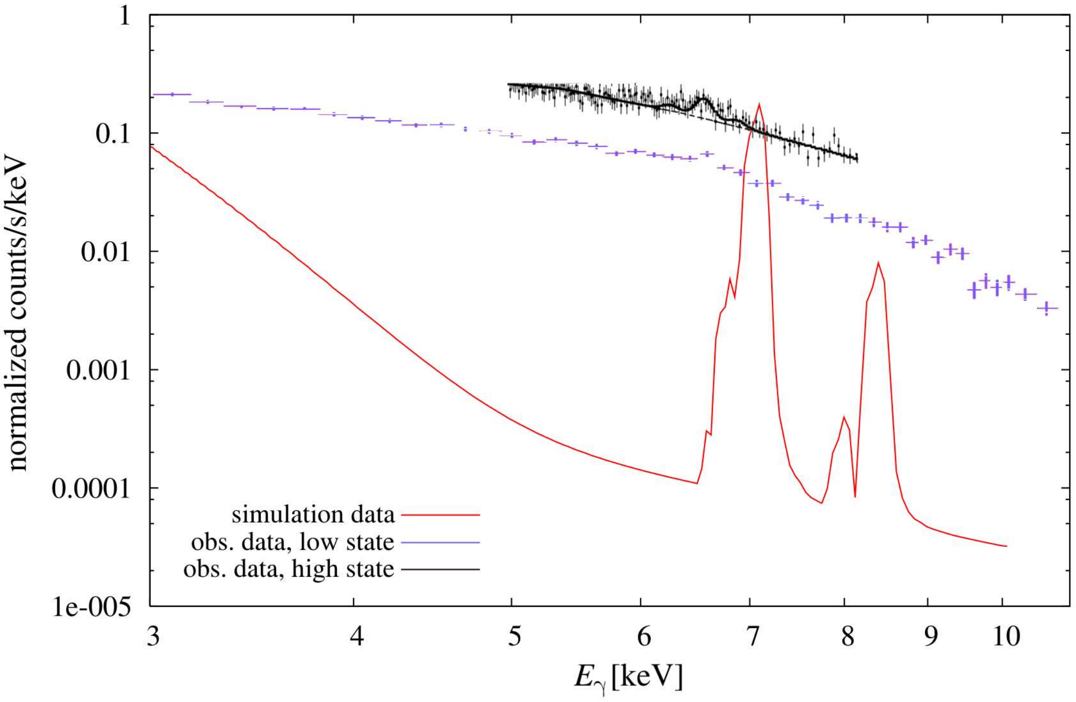

Figure 5.20. X-ray fluxes from the simulation data (red) and from observations while the source was in its low state (blue, Okajima et al. (2006)) and in its high state (black, Strickland & Heckman (2008)).

can be fitted adequately by a broken power law with a transition at $E_{\mathrm{tr}} = 6.0 \pm 0.5\,$keV and $\alpha_< = 0.7$, $\alpha_> = 2.0$. In its high state, the spectrum steepens significantly and can be fitted again by a broken power law with $E_{\mathrm{tr}} = 6.0 \pm 0.5\,$keV and $\alpha_< = 1.6$, $\alpha_> = 2.6$ (values are taken from Strickland & Heckman (2008, Table 3)).

Increasing the continuum emission in our model by a factor of 1000, as suggested from Fig. 5.20 and from the comparison of the integrated X-ray luminosities in Table 5.6, would lower the equivalent widths of the iron K emission (and absorption) lines by approximately the same factor. This would lead to much more reasonable equivalent widths EW $\mathrm{K}_\alpha = -450\,$eV and EW $\mathrm{K}_\beta = -37\,$eV for the emission lines and vanishing absorption features. It makes sense to assume that the fully resolved emission lines of our simulations are somewhat larger than the observed ones. The observed lines are influenced by the limited instrumental resolution and by the contamination of the ULX emission from its host galaxy, in particular from the diffuse continuum.

We want to remark that also the Doppler shift of the emission lines in our synthetic spectrum does not fit to the observations, which show basically no shift of the line frequencies. Whether this is due solely to our simplified atmospheric model, where the radial velocity stays constant, cannot be answered within this investigation. Alternatively, the data from the underlying simulations might simply show too high velocities. Also the question about the central black hole mass is left open, but our results confirm that a hyperaccreting stellar mass black hole can account for the observed super-Eddington luminosities.

5.7 Conclusions

In the previous section, we presented the results for five sets of simulation data and discussed them in detail. We also extrapolated the stellar mass simulation data towards a $25M_\odot$ black hole and compared it to the ULX M82 X-1. We found that in all six cases, the computational box is too small for a proper treatment of these highly super-Eddington accretion disk systems. The iron line emission from the computational box is unusually strong in all cases, with equivalent widths of the order of tens to hundreds of keV. No absorption lines can be detected at the boundary of the computational box, regardless of the orientation of the disk relative to the observer.

Despite these doubtable absolute numbers, their relative values suggest that the equivalent width ratio EW K_β/EW K_α can be an indicator for the central black hole mass. While this ratio adopts values of 0.12 for $M_\mathrm{c} = 10M_\odot$, it decreases steadily to 0.08 for $M_\mathrm{c} = 25M_\odot$, 0.06 for $M_\mathrm{c} = 10^4 M_\odot$ and 0.02 for $M_\mathrm{c} = 10^8 M_\odot$. The inclination angle also influences this ratio: for a stellar mass black hole, the face-on ratio is about 20% larger than the edge-on ratio. For higher black hole masses, this effect seems to weaken, but the validity of the high mass simulation data itself forbids a definitive statement. At the same time, the influence of the accretion rate on the EW ratio is negligibly small, so that we cannot even separate it from the intrinsic errors.

The emission lines at the boundary of the computational box are generally composed of a complex line from the low velocity outflow ($v/c = 0.02$) and a stronger, complex line from the high velocity outflow($v/c = 0.08$) for both K_α and K_β. The individual lines are generated from a mixture of low and high ionization degrees of iron, reaching up to Fe XXIII for the low velocity line, and up to hydrogen-like Fe XXVI for the high velocity line. The line shifts are almost insensitive to the accretion rate and the central mass.

We introduced a simple atmospheric model in order to investigate the effects of the disk's surroundings on the spectrum. We found that its influence differs significantly for the face-on case and the edge-on case. In the former case, highly blueshifted narrow absorption dips from the highest ionization degrees of iron can be found for a stellar mass black hole, next to and overlaid on strong emission lines. In the latter case, the emission lines disappear completely and broader absorption lines are generated in the stellar mass case with high accretion rates. For higher central masses, the modeling breaks down completely. It is therefore absolutely necessary to run the simulations with a larger computational domain.

In general, we advise that the 2D RHD simulations should not be extended towards central masses larger than $M_\mathrm{c} \approx 10^4 M_\odot$. The physical assumptions and processes included in the model are not sufficient or appropriate for the required densities and temperatures. A further improvement, although unrealistic with current computational limitations, would be to incorporate a frequency dependent radiative transfer calculation in the simulations directly. Until this becomes possible, a rethinking of the spectral energy distribution of the radiation field and the gas emission in the computational box is necessary. Our results, in particular the underestimation of the X-ray continuum flux in M82 X-1, suggest that a power law distribution is more appropriate than a blackbody spectrum in this energy range. However, including this is not straightforward since it requires a consistent modeling of the emission from the radiation field and the gas over a large energy range in order to preserve the good agreement on the total luminosity.

Indeed, from the bolometric luminosities, emanating photon numbers and average photon energies we find an excellent agreement with the theoretical expectations. For an extremely high accretion rate of $\dot{M} = 10^3 \dot{M}_\mathrm{E}$, the total luminosity exceeds the Eddington limit by a factor of 1 to 6, depending on the inclination angle, but regardless of the central black hole mass. The results are not only consistent with the observations of M82 X-1, but also with the theoretical expectations for slim disk models when the photon trapping mechanism is considered properly (Ohsuga et al., 2002). Moreover, they also show a logarithmic dependence of L_{bol} on the accretion rate, which is expected from semi-analytical calculations (Watarai et al., 2000; Fukue, 2004). Also the average photon energies drop for higher central masses, as expected.

From this point of view, it is quite possible that ULXs are powered by hyperaccreting stellar mass black holes, shining at a few times the Eddington luminosity. Mild relativistic beaming effects further influence the ratio L/L_{E} for small inclination angles. In summary, our results suggest to concentrate on constraining the inclination angle and the ratio of the equivalent widths by observations of known and potential low mass ULXs with the latest X-ray observatories. We propose a follow-up observation of M82 X-1 with *NeXT* to investigate the presence – and if present, the strength – of a K_{β} emission line.

6 Epilog

In this dissertation, we studied two different aspects of black hole accretion disks. In the first part, we concentrated on modeling their internal structure. From a detailed examination of the role of convection, we found that it contributes significantly to the energy transport in the disk. Convective turbulence also adds considerably to the total viscosity, although it cannot account for it on its own. We briefly discussed how it may act jointly with differential rotation and magneto-rotational instabilities. We closed the discussion by stressing the need for a further investigation of such a combined viscosity, especially in the *dead zones* of the MRI and in the self-gravitating regions of the disk, where convective feedback processes on the energy transport set in.

In the second part of the thesis, we switched from the purely theoretical side of the table to an observational one. We investigated the spectral energy distribution of two-dimensional radiation-hydrodynamic simulations of highly accreting black holes. We first studied their over-all continuum features and found that the orientation of the disk relative to the observer has a strong influence on the emerging spectra, not least due to mild relativistic beaming effects. Inauspiciously, the orientation is one of the parameters that is often hard to determine from the observations. A possible indicator, however, are line transitions. We continued the spectral analysis by studying the iron K line emission of the super-Eddington flows. Apart from the disk's orientation, we also investigated the influence of the central mass and the accretion rate on the emanating lines. One important outcome was the dependence of the relative strength of the K_β lines to the K_α lines on the central mass, another one the broadening of the lines for higher inclinations.

However, we saw that the absolute strengths of the lines do not fit to the observations: we found equivalent widths which were a factor of 1000 higher than expected. During the discussion of the possible reasons for these inconsistencies, we ignored a potential bug in our radiative transfer code. This argument is supported by further tests of our code with the most recent simulation data by Ohsuga (priv.comm.), this time modeling a $100M_\odot$ black hole showing limit-cycle oscillations. The corresponding accretion rates are significantly lower, around $65\dot{M}_\mathrm{E}$ in the high state and $0.7\dot{M}_\mathrm{E}$ in the low state, respectively. This system shows quasi-periodic oscillations with duration times of about 40 s (high state) and 60 s (low state). For the source being in its low/hard state, we found a complex absorption feature for the face-on case and reasonably strong emission lines for an edge-on view on the disk. We were also able to fit a power law to the X-ray continuum with $n_\gamma \propto E_\gamma^{-1.8}$. A detailed investigation and analysis of these data will be published elsewhere.

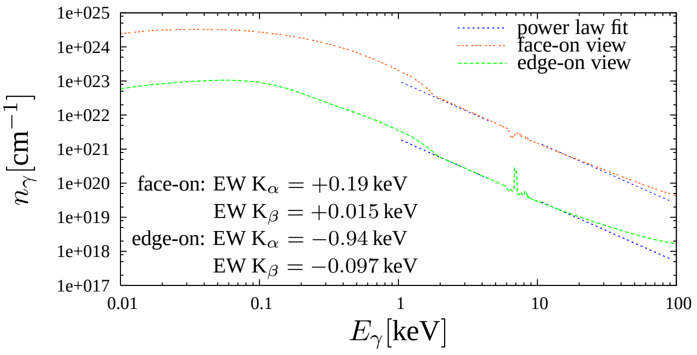

To conclude, we demonstrated the potential diagnostic power of the iron lines for the accretion process. Yet, we were not able to draw quantitativ conclusions from our investigation. To do so, we need a better description for the emission spectrum of the gas and the radiation field in the simulations – or, even better, frequency-dependent RHD simulations. This, however, is hardly feasible with current computational power. On the contrary, an extension of the simulations towards larger radii and towards disks around supermassive black holes is much more realistic. In future work, we will therefore focus on an improvement of the emission spectra. We will also upgrade the method of the ray-tracing radiative transfer calculation to a Monte-Carlo method. This last step will strongly profit from the decoupling of the opacity calculations from the actual radiative transfer scheme.

Acknowledgements

This dissertation would not have been possible without the help of many people. But, where to start? Probably with Max Planck, since quite a bit of the physics used in this work would not have been invented without him . . .

Seriously, in first place I want to thank my advisor Prof. Wolfgang Duschl and my Japanese host and collaborator Prof. Shin Mineshige for their enduring support and guidance. Sincere thanks to both of them for giving me the opportunity to live and work in Kyoto for part of my thesis. It was definitely the most exciting time of my life.

Special thanks also to Dr. Ken Ohsuga for providing me his simulation data, for a fruitful collaboration and for supporting my visit to Tokyo. I also want to thank Prof. Atsuo Okazaki for inviting me to Hokkaido University and guiding me through Sapporo.

I want to thank Profs. Detlef Koester, Hans-Walter Rix, Werner Tscharnuter and Rainer Wehrse for interesting discussions and their assistance with many questions, and Prof. Christian Fendt on behalf of the IMPRS Heidelberg for his great tolerance with the move from Heidelberg to Kiel and for generous travel grants.

A big thank you to Drs. Tobias Illenseer and Hannes Horst for proofreading, and to the fleet of native speakers for corrections of the English text and making this thesis a British-Irish-New Zealandish-American-German coproduction: Juliet Datson, Dominic Edsall, Ronan Higgins, Lisa Perry, Dr. Chris Rasmussen, Renée Rasmussen.

I want to thank my colleagues for the enjoyable atmosphere and for keeping the coffee club going while I was absent. A special thank to Jan Hofmann for the comprehensive sports program that saved me from becoming too much of a workaholic.

Many thanks to my parents Martin and Sylvia Heinzeller for their restless encouragement and for making each trip home a real holiday; to my brother Korbinian Heinzeller and to my climbing partners all over the world for the unforgettable memories that helped me to complete this work.

And last but not least to Daniela: it is hard enough that one of us is complicated – I am glad you are not. Thank you for everything!

This thesis was financially supported by the International Max Planck Research School for Astronomy and Cosmic Physics at the University of Heidelberg, by the Grants-in-Aid of the Ministry of Education, Science, Culture, and Sport (14079205, 16340057 S.M.), by the Grant-in-Aid for the 21st Century COE “Center for Diversity and Universality in Physics” from the Ministry of Education, Culture, Sports, Science and Technology (MEXT) of Japan, and by the Japanese Society for the Promotion of Science (JSPS).

The numerical calculations were carried out on the Linux cluster (rzcluster) at the datacenter of the University of Kiel and on the Altix3700 BX2 at the Yukawa Institute for Theoretical Physics in Kyoto University.

Bibliography

Abramowicz M.A., Czerny B., Lasota J.P., Szuzkiewicz E., 1988, ApJ, 332, 646

Agrawal V.K., Misra R., 2006, ApJ, 638, L83

Argonne National Laboratory, Mathematics and Computer Science, 2008, The Message Passing Interface (MPI) standard, `http://www-unix.mcs.anl.gov/mpi`

Awaki H., Anabuki N., Fukazawa Y., Gallo L., Ikeda S., Isobe N., Itoh T., Kunieda H., Makishima K., Markowitz A.G., Miniutti G., Mizuno T., Okajima T., Ptak A., Reeves J.N., Takahashi T., Terashima Y., Yaqoob T., 2007, `http://arxiv.org/abs/0707.2425v1`

Balbus S.A., Hawley J.F., 1991, ApJ, 376, 214

Bautista M., Romano P., Pradhan A.K., 1998, ApJS, 118, 259

Begelman M.C., 1978, MNRAS, 184, 53

Begelman M.C., Pringle J.E., 2007, MNRAS, 375, 1070

Bell K.R., Lin D.N.C., 1994, ApJ, 427, 987

Bianchi S., Miniutti G., Fabian A.C., Iwasawa K., 2005, MNRAS, 360, 380

Burger H.L., Katz J.I., 1980, ApJ, 236

Canizares C.R., Davis J.E., Dewey D., Flanagan K.A., Galton E.B., Huenemoerder D.P., Ishibashi K., Markert T.H., Marshall H.L., McGuirk M., Schattenburg M.L., Schulz N.S., Smith H.I., Wise M., 2005, PASP, 117, 1144

Cao X., Xu Y.-D., 2003, PASJ, 55, 149

Czerny B., Elvis M., 1987, ApJ, 321, 305

Chandrasekhar S., 1960, PNAS, 46, 253

Cox A.N., 1965, Stellar Structure, in: Stars and Stellar Systems vol. 8 (Eds: Aller L.H., McLaughlin D.B.), University of Chicago Press, Chicago, p. 218

Cox J.P., Giuli R.T., 1968, Principles of stellar structure, Volume 1, Physical Principles, Gordon & Breach, New-York–London–Paris

Cropper M., Soria R., Mushotzky R.F., Wu K., Markwardt C.B., Pakull M., 2004, MNRAS, 349, 39

Dewangan G.C., Titarchuk L., Griffiths R.E., 2006, ApJ, 637, L21

Dörrer T., Riffert H., Staubert R., Ruder H., 1996, A&A, 311, 69

Duschl W.J., 1983, A&A, 121, 153

Duschl W.J., 1989, A&A, 225, 105

Duschl W.J., Tscharnuter W.M., 1991, A&A, 241, 153

Duschl W.J., Strittmatter P.A., Biermann P.L., 2000, A&A, 357, 1123

Ebisawa K., Zycki P., Kubota A., Mizuno T., Watarai K.-y., 2003, CHJAA, 3, Suppl., 415

Ferguson J.W., Alexander D.R., Allard F., Barman T., Bodnarik J.G., Hauschildt P.H., Heffner-Wong A., Tamanai A., 2005, ApJ, 623, 585

Ferguson J.W., 2008, Research in Low Temperature Astrophysics at Wichita State University, `http://webs.wichita.edu/physics/opacity/`

Fiorito R., Titarchuk L., 2004, ApJ, 614

Fuhr J.R., Martin G.A., Wiese W.L., 1988, Journal of physical and chemical reference data 17, supplement 4: Atomic transition probabilities: Iron through nickel, National Bureau of Standards, Institute of Physics, New York, N.Y.

Fukue J., 2000, PASJ, 52, 829

Fukue J., 2004, PASJ, 56, 569

Gammie C.F., 1996, ApJ, 457, 355

Gammie C.F., 1999, ApJ, 522, L57

Gingerich O., 1964, Review of opacity calculations, Harvard Smithsonian Conference on stellar atmospheres, S.A.0. Special Report No. 167, Cambridge, Smithsonian Astrophysical Observatory

Goldman I., Wandel A., 1995, ApJ, 443, 187

Gonzalez J.-F., LeBlanc F., Atru M.-C., Michaud G., 1995, A&A, 297, 223

Grevesse N., Sauval A.J., 1998, Space Science Reviews, 85, 161

Hayashi C., Hoshi R., Sugimoto D., 1962, Progr. Theoret. Phys. Supp., 22, 1

Heinzeller D., Mineshige S., Ohsuga K., 2006, MNRAS, 372, 1208

Heinzeller D., Duschl W.J., 2007, MNRAS, 374, 1146

Henyey L.G., Forbes J.E., Gould N.L., 1964, ApJ, 139, 306

Hofmann J., 2005, Zeitentwicklung und Vertikalstruktur protostellarer Akkretionsscheiben, Diploma thesis, Heidelberg

ISAS/JAXA, 2008, X-ray Astronomy SUZAKU (ASTRO-EII) Mission, `http://www.isas.jaxa.jp/e/enterp/missions/suzaku/index.shtml`

Kaastra J.S., Mewe R., 1993, A&AS, 97, 443

Karzas W.J., Latter R., 1961, ApJS, 6, 167K

Kato S., Fukue J., Mineshige S., 1998, Black-Hole Accretion Disks, Kyoto University Press, Kyoto

Kawaguchi T., 2003, ApJ, 593, 69

Kelley R.L., Mitsuda K., Allen C.A., Arsenovic P., Audley M.D., Bialas T.G., Boyce K.R., Boyle R.F., Breon S.R., Brown G.V., Cottam J., Dipirro M.J., Fujimoto R., Furusho T., Gendreau K.C., Gochar G.G., Gonzalez O., Hirabayashi M., Holt S.S., Inoue H., Ishida M., Ishisaki Y., Jones C.S., Keski-Kuha R., Kilbourne C.A., McCammon D., Morita U., Moseley S.H., Mott B., Narasaki K., Ogawara Y., Ohashi T., Ota N., Panek J.S., Porter F.S., Serlemitsos A., Shirron P.J., Sneiderman G.A., Szymkowiak A.E., Takei Y., Tveekrem J.L., Volz S.M., Yamamoto M., Yamasaki N.Y., 2007, PASJ, 59, 77

King A.R., Davies M.B., Ward M.J., Fabbiano G., Elvis M., 2001, ApJ, 552, L109

King A.R., Pringle J.E., Livio M., 2007, MNRAS, 376, 1740

Kley W., 1989, A&A, 208, 98

Klim A., 1981, Journal of Quantitative Spectroscopy and Radiative Transfer, 26, 537

Körding E., Colbert E., Falcke H., 2004, Progr. Theoret. Phys. Supp., 155, 365

Krolik J.H., 1999, ApJ, 515, L73

Kubota A., Ebisawa K., Makishima K., Nakazawa K., 2005, ApJ, 631, 1062

Kusch H.J., 1958, Zeitschrift für Astrophysik, 45, 1

Levermore C.D., Pomraning G.C., 1981, ApJ, 248, 321

Liu J.-F., Bregman, J.N., Irwin J., Seitzer P., 2002, ApJ, 581, L93

Machida M., Nakamura K., Matsumoto R., 2004, PASJ, 56, 671

Makishima K., Kubota A., Mizuno T., Ohnishi T., Tashiro M., Aruga Y., Asai K., Dotani T., Mitsuda K., Ueda Y., Uno S.'I., Yamaoka, K., Ebisawa, K., Kohmura, Y., Okada, K., 2000, ApJ, 535, 632

Markowitz A., Reeves J.N., Miniutti G., Serlemitsos P., Kunieda H., Yaqoob T., Fabian A.C., Fukazawa Y., Mushotzky R., Okajima T., Gallo L.C., Awaki H., Griffiths R.E., 2008, PASJ, 60, S277

Matsumoto H., Tsuru T.G., Koyama K., Awaki H., Canizares C.R., Kawai N., Matsushita S., Kawabe, R., 2001, ApJ, 547, L25

Mendoza C., Kallman T.R., Bautista M.A., Palmeri P., 2004, A&A, 414, 377

Michaud G., Charland Y., Vauclair S., Vauclair G., 1976, ApJ, 210, 447

Mihalas D., 1970, Stellar atmospheres, W.H. Freeman and Company, San Francisco

Miller J.M., Fabbiano G., Miller, M.C., Fabian A.C., 2003, ApJ, 585, L37

Miller J.M., ARA&A, 45, 441

Mineshige S., Hirano A., Kitamoto S., Yamada T., Fukue J., 1994, ApJ, 426, 308

Mineshige S., Kawaguchi T., Takeuchi M., Hayashida K., 2000, PASJ, 52, 499

NIST Atomic Spectra Database, 2006, version 3.0, `http://physics.nist.gov/PhysRefData/ASD/index.html`

Ohsuga K., Mineshige S., Mori M., Umemura M., 2002, ApJ, 574, 315

Ohsuga K., Mori M., Nakamoto T., Mineshige S., 2005, ApJ, 628, 368

Ohsuga K., 2007, ApJ, 659, 205

Okajima T., Ebisawa K., Kawaguchi T., 2006, ApJ, 652, L105

Origlia L., Ranalli P., Comastri A., Maiolino R., 2004, ApJ, 606, 862

Paczyński B., Wiita P.J., 1980, A&A, 88, 23

Paczyński B., 2000, `http://arxiv.org/abs/astro-ph/0004129v1`

Patruno A., Portegies Zwart S., Dewi, J., Hopman, C., 2006, MNRAS Letters, 370, L6

Pessah M.E., Chan C.-K., Psaltis D., 2008, MNRAS, 383, 683

Plonka-Hoch G., 2004, Vorlesung numerische Mathematik III, `http://www.uni-duisburg.de/FB11/STAFF/PLONKA`

Poppe G.P.M., Wijers C.M.J., 1990, ACM Transactions on Mathematical Software (TOMS) archive, 16, 47

Pounds K.A., Reeves J.N., King A.R., Page K.L., O’Brien P.T., Turner, M.J.L., 2003, MNRAS, 345, 705

Prendergast K.H., Burbidge G.R., 1968, ApJ, 151, L83

Press W.H., Teukolsky S.A., Vetterling W.T., Flannery B.P., 2001, Numerical Recipes in Fortran 77, Volume 1 of Numerical Recipes in Fortran, Cambridge University Press, Cambridge

Pringle J.E., Rees M.J., 1972, A&A, 21, 1

Psaltis D., Lamb F.K., 1997, ApJ, 488, 881

Reeves J.N., Porquet D., Turner T.J., 2004, ApJ, 615, 150

Reynolds C.S., Young A.J., Begelman M.C., Fabian A.C., 1999, ApJ, 514, 164

Reynolds C.S., 2007, Revista Mexicana de Astronomía y Astrofísica, 27, 36

Richard D., Zahn J.-P., 1999, A&A, 347 734

Richard, D., 2001, Instabilités Hydrodynamiques dans les Ecoulements en Rotation Différentielle, PhD thesis, Paris

Roberts T.P., 2007, Astrophysics and Space Science, 311, 203

Ross R.R., Fabian A.C., Mineshige S., 1992, MNRAS, 258, 189

Ruden S.P., Papaloizou J.C.B., Lin D.N.C., 1988, ApJ, 329, 739

Rybicki G.B., Lightman A.P., 1979, Radiative processes in astrophysics, Wiley & Sons, New York

Ryu D., Goodman J., 1992, ApJ, 388, 438

Schweitzer A., Hauschildt P.H., Allard F., Basri G., 1996, MNRAS, 283, 821

Serlemitsos P.J., Boldt E.A., Holt S.S., Ramaty R., Brisken A.F., ApJ, 184, L1

Shakura N.I., Sunyaev R.A., 1973, A&A, 24, 337

Shirai T., Sugar J., Musgrove A., Wiese W.L., 2000, Journal of Physical and Chemical Reference Data, Monograph No. 8: Spectral Data for Highly Ionized Atoms: Ti, V, Cr, Mn, Fe, Co, Ni, Cu, Kr, and Mo, National Institute of Standards and Technology, Gaithersburg, Maryland

Socrates A., Davis S.W., Blaes O., 2004, ApJ, 601, 405

Soria R., Puchnarewicz E.M., 2002, MNRAS, 329, 456

Strickland D.K., Heckman T.M., 2008, ApJ, 658, 258

Strohmayer T.E., Mushotzky R.F., 2003, ApJ, 586, L61

Szuszkiewicz E., Malkan M.A., Abramowicz M.A., 1996, ApJ, 458, 474

Taylor G.I., 1936, Proc. Roy. Soc. London A, 157, 546

van Teeseling A., Kaastra J.S., Heise J., 1996, A&A, 312, 186

TOPS Astrophysical Opacities: Los Alamos National Laboratory, 2008,, Atomic and Optical Theory, `http://www.t4.lanl.gov/cgi-bin/opacity/astro.pl`

Traving G., Baschek B., Holweger H., 1966, Abhandlungen aus der Hamburger Sternwarte, 8, 1

Unsöld A., 1955, Physik der Sternatmosphären, Springer, Berlin - Heidelberg - New York

Unsöld A., Baschek B., 2002, Der neue Kosmos, Springer, Heidelberg

Vehoff S., 2005, Struktur und Entwicklung von Akkretionsscheiben in den Kernen aktiver Galaxien, Diploma thesis, Heidelberg

Velikhov E.P., 1959, J. Exptl. Theoret. Phys., 36, 1398

Vierdayanti K., Mineshige S., Ebisawa K., Kawaguchi T., 2006, PASJ, 58, 915

Vila S.C., 1981, ApJ, 247, 499

Wang J.-M., Zhou Y.-Y., 1999, ApJ, 516, 420

Wang J.-M., Szuszkiewicz E., Lu F.-J., Zhou Y.-Y., 1999, ApJ, 522, 839

Watarai K.-y., Fukue J., Takeuchi M., Mineshige S., 2000, PASJ, 52, 133

Watarai K.-y., Mizuno T., Mineshige S., 2001, ApJ, 549, L77

Watarai K.-y., Ohsuga K., Takahashi R., Fukue J., 2005, PASJ, 57, 513

Weizsäcker C.F., 1948, Z. Naturforsch, 3a, 524

Wendt F., 1933, Ingenieur-Archiv, 4, 577

Wehrse R., Liebert J., 1980, A&A, 86, 139

NASA Heasarc Software, 2007, Xstar Version 2.1kn7, `http://heasarc.gsfc.nasa.gov/docs/software/xstar/xstar.html`

Appendix

A.1 Physical constants in the cgs system of units

Table A.1. Fundamental physical constants in the cgs system of units.

quantity	symbol	value	units
gravitational constant	G	$6.673 \cdot 10^{-8}$	$\mathrm{dyn\,cm^{2}\,g^{-2}}$
speed of light	c	$2.998 \cdot 10^{10}$	$\mathrm{cm\,s^{-1}}$
Planck constant	h	$6.624 \cdot 10^{-27}$	erg s
elementary charge	e	$4.803 \cdot 10^{-10}$	$\mathrm{g^{1/2}\,cm^{3/2}\,s^{-1}} = \mathrm{esu}$
electron mass	m_{e}	$9.105 \cdot 10^{-28}$	g
proton mass	m_{p}	$1.672 \cdot 10^{-24}$	g
mass of hydrogen atom	m_{H}	$1.673 \cdot 10^{-24}$	g
Rydberg frequency	Ry	$3.290 \cdot 10^{15}$	$\mathrm{s^{-1}}$
Boltzmann constant	k_{B}	$1.1380 \cdot 10^{-16}$	$\mathrm{erg\,K^{-1}}$
gas constant (for hydrogen)	$\mathfrak{R}$	$8.314 \cdot 10^{7}$	$\mathrm{erg\,K^{-1}\,g^{-1}}$
Stefan-Boltzmann constant	σ_{SB}	$5.671 \cdot 10^{-5}$	$\mathrm{erg\,cm^{-2}\,s^{-1}\,K^{-4}}$
radiation constant	$a_{\mathrm{rad}} = 4\sigma_{\mathrm{SB}}/c$	$7.567 \cdot 10^{-15}$	$\mathrm{erg\,cm^{-3}\,K^{-4}}$

Table A.2. Astronomical constants in the cgs system of units.

quantity	symbol	value	units
solar mass	$M_{\odot}$	$1.983 \cdot 10^{33}$	g
solar radius	$R_{\odot}$	$6.953 \cdot 10^{10}$	cm
astronomical unit	AU	$1.495 \cdot 10^{13}$	cm
light year	ly	$9.460 \cdot 10^{17}$	cm
parsec	pc	$3.084 \cdot 10^{18}$	cm

A.2 The Henyey method

A.2.1 Introduction

The Henyey method, originally introduced in 1961 for the calculation of stellar structure and evolution, is a special Newton-Raphson method adapted to a particular problem: the solution of a set of differential equations with real boundary conditions (i. e., given values for certain variables at one boundary, for other variables at the other boundary, in contrast to initial value problems where all boundary conditions are set at one point).

In the following, we present a detailed description of the numerical scheme and the underlying mathematical principles. We apply the method to our specific problem and derive the set of discretized equations in Sect. A.2.2. We then describe how the resulting system of linear equations is solved and stored in an efficient way (Sect. A.2.3).

Basic Newton-Raphson method Starting from the simplest case, the prototype for the application of a Newton-Raphson solver, the equation

$$\frac{dy}{dx} = f(x,y) \qquad y(x_1) = y_1 \tag{A.1}$$

needs to be solved in the domain $x = x_1, \ldots, x_{N_i}$. The discretization of the x-interval divides it into segments x_i with $i = 1, \ldots, N_i$. We call an initial guess for the solution the zeroth iteration. The left hand side of (A.1) is then given by

$$\left(\frac{dy}{dx}\right)_{i-1/2} = \frac{y_i - y_{i-1}}{x_i - x_{i-1}}\,, \tag{A.2}$$

while the right hand side can be calculated from

$$f_{i-1/2} = f\left(\frac{x_i + x_{i-1}}{2},\frac{y_i + y_{i-1}}{2}\right)\,. \tag{A.3}$$

This leads to a set of N_i differential equations for $i = 1, \ldots, N_i$:

$$g_i := (y_i - y_{i-1}) - f_{i-1/2} \cdot (x_i - x_{i-1}) = 0\,. \tag{A.4}$$

In general, $g_i \neq 0$; otherwise the correct solution $y(x)$ is found. An initial guess $y^{\{0\}}(x)$ is improved successively by Newton's root solver, i. e., a first-order approximation. Given a function $g(y) = 0$ and an initial guess $y^{\{0\}}$, the first an subsequent iterations of the root $y^{\{k\}}$ are attained by

$$y^{\{k\}} = y^{\{k-1\}} + \delta y^{\{k-1\}}\,, \tag{A.5}$$

with the correction $\delta y^{\{k-1\}}$ given by

$$g\left(y^{\{k-1\}}\right) + \left(\frac{\partial g}{\partial y}\right)^{\{k-1\}} \delta y^{\{k-1\}} = 0\,, \quad \text{where} \quad \left(\frac{\partial g}{\partial y}\right)^{\{k-1\}} = \left(\frac{\partial g}{\partial y}\right)\Bigg|_{y=y^{\{k-1\}}}. \tag{A.6}$$

The "correct solution" is found once $g\left(y^{\{k\}}\right) < \varepsilon$ where ε stands for a reasonable accuracy depending on the related problem.

Extension towards the Henyey method Exactly similar to our vertical stratification calculation, the classical stellar structure and evolution problem consists of a set of four differential equations with two given values at one boundary, and two given values at the other boundary. Given a function $g = g(y_1, \ldots, y_4)$ depending on $J = 4$ variables y_j, the analogue to (A.6) is

$$\underbrace{g\left(y_1^{\{k\}}, \ldots, y_4^{\{k\}}\right)}_{=:g^{\{k\}}} + \sum_{j=1}^{4} \left(\frac{\partial g}{\partial y_j}\right)^{\{k\}} \delta y_j^{\{k\}} = 0\,. \tag{A.7}$$

For better reading, we drop the notation of the iterative indices $\{k\}$ from the above equations and use $(j) = (1, \ldots, 4)$ to define the four differential equations and $i = 1, \ldots, N_i$ to identify the discrete grid points. Again, we use x_i as the independent variable and $y_i^{(j)}$ as the dependent variables. The functions $g_i^{(j)}$ are given by

$$\begin{aligned} g_i^{(j)}\left(x_i, x_{i-1}, y_i^{(1)}, y_{i-1}^{(1)}, y_i^{(2)}, y_{i-1}^{(2)}, y_i^{(3)}, y_{i-1}^{(3)}, y_i^{(4)}, y_{i-1}^{(4)}\right) &= \left(y_i^{(j)} - y_{i-1}^{(j)}\right) \\ -f_{i-1/2}^{(j)}\left(x_i, x_{i-1}, y_i^{(1)}, y_{i-1}^{(1)}, y_i^{(2)}, y_{i-1}^{(2)}, y_i^{(3)}, y_{i-1}^{(3)}, y_i^{(4)}, y_{i-1}^{(4)}\right) &\cdot \left(x_i - x_{i-1}\right)\,. \end{aligned} \tag{A.8}$$

The generalization of (A.4) becomes

$$g_i^{(j)} + \sum_{l=1}^{4} \left(\frac{\partial g^{(j)}}{\partial y^{(l)}}\right)_{x=x_i} \delta y_i^{(l)} + \sum_{l=1}^{4} \left(\frac{\partial g^{(j)}}{\partial y^{(l)}}\right)_{x=x_{i-1}} \delta y_{i-1}^{(l)} = 0\,. \tag{A.9}$$

All in all, the $4N_i$ equations and the four boundary conditions allow us to solve for the $4(N_i + 1)$ variations $\delta y_i^{(j)}$ by a scheme first presented by Henyey et al. (1964):

1. At grid point $i = 1$, two boundary conditions are given. Together with the four equations $g_2^{(j)}$, only two variations are left open while the remaining six variations can be expressed as functions of them, for example

$$\begin{array}{rcccccc} \delta y_1^{(1)} &=& U_1^{(1)} \delta y_2^{(1)} &+& V_1^{(1)} \delta y_2^{(2)} &+& W_1^{(1)}\,, \\ \delta y_1^{(2)} &=& U_1^{(2)} \delta y_2^{(1)} &+& V_1^{(2)} \delta y_2^{(2)} &+& W_1^{(2)}\,, \\ \delta y_1^{(3)} &=& U_1^{(3)} \delta y_2^{(1)} &+& V_1^{(3)} \delta y_2^{(2)} &+& W_1^{(3)}\,, \\ \delta y_1^{(4)} &=& U_1^{(4)} \delta y_2^{(1)} &+& V_1^{(4)} \delta y_2^{(2)} &+& W_1^{(4)}\,, \\ \delta y_2^{(3)} &=& U_2^{(3)} \delta y_2^{(1)} &+& V_2^{(3)} \delta y_2^{(2)} &+& W_2^{(3)}\,, \\ \delta y_2^{(4)} &=& U_2^{(4)} \delta y_2^{(1)} &+& V_2^{(4)} \delta y_2^{(2)} &+& W_2^{(4)}\,. \end{array} \tag{A.10}$$

   This requires to calculate numerically and store 18 coefficients.

2. For $i = 2, \ldots, N_i - 1$, the procedure is as follows: with the aid of the four differential equations $g_{i+1}^{(j)}$ and the variations $\delta y_i^{(3)}$, $\delta y_i^{(4)}$ from the previous step, we have two free variations. Thus, we can express the remaining four variations as

$$\begin{array}{rcrcrcrl}
\delta y_i^{(1)} & = & U_i^{(1)}\delta y_{i+1}^{(1)} & + & V_i^{(1)}\delta y_{i+1}^{(2)} & + & W_i^{(1)}\,, \\
\delta y_i^{(2)} & = & U_i^{(2)}\delta y_{i+1}^{(1)} & + & V_i^{(2)}\delta y_{i+1}^{(2)} & + & W_i^{(2)}\,, \\
\delta y_{i+1}^{(3)} & = & U_{i+1}^{(3)}\delta y_{i+1}^{(1)} & + & V_{i+1}^{(3)}\delta y_{i+1}^{(2)} & + & W_{i+1}^{(3)}\,, \\
\delta y_{i+1}^{(4)} & = & U_{i+1}^{(4)}\delta y_{i+1}^{(1)} & + & V_{i+1}^{(4)}\delta y_{i+1}^{(2)} & + & W_{i+1}^{(4)}\,.
\end{array} \tag{A.11}$$

This requires to calculate numerically and store 12 coefficients per step.

3. At $i = N_i$, the four differential equations, the two known variations $\delta y_{N_i}^{(3)}$, $\delta y_{N_i}^{(4)}$ and the remaining two boundary conditions allow to solve for $\delta y_{N_i}^{(1)}$, $\delta y_{N_i}^{(2)}$, $\delta y_{N_i-1}^{(1)}$ and $\delta y_{N_i-1}^{(2)}$ explicitly. In successive backward steps down to $i = 1$, all variations can be calculated and added to the current solutions.

A.2.2 Derivation of the discretized equations $G_i^{(j)}$

We now apply the Henyey method to our specific problem of the calculation of the vertical disk stratification. We introduce a discretization in the vertical direction by transferring the continuous variables F_z, z, T, Σ_z, ρ to discrete values $F_{z,i}$, … with $i = 1, \ldots, N_i$. Thereby, $F_{z,1} = 0$ and $F_{z,N_i} = F$. The set of differential equations (3.25)–(3.28) has to be discretized as well, leading to four equations $G_i^{(j)}$, $j = 1, \ldots, 4$.

With $x_{i-1/2}$, we abbreviate the mean value of a quantity x for i and $i-1$: $x_{i-1/2} = (x_i + x_{i-1})/2$. We now repeat the individual differential equations for the vertical stratification (3.25)–(3.28) and derive the corresponding, discretized Henyey equations.

For the geometric coordinate z, we get:

$$\begin{array}{rcl}
\dfrac{\partial z}{\partial F_z} & = & \dfrac{\Upsilon}{\rho\nu} \\
& \Downarrow & \\
G_i^{(1)} & = & (z_i - z_{i-1})\rho_{i-1/2}\,\nu_{i-1/2} - \Upsilon(F_{z,i} - F_{z,i-1}) \;=\; 0\,.
\end{array} \tag{A.12}$$

The temperature stratification is given as follows:

$$\begin{array}{rcl}
\dfrac{\partial T}{\partial F_z} & = & \dfrac{\Upsilon}{\rho\nu}\cdot\wp \\
& \Downarrow & \\
G_i^{(2)} & = & (T_i - T_{i-1})\rho_{i-1/2}\,\nu_{i-1/2} - \Upsilon(F_{z,i} - F_{z,i-1})\wp_{i-1/2} \;=\; 0\,.
\end{array} \tag{A.13}$$

The surface density equation converts to:

$$\begin{array}{rcl}
\dfrac{\partial \Sigma_z}{\partial F_z} & = & \dfrac{\Upsilon}{\nu} \\
& \Downarrow & \\
G_i^{(3)} & = & (\Sigma_{z,i} - \Sigma_{z,i-1})\nu_{i-1/2} - \Upsilon(F_{z,i} - F_{z,i-1}) \;=\; 0\,.
\end{array} \tag{A.14}$$

Finally, the Henyey equation for the density becomes:

$$\begin{aligned}
\frac{\partial \rho}{\partial F_z} &= -\frac{\Xi\Upsilon}{\nu}\cdot\aleph \\
&\Downarrow \\
G_i^{(4)} &= (\rho_i - \rho_{i-1})\nu_{i-1/2} + \Xi\Upsilon(F_{z,i} - F_{z,i-1})\aleph_{i-1/2} \;=\; 0\,.
\end{aligned} \tag{A.15}$$

The boundary conditions (3.36)–(3.39) allow to rewrite these equations partially for $i = 1$ and $i = N_i + 1$ as follows:

$$G_1^{(1)} \;=\; z_1 \;=\; 0\,, \tag{A.16}$$

$$G_{N_i+1}^{(2)} \;=\; T_{N_i} - T_{\text{eff}} \;=\; 0\,, \tag{A.17}$$

$$G_1^{(3)} \;=\; \Sigma_{z,1} \;=\; 0\,, \tag{A.18}$$

$$G_{N_i+1}^{(4)} \;=\; \rho_{N_i} - \rho_{\text{eff}} \;=\; 0\,. \tag{A.19}$$

The Henyey method requires the computation of the derivatives of $G_{j,i}$ for $j = 1\ldots4$ and $i = 1\ldots N_i$ with respect to all four variables z, T, Σ_z, ρ. Theoretically, these derivatives can be calculated analytically and applied to the numerical calculation. However, following Press et al. (2001), it is advisable to calculate these derivatives numerically, since the analytical formulas are a potential source of numerical problems. Generally, the numeric derivatives are given by

$$D^{G_{i_1}^{(j)},y_{i_2}^{(l)}} = \frac{\partial G_{i_1}^{(j)}}{\partial y_{i_2}^{(l)}} \approx \frac{G_{i_1}^{(j)}\big(\ldots,y_{i_2}^{(l)} + \delta y_{i_2}^{(l)},\ldots\big) - G_{i_1}^{(j)}\big(\ldots,y_{i_2}^{(l)},\ldots\big)}{\delta y_{i_2}^{(l)}}\,. \tag{A.20}$$

The Henyey method couples only adjacent grid cells, which can be seen from the Henyey equations (A.12)–(A.15): at grid cell i, only the values from grid cells i and $i-1$ enter the equations. Thus, the derivatives (A.20) vanish for all $i_2 \neq \{i_1, i_1 - 1\}$.

In the special cases $i = 1$ and $i = N_i + 1$, the standard Henyey equations (A.12)–(A.15) are replaced by the boundary equations (A.16)–(A.19).

A.2.3 Numerical solution of the system of equations

The solution of the original differential equations (3.25)–(3.28) and its boundary conditions (3.36)–(3.39) can be obtained with the aid of the derivatives presented above in an iterative procedure. Initial guesses for $z(F_z)$, $T(F_z)$, $\Sigma_z(F_z)$ and $\rho(F_z)$ need to provided. Numerically, the Henyey method corresponds to solving the following set of equations for each iteration step:

$$\mathcal{H}\cdot\Delta\mathcal{G} = -\mathcal{G}\,. \tag{A.21}$$

$\mathcal{H}$ represents the $(4N_i \times 4N_i)$ Henyey matrix

$$\mathcal{H} = \left(\begin{array}{c|c|c|c|c} \mathcal{H}_{11} & 0 & 0 & 0 & 0 \\ \hline \mathcal{H}_{21} & \mathcal{H}_{22} & 0 & 0 & 0 \\ \hline 0 & \ddots & \ddots & 0 & 0 \\ \hline 0 & 0 & \ddots & \ddots & 0 \\ \hline 0 & 0 & 0 & \mathcal{H}_{N_iN_i-1} & \mathcal{H}_{N_iN_i} \\ \hline 0 & 0 & 0 & 0 & \mathcal{H}_{N_i+1\,N_i} \end{array}\right) \tag{A.22}$$

with the special block matrices $\mathcal{H}_{11}$ and $\mathcal{H}_{N_{i+1}N_i}$ for the boundary conditions,

$$\begin{aligned} \mathcal{H}_{11} &= \begin{pmatrix} D^{G_1^{(1)},z_1} & D^{G_1^{(1)},T_1} & D^{G_1^{(1)},\Sigma_{z,1}} & D^{G_1^{(1)},\rho_1} \\ D^{G_1^{(3)},z_1} & D^{G_1^{(3)},T_1} & D^{G_1^{(3)},\Sigma_{z,1}} & D^{G_1^{(3)},\rho_1} \end{pmatrix} \\ &= \begin{pmatrix} 1 & 0 & 0 & 0 \\ 0 & 0 & 1 & 0 \end{pmatrix}, \\ \mathcal{H}_{N_i+1\,N_i} &= \begin{pmatrix} D^{G_{N_i+1}^{(2)},z_{N_i}} & D^{G_{N_i+1}^{(2)},T_{N_i}} & D^{G_{N_i+1}^{(2)},\Sigma_{z,N_i}} & D^{G_{N_i+1}^{(2)},\rho_{N_i}} \\ D^{G_{N_i+1}^{(4)},z_{N_i}} & D^{G_{N_i+1}^{(4)},T_{N_i}} & D^{G_{N_i+1}^{(4)},\Sigma_{z,N_i}} & D^{G_{N_i+1}^{(4)},\rho_{N_i}} \end{pmatrix} \\ &= \begin{pmatrix} 0 & 1 & 0 & 0 \\ 0 & 0 & 0 & 1 \end{pmatrix}, \end{aligned}$$

and the general block matrices

$$\mathcal{H}_{ij} = \begin{pmatrix} D^{G_i^{(1)},z_j} & D^{G_i^{(1)},T_j} & D^{G_i^{(1)},\Sigma_{z,j}} & D^{G_i^{(1)},\rho_j} \\ D^{G_i^{(2)},z_j} & D^{G_i^{(2)},T_j} & D^{G_i^{(2)},\Sigma_{z,j}} & D^{G_i^{(2)},\rho_j} \\ D^{G_i^{(3)},z_j} & D^{G_i^{(3)},T_j} & D^{G_i^{(3)},\Sigma_{z,j}} & D^{G_i^{(3)},\rho_j} \\ D^{G_i^{(4)},z_j} & D^{G_i^{(4)},T_j} & D^{G_i^{(4)},\Sigma_{z,j}} & D^{G_i^{(4)},\rho_j} \end{pmatrix}.$$

The $(4N_i \times 1)$-matrix $\Delta\mathcal{G}$ stands for the successive iterative corrections (“variations”) starting from the initial guesses for the four dependent variables z, T, Σ_z, ρ at each grid point $i = 1, \ldots, N_i$:

$$\Delta\mathcal{G} = (\delta z_1, \delta T_1, \delta\Sigma_{z,1}, \delta\rho_1 \,|\, \ldots \,|\, \delta z_i, \ldots, \delta\rho_i \,|\, \ldots \,|\, \delta z_{N_i}, \delta T_{N_i}, \delta\Sigma_{z,N_i}, \delta\rho_{N_i})^{\mathrm{tr}} \,.$$

Finally, the $(4N_i \times 1)$-matrix $\mathcal{G}$ gives the actual deviations from the correct solution $\mathcal{G} = 0$ for the current values of the four variables at grid points $i = 1, \ldots, N_{i+1}$:

$$\mathcal{G} = \left(G_1^{(1)}, G_1^{(3)} \,|\, \ldots \,|\, G_i^{(1)}, G_i^{(2)}, G_i^{(3)}, G_i^{(4)} \,|\, \ldots \,|\, G_{N_i+1}^{(2)}, G_{N_i+1}^{(4)}\right)^{\mathrm{tr}} \,.$$

To illustrate how this system of linear equations can be stored and solved efficiently, we plot the Henyey matrix for $N_i = 4$ with $\mathcal{D}^{l\,x}_{i_1\,i_2} \equiv D^{G^{(l)}_{i_1}, x_{i_2}}$.

$$\mathcal{H} = \left(\begin{array}{cccc|cccc|cccc|cccc}
\mathcal{D}^{1\,z}_{1\,1} & \mathcal{D}^{1\,T}_{1\,1} & \mathcal{D}^{1\,\Sigma_z}_{1\,1} & \mathcal{D}^{1\,\rho}_{1\,1} & & & & & & & & & & & & \\
\mathcal{D}^{3\,z}_{1\,1} & \mathcal{D}^{3\,T}_{1\,1} & \mathcal{D}^{3\,\Sigma_z}_{1\,1} & \mathcal{D}^{3\,\rho}_{1\,1} & & & & & & & & & & & & \\
\hline
\mathcal{D}^{1\,z}_{2\,1} & \mathcal{D}^{1\,T}_{2\,1} & \mathcal{D}^{1\,\Sigma_z}_{2\,1} & \mathcal{D}^{1\,\rho}_{2\,1} & \mathcal{D}^{1\,z}_{2\,2} & \mathcal{D}^{1\,T}_{2\,2} & \mathcal{D}^{1\,\Sigma_z}_{2\,2} & \mathcal{D}^{1\,\rho}_{2\,2} & & & & & & & & \\
\mathcal{D}^{2\,z}_{2\,1} & \mathcal{D}^{2\,T}_{2\,1} & \mathcal{D}^{2\,\Sigma_z}_{2\,1} & \mathcal{D}^{2\,\rho}_{2\,1} & \mathcal{D}^{2\,z}_{2\,2} & \mathcal{D}^{2\,T}_{2\,2} & \mathcal{D}^{2\,\Sigma_z}_{2\,2} & \mathcal{D}^{2\,\rho}_{2\,2} & & & & & & & & \\
\mathcal{D}^{3\,z}_{2\,1} & \mathcal{D}^{3\,T}_{2\,1} & \mathcal{D}^{3\,\Sigma_z}_{2\,1} & \mathcal{D}^{3\,\rho}_{2\,1} & \mathcal{D}^{3\,z}_{2\,2} & \mathcal{D}^{3\,T}_{2\,2} & \mathcal{D}^{3\,\Sigma_z}_{2\,2} & \mathcal{D}^{3\,\rho}_{2\,2} & & & & & & & & \\
\mathcal{D}^{4\,z}_{2\,1} & \mathcal{D}^{4\,T}_{2\,1} & \mathcal{D}^{4\,\Sigma_z}_{2\,1} & \mathcal{D}^{4\,\rho}_{2\,1} & \mathcal{D}^{4\,z}_{2\,2} & \mathcal{D}^{4\,T}_{2\,2} & \mathcal{D}^{4\,\Sigma_z}_{2\,2} & \mathcal{D}^{4\,\rho}_{2\,2} & & & & & & & & \\
\hline
 & & & & \mathcal{D}^{1\,z}_{3\,2} & \mathcal{D}^{1\,T}_{3\,2} & \mathcal{D}^{1\,\Sigma_z}_{3\,2} & \mathcal{D}^{1\,\rho}_{3\,2} & \mathcal{D}^{1\,z}_{3\,3} & \mathcal{D}^{1\,T}_{3\,3} & \mathcal{D}^{1\,\Sigma_z}_{3\,3} & \mathcal{D}^{1\,\rho}_{3\,3} & & & & \\
 & & & & \mathcal{D}^{2\,z}_{3\,2} & \mathcal{D}^{2\,T}_{3\,2} & \mathcal{D}^{2\,\Sigma_z}_{3\,2} & \mathcal{D}^{2\,\rho}_{3\,2} & \mathcal{D}^{2\,z}_{3\,3} & \mathcal{D}^{2\,T}_{3\,3} & \mathcal{D}^{2\,\Sigma_z}_{3\,3} & \mathcal{D}^{2\,\rho}_{3\,3} & & & & \\
 & & & & \mathcal{D}^{3\,z}_{3\,2} & \mathcal{D}^{3\,T}_{3\,2} & \mathcal{D}^{3\,\Sigma_z}_{3\,2} & \mathcal{D}^{3\,\rho}_{3\,2} & \mathcal{D}^{3\,z}_{3\,3} & \mathcal{D}^{3\,T}_{3\,3} & \mathcal{D}^{3\,\Sigma_z}_{3\,3} & \mathcal{D}^{3\,\rho}_{3\,3} & & & & \\
 & & & & \mathcal{D}^{4\,z}_{3\,2} & \mathcal{D}^{4\,T}_{3\,2} & \mathcal{D}^{4\,\Sigma_z}_{3\,2} & \mathcal{D}^{4\,\rho}_{3\,2} & \mathcal{D}^{4\,z}_{3\,3} & \mathcal{D}^{4\,T}_{3\,3} & \mathcal{D}^{4\,\Sigma_z}_{3\,3} & \mathcal{D}^{4\,\rho}_{3\,3} & & & & \\
\hline
 & & & & & & & & \mathcal{D}^{1\,z}_{4\,3} & \mathcal{D}^{1\,T}_{4\,3} & \mathcal{D}^{1\,\Sigma_z}_{4\,3} & \mathcal{D}^{1\,\rho}_{4\,3} & \mathcal{D}^{1\,z}_{4\,4} & \mathcal{D}^{1\,T}_{4\,4} & \mathcal{D}^{1\,\Sigma_z}_{4\,4} & \mathcal{D}^{1\,\rho}_{4\,4} \\
 & & & & & & & & \mathcal{D}^{2\,z}_{4\,3} & \mathcal{D}^{2\,T}_{4\,3} & \mathcal{D}^{2\,\Sigma_z}_{4\,3} & \mathcal{D}^{2\,\rho}_{4\,3} & \mathcal{D}^{2\,z}_{4\,4} & \mathcal{D}^{2\,T}_{4\,4} & \mathcal{D}^{2\,\Sigma_z}_{4\,4} & \mathcal{D}^{2\,\rho}_{4\,4} \\
 & & & & & & & & \mathcal{D}^{3\,z}_{4\,3} & \mathcal{D}^{3\,T}_{4\,3} & \mathcal{D}^{3\,\Sigma_z}_{4\,3} & \mathcal{D}^{3\,\rho}_{4\,3} & \mathcal{D}^{3\,z}_{4\,4} & \mathcal{D}^{3\,T}_{4\,4} & \mathcal{D}^{3\,\Sigma_z}_{4\,4} & \mathcal{D}^{3\,\rho}_{4\,4} \\
 & & & & & & & & \mathcal{D}^{4\,z}_{4\,3} & \mathcal{D}^{4\,T}_{4\,3} & \mathcal{D}^{4\,\Sigma_z}_{4\,3} & \mathcal{D}^{4\,\rho}_{4\,3} & \mathcal{D}^{4\,z}_{4\,4} & \mathcal{D}^{4\,T}_{4\,4} & \mathcal{D}^{4\,\Sigma_z}_{4\,4} & \mathcal{D}^{4\,\rho}_{4\,4} \\
\hline
 & & & & & & & & & & & & \mathcal{D}^{2\,z}_{5\,4} & \mathcal{D}^{2\,T}_{5\,4} & \mathcal{D}^{2\,\Sigma_z}_{5\,4} & \mathcal{D}^{2\,\rho}_{5\,4} \\
 & & & & & & & & & & & & \mathcal{D}^{4\,z}_{5\,4} & \mathcal{D}^{4\,T}_{5\,4} & \mathcal{D}^{4\,\Sigma_z}_{5\,4} & \mathcal{D}^{4\,\rho}_{5\,4}
\end{array}\right)$$

The red line indicates the diagonal of the 16×16 Henyey matrix. Obviously, the matrix adopts a band structure with only 5 entries left/below and 5 entries right/above the diagonal not being zero. The general definition of a band matrix with elements a_{ij} is that

$$a_{ij} = 0 \quad \text{when} \quad i > j + m_1 \quad \text{or} \quad j > i + m_2 \,.$$

Thus, $m_1 = m_2 = 5$ in our case. A band matrix is usually stored and manipulated in a so-called compact form, which results if the matrix is rotated by 45° clockwise. All non-zero elements lie in a long, narrow matrix with $M = m_1 + 1 + m_2 (= 11$ in our case$)$ columns and $N (= 4N_i$ in our case$)$ rows. For the above example, the compact form of $\mathcal{H}$ is denoted by $\tilde{\mathcal{H}}$, which is a 11×16 array.

$$\tilde{\mathcal{H}} = \left(\begin{array}{ccccccccccc}
 & & & & & {\color{red}\mathcal{D}^{1\,z}_{1\,1}} & \mathcal{D}^{1\,T}_{1\,1} & \mathcal{D}^{1\,\Sigma_z}_{1\,1} & \mathcal{D}^{1\,\rho}_{1\,1} & & \\
 & & & & \mathcal{D}^{3\,z}_{1\,1} & {\color{red}\mathcal{D}^{3\,T}_{1\,1}} & \mathcal{D}^{3\,\Sigma_z}_{1\,1} & \mathcal{D}^{3\,\rho}_{1\,1} & & & \\
\hline
 & & & \mathcal{D}^{1\,z}_{2\,1} & \mathcal{D}^{1\,T}_{2\,1} & {\color{red}\mathcal{D}^{1\,\Sigma_z}_{2\,1}} & \mathcal{D}^{1\,\rho}_{2\,1} & \mathcal{D}^{1\,z}_{2\,2} & \mathcal{D}^{1\,T}_{2\,2} & \mathcal{D}^{1\,\Sigma_z}_{2\,2} & \mathcal{D}^{1\,\rho}_{2\,2} \\
 & & \mathcal{D}^{2\,z}_{2\,1} & \mathcal{D}^{2\,T}_{2\,1} & \mathcal{D}^{2\,\Sigma_z}_{2\,1} & {\color{red}\mathcal{D}^{2\,\rho}_{2\,1}} & \mathcal{D}^{2\,z}_{2\,2} & \mathcal{D}^{2\,T}_{2\,2} & \mathcal{D}^{2\,\Sigma_z}_{2\,2} & \mathcal{D}^{2\,\rho}_{2\,2} & \\
 & \mathcal{D}^{3\,z}_{2\,1} & \mathcal{D}^{3\,T}_{2\,1} & \mathcal{D}^{3\,\Sigma_z}_{2\,1} & \mathcal{D}^{3\,\rho}_{2\,1} & {\color{red}\mathcal{D}^{3\,z}_{2\,2}} & \mathcal{D}^{3\,T}_{2\,2} & \mathcal{D}^{3\,\Sigma_z}_{2\,2} & \mathcal{D}^{3\,\rho}_{2\,2} & & \\
\mathcal{D}^{4\,z}_{2\,1} & \mathcal{D}^{4\,T}_{2\,1} & \mathcal{D}^{4\,\Sigma_z}_{2\,1} & \mathcal{D}^{4\,\rho}_{2\,1} & \mathcal{D}^{4\,z}_{2\,2} & {\color{red}\mathcal{D}^{4\,T}_{2\,2}} & \mathcal{D}^{4\,\Sigma_z}_{2\,2} & \mathcal{D}^{4\,\rho}_{2\,2} & & & \\
\hline
 & & & \mathcal{D}^{1\,z}_{3\,2} & \mathcal{D}^{1\,T}_{3\,2} & {\color{red}\mathcal{D}^{1\,\Sigma_z}_{3\,2}} & \mathcal{D}^{1\,\rho}_{3\,2} & \mathcal{D}^{1\,z}_{3\,3} & \mathcal{D}^{1\,T}_{3\,3} & \mathcal{D}^{1\,\Sigma_z}_{3\,3} & \mathcal{D}^{1\,\rho}_{3\,3} \\
 & & \mathcal{D}^{2\,z}_{3\,2} & \mathcal{D}^{2\,T}_{3\,2} & \mathcal{D}^{2\,\Sigma_z}_{3\,2} & {\color{red}\mathcal{D}^{2\,\rho}_{3\,2}} & \mathcal{D}^{2\,z}_{3\,3} & \mathcal{D}^{2\,T}_{3\,3} & \mathcal{D}^{2\,\Sigma_z}_{3\,3} & \mathcal{D}^{2\,\rho}_{3\,3} & \\
 & \mathcal{D}^{3\,z}_{3\,2} & \mathcal{D}^{3\,T}_{3\,2} & \mathcal{D}^{3\,\Sigma_z}_{3\,2} & \mathcal{D}^{3\,\rho}_{3\,2} & {\color{red}\mathcal{D}^{3\,z}_{3\,3}} & \mathcal{D}^{3\,T}_{3\,3} & \mathcal{D}^{3\,\Sigma_z}_{3\,3} & \mathcal{D}^{3\,\rho}_{3\,3} & & \\
\mathcal{D}^{4\,z}_{3\,2} & \mathcal{D}^{4\,T}_{3\,2} & \mathcal{D}^{4\,\Sigma_z}_{3\,2} & \mathcal{D}^{4\,\rho}_{3\,2} & \mathcal{D}^{4\,z}_{3\,3} & {\color{red}\mathcal{D}^{4\,T}_{3\,3}} & \mathcal{D}^{4\,\Sigma_z}_{3\,3} & \mathcal{D}^{4\,\rho}_{3\,3} & & & \\
\hline
 & & & \mathcal{D}^{1\,z}_{4\,3} & \mathcal{D}^{1\,T}_{4\,3} & {\color{red}\mathcal{D}^{1\,\Sigma_z}_{4\,3}} & \mathcal{D}^{1\,\rho}_{4\,3} & \mathcal{D}^{1\,z}_{4\,4} & \mathcal{D}^{1\,T}_{4\,4} & \mathcal{D}^{1\,\Sigma_z}_{4\,4} & \mathcal{D}^{1\,\rho}_{4\,4} \\
 & & \mathcal{D}^{2\,z}_{4\,3} & \mathcal{D}^{2\,T}_{4\,3} & \mathcal{D}^{2\,\Sigma_z}_{4\,3} & {\color{red}\mathcal{D}^{2\,\rho}_{4\,3}} & \mathcal{D}^{2\,z}_{4\,4} & \mathcal{D}^{2\,T}_{4\,4} & \mathcal{D}^{2\,\Sigma_z}_{4\,4} & \mathcal{D}^{2\,\rho}_{4\,4} & \\
 & \mathcal{D}^{3\,z}_{4\,3} & \mathcal{D}^{3\,T}_{4\,3} & \mathcal{D}^{3\,\Sigma_z}_{4\,3} & \mathcal{D}^{3\,\rho}_{4\,3} & {\color{red}\mathcal{D}^{3\,z}_{4\,4}} & \mathcal{D}^{3\,T}_{4\,4} & \mathcal{D}^{3\,\Sigma_z}_{4\,4} & \mathcal{D}^{3\,\rho}_{4\,4} & & \\
\mathcal{D}^{4\,z}_{4\,3} & \mathcal{D}^{4\,T}_{4\,3} & \mathcal{D}^{4\,\Sigma_z}_{4\,3} & \mathcal{D}^{4\,\rho}_{4\,3} & \mathcal{D}^{4\,z}_{4\,4} & {\color{red}\mathcal{D}^{4\,T}_{4\,4}} & \mathcal{D}^{4\,\Sigma_z}_{4\,4} & \mathcal{D}^{4\,\rho}_{4\,4} & & & \\
\hline
 & & & \mathcal{D}^{2\,z}_{5\,4} & \mathcal{D}^{2\,T}_{5\,4} & {\color{red}\mathcal{D}^{2\,\Sigma_z}_{5\,4}} & \mathcal{D}^{2\,\rho}_{5\,4} & & & & \\
 & & \mathcal{D}^{4\,z}_{5\,4} & \mathcal{D}^{4\,T}_{5\,4} & \mathcal{D}^{4\,\Sigma_z}_{5\,4} & {\color{red}\mathcal{D}^{4\,\rho}_{5\,4}} & & & & &
\end{array}\right)$$

Already in our minimalistic example, the compact form $\tilde{\mathcal{H}}$ is considerably smaller than the original matrix $\mathcal{H}$ (176 entries against 256 entries, or 68.75% of the original size). For serious applications, the number of grid cells N_i is of the order of hundreds. Given, for example, $N_i = 10^2$, the compact form requires only 4400 entries to be stored, compared to 160000 for the original matrix. In other words, the original size is reduced to $11/400 = 2.75\%$.

In order to calculate and address the entries of $\tilde{\mathcal{H}}$ directly, we note that $\mathcal{D}^{l\,x}_{i_1\,i_2}$ is stored in element $\tilde{\mathcal{H}}_{u_x\,v_x}$ with

$$\begin{array}{rcl@{\qquad}rclclcl}
u_z & = & 2 + 4\cdot(i_1 - 2) + l\,, & u_z & = & u_T & = & u_{\Sigma_z} & = & u_\rho\,, \\
v_z & = & 4\cdot(i_2 - i_1 + 2) - (l-1)\,, & v_z & = & v_T - 1 & = & v_{\Sigma_z} - 2 & = & v_\rho - 3
\end{array}$$

for the general case $i_1 \neq \{1, N_i + 1\}$. For the special case $i_1 = 1$,

$$\begin{array}{rcl@{\qquad}rclclcl}
u_z & = & 1 + (l-1)/2\,, & u_z & = & u_T & = & u_{\Sigma_z} & = & u_\rho\,, \\
v_z & = & 6 - (l-1)/2\,, & v_z & = & v_T - 1 & = & v_{\Sigma_z} - 2 & = & v_\rho - 3\,,
\end{array}$$

and for $i_1 = N_i + 1$,

$$\begin{array}{rcl@{\qquad}rclclcl}
u_z & = & 2 + 4\cdot(i_1 - 2) + l/2\,, & u_z & = & u_T & = & u_{\Sigma_z} & = & u_\rho\,, \\
v_z & = & 4 - (l-2)/2\,, & v_z & = & v_T - 1 & = & v_{\Sigma_z} - 2 & = & v_\rho - 3\,.
\end{array}$$

The solution $\Delta\mathcal{G}$ for of the set of linear equations (A.21) is calculated efficiently by a LU-decomposition of the compact matrix $\tilde{\mathcal{H}}$ with a subsequent backsubstitution using the values of $\mathcal{G}$ from the current solutions for z, T, Σ_z and ρ. We apply the routines `bandec` and `banbks` from Press et al. (2001, p. 45–46) for these two steps.

A.3 Iron K-shell fluorescence data

Table A.3. Iron K-shell fluorescence data. Fluorescence yields and line energies are taken from Kaastra & Mewe (1993).

ion	line	E [eV]	γ_{rad} [s^{-1}]	Y_i
Fe I	$\mathrm{K}_{\alpha 2}$	$6.391E+03$	$2.000E+14$	$1.013E-01$
	$\mathrm{K}_{\alpha 1}$	$6.405E+03$	$1.000E+14$	$2.026E-01$
	$\mathrm{K}_{\beta 2}$	$7.057E+03$	$1.000E+14$	$0.127E-01$
	$\mathrm{K}_{\beta 1}$	$7.058E+03$	$5.000E+13$	$0.254E-01$
Fe II	$\mathrm{K}_{\alpha 2}$	$6.408E+03$	$2.000E+14$	$1.014E-01$
	$\mathrm{K}_{\alpha 1}$	$6.419E+03$	$1.000E+14$	$2.028E-01$
	$\mathrm{K}_{\beta 2}$	$7.081E+03$	$1.000E+14$	$0.127E-01$
	$\mathrm{K}_{\beta 1}$	$7.083E+03$	$5.000E+13$	$0.255E-01$
Fe III	$\mathrm{K}_{\alpha 2}$	$6.422E+03$	$2.000E+14$	$1.015E-01$
	$\mathrm{K}_{\alpha 1}$	$6.434E+03$	$1.000E+14$	$2.030E-01$
	$\mathrm{K}_{\beta 2}$	$7.106E+03$	$1.000E+14$	$0.127E-01$
	$\mathrm{K}_{\beta 1}$	$7.107E+03$	$5.000E+13$	$0.255E-01$
Fe IV	$\mathrm{K}_{\alpha 2}$	$6.436E+03$	$2.000E+14$	$1.016E-01$
	$\mathrm{K}_{\alpha 1}$	$6.449E+03$	$1.000E+14$	$2.032E-01$
	$\mathrm{K}_{\beta 2}$	$7.129E+03$	$1.000E+14$	$0.128E-01$
	$\mathrm{K}_{\beta 1}$	$7.132E+03$	$5.000E+13$	$0.255E-01$
Fe V	$\mathrm{K}_{\alpha 2}$	$6.449E+03$	$2.000E+14$	$1.017E-01$
	$\mathrm{K}_{\alpha 1}$	$6.462E+03$	$1.000E+14$	$2.034E-01$
	$\mathrm{K}_{\beta 2}$	$7.152E+03$	$1.000E+14$	$0.128E-01$
	$\mathrm{K}_{\beta 1}$	$7.153E+03$	$5.000E+13$	$0.255E-01$
Fe VI	$\mathrm{K}_{\alpha 2}$	$6.464E+03$	$2.000E+14$	$1.018E-01$
	$\mathrm{K}_{\alpha 1}$	$6.477E+03$	$1.000E+14$	$2.035E-01$
	$\mathrm{K}_{\beta 2}$	$7.176E+03$	$1.000E+14$	$0.128E-01$
	$\mathrm{K}_{\beta 1}$	$7.180E+03$	$5.000E+13$	$0.255E-01$
Fe VII	$\mathrm{K}_{\alpha 2}$	$6.479E+03$	$2.000E+14$	$1.018E-01$
	$\mathrm{K}_{\alpha 1}$	$6.492E+03$	$1.000E+14$	$2.037E-01$
	$\mathrm{K}_{\beta 2}$	$7.203E+03$	$1.000E+14$	$0.128E-01$
	$\mathrm{K}_{\beta 1}$	$7.204E+03$	$5.000E+13$	$0.256E-01$
Fe VIII	$\mathrm{K}_{\alpha 2}$	$6.494E+03$	$2.000E+14$	$1.019E-01$
	$\mathrm{K}_{\alpha 1}$	$6.507E+03$	$1.000E+14$	$2.038E-01$
	$\mathrm{K}_{\beta 2}$	$7.224E+03$	$1.000E+14$	$0.128E-01$
	$\mathrm{K}_{\beta 1}$	$7.228E+03$	$5.000E+13$	$0.256E-01$
Fe IX	$\mathrm{K}_{\alpha 2}$	$6.509E+03$	$2.000E+14$	$1.020E-01$
	$\mathrm{K}_{\alpha 1}$	$6.521E+03$	$1.000E+14$	$2.040E-01$
Fe IX	$\mathrm{K}_{\beta 2}$	$7.249E+03$	$1.000E+14$	$0.128E-01$
	$\mathrm{K}_{\beta 1}$	$7.251E+03$	$5.000E+13$	$0.256E-01$
Fe X	$\mathrm{K}_{\alpha 2}$	$6.522E+03$	$2.000E+14$	$1.046E-01$
	$\mathrm{K}_{\alpha 1}$	$6.534E+03$	$1.000E+14$	$2.092E-01$
	$\mathrm{K}_{\beta 2}$	$7.273E+03$	$1.000E+14$	$0.131E-01$
	$\mathrm{K}_{\beta 1}$	$7.273E+03$	$5.000E+13$	$0.197E-01$
Fe XI	$\mathrm{K}_{\alpha 2}$	$6.536E+03$	$2.000E+14$	$1.074E-01$
	$\mathrm{K}_{\alpha 1}$	$6.549E+03$	$1.000E+14$	$2.147E-01$
	$\mathrm{K}_{\beta 2}$	$7.295E+03$	$1.000E+14$	$0.135E-01$
	$\mathrm{K}_{\beta 1}$	$7.295E+03$	$5.000E+13$	$0.135E-01$
Fe XII	$\mathrm{K}_{\alpha 2}$	$6.551E+03$	$2.000E+14$	$1.102E-01$
	$\mathrm{K}_{\alpha 1}$	$6.563E+03$	$1.000E+14$	$2.204E-01$
	$\mathrm{K}_{\beta 2}$	$7.305E+03$	$1.000E+14$	$0.138E-01$
	$\mathrm{K}_{\beta 1}$	$7.305E+03$	$5.000E+13$	$0.069E-01$
Fe XIII	$\mathrm{K}_{\alpha 2}$	$6.563E+03$	$2.000E+14$	$1.132E-01$
	$\mathrm{K}_{\alpha 1}$	$6.577E+03$	$1.000E+14$	$2.264E-01$
	$\mathrm{K}_{\beta 2}$	$7.325E+03$	$1.000E+14$	$0.142E-01$
Fe XIV	$\mathrm{K}_{\alpha 2}$	$6.578E+03$	$2.000E+14$	$1.162E-01$
	$\mathrm{K}_{\alpha 1}$	$6.590E+03$	$1.000E+14$	$2.325E-01$
	$\mathrm{K}_{\beta 2}$	$7.345E+03$	$1.000E+14$	$0.073E-01$
Fe XV	$\mathrm{K}_{\alpha 2}$	$6.590E+03$	$2.000E+14$	$1.194E-01$
	$\mathrm{K}_{\alpha 1}$	$6.602E+03$	$1.000E+14$	$2.389E-01$
Fe XVI	$\mathrm{K}_{\alpha 2}$	$6.602E+03$	$2.000E+14$	$1.213E-01$
	$\mathrm{K}_{\alpha 1}$	$6.615E+03$	$1.000E+14$	$2.425E-01$
Fe XVII	$\mathrm{K}_{\alpha 2}$	$6.613E+03$	$2.000E+14$	$1.231E-01$
	$\mathrm{K}_{\alpha 1}$	$6.627E+03$	$1.000E+14$	$2.461E-01$
Fe XVIII	$\mathrm{K}_{\alpha 2}$	$6.631E+03$	$2.000E+14$	$1.606E-01$
	$\mathrm{K}_{\alpha 1}$	$6.631E+03$	$1.000E+14$	$2.409E-01$
Fe XIX	$\mathrm{K}_{\alpha 2}$	$6.631E+03$	$2.000E+14$	$2.202E-01$
	$\mathrm{K}_{\alpha 1}$	$6.631E+03$	$1.000E+14$	$2.202E-01$
Fe XX	$\mathrm{K}_{\alpha 2}$	$6.605E+03$	$2.000E+14$	$3.258E-01$
	$\mathrm{K}_{\alpha 1}$	$6.605E+03$	$1.000E+14$	$1.229E-01$
Fe XXI	$\mathrm{K}_{\alpha 2}$	$6.596E+03$	$2.000E+14$	$5.521E-01$
	$\mathrm{K}_{\alpha 2}$	$6.586E+03$	$2.000E+14$	$4.903E-01$